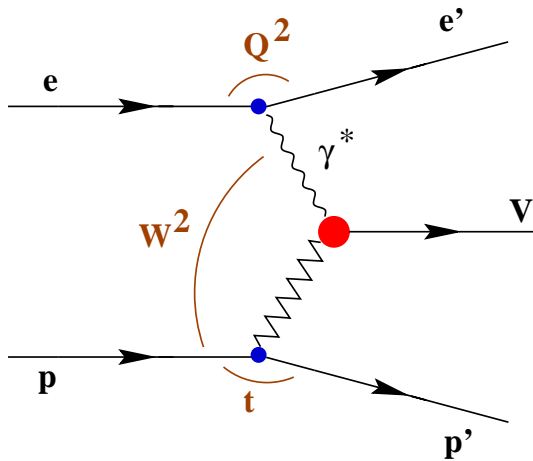

Diffractive Production of ρ^0 and ω Vector Mesons at HERMES



Michael Tytgat



Faculteit Wetenschappen
Vakgroep Subatomaire en Stralingsfysica
Academiejaar 2000-2001

Mother Nature is a mad scientist !
Kramer (Seinfeld, Episode 152)

Diffraction Production of ρ^0 and ω Vector Mesons at HERMES

Diffraction productie van ρ^0 en ω vector mesonen in HERMES

Promotor: Prof. Dr. D. Ryckbosch

Proefschrift ingediend tot het verkrijgen van de graad van
Doctor in de Wetenschappen, groep Natuurkunde
door

Michael Tytgat

Contents

3.2	Beam Polarization at HERMES	51
3.2.1	Spontaneous Polarization in Storage Rings	51
3.2.2	The HERA Spin Rotators	53
3.2.3	The HERMES Polarimeters	54
3.3	The HERMES Internal Gas Target	56
3.3.1	The Polarized ^3He Target	58
3.3.2	The Polarized H-D Target	59
3.4	The HERMES Spectrometer	62
3.4.1	Tracking Detectors	63
3.4.1.1	The Vertex Chambers	64
3.4.1.2	The Drift Chambers	65
3.4.1.3	The Magnet Chambers	66
3.4.2	The Laser Alignment System	66
3.4.3	Particle Identification Detectors	66
3.4.3.1	The Čerenkov Detector	67
3.4.3.2	The Transition Radiation Detector	68
3.4.3.3	The Hodoscopes	70
3.4.3.4	The Calorimeter	71
3.4.4	The Luminosity Monitor	74
3.4.5	The Gain Monitoring System	75
3.4.6	The Trigger	75
3.4.7	Data Acquisition	77
3.4.8	Online Monitoring	77
4	The HERMES Ring Imaging Čerenkov Detector	79
4.1	Physics Motivation of the RICH	79
4.2	General Design of the RICH	80
4.3	The PCOS4 System	83
4.4	The PMT Testbench	84
4.5	The Photon Detector	86
4.6	The Aerogel Radiator	89
4.7	The Readout System	90
4.8	Particle Identification Algorithms	91
4.8.1	Inverse Ray Tracing Based Algorithm	92
4.8.2	Direct Ray Tracing Based Algorithm	93
4.8.3	First Results of the RICH	94
5	Event Reconstruction and Data Analysis	97
5.1	The HERMES Data Organization	97
5.2	Data Production	98
5.3	Tracking and Clustering	99
5.4	Particle Identification	101
5.5	The HERMES Monte Carlo	104
1	Introduction	1
5	2 Diffractive Vector Meson Production	5
5	2.1 Kinematics	5
7	2.2 Deep Inelastic Scattering	7
10	2.3 Photon Fluxes	10
11	2.4 Diffraction	11
12	2.5 Optical Model of Diffraction	12
15	2.6 Regge Theory	15
21	2.7 Partonic Structure of the Pomeron	21
23	2.8 Vector Meson Dominance Model	23
26	2.9 Generalized Vector Meson Dominance Model	26
27	2.10 Off-forward Parton Distributions	27
29	2.11 Nonperturbative Models	29
29	2.11.1 The Donnachie and Landshoff Model	29
29	2.11.2 The Model of Haakman <i>et al.</i>	29
31	2.12 Perturbative QCD Models	31
32	2.12.1 The Ryskin Model	32
34	2.12.2 The Model of Brodsky <i>et al.</i>	34
35	2.12.3 The Model of Martin <i>et al.</i>	35
37	2.12.4 The Model of Vanderhaeghen <i>et al.</i>	37
38	2.12.5 The Model of Royen <i>et al.</i>	38
39	2.13 Vector Meson Polarization	39
39	2.13.1 The Photon Spin Density Matrix	39
41	2.13.2 The Vector Meson Spin Density Matrix	41
42	2.13.3 Vector Meson Decay Angular Distribution	42
44	2.13.4 s -Channel Helicity Conservation	44
45	2.13.5 Natural and Unnatural Parity Exchange	45
46	2.13.6 Model Calculations	46
47	2.13.7 Double Polarized Formalism	47
47	2.14 Measurements of Vector Meson Production	47
49	3 The HERMES Experimental Setup	49
49	3.1 The HERA Storage Ring Facility	49

6 Data Quality and Event Selection	107
6.1 Data Quality	107
6.1.1 Beam and Target Criteria	108
6.1.2 Luminosity	109
6.1.3 Data Acquisition	109
6.1.4 Tracking Chambers	110
6.1.5 Trigger and Particle Identification Detectors	110
6.1.6 Overall Stability	111
6.2 Event Selection	112
6.2.1 Selection of Scattered Positrons, Hadrons and Photons	115
6.2.2 Selection of Exclusive, Diffractive Events	116
6.2.2.1 Selection of ρ^0 Events	119
6.2.2.2 Selection of ω Events	122
6.2.3 Selection of Quasi-real ω Photoproduction Events	126
6.3 Addendum 1: Charged ρ Production	127
6.4 Addendum 2: η Production	127
7 Monte Carlo Studies	131
7.1 The VDM ρ^0 Generator	131
7.2 The DIPSI Generator	132
7.3 Data to Monte Carlo Comparison	133
7.4 Acceptance and Reconstruction Efficiency	134
7.5 Resolution	137
7.6 Monte Carlo DIS Background Studies	140
8 ρ^0 and ω Invariant Mass Distribution	143
8.1 ρ^0 Invariant Mass Distribution	143
8.1.1 Background Treatment	144
8.1.2 ρ^0 Invariant Mass Acceptance	145
8.1.3 The Breit-Wigner Lineshape	146
8.1.4 The Ross-Stodolsky Lineshape	147
8.1.5 The Söding Lineshape	148
8.1.6 ρ^0 - ω Interference	150
8.1.7 Kinematical Dependence of the Invariant Mass Distribution	154
8.2 ω Invariant Mass Distribution	160
9 The γ^*p Cross Sections	163
9.1 Extraction of Absolute γ^*p Cross Section	163
9.2 Luminosity Determination	164
9.3 Acceptance Correction	167
9.4 DIS Background Subtraction	168
9.4.1 DIS Monte Carlo Method	169
9.4.2 Zone Method	169

9.4.3 Fit Method	170
9.5 Double Dissociative Background	171
9.6 Radiative Corrections	173
9.7 The ρ^0 and ω Cross Section	177
9.8 Q^2 -Dependence of the γ^*p Cross Sections	180
9.9 World Data on ρ^0 and ω Production	185
9.10 Comparison to Model Calculations	185
9.11 Cross Section Ratios	189
9.12 Slope Parameters	190
9.13 Nuclear Transparency	198
9.14 Coherent vs. Incoherent Cross Section	201
10 The ω Real Photoproduction Cross Section	203
10.1 Reconstruction of Photoproduction Trigger Event Kinematics	203
10.2 Photoproduction Trigger Efficiency	205
10.3 Determination of the Real Photon Flux	205
10.4 Non-exclusive Background Subtraction	207
10.5 Acceptance Correction	207
10.6 Extraction of the Absolute γp Cross Section	210
11 ρ^0 Decay Angle Distribution Analysis	215
11.1 Spin Density Matrix Element Extraction Algorithms	215
11.1.1 The Method of Moments	215
11.1.2 Modified Method of Moments	217
11.1.3 The Maximum Likelihood Method	217
11.1.4 1-dimensional Least Square Fitting Method	218
11.1.5 Discussion of Different Extraction Methods	218
11.1.6 Monte Carlo Tests	219
11.2 Radiative Corrections	221
11.3 The ρ^0 Spin Density Matrix Elements	222
11.4 Theory Predictions	227
11.5 Natural Parity Exchange	227
11.6 s -Channel Helicity Conservation	230
11.7 1-dimensional Decay Angle Distributions	232
11.8 Extraction of Helicity Amplitudes	234
11.9 Extraction of R_ρ	236
11.10 Extraction of δ	238
12 Conclusions	241
A Data Quality Summary Tables	245
B Tables	247

C Additional Figures	253
D Vector Meson Spin Density Matrix Elements	259
Bibliography	261
Samenvatting	269
Acknowledgements	275

state. These mesons appear in pure fragmentation processes in deep inelastic scattering, but can also be produced in exclusive scattering reactions, which is where they prove to be of most interest.

Exclusive vector meson production gives access to a large variety of topics both in particle and nuclear physics. It is related to the off-forward parton distribution formalism, which not only provides the link between several different exclusive production processes, but may eventually lead to a very first determination of the quark and gluon orbital angular momentum contribution to the nucleon spin. In the vector meson dominance model exclusive photoproduction of vector mesons is closely related to hadronic scattering and therefore fits into a uniform description of hadron-hadron and photon-hadron processes and allows a detailed study of the hadronic properties of the photon. In the perturbative QCD regime vector meson production is connected to the gluon content of the proton and may provide a valuable tool to measure the gluon distribution. It also serves as a nice experimental way to provide more insight in the nature of strong interactions and to check the various different QCD models describing high energy and hard interactions. The study of vector meson production on compound nuclear targets provides information on initial and final state interactions and could be a way to observe new phenomena like color transparency.

In this work exclusive production of ρ^0 and ω vector mesons is studied in the kinematic regime accessible with the HERMES experiment. Based on the similar quark content of these mesons, both production processes are expected to exhibit similar features in this energy region, which is one of the issues we try to confirm here. In terms of vector meson production HERMES is situated in the intermediate energy region where a transition is expected between the low energy production physics probed by various fixed target experiments in the past and the high energy domain which is now actively under study also at HERA. The layout of the HERMES detector allows to study the production of different kinds of vector mesons at the same time, yielding a very complete picture of these processes in this particular kinematic region. Moreover, with its polarized target and the polarized HERA lepton beam, HERMES has the unique possibility to perform measurements of polarized exclusive vector meson production.

Chapter 2 is devoted to an overview of the theory associated with exclusive vector meson production. Several models and tools to describe this kind of processes in the different kinematical domains are presented. A few of these models will be tested against our results in the following chapters.

The experimental setup is described in chapter 3, where we start with a short overview of the HERA accelerator complex. Next, the different HERMES targets are presented in more detail, followed by a description of the various spectrometer components and the data acquisition system.

After the 1995-97 HERA physics run, the HERMES spectrometer was partially upgraded to improve its capabilities for semi-inclusive measurements. The existing threshold Čerenkov counter was replaced by a Ring Imaging Čerenkov detector. The Gent group was involved in the construction and start-up phase of the detector whose design is presented in chapter 4.

The decoding and reconstruction of the measured data is explained in chapter 5,

Chapter 1

Introduction

Understanding the fundamental structure of matter has been a major challenge for both theoretical and experimental physics since the beginning of the previous century. The standard model in particle physics considers the basic building blocks of matter to be six quarks and six leptons. Gluons, the gauge bosons of the strong force in quantum chromodynamics (QCD), bind the quarks together to form hadrons. Baryons are composed of three quarks and mesons contain a quark and antiquark. Scattering experiments have always been an excellent tool to study the substructure of matter. In general the continuous increase in available beam energies in particle accelerators has allowed a more and more consistent description of matter and the strong interaction.

Historically, deep inelastic scattering experiments provided the first indication of the point-like constituents in the nucleon. While the basic nucleon structure is nowadays well understood, a surprising discovery was made when polarized inclusive deep inelastic scattering revealed that less than half of the nucleon spin was carried by the quarks. The missing part of the nucleon spin could then be due to the gluons and/or the orbital angular momentum of the quarks and gluons. The HERMES (HERA MEasurement of Spin) experiment at HERA (Hadron-Electron Ring Accelerator) was designed as a high precision tool to study the puzzle of the spin structure of the nucleon by scattering a polarized lepton beam deeply inelastic off a polarized nucleon target. To accomplish this task a multipurpose forward spectrometer was built capable of performing both (un)polarized inclusive and semi-inclusive measurements. Inclusive spin asymmetries lead to the determination of g_1 [1], the spin dependent nucleon structure function, while semi-inclusive hadron asymmetries yield detailed information on the individual quark flavor spin distributions [2] and possibly even on the gluon spin distribution [3].

The particle identification capabilities of the HERMES detector allow, apart from an extensive spin physics program, also the study of a wide variety of meson production processes. Important topics include e.g. charm detection, which may lead to a determination of the gluon spin distribution. Another major issue is the study of a special class of mesons, called vector mesons, where the spin-1/2 quark and antiquark couple to a spin-1

where the offline software chain and in particular the tracking routine and the particle identification algorithm are described. A short presentation is given of the general Monte Carlo code used to simulate the HERMES detector.

The physics analysis part of this work starts in chapter 6, where we begin with a detailed description of the selection of the data and event samples to be used in the following analysis sections.

The analysis presented here relies heavily on Monte Carlo simulations of the experiment. The different generators used in this work, together with some applications of these simulations in our vector meson analysis are described in chapter 7.

Chapter 8 deals with a detailed study of the ρ^0 and ω invariant mass distribution. Especially for the ρ^0 interesting phenomena like the skewing of the invariant mass distribution and $\rho^0 - \omega$ interference are investigated.

The extraction of the absolute ρ^0 and ω production cross sections by virtual photons, together with the dependencies on different kinematical variables is described in chapter 9. The predictions of several theoretical models are tested against the results. The ω/ρ^0 production ratio is determined and the virtual photoproduction cross sections are extrapolated to the real photoproduction region. The chapter is ended with a discussion on nuclear medium effects in vector meson production on composite nuclei.

Chapter 10 deals with an alternative extraction of the real photoproduction cross section for ω mesons.

The analysis of the vector meson angular decay related to the description of the helicity transfer in the production mechanism, is presented in chapter 11. Different algorithms to extract the helicity information from the data are discussed. The results for the ρ^0 spin density matrix elements and the helicity amplitude ratios are compared to theoretical model calculations.

The final results and conclusions are summarized in chapter 12.

is given by

$$Q^2 \equiv -q^2 = -(k - k')^2 \approx 4 E E' \sin^2 \left(\frac{\theta}{2} \right), \quad (2.2)$$

which has positive values for a spacelike photon. In this equation the electron rest mass is neglected with respect to the lepton momentum. The Bjorken scaling variable x is defined as

$$x \equiv \frac{Q^2}{2 p \cdot q} = \frac{Q^2}{2 M \nu}, \quad (2.3)$$

with

$$\nu \equiv \frac{p \cdot q}{M} \equiv E - E', \quad (2.4)$$

so that ν represents the energy transfer from the incoming lepton to the virtual photon in the laboratory frame. The Bjorken scaling variable y is given by

$$y = \frac{p \cdot q}{p \cdot k} \frac{\nu}{E}, \quad (2.5)$$

which in the laboratory system denotes the fractional energy of the virtual photon with respect to the beam energy.

The squared center-of-mass energy of the photon-proton system is given by

$$W^2 = (q + p)^2 = M^2 + 2 M \nu - Q^2 = M^2 + Q^2 \frac{1-x}{x}. \quad (2.6)$$

The last part of the equation shows that for $x = 1$, one finds $W = M$, which corresponds to elastic scattering. The square of the lepton-proton center of mass energy is denoted as

$$s \equiv (k + p)^2 \approx M^2 + 2 M E, \quad (2.7)$$

which in the case of HERMES with a beam energy of 27.5 GeV gives $\sqrt{s} = 7.2$ GeV.

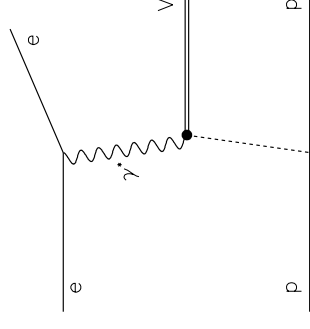


Figure 2.1: Schematic representation of exclusive vector meson production in electron scattering.

In the context of diffractive vector meson production as depicted in figure 2.1 one commonly uses the squared four-momentum transfer to the hadronic vertex

$$t = (q - v)^2 = (p - p')^2, \quad (2.8)$$

Chapter 2

Diffractive Vector Meson Production

In this chapter the concept of diffractive interactions is explained with emphasis on exclusive, diffractive vector meson production. First, a general introduction to deep inelastic scattering is given as some of its concepts reappear in the description of vector meson production. Of practical use is the derivation of the relation between electro- and photoproduction cross sections and of the photon flux factors, which prove their usefulness in the analysis performed in this work. Next, the key features of diffractive interactions are described. Before dealing with several theoretical descriptions of vector meson production, an introduction is given to basic ingredients of these model calculations, i.e. Regge theory, the vector meson dominance model and the off-forward parton distribution framework. Some of the theoretical models presented here will be used to describe results obtained in this work. The chapter ends with a detailed discussion of the vector meson polarization formalism, which forms the basis of part of the analysis presented later on in this work.

Throughout this work natural units will be used in which $\hbar = c = 1$.

2.1 Kinematics

The four-momenta of the incoming and outgoing lepton are denoted as k and k' respectively. The target nucleon has a four-momentum p and rest mass M . The four-momentum and energy of the hadronic final state is p' and $E_{p'}$. In the HERMES laboratory frame (lab) the target is at rest and the energy of the initial and scattered lepton is denoted as E and E' respectively, while the scattering angle between the incoming and outgoing lepton momentum is θ .

The four-momentum of the exchanged virtual photon is then

$$q \equiv k - k'. \quad (2.1)$$

The negative square of the four-momentum of the virtual photon or the photon virtuality

where v is the four-momentum of the vector meson. In the laboratory system one obtains from the second part of the latter equation for exclusive scattering

$$t = 2M(M - E_p), \quad (2.9)$$

which gives a simple expression for the recoil target energy as function of t .

An often encountered variable is the polarization parameter

$$\epsilon = \frac{1-y}{1-y+y^2/2} \frac{lab}{\equiv} \left(1 + 2(1 + \frac{v^2}{Q^2}) \tan^2 \frac{\theta}{2} \right)^{-1}, \quad (2.10)$$

expressing the ratio of the longitudinal to transverse photon flux.

2.2 Deep Inelastic Scattering

The deep inelastic scattering process (DIS) of an electron or positron from a nucleon or nuclear target is depicted in lowest order in figure 2.2. Here we consider only the diagram where the exchanged boson is a virtual photon, as weak interaction processes mediated by the exchange of a heavy intermediate vector boson W^\pm or Z^0 can be neglected for the energy and momentum transfers reachable in the HERMES experiment. Multi-photon exchange diagrams are suppressed by a factor of α_{em} and may be taken into account via so-called radiative corrections.

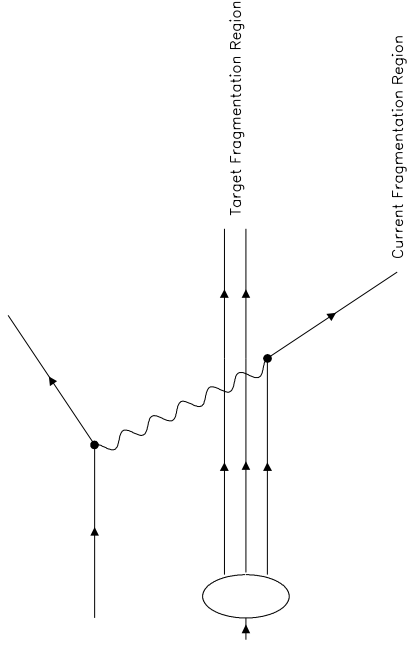


Figure 2.2: Schematic representation of the deep-inelastic scattering process in the quark-parton model with the one-photon exchange approximation.

The kinematics of an inclusive event are completely constrained by two independent variables, where often Q^2 and x are chosen. The DIS regime is usually defined via the kinematical constraints to have a large momentum transfer (e.g. $Q^2 > 1 \text{ GeV}^2$) and a

large photon-nucleon center of mass energy (e.g. $W^2 > 4 \text{ GeV}^2$). The cross section for DIS can in the one-photon exchange approximation be written in terms of the leptonic and hadronic tensor $L_{\mu\nu}$ and $W_{\mu\nu}$ [4]

$$\frac{d^2\sigma^{ep}}{d\Omega dE'} = \frac{\alpha^2 E'}{Q^4 E} L^{\mu\nu} \mu\nu, \quad (2.11)$$

where $\alpha \approx 1/137$ is the fine-structure constant. The leptonic tensor describes the emission of the virtual photon by the incoming lepton and is exactly calculable in quantum electrodynamics (QED) giving

$$L^{\mu\nu} = 2 [k^\mu k'^\nu + k'^\mu k^\nu + (m_e^2 - k \cdot k') g^{\mu\nu}] - 2i \epsilon^{\mu\nu\alpha\beta} q_\alpha s_\beta, \quad (2.12)$$

where $g^{\mu\nu}$ is the metric tensor, $\epsilon^{\mu\nu\alpha\beta}$ the totally anti-symmetric Levi-Civita tensor and m_e the electron mass. The first part is symmetric, while the second term is anti-symmetric and describes the dependence on the initial lepton spin s_β . The hadronic tensor cannot be calculated exactly and is therefore parametrized in terms of structure functions which need to be determined experimentally. Symmetry arguments and current conservation at the hadronic vertex lead to a description with two independent structure functions W_1 and W_2 for the symmetric part and two functions G_1 and G_2 for the spin dependent part

$$W_{\mu\nu} = W_1 \left(-g_{\mu\nu} + \frac{q_\mu q_\nu}{q^2} \right) + \frac{W_2}{M^2} \left(p_\mu - \frac{p \cdot q}{q^2} q_\mu \right) \left(p_\nu - \frac{p \cdot q}{q^2} q_\nu \right) + i \epsilon^{\mu\nu\alpha\beta} q^\alpha M S^\beta G_1 + i \epsilon^{\mu\nu\alpha\beta} q^\alpha [(p \cdot q) S^\beta - (S \cdot q) p^\beta] \frac{G_2}{M}, \quad (2.13)$$

where S denotes the polarization vector of the spin-1/2 target nucleon. The cross section is usually written in terms of the four dimensionless structure functions

$$F_1(x, Q^2) = M W_1(Q^2, \nu), \quad F_2(x, Q^2) = \nu W_2(Q^2, \nu), \quad (2.14)$$

$$g_1(x, Q^2) = M^2 \nu G_1(Q^2, \nu), \quad g_2(x, Q^2) = M \nu^2 G_2(Q^2, \nu).$$

These functions describe the internal structure of the target nucleon and exhibit scaling behavior, which means that they appear to be approximately independent of the Q^2 -scale and are only a function of the Bjorken variable x . As the distance scale probed by the photon goes like $1/Q$, the Q^2 -scale defines the ‘resolution’ of the scattering process. The observed scaling behavior of the structure functions therefore leads to the interpretation that the scattering occurs on nucleon internal components which are much smaller than the distance scale of the process and can be treated as point-like objects. In the quark-parton model the nucleon is actually described as being composed of non-interacting point-like on-shell particles, which can be identified as spin 1/2 quarks. In the Bjorken limit, i.e. for $Q^2 \rightarrow \infty$ and $\nu \rightarrow \infty$ while keeping x constant, the quarks behave as free particles, due to the asymptotic freedom of QCD. In this limit deep-inelastic scattering can be regarded as elastic scattering off these quasi-free quarks, which leads to the picture of DIS as shown in figure 2.2 : in the scattering process the virtual photon is absorbed by one of the quarks in the nucleon; the struck quark leaves the target and fragments independently of the remains of the nucleon.

To finally come to the unpolarized DIS cross section one has to sum over the initial lepton and hadron spin states so that the anti-symmetric parts of the leptonic and hadronic

tensors cancel out and equation 2.11 becomes

$$\frac{d^2\sigma}{dx dQ^2} = \frac{4\pi\alpha^2}{Q^4} \left[F_1(x, Q^2) y^2 \left(1 - \frac{2m_e^2}{Q^2}\right) + \frac{F_2(x, Q^2)}{x} \left(1 - y - \frac{Mxy}{2E}\right) \right]. \quad (2.15)$$

In the infinite momentum frame where the nucleon has an infinitely large momentum so that the masses and transverse momenta of the quarks can be neglected, the Bjorken variable x can be interpreted as the momentum fraction carried by the struck quark relative to the total nucleon momentum. One can now define quark distribution functions $q_f(x, Q^2)$, which represent the probability to find a quark of flavour f with momentum fraction x inside the nucleon. Calculating in the quark-parton model the hadronic tensor for the elastic scattering cross section off quarks in the nucleon leads after comparison to equation 2.13 to the following interpretation of the nucleon structure functions

$$F_1(x, Q^2) = \frac{1}{2} \sum_f e_f^2 (q_f^+(x, Q^2) + q_f^-(x, Q^2)), \quad (2.16)$$

$$F_2(x, Q^2) = \sum_f e_f^2 x (q_f^+(x, Q^2) + q_f^-(x, Q^2)), \quad (2.17)$$

$$g_1(x, Q^2) = \frac{1}{2} \sum_f e_f^2 (q_f^+(x, Q^2) - q_f^-(x, Q^2)), \quad (2.18)$$

$$g_2(x, Q^2) = 0. \quad (2.19)$$

In the unpolarized quark distribution function $q_f = q_f^+ + q_f^-$ and the polarized quark distribution function $\Delta q_f = q_f^+ - q_f^-$, $q^{+(\pm)}(x, Q^2)$ denotes the probability to find a quark with momentum fraction x and spin parallel (anti-parallel) to the nucleon spin. The unpolarized (polarized) structure function F_1 (g_1) is proportional to the sum of the unpolarized (polarized) quark density functions weighted by the squared quark charge. Combining equation 2.16 and 2.17 one finds the so-called Callan-Gross relation

$$F_2(x, Q^2) = 2x F_1(x, Q^2). \quad (2.20)$$

In the quark-parton model where quark masses and transverse momenta are neglected the g_2 structure function is equal to zero.

As already mentioned, in the Bjorken limit these structure functions become independent of Q^2 . Experimentally one finds a weak scaling violation due to the quark interactions mediated by gluons, which are not considered in the simple quark-parton model. The presence of the gluons in the nucleon lie behind the violation of the Callan-Gross relation and the momentum sum rule

$$\sum_f \int dx x q_f(x) = 1. \quad (2.21)$$

The gluons carry a large fraction of the nucleon momentum and they modify the structure functions via QCD radiative corrections. With increasing Q^2 the scale that is probed inside the nucleon decreases and finer structures can be resolved: the radiation of gluons from quarks, quark-antiquark pair production or gluon splitting. In this way the quark distributions interacting with the photon will evolve with Q^2 and the Q^2 dependence of

the parton distribution functions or structure functions has to be described via QCD evolution equations. Depending on the kinematic region in x and Q^2 different equation have to be applied. The region of moderate Bjorken- x is described by the Gribov-Lipatov-Altarelli-Parisi (GLAP) equations [5] for each quark flavor. Towards very small $x \ll 1$, at moderate Q^2 the Balitsky-Fadin-Kuraev-Lipatov (BFKL) equation [6] is used. Here the gluon density is predicted to behave as $xg \stackrel{x \rightarrow 0}{\sim} x^{-\beta_g}$ with $\beta_g \approx 0.5$, and thus rises very rapidly at low x .

2.3 Photon Fluxes

The interesting physics one tries to study in electron scattering processes is actually contained in the hadronic vertex. It is therefore natural to consider the $\gamma^* p$ process, while strictly speaking one measures ep reactions. In the Weizsäcker-Williams approach (WWA) the lepton-hadron scattering is divided up into two parts, where the emission probability of a virtual photon is calculated separately from the absorption of a photon by the hadron. The cross section is then transformed into a product of a photon spectrum and a photon absorption cross section at the hadronic vertex. In general one has contributions from transverse and longitudinally polarized photons giving

$$\frac{d^2\sigma}{dx dQ^2} = \Gamma_T(Q^2, x) \sigma_T^{*p}(Q^2, x) + \Gamma_L(Q^2, x) \sigma_L^{*p}(Q^2, x), \quad (2.22)$$

where Γ_T and Γ_L represent the flux of transverse and longitudinal virtual photons respectively. The definition of these fluxes is really a matter of convention as only the product of the flux with $\sigma_{T,L/T}$ is uniquely defined.

Representing the incident photon flux as K , then the cross section for the nucleon photonabsorption cross section for a photon moving along the z -axis is [4]

$$\sigma_\lambda^{\gamma p} = \frac{4\pi^2\alpha}{K} \epsilon_\lambda^{\mu\nu} W_{\mu\nu}, \quad (2.23)$$

where the hadronic tensor is given by equation 2.13 and ϵ_λ is the polarization vector of the photon. A real photon can have helicity $\lambda = \pm 1$. A virtual photon can apart from being transversely ($\lambda = \pm 1$) polarized, also have a longitudinally ($\lambda = 0$) polarized component. The polarization vectors are taken as

$$\epsilon^{\pm 1} = \frac{1}{\sqrt{2}}(0, 1, \pm i, 0), \quad (2.24)$$

$$\epsilon_0 = \frac{1}{\sqrt{Q^2}}(\sqrt{\nu^2 + Q^2}, 0, 0, \nu). \quad (2.25)$$

From equation 2.23 one can deduce that together with equations 2.24, 2.25 and 2.13

$$\sigma_f^{\gamma p} = \frac{1}{2} (\sigma_{+1}^{\gamma p} + \sigma_{-1}^{\gamma p}) = \frac{4\pi^2\alpha}{K} W_1, \quad (2.26)$$

$$\sigma_L^{\gamma p} = \sigma_0^{\gamma p} = \frac{4\pi^2\alpha}{K} \left[\left(1 + \frac{\nu^2}{Q^2}\right) W_2 - W_1 \right]. \quad (2.27)$$

As one can see the two independent photoabsorption cross sections σ_T and σ_L cause the electron scattering cross section to have two independent structure functions W_1 and W_2 .

For real photons ($Q^2 = 0$) the photon flux is $K = \nu$. For virtual photons the definition of the flux becomes somewhat arbitrary. The convention proposed by Gilman [7] is to choose

$$K_{Gilman} = \sqrt{\nu^2 + Q^2}. \quad (2.28)$$

Here we follow the approach made earlier by Hand [8] where K is chosen as the energy equal to that of a real photon which would produce the same center of mass energy as a virtual photon with energy ν , i.e. $W_{\gamma p}^2 = M^2 + 2M K_{Hand}$ leading to

$$K_{Hand} = \nu(1 - x). \quad (2.29)$$

Note that both approaches result in $K \rightarrow \nu$ in the real photon limit $Q^2 \rightarrow 0$. The structure functions W_1 and W_2 are well defined as they are determined by an experimentally measurable cross section like equation 2.11. The photoabsorption cross sections are then derived using equations 2.26 and 2.27 together with the arbitrary flux factor.

Equations 2.26 and 2.27 allow to express F_1 and F_2 in terms of $\sigma_T^{\gamma p}$ and $\sigma_L^{\gamma p}$ via equation 2.14. Equation 2.15 can then be rewritten as

$$\frac{d^2\sigma^{ep}}{dW dQ^2} = \frac{\alpha K M}{2\pi Q^2 W \nu^2} \left\{ y^2 \left(1 - \frac{2m_e^2}{Q^2} \right) + \frac{2}{1 + Q^2/\nu^2} \left(1 - y - \frac{Q^2}{4E^2} \right) \right\} \sigma_T^{\gamma p} + \frac{2}{1 + Q^2/\nu^2} \left(1 - y - \frac{Q^2}{4E^2} \right) \sigma_L^{\gamma p}, \quad (2.30)$$

where the transition is made to the differential dependence on W instead of x , which is more convenient for usage in the analysis presented in this work. Comparing this latter expression with equation 2.22 identifies the flux factors $\Gamma_T(Q^2, W)$ and $\Gamma_L(Q^2, W)$.

2.4 Diffraction

The name diffraction stems from the well-known phenomenon observed in optics when a light wave incident on an obstacle produces a characteristic pattern behind the object. In its most simple description diffraction is any deviation from geometrical optics due to the presence of an obstruction to a wavefront of light. Diffraction can in that case be explained by the Huygens-Fresnel principle of superposition of scattered waves : every point on a given wavefront can be treated as a source of secondary spherical wavelets and the total field at any point behind the wavefront is the superposition of all these individual wavelets taking into account their phases and amplitudes. In quantum mechanics the principle of superposition is also valid for probability amplitudes due to the linearity of the Schrödinger equation and because of the particle-wave duality one can expect a similar diffraction phenomenon in hadron scattering as in optics.

The term diffraction was introduced in high energy nuclear physics in the fifties, where it was used in analogy to the optical phenomenon, to denote the observation of diffractive minima and maxima in angular distribution spectra in elastic scattering on nuclear

targets. Later on, similar observations were also made in elastic hadron scattering. In particle physics terms one can say that every high energy reaction which occurs without any exchange of quantum numbers between the colliding particles, is dominated asymptotically by diffraction¹. The distinctive features observed in diffractive hadronic interactions are the following :

- Diffractive interactions exhibit very steep momentum transfer or angular distributions. This is the simplest feature and is already observed in optics.
- The high energy total cross sections increase slowly with energy.
- The slopes of the angular distributions increase slowly with energy, i.e. they become steeper.

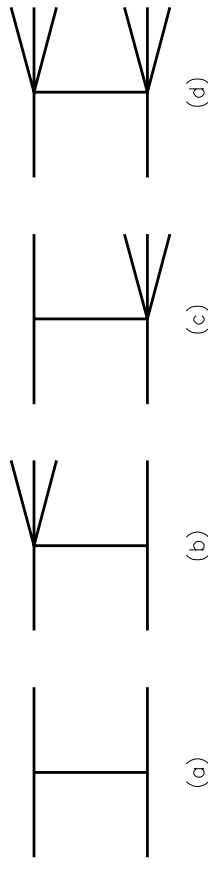


Figure 2.3: Different types of diffraction : (a) elastic scattering, (b) and (c) single diffraction, (d) double diffraction.

When the incident particles are left intact after the collision, the reaction is called elastic. If one of the incoming particles remains unscathed, while the other one gives rise to a resonance or a bunch of final particles whose total quantum numbers match exactly those of the initial particle, then one speaks of a single diffraction reaction. In case both particles produce a resonance or particle bunch with exactly the same quantum numbers as for the initial states, then the reaction is called double diffractive. The different types of diffractive reactions are depicted in figure 2.3.

2.5 Optical Model of Diffraction

The most simple model of diffraction is that of an incident plane wave which scatters on a totally absorbing black disk of well-defined radius R . The angular distribution of the elastic scattering is the Fourier transform of the spatial distribution of the obstacle. The irradiance is then given by [10]

$$\frac{I(\theta)}{I(\theta=0)} = \left(\frac{2J_1(x)}{x} \right)^2 \approx 1 - \frac{R^2}{4} (k\theta)^2, \quad (2.31)$$

¹Note that this description of diffraction cannot exclude reactions with exchange of scalar systems, which are non-diffractive. Their contribution however becomes less important towards higher energies [9].

with the Bessel function J_1 , $k = 2\pi/\lambda$ the light wave number and $x = kR \sin \theta \approx kR\theta$. The second part of the equation is valid for small θ . The irradiance ($J_1(x)/x$) has its maximum at the center of the formed pattern, i.e. for $\theta = 0$. The pattern is symmetrical around the optical axis through the center of the aperture and exhibits minima for $|x| = 3.83, 7.02, \dots$

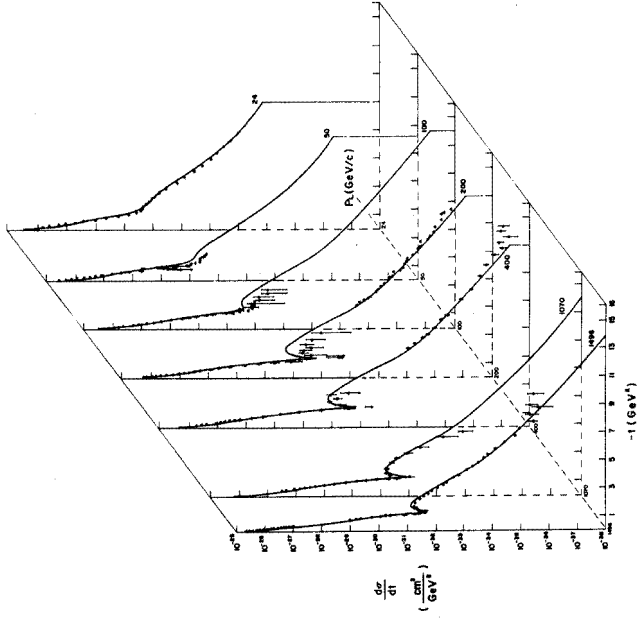


Figure 2.4: The differential elastic pp cross section $d\sigma/dt$ for different incident proton momenta [11].

A similar pattern is observed in elastic hadron-hadron scattering reactions, where an example of elastic pp scattering is shown in figure 2.4. In the center-of-mass frame, the momentum transfer squared between the two hadrons is $t = (p_1 - p'_1)^2 = (p_2 - p'_2)^2$ and can be expressed as $-t = q^2 = (2p \sin \theta/2)^2$ with p the momentum of the colliding particles and θ the scattering angle. The differential cross section for elastic scattering depends primarily on q . In the impact parameter space, with the impact parameter b being the distance between the two particles along the direction perpendicular to the direction of the incoming particle, one represents in the black disk model the target particle as a disk of radius R , where the absorption is total for $b \leq R$, while there is no interaction for $b > R$. The scattering amplitude is purely imaginary and has as function of t and the

center-of-mass energy s a dependence according to [12]

$$T(s, t) \propto \frac{J_1(qR)}{qR} s, \quad (2.32)$$

with $\sigma_{el}(s) = \sigma_{tot}(s) = \pi R^2$. For large values of qR the elastic cross section exhibits minima and maxima characteristic of diffraction phenomena, where minima occur now for $qR = 3.83, 7.02, \dots$. From figure 2.4 one can see that the first minimum at high energy appears around $q^2 = 1.15 \text{ GeV}^2$ corresponding to a nucleon interaction radius of about 0.7 fm. The cross section at low $|t|$ varies only very little with energy. One also notices that the first minimum in $|t|$ decreases slowly with increasing energy, which indicates an increase in the effective size of the ‘disk’ or interaction radius.

This black disk model of diffraction can predict qualitative features of elastic hadron-hadron scattering, but it fails at some points. It suggests that $\sigma_{el}/\sigma_{tot} = 0.5$, while in reality this ratio is far below 0.5 and decreases with increasing energy [13]. This oversimplified model can also not account for the energy dependence of the cross section.

The totally absorbing disk model can be improved to a more realistic one when the sharp edge of the black disk is replaced by a smooth ‘grey’ edge. In that case the scattering amplitude modifies to

$$T(s, t) \propto \frac{J_1(qR)}{qR} \exp(-R_1^2 q^2) s, \quad (2.33)$$

where R_1 characterizes the width of the edge in the impact parameter space. If at high energy the elastic scattering amplitude is purely imaginary, then one obtains the scattering amplitude in the b -space directly from measurements of $d\sigma/dt$ [12].

For inelastic, diffractive processes, the geometric picture presented above leads to the conclusion that when the absorption of the incoming particle is strong enough for $b < R$, then the inelastic diffraction can only occur in the region of the edge where $b \approx R$. The amplitude then becomes

$$T_{diff}(s, t) \propto J_0(qR) \exp(-q^2 R_2^2), \quad (2.34)$$

where $R_2 \sim R_1$ is again related to the width of the disk edge in the impact parameter space. This amplitude also gives rise to diffractive minima and maxima, but now the first minimum appears at a smaller value of $|t|$ as compared to elastic scattering.

Diffractive scattering of hadrons can in the so-called s -channel picture be seen as the differential absorption by the target of the large number of hadronic states or waves that build up the initial state hadron. These hadronic states scatter on the target with different cross sections and lead to a reorganization of the system which results in the production of final hadronic states with different masses than the initial system. The geometrical models for diffractive scattering are usually based on the idea presented above that for strong absorption reactions the impact parameter profile is central for elastic scattering, while peripheral for inelastic diffractive processes. Theoretical difficulties arise due to the uncertainties on the main model parameters being the radius of interaction, the ‘opacity’ of the hadrons, the width of the edges and also the energy dependence of the radius.

In elastic hadron-hadron scattering one usually parametrizes the diffractive peak in

the forward region, i.e. for $|t| \lesssim 0.5 \text{ GeV}^2$, as

$$\frac{d\sigma/dt}{(d\sigma/dt)_{t=0}} = e^{bt} \approx 1 - b(p\theta)^2, \quad (2.35)$$

with p the center-of-mass momentum of the particles. Comparison with equation 2.31 yields the following relation between the radius of interaction and the slope parameter

$$b = \frac{R^2}{4}. \quad (2.36)$$

This means that just like in optics, the slope of the forward elastic peak reflects the size of the scattering object or the interaction radius. Taking as an example the typical radius for strong interactions $R = 1/m_\pi$ with m_π the pion mass, gives $b = 12.8 \text{ GeV}^{-2}$, which is inside the range of experimentally measured slope factors in elastic pp scattering [14] at high energy.

2.6 Regge Theory

In the late fifties Regge showed it proved useful to regard the angular momentum l as a complex variable. The basis of Regge theory used in particle physics lies in the analytical continuation of a scattering amplitude into the complex angular momentum plane [15]. The scattering amplitude singularities encountered in the complex l plane were poles, called Regge poles. These poles correspond to bound states or resonances if they occur for positive integer values of l .

Regge theory makes use of the so-called crossing symmetry principle : an incoming particle of momentum p can be viewed as an outgoing antiparticle of momentum $-p$. The reaction $a(p_a) + b(p_b) \rightarrow c(p_c) + d(p_d)$ has squared center of mass energy $s = (p_a + p_b)^2 > 0$ and the scattering angle is related to the momentum transfer $t = (p_a - p_c)^2 < 0$. For the crossed reaction $a(p_a) + \bar{c}(-p_c) \rightarrow \bar{b}(-p_b) + d(p_d)$ one has that the center of mass energy squared is given by $(p_a - p_c)^2 > 0$ and the scattering angle is now related to the momentum transfer $(p_a + p_b)^2 < 0$. As one can see, the positive region of t and the negative region of s of the first reaction play the role of the center of mass energy squared and the momentum transfer respectively of the crossed process. The first reaction is called an s -channel reaction, while the second process is referred to as the t -channel counterpart of the first one. Both reactions are described by the same amplitude, however in different and non-overlapping kinematical regions in s and t .

To demonstrate the basic principles of Regge theory we start with the standard decomposition of a scattering amplitude $A(s, t)$ into partial waves A_l with angular momentum l

$$A(s, t) = \sum_{l=0}^{\infty} (2l+1) A_l(t) P_l(z_l), \quad (2.37)$$

with P_l the Legendre polynomials of the first kind, $z_l = \cos\theta$ where θ is the scattering angle, which is a function of s and t , and the partial wave amplitudes A_l given by

$$A_l(t) = \frac{1}{2} \int_{-1}^{+1} P_l(z_l) A(s(z_l, t), t) dz_l. \quad (2.38)$$

One assumes that $A_l(t)$ only has isolated singularities in l so that it can be continued into the complex angular momentum plane, which is one of the basic postulates of Regge theory in particle physics and is sometimes called postulate of maximal analyticity of the second kind. Thus when regarding the angular momentum l as a complex variable, one can rely on Cauchy's theorem to replace equation 2.37 by

$$A(s, t) = -\frac{1}{2i} \int_{C_1} (2l+1) A_l(t) \frac{P_l(-z_l)}{\sin \pi l} dl, \quad (2.39)$$

where the integral is evaluated in the complex l plane along path C_1 avoiding any singularities of $A_l(t)$ as shown in figure 2.5.

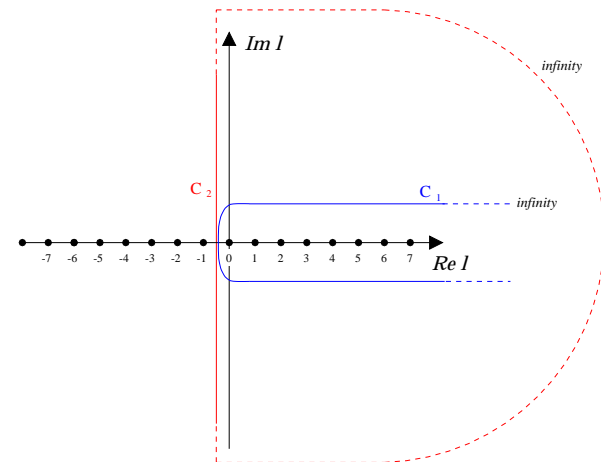


Figure 2.5: The complex angular momentum l plane. Indicated are the integration paths C_1 and C_2 as used in equations 2.39 and 2.40 respectively.

One can now enlarge the integration path in equation 2.39 to C_2 which encloses the entire complex l plane with positive real part as indicated in figure 2.5. In this case the path will pass along complex poles of A_l , where we assume for illustrative purposes that there is only one pole $l = \alpha(t) = \beta(t)/(l - \alpha(t))$. Equation 2.39 then becomes

$$A(s, t) = -\pi(2\alpha(t) + 1)\beta(t) \frac{P_{\alpha(t)}(-z_l)}{\sin \pi \alpha(t)} - \frac{1}{2i} \int_{C_2} (2l+1) A_l(t) \frac{P_l(-z_l)}{\sin \pi l} dl \quad (2.40)$$

The second term in the previous equation is called the background integral and can be proven to be proportional to $s^{-1/2}$ [15] and therefore vanishes as s goes to infinity. The first term, corresponding to the pole in the complex l plane, is called a Regge pole term² and will be denoted as $A^{\mathbb{R}}$ in the following. This Regge pole is the dominant contribution

²The expression for the Regge pole term give here actually corresponds to what is referred to as a

to the scattering amplitude at high energy and can also be decomposed into partial waves with amplitudes

$$A_l^{\mathbb{R}}(t) = \frac{1}{2} \int_{-1}^{+1} P_l(z_t) A^{\mathbb{R}}(s, t) dz_t = \frac{(2\alpha(t) + 1)\beta(t)}{(l - \alpha(t))(l + \alpha(t) + 1)}, \quad (2.42)$$

which in the limit of $l \rightarrow \alpha(t)$ reduces back to $\beta(t)/(l - \alpha(t))$ confirming that the Regge pole term in equation 2.40 really gives rise to a pole in the l plane. One can now decompose $\alpha(t)$ into its real and imaginary part $\alpha_R(t)$ and $\alpha_I(t)$ and make an expansion at the point t_r where $\alpha_R(t_r) = l$ with l a positive integer value. This gives in first order

$$\alpha(t) \approx l + \alpha'_R(t_r)(t - t_r) + i\alpha_I(t_r) + i\alpha'_I(t_r)(t - t_r). \quad (2.43)$$

Assuming that $\alpha'_I \ll \alpha'_R$ [15], one obtains for $\alpha_R \approx l$

$$A_l^{\mathbb{R}}(t) \approx \frac{\beta(t_r)/\alpha'_R(t_r)}{t_r - t - i\alpha_I(t_r)/\alpha'_R(t_r)}, \quad (2.44)$$

which denotes the Breit-Wigner formula for a resonance with mass $M_r^2 = t_r$ and width $\Gamma_r = \alpha_I(t_r)/\alpha'_R(t_r)M_r$, indicating that the occurrence of a Regge pole corresponds to a resonance or a physical particle exchange in the t -channel. This basically holds for any arbitrary number of poles; as $l = \alpha(t)$ moves around in the complex l -plane, each time a positive integer is crossed, a resonance in the Regge amplitude will occur.

Strong interacting elementary particles, hadrons, can be classified according to a series of quantum numbers, like e.g. isospin, strangeness and baryon number. For a given set of these quantum numbers particles exist which only differ in their spin and mass. Plotting the spin of the particles versus their mass squared $t = M^2$, they all seem to align in different families on straight lines. These trajectories can be parametrized as

$$\alpha(t) = \alpha(0) + \alpha' t, \quad (2.45)$$

and are called Regge trajectories. When adding to this so-called Chew-Frautschi plot experimental results of diffractive scattering processes³, which have negative momentum transfer t , the data points seem to align along the extensions to $t < 0$ of the Regge trajectories, whose quantum numbers match possible resonances that could be exchanged in the crossed process. In view of the discussion of the Regge poles given above, one can picture these scattering reactions as being mediated by the exchange of resonances in the t -channel whose interpolation is given by a Regge trajectory or Reggeon $\alpha(t)$. An example is depicted in figure 2.6 for the reaction $\pi^- p \rightarrow \pi^0 n$. The parity transfer in the

signature amplitude. The physical amplitude is given by

$$A^{\mathbb{R}}(s, t) = -\pi(2\alpha(t) + 1)\beta(t)(1 + S e^{-i\pi\alpha(t)}) \frac{P_{\alpha(t)}(-z_t)}{\sin \pi\alpha(t)}, \quad (2.41)$$

where the factor $(1 + S e^{-i\pi\alpha(t)})$ is called the signature factor which ensures that a trajectory of given signature $S = \pm 1$ leads to a pole in the scattering amplitude only when $\alpha(t)$ passes through the right-signature integer, i.e. even integers ($l = 0, 2, 4, \dots$) for even signature $S = +1$ and odd integers ($l = 1, 3, 5, \dots$) for odd signature $S = -1$.

³The real part of $\alpha(t)$ can be derived from experimental data using equation 2.47, as will be discussed further on in the text.

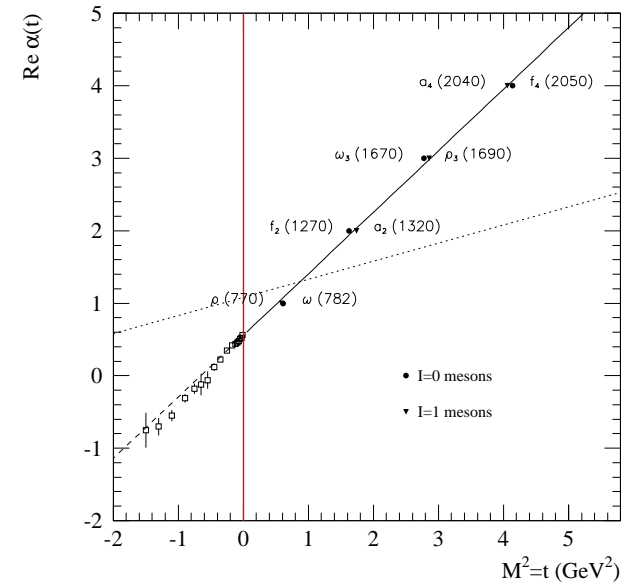


Figure 2.6: Chew-Frautschi plot for two different (however almost identical) Regge trajectories corresponding to natural parity exchange. The full line shows a fit to the mesons according to equation 2.45, while the dashed line is the extension of the fit to $t < 0$. The points at $t < 0$ were derived from $\pi^- p \rightarrow \pi^0 n$ scattering data [16]. The dotted line represents the trajectory corresponding to Pomeron exchange.

reaction is positive and given by $\Delta P = (-1)^J P$ with J and P the angular momentum and parity of the object exchanged in the t -channel. To conserve all quantum numbers, the reaction can therefore only proceed via exchange of ρ , a_2 and ρ_3 with quantum numbers $J^P = 1^-, 2^+$ and 3^- , which all lie on the Regge trajectory passing through the measured data points. This Regge trajectory is actually nearly identical to the ω/f trajectory also shown in the figure.

To determine a cross section the scattering amplitude needs to be evaluated in the s -channel region with $t < 0$. Assuming $|t| \ll s$ we have for high energy that $P_{\alpha(t)} \approx e^{-\pi\alpha(t)}(s/s_0)^{\alpha(t)}$ leading to the Regge pole term given by

$$A^{\mathbb{R}}(s, t) \approx \beta(t) \left(\frac{s}{s_0} \right)^{\alpha(t)}, \quad (2.46)$$

where $\beta(t)$ represents the part of the Regge pole independent of s and s_0 is a mass scale factor. This illustrates that the asymptotic behavior in a given channel of a process is

provided by $\alpha(t)$, an interpolation of resonances exchanged in the crossed channel. The differential cross section corresponding to the previous amplitude is then

$$\frac{d\sigma}{dt} \propto \frac{1}{s^2} |A^{\mathcal{R}}(s, t)|^2 = |\beta(t)|^2 \left(\frac{s}{s_0}\right)^{2\alpha(t)-2}. \quad (2.47)$$

The equation above shows that the Regge trajectory for the process can be determined from experimental data by analyzing $\ln d\sigma/dt$ as function of $\ln s$ at fixed t . The hadronic mass scale factor s_0 was determined from data to be about 1 GeV² [17]. This value indicates that Regge theory is expected to work well for roughly $s > 10$ GeV², i.e. energies above the resonance region. The optical theorem relates the imaginary part of the forward scattering amplitude to the total cross section

$$\sigma_{tot} = \frac{1}{s} \text{Im}(A|_{t=0}), \quad (2.48)$$

so that the forward differential cross section can be written as

$$\left. \frac{d\sigma}{dt} \right|_{t=0} = \frac{1}{16\pi} (1 + \eta^2) \sigma_{tot}^2, \quad (2.49)$$

with η the ratio of the real to the imaginary part of the forward scattering amplitude. Together with equation 2.47 this leads to

$$\sigma_{tot} \propto s^{\alpha(t=0)-1}. \quad (2.50)$$

This means that the high energy behavior of the total cross section is dominated by the highest lying Regge trajectories, which in the Chew-Frautschi plot are the degenerated ρ/ω_2 and ω/f trajectories with an intercept of about $\alpha_{\rho,\omega}(0) \approx 0.5$. One would therefore expect to find a total cross section going like $\sigma_{tot} \propto s^{-1/2}$. However, this behavior is not observed in hadron-proton scattering at high energy. Instead the cross sections appear to be rather constant with energy and even tend to rise slowly above about 10 GeV. To explain this observation in terms of Regge pole exchange one would need a trajectory with $\alpha(0) \approx 1$, while all known particles have $\alpha(0) < 1$. Furthermore, the exchanged particle needs to have the quantum numbers of the vacuum. This lead to the postulation of a new linear trajectory called the Pomeron trajectory with $\alpha_{\mathbb{P}}(0) = 1 + \epsilon$ and $0 < \epsilon \ll 1$

$$\alpha_{\mathbb{P}} = 1 + \epsilon + \alpha_{\mathbb{P}}' t. \quad (2.51)$$

Total hadron-hadron and photon-hadron cross sections can be well described by a sum of two terms

$$\sigma_{tot} = X s^{\epsilon} + Y s^{-\eta}, \quad (2.52)$$

where the second term corresponds to exchange of the highest lying Reggeon trajectory ($\rho/\omega_2, \omega/f$) and the first one to Pomeron exchange. The effective exponents ϵ and η for Pomeron and Reggeon exchange respectively, can be determined from fits to experimental data and are assumed to be independent of the interacting hadrons, while X and Y depend on the specific process. Donnachie and Landshoff [18] applied the fit to pp and $p\bar{p}$ data with $\sqrt{s} > 10$ GeV and found values of $\epsilon = 0.0808$ and $\eta = 0.4525$ as displayed in figure 2.7. A re-evaluation of these fits by Cudell *et al.* [19] using non-degenerated Regge

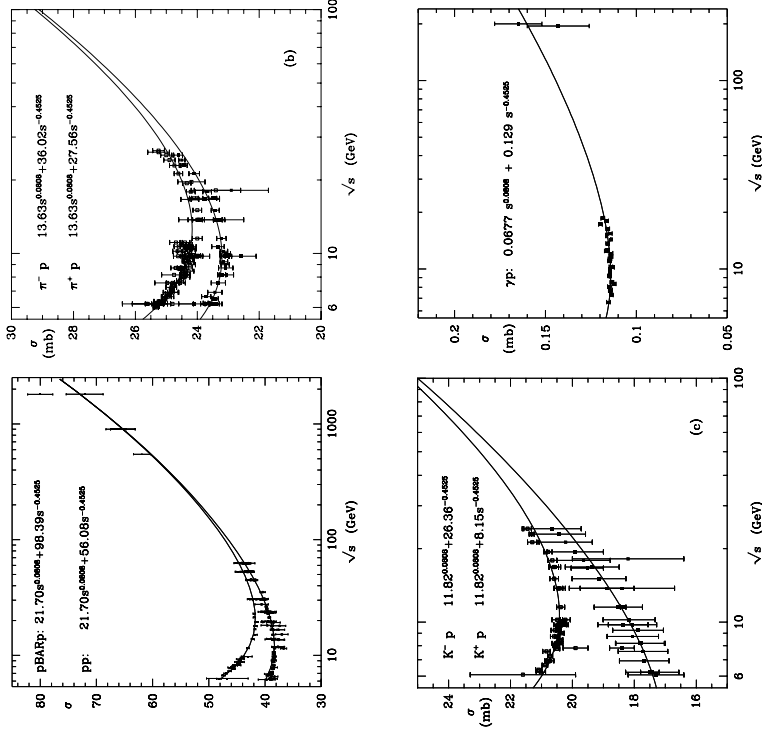


Figure 2.7: Total cross sections [18] for (a) $p\bar{p}$ and $p\bar{p}$, (b) π^-p and π^+p ; (c) K^-p and K^+p and (d) γp . The fitted curves correspond to equation 2.52. Note that the exponents ϵ and η were fixed at the values found in the pp and $p\bar{p}$ fit. According to the Pomeronchuk theorem [13] the cross section for particle and antiparticle on the same target should become identical at high energy, which is supported by the data displayed here. In the fits, the coefficient X of the Pomeron trajectory was required to be the same for $\sigma(ab)$ and $\sigma(\bar{a}\bar{b})$.

trajectories $\sigma_{tot} = X s^\epsilon + Y_- s^{-\eta_-} + Y_+ s^{-\eta_+}$ yielded a best value for $\epsilon = 0.096_{-0.009}^{+0.012}$, but good χ^2 values were obtained for the range $0.07 < \epsilon < 0.11$.

For diffractive interactions at small $|t|$, one finds that the elastic differential cross section falls exponentially with $|t|$ [15], so that we can use $|\beta(t)|^2 \sim e^{b_0 t}$ in equation 2.47 giving together with equation 2.45

$$\frac{d\sigma}{dt} \propto e^{b_0 t} \left(\frac{s}{s_0}\right)^{2\alpha(t)-2} = \left(\frac{s}{s_0}\right)^{2\alpha(0)-2} e^{b_0 + 2\alpha' \ln(s/s_0)} \quad (2.53)$$

$$= \frac{d\sigma}{dt} \Big|_{t=0} e^{-b|t|}, \quad (2.54)$$

where

$$b = b_0 + 2\alpha' \ln\left(\frac{s}{s_0}\right). \quad (2.55)$$

This means that according to Regge theory the slope of the forward diffractive peak increases with energy, making the peak more narrow. This phenomenon is called shrinkage. Experimental measurements of this shrinkage effect can be used to determine the slope α' of the exchanged Regge trajectory. The slope of the Pomeron trajectory was extracted from elastic pp and $p\bar{p}$ scattering at high energy yielding [20]

$$\alpha'_\mathbb{P} = 0.25 \text{ GeV}^2. \quad (2.56)$$

2.7 Partonic Structure of the Pomeron

At the end of the 1980's, the observation of high- p_T jet production in diffractive $p\bar{p}$ interactions by the UA8 Collaboration [21] supported the idea of Ingelman and Schlein [22] that the Pomeron has a partonic structure.

Indications for the structure of the Pomeron can be found in inclusive diffractive scattering. The cross section for the diffractive process

$$e + p \rightarrow e + X + p, \quad (2.57)$$

where the proton remains intact and the photon dissociates into a system X can in analogy with non-diffractive DIS be expressed in terms of a diffractive structure function F_2^D

$$\frac{d^4\sigma^{e+p \rightarrow e+X+p}}{dQ^2 dx_{\mathbb{P}} d\beta dt} = \frac{4\pi\alpha^2}{\beta Q^4} \left[1 - y + \frac{y^2}{2(1+R_D)} \right] F_2^D(Q^2, x_{\mathbb{P}}, \beta, t), \quad (2.58)$$

where the kinematics are determined by four kinematical variables Q^2 , t , $x_{\mathbb{P}}$ and β . The latter two are defined as

$$x_{\mathbb{P}} \simeq \frac{Q^2 + M_X^2}{Q^2 + W^2}, \quad (2.59)$$

$$\beta \simeq \frac{Q^2}{Q^2 + M_X^2}, \quad (2.60)$$

and represent in the proton infinite momentum frame the fraction of the proton momentum carried by the Reggeon or Pomeron exchange and the fraction of the exchanged

momentum carried by the quark which was struck by the photon, respectively. The two variables are related to the Bjorken scaling variable x via $x = \beta x_{\mathbb{P}}$. The ratio R_D of the longitudinal to the transverse diffractive cross section is not known yet and is commonly put to zero in equation 2.58. Also the momentum transfer t is usually integrated over. The diffractive structure function itself can in a Regge approach be written in a factorized form

$$\begin{aligned} F_2^D(Q^2, x_{\mathbb{P}}, \beta) &= \Phi^{\mathbb{P}}(x_{\mathbb{P}}) F_2^{\mathbb{P}}(Q^2, \beta) + \Phi^{\mathbb{R}}(x_{\mathbb{P}}) F_2^{\mathbb{R}}(Q^2, \beta) + \text{interf.} \\ &= x_{\mathbb{P}}^{2-\alpha_{\mathbb{P}}} F_2^{\mathbb{P}}(Q^2, \beta) + x_{\mathbb{P}}^{2-\alpha_{\mathbb{R}}} F_2^{\mathbb{R}}(Q^2, \beta) + \text{interf.} \end{aligned} \quad (2.61)$$

If this factorization holds, $\Phi(x_{\mathbb{P}})$ can be interpreted as an effective Pomeron or Reggeon flux in the proton, whereas $F_2^D(Q^2, \beta)$ describes the structure of the Pomeron or Reggeon with β taking up the role of Bjorken- x for hadron structure functions. Fitting the latter equation to diffraction data [23] in the region $0.4 < Q^2 < 75 \text{ GeV}^2$ yields intercepts for the Reggeon and Pomeron of $\alpha_{\mathbb{R}}(0) = 0.50 \pm 0.18$ and $\alpha_{\mathbb{P}}(0) = 1.20 \pm 0.04$ respectively. The Reggeon intercept matches the one for the ρ/ω trajectory, while the Pomeron intercept is higher than the one found for soft hadron-hadron interactions ($\alpha_{\mathbb{P}} = 1.08$, see paragraph 2.6). The Pomeron contribution is seen to be rather flat in β , whereas the Reggeon contribution increases towards smaller values of β . The latter one also increases with larger values of $x_{\mathbb{P}}$, corresponding to smaller energy.

The understanding of diffractive processes in terms of partonic structure is aided by two complementary pictures : hadronic fluctuations of the photon and Pomeron structure function.

The first approach is based on viewing the diffractive reaction in the proton rest frame. In this frame, the fast moving photon fluctuates into a hadronic system a long distance before the target and appears to be frozen during the short, hard interaction with the proton. The diffractive process is in this case described by a convolution of three factors : the photon hadronic structure, the diffractive interaction between the hadronic photon fluctuation and the proton and the final state hadronization. In this kind of calculations only the lowest Fock states are considered ($q\bar{q}$, $g\bar{q}g$). The Pomeron is modeled as a 2-gluon system or Lipatov ladder, which is color neutral and flavor blind. This approach will be applied in models describing diffractive vector meson production (see section 2.12).

The Pomeron structure function approach is viewed from the proton infinite momentum frame. The Pomeron is then seen as a color neutral object ($q\bar{q}$ or $g\bar{g}$) emitted from the proton. In a similar way as in DIS, where the virtual photon probes the proton structure, here the photon sees the Pomeron structure. The QCD evolution of the Pomeron structure function is then governed by the GLAP equations. Measurements performed by H1 [23] of $x_{\mathbb{P}} F_2^D(Q^2, x_{\mathbb{P}}, \beta)$, interpolated to $x_{\mathbb{P}} = 0.003$, reveal a scaling violation with positive slope of the diffractive structure function up to large values of β . The parton distributions of the Pomeron can be extracted from these data via GLAP fits. The H1 data indicate that gluons make up more than 80 % of the Pomeron partonic content and that the parton distribution functions are dominated by hard gluons. A similar study by ZEUS [24] shows that at a scale of 4 GeV², the Pomeron momentum fraction carried by gluons lies between 0.64 and 0.94.

2.8 Vector Meson Dominance Model

The concept of the photon originated in the early 20th century when M. Planck assumed that black body radiation appeared in the form of energy quanta. A. Einstein suggested that light was actually composed of independent particles of energy or particles of light. Experimental evidence for this particle-like nature of light came with the scattering of X-rays on electrons. When Quantum Electrodynamics was first introduced the photon was regarded as a massless, chargeless gauge boson with a pointlike coupling to elementary charged particles. Later on, as the scale of the energy increased, it was found that photons could actually fluctuate or materialize into electron-positron pairs ($\gamma \rightarrow e^+e^-$) through the interaction with a Coulomb field. This phenomenon was one of the first indications that the photon had a more sophisticated structure than originally thought. In quantum field theory the electromagnetic field couples to all particles carrying electromagnetic current enabling a photon to fluctuate into more complex virtual states. In this way the photon also acquires a hadronic internal structure, which however occurs with a relative probability only of the order of $\alpha \sim 1/137$ as compared to the bare particle. Bare particle states are described by free Hamiltonians. However, a physical particle is an eigenstate of the complete Hamiltonian and therefore contains, apart from the bare particle state, also contributions from all bare states it can couple to.

The hadronic properties of the photon were first observed in photon scattering processes on the proton performed in the 1960's. These reactions showed very remarkable similarities with pure hadronic interactions :

- The total cross section for photon and hadron induced reactions shows a similar behavior. Both exhibit spectacular resonances at low energies and above a few GeV they become structureless and vary very little with energy. The photon cross section is however smaller than the hadron cross section by a factor approximately equal to the fine structure constant α .
- The photon total cross sections on neutrons and protons are nearly identical, indicating that photon interactions in a first approximation do not depend on the charge of the target.
- The momentum transfer $|t|$ distributions for photon processes show a falloff very similar to those of hadronic interactions.
- Photoproduction processes have an important diffractive component, which reveals itself by the copious production of neutral vector mesons, especially ρ^0 mesons. The amplitudes for exclusive vector meson photoproduction $\gamma p \rightarrow Vp$ can be considered as the photon analog of hadronic elastic amplitudes, i.e. they tend to a nearly energy independent limit and they have the same typical falloff in t .
- Both hadron and photon interactions on composite nuclei exhibit shadowing effects, meaning that the initial interaction of the incoming particle occurs almost always with a nucleon on the incident side of the nucleus and thereby leaves a 'shadow' on the nucleons which are more inside the nucleus.

The way to understand these observations was to assume that the physical photon could be modeled as a superposition of a bare photon $|\gamma_B\rangle$ undergoing only pure electromagnetic interactions with the target and a small hadronic component $|\gamma_h\rangle$ which takes part in pure hadronic interactions

$$|\gamma\rangle \simeq \sqrt{Z_3}|\gamma_B\rangle + \sqrt{\alpha}|\gamma_h\rangle, \quad (2.62)$$

where Z_3 assures the proper normalization of $|\gamma\rangle$. Conservation laws dictate that $|\gamma_h\rangle$ has the same quantum numbers as the bare photon, namely $J^{PC} = 1^{--}$, $Q = S = B = 0$. The contribution of the bare photon to the interaction can be neglected as it is several orders of magnitude smaller than the contribution of the hadronic part of the photon. The relatively large cross section for production of the light vector mesons ρ^0 , ω and ϕ suggests that the latter constitute the dominant contribution to the hadronic photon component $|\gamma_h\rangle$. The so-called vector meson dominance model (VDM) is based on the assumptions that these three mesons are the only hadronic constituents of the photon and that the bare photon component $|\gamma_B\rangle$ does not interact with hadrons at all.

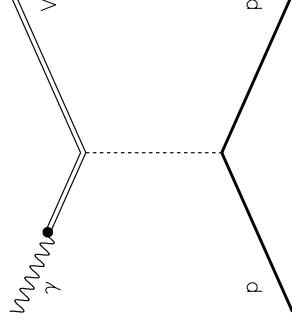


Figure 2.8: Photoproduction of vector mesons in the vector meson dominance model. The photon is assumed to virtually dissociate into a vector meson V , which subsequently scatters off a nucleon.

The photoproduction of vector mesons can be quite successfully described by this vector meson dominance model. The fluctuation or formation time of a photon into a $q\bar{q}$ or virtual vector meson state is given by [128]

$$t_f \approx \frac{2\nu}{Q^2 + M_V^2}. \quad (2.63)$$

If t_f is long enough to allow the virtual vector meson to travel over a distance much larger than the nucleon radius of about 1 fm, the photon fluctuates long before it hits the target and the interaction occurs between the virtual meson and the nucleon as depicted in figure 2.8. Consequently photoproduction of vector mesons is closely related to elastic vector meson scattering off a nucleon.

In perturbation theory [128] one has for the second term in equation 2.62 to lowest order in the electromagnetic photon-hadron interaction \mathcal{H}

$$\sqrt{\alpha}|\gamma_h\rangle = \mathcal{S}_n \frac{|n\rangle \langle n|\mathcal{H}|\gamma_B\rangle}{\nu - E_n}, \quad (2.64)$$

where $|n\rangle$ is a hadronic state with energy E_n and momentum k and $|\gamma_B\rangle$ here includes the hadronic vacuum and the bare photon state with energy ν and momentum k . S_n represents the sum and integrals over all appropriate labels in n . For high energy the denominator in the equation may be approximated by $\nu - E_n = -(\mathcal{M}^2 + Q^2)/2\nu$ where \mathcal{M} is the invariant mass of state $|n\rangle$. The equation can then be rewritten as [25]

$$\sqrt{\alpha}|\gamma_h\rangle = -(2\pi)^3 \int \frac{d\mathcal{M}^2}{\mathcal{M}^2 + Q^2} S_{n_i}|k, \mathcal{M}, n_i\rangle \mathcal{H}|\gamma_B\rangle, \quad (2.65)$$

which is only valid for low-mass components of the photon and where the sum now extends over all internal quantum numbers at fixed k and \mathcal{M} . In a model where $|n_i\rangle$ are transversely polarized vector meson states of definite mass, the matrix element of \mathcal{H} is independent of k and the integral breaks down in a discrete sum

$$\sqrt{\alpha}|\gamma_h\rangle = \sum_V \frac{e}{f_V} \left(1 + \frac{Q^2}{M_V^2}\right)^{-1} |V\rangle, \quad (2.66)$$

where the vector meson states $|V\rangle$ have momentum k and f_V denotes the $\gamma \leftrightarrow V$ coupling constant. The VDM coupling can be related to the mass of the vector meson and to its leptonic decay width Γ_{ee}^V according to [128]

$$\frac{4\pi}{f_V^2} = \frac{3\Gamma_{ee}^V}{\alpha^2 M_V}. \quad (2.67)$$

The Q^2 dependence in equation 2.66 is entirely contained in the vector meson propagator. Equation 2.65 can actually be seen as a continuous superposition of vector meson states of momentum k . Since the probability amplitudes for these states depend only on \mathcal{M} , the superposition appears ‘frozen in’, independent of k . For longitudinally polarized photons (only for $Q^2 \neq 0$) the \mathcal{H} matrix element does depend on k . However, one eventually finds a similar frozen longitudinal structure as in the transverse case.

Following the discussion given above, the VDM framework provides us with a model for the Q^2 dependence of the vector meson production cross section. The Q^2 behavior is determined by the propagation of single vector meson states only as expressed in equation 2.66. This leads to the VDM cross section predictions given separately for transversely and longitudinally polarized photons

$$\sigma_T^{\gamma p}(Q^2, W) = \sum_V \frac{e^2}{f_V^2} \left(1 + \frac{Q^2}{M_V^2}\right)^{-2} \sigma_T^{Vp}(W), \quad (2.68)$$

$$\sigma_L^{\gamma p}(Q^2, W) = \sum_V \frac{e^2}{f_V^2} \left(1 + \frac{Q^2}{M_V^2}\right)^{-2} \xi_V^2 \frac{Q^2}{M_V^2} \sigma_T^{Vp}(W), \quad (2.69)$$

where σ_T^{Vp} is the total cross section for the transversely polarized vector meson. The longitudinal Vp cross section need not be the same as the transverse one, which justifies the introduction of the factor ξ_V^2 representing the ratio of the two. In VDM it is predicted to be $\mathcal{O}(1)$ [26]. However, experimental results on ρ^0 production indicate that this ratio is lower (see e.g. [27, 99]). One also notices from equation 2.69 that the longitudinal cross section vanishes at $Q^2 = 0$, i.e. for real photons.

Using these VDM predictions one arrives at the relation between the total virtual photoproduction and the real photoproduction cross section

$$\sigma^{\gamma p}(Q^2, W) = \left(1 + \epsilon \xi_V^2 \frac{Q^2}{M_V^2}\right) \left(1 + \frac{Q^2}{M_V^2}\right)^{-2} \sigma^{\gamma p}(W), \quad (2.70)$$

where $\epsilon = \Gamma_L/\Gamma_T$ is the ratio between the longitudinal and transverse photon flux. The ratio of equations 2.69 and 2.68 gives us the important VDM prediction for the ratio of the longitudinal and transverse photoproduction cross section

$$R = \frac{\sigma_L}{\sigma_T} = \xi_V^2 \frac{Q^2}{M_V^2}. \quad (2.71)$$

2.9 Generalized Vector Meson Dominance Model

In the vector meson dominance model one neglects the off-diagonal transitions in which the photon virtually converts into a more massive spin 1 state, V' , which then scatters from the nucleon into a vector meson V via $V'p \rightarrow Vp$. These transitions are assumed to be suppressed due to the smaller hadronic amplitudes for diffraction dissociation $V'p \rightarrow Vp$ as compared to the elastic case $Vp \rightarrow Vp$ and due to the smaller coupling of the photon to the higher mass states. The neglect of these off-diagonal terms seems justified by the experimental data for photoproduction ($Q^2 = 0$), where the relations between the vector meson nucleon total cross sections and ρ^0 , ω and ϕ photoproduction at $t = 0$ have been confirmed. The relative importance of these off-diagonal transitions however, becomes increasingly more important for higher Q^2 due to the propagator factor $(Q^2/M_V^2 + 1)^{-1}$ in the amplitude.

Experimental indications for the need to include higher mass states coupling to the photon comes from the determination of the fractional contributions of the light vector mesons to the total γp cross section written as [28]

$$\sigma^{\gamma p}(W) = \sum_{V=\rho^0, \omega, \phi} \sqrt{16\pi} \left(\frac{e}{f_V}\right)^2 \left(\frac{d\sigma^{p \rightarrow Vp}}{dt}(W)\right) \Big|_{t=0}^{1/2} (1 + \eta_V^2)^{-1/2}. \quad (2.72)$$

η_V stands for the ratio of the real to the imaginary part of the forward vector meson production amplitude, which is but a small contribution to the equation [29]. The obtained fractional contributions were

$$r_{\rho^0} = 0.65, \quad r_{\omega} = 0.08, \quad r_{\phi} = 0.05, \quad (2.73)$$

adding up to only 78 % of the total photoproduction cross section.

The generalized vector meson dominance model (GVDM) takes these higher mass states and the off-diagonal transitions into account. In e.g. [30] the higher mass states were included via an infinite series of vector mesons, where only transitions between the neighbouring mesons were considered. This lead to similar expressions for the cross section as in VDM, however with a new effective mass scale for the longitudinal and transverse cross section $M_L, M_T < M_V$. In [29] a continuous mass spectrum is considered, which gave effective masses $M_T < M_L < M_V$.

2.10 Off-forward Parton Distributions

As was shown in section 2.2 the structure of nucleons is described in deep-inelastic scattering in terms of unpolarized and polarized parton distribution functions. A generalization of these parton distributions are the so-called off-forward parton distributions (OFPD's), which are sometimes also referred to as skewed or off-diagonal parton distributions. They allow a unified theoretical approach to a wide variety of exclusive processes in perturbative QCD and provide an interpretation of these reactions in terms of the nucleon structure. Recent theoretical interest for these OFPD's has risen since it was shown [35] that the second moment of these distributions is related to the contribution of the spin and orbital angular momentum of the quarks to the nucleon spin.

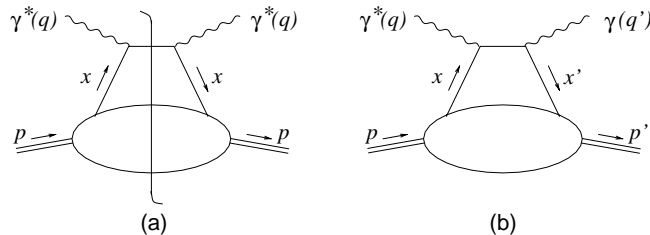


Figure 2.9: (a) The Born level diagram of the forward Compton amplitude. The blob denotes the quark and antiquark distributions in the proton. (b) The Born diagram for deep virtual Compton scattering. Here the blob is described by OFPD's.

A good example [36] to demonstrate the meaning of these OFPD's and how they are connected to the usual parton densities is provided by the amplitude for virtual Compton scattering. The optical theorem links the imaginary part of the forward Compton amplitude $\gamma^*p \rightarrow \gamma^*p$ to the inclusive deep-inelastic scattering cross section $\gamma^*p \rightarrow X$. In the Bjorken limit this can be calculated as a parton-photon scattering amplitude times the usual parton distributions in the proton. As depicted in figure 2.9 (a), no momentum is transferred across the cut in the diagram ($t = 0$) and the parton lines connecting to the proton have the same momentum fractions equal to Bjorken- x . If now the virtual photon on the righthand side of the diagram is replaced by a real photon as in figure 2.9 (b), one obtains the amplitude of the deep virtual Compton scattering (DVCS) $\gamma^*p \rightarrow \gamma p$ process. In this case there is a momentum transfer $t = \Delta^2 = (p' - p)^2 = (q - q')^2$ between the proton on the left and right side. The parton lines connecting to the proton have different momentum fractions, which introduces a sort of imbalance or skewedness in the graph. The factorization shown in the so-called handbag diagram in figure 2.9 (b) is valid for the DVCS amplitude at large Q^2 and fixed Bjorken- x , and small and fixed t . The amplitude is factorized in a hard scattering part calculable in pQCD, and a non-perturbative nucleon structure part which is described in terms of OFPD's. In [37] (see also section 2.12) a general proof of factorization was given also for hard exclusive production by longitudinal photons of vector mesons (ρ, ω, \dots) and pseudo-scalar mesons (π, η, \dots) so that OFPD's can be accessed via these reactions too.

The nucleon structure information contained in these handbag diagrams can be parametrized in leading order QCD in terms of four generalized structure functions, which in the notation of [35] are the OFPD's H_f, \tilde{H}_f, E_f and \tilde{E}_f for each quark flavor f (u, d and s). The OFPD's are function of three independent kinematical variables denoted as x, ξ and t . These variables are defined in a frame where the virtual photon momentum q^μ and nucleon momentum P^μ are collinear along the z -axis and in opposite direction. The physical momenta are then expressed as function of the two lightlike vectors $p^\mu = P^+/\sqrt{2} \cdot (1, 0, 0, 1)$ and $n^\mu = 1/\sqrt{2}P^+ \cdot (1, 0, 0, -1)$, where the light-cone components are defined as $a^\pm = (a^0 \pm a^3)/\sqrt{2}$. x is the light-cone momentum fraction of the exchanged parton with respect to the incoming nucleon as defined by $x = k/P^+$; the variable $\xi = -\Delta^+/2P^+$, where $\Delta = p' - p$ and $t = \Delta^2$. In the Bjorken limit one has that $2\xi \rightarrow x_B/(1 - x_B/2)$ with x_B the Bjorken- x variable. The light-cone momentum fraction is restricted to $[-1, 1]$, where positive (negative) values correspond to quarks (antiquarks). The difference between the parton fractional momenta $x - x'$ is approximately equal to Bjorken- x .

The usual parton densities are matrix elements of an operator between identical nucleon states. They express the squared amplitude or probability for a nucleon to emit a parton of given momentum fraction x . The OFPD's are matrix elements of the same operators, but now between different nucleon states. They represent the amplitude for a nucleon to emit a parton with momentum fraction x times the conjugated amplitude expressing the absorption of a parton with a different momentum fraction x' . In case $x > 0$ and $x' < 0$, one can interpret the parton with negative momentum fraction x' as an antiparton with positive momentum fraction $-x'$, which leads to the picture of a nucleon emitting a quark-antiquark pair.

In the forward direction the OFPD's H and \tilde{H} reduce to the familiar quark density and spin distribution functions

$$H_f^q(x, 0, 0) = q_f(x), \quad \tilde{H}_f^q(x, 0, 0) = \Delta q_f(x). \quad (2.74)$$

The first moments of the OFPD's are related [35] to the elastic form factors⁴

$$\int_{-1}^{+1} dx H(x, \xi, t) = F_1(t), \quad \int_{-1}^{+1} dx E(x, \xi, t) = F_2(t), \\ \int_{-1}^{+1} dx \tilde{H}(x, \xi, t) = G_A(t), \quad \int_{-1}^{+1} dx \tilde{E}(x, \xi, t) = G_P(t), \quad (2.75)$$

where F_1 and F_2 are the Dirac and Pauli form factors and G_A and G_P are axial-vector and pseudo-scalar form factors. The second moments of the unpolarized OFPD's at $t = 0$ give

$$\frac{1}{2} \int_{-1}^{+1} dx x [H^q(x, \xi, 0) + E^q(x, \xi, 0)] = \frac{1}{2} \Delta \Sigma + L_q = J_q, \quad (2.76)$$

where $\Delta \Sigma/2$ and L_q are the quark spin and orbital angular momentum contribution to the nucleon spin. The former quantity is also accessed in polarized DIS measurements, so that the measurement of the sum rule (2.76) would lead to the determination of the quark orbital momentum contribution to the nucleon spin and according to

$$\frac{1}{2} = J_q + J_g \quad (2.77)$$

⁴This is after an appropriate summation over the quark flavors depending on the nucleon type [45].

also to the total gluon contribution J_g . A unique feature of this OFPD framework is that it gives access to nucleon spin information without the need of a polarized beam or target.

As already mentioned these OFPD's provide a tool to describe various types of exclusive reactions. However, different types of exclusive processes are related to different (combinations of the) OFPD's. At leading order pQCD the longitudinally polarized vector meson channels (ρ_L, ω_L, ϕ_L) are sensitive to the unpolarized OFPD H and E only, while the pseudo-scalar meson channels (π, η) have sensitivity to the polarized \tilde{H} and \tilde{E} [37]. All four OFPD's contribute in the description of deeply virtual Compton scattering [35].

2.11 Nonperturbative Models

2.11.1 The Donnachie and Landshoff Model

Donnachie and Landshoff [31] used their Regge type fits of hadron-hadron cross sections in combination with the additive quark model and vector meson dominance to predict the energy behavior of the ρ^0 real photoproduction cross section. Combining expression 2.49 of the optical theorem with VDM yields

$$\left. \frac{d\sigma^{\gamma p \rightarrow \rho^0 p}}{dt} \right|_{t=0} = \frac{c^2}{f_{\rho^0}^2} \left. \frac{d\sigma^{\rho^0 p \rightarrow \rho^0 p}}{dt} \right|_{t=0} = \frac{1}{16\pi} \frac{c^2}{f_{\rho^0}^2} (1 + \eta^2) (\sigma_{tot}^{\rho^0 p})^2. \quad (2.78)$$

The total $\rho^0 p$ cross section can be related to those of the $\pi^\pm p$ interactions using the additive quark model

$$\sigma_{tot}^{\rho^0 p} \approx \frac{1}{2} (\sigma_{tot}^{+\pi p} + \sigma_{tot}^{-\pi p}). \quad (2.79)$$

Inserting their Regge type (see expression 2.52) cross section fits [18] to $\pi^- p$ and $\pi^+ p$ scattering gave a total $\rho^0 p$ scattering cross section in millibarns

$$\sigma_{tot}^{\rho^0 p} = 13.6 s^{0.08} + 31.8 s^{-0.45}. \quad (2.80)$$

This model provides a good description of the energy behavior of the cross section, however the absolute magnitude is predicted about 15 % higher than the measured values.

This overestimation of the cross section is explained by the $\gamma - V$ coupling constant f_{ρ^0} used in the model. The coupling was related to the e^+e^- decay width via equation 2.67, while vector meson photoproduction measurements yield a coupling which is larger [32]. Using the Donnachie and Landshoff Regge fits together with a coupling constant derived from photoproduction measurements in the center-of-mass energy region $9 < W < 18$ GeV, results in a much better agreement with the data [32].

2.11.2 The Model of Haakman *et al.*

In the model of Haakman *et al.* [33] the energy dependence of vector meson production is related to the inclusive nucleon structure function F_2 . The high energy behavior of diffractive processes is governed by the Pomeron singularity. In the model an effective

Pomeron intercept is derived where not only single Pomeron exchange characterized by a fixed intercept at $t = 0$ $\alpha_{\mathbb{P}}(0)$ is considered, but also contributions of multiple Pomeron exchange.

The overall energy dependence of the scattering amplitude is determined by this effective intercept, where the relative importance of the multiple Pomeron exchange contribution becomes lower with increasing photon virtuality. This can be understood in the picture that real photon production processes with a low resolution probe cannot resolve single and multiple Pomeron exchanges, while higher photon virtuality reactions with an increased resolution, are able to probe single Pomeron exchanges. This leads to a Q^2 dependence in the intercept $\alpha_{\mathbb{P}}^{eff}(0, Q^2)$ and therefore also in the exponent dictating the energy dependence of the total photon cross section, $\Delta_{\mathbb{P}}^{eff}(Q^2) = \alpha_{\mathbb{P}}^{eff}(0, Q^2) - 1$. For real photons one has $\Delta^{eff} \approx 0.08$, while for high Q^2 $\Delta^{eff} \approx 0.24$ coming from the single Pomeron pole. As one can see the intercept $\alpha_{\mathbb{P}}^{eff}(0) = 1.08$ which is also found in soft hadronic interactions is much smaller than the intercept of the actual single Pomeron pole itself. The parametrization of the effective energy exponent is taken to be

$$\Delta^{eff}(Q^2) = \Delta(0) \left(1 + \frac{2Q^2}{d + Q^2} \right), \quad (2.81)$$

with the free parameters $\Delta(0) = 0.077$ and $d = 1.117$ GeV² as determined from fits to the low x behavior of $F_2 \sim x^{-\Delta(Q^2)}$ [34]. At very large Q^2 QCD evolution effects should be taken into account, which lead to an even stronger increase of the energy dependence with Q^2 .

Taking the effective intercept into account in the amplitude for vector meson photoproduction gives

$$T(s, t, Q^2, M_V^2) = f(Q^2, M_V^2, t) \left(\frac{s}{s_0} \right)^{\alpha_{\mathbb{P}}^{eff}(t, Q^2)} \eta(\alpha_{\mathbb{P}}^{eff}), \quad (2.82)$$

where $\eta(\alpha)$ is the signature factor and the center of mass energy squared $s = W^2$ dependence is governed by the effective Pomeron trajectory

$$\alpha_{\mathbb{P}}^{eff}(t, \bar{Q}^2) = 1 + \Delta^{eff}(\bar{Q}^2) + \alpha_{\mathbb{P}}^t, \quad (2.83)$$

with $\alpha_{\mathbb{P}}^t = 0.25$ GeV⁻² as obtained in hadronic interactions. For the production of light quark (u, d, s) states $\bar{Q}^2 = Q^2$, while for heavy quark systems $\bar{Q}^2 = c m_q^2 + Q^2$ with $c \sim 1$ and m_q the quark mass. This accounts for the fact that for heavy quarks the contribution of multiple Pomeron exchange is already small at low Q^2 .

The t -dependence of the amplitude is assumed to be exponential

$$f(Q^2, M_V^2, t) = \tilde{f}(Q^2, M_V^2) e^{R^2 t}, \quad (2.84)$$

with $R^2 = R_p^2 + R_V^2(Q^2)$ in which $R_p^2 = 2$ GeV⁻² and $R_V^2 = R_{0V}^2 M_V^2 / (M_V^2 + Q^2)$ with $R_{0V}^2 = 1$ GeV⁻² taking into account the variation of the interaction radius with Q^2 .

The Pomeron contribution to the differential cross section is then

$$\frac{d\sigma}{dt} = \mathcal{F}(Q^2, M_V^2) \left(\frac{s}{s_0} \right)^{2\Delta^{eff}(Q^2)} e^{\lambda(s)t}, \quad (2.85)$$

with $\mathcal{F} \propto |\tilde{f}\eta(\alpha)|^2$ and the slope of the diffractive cone $\lambda(s) = 2(R^2 + \alpha'_p \ln(s/s_0))$. The energy scale factor is chosen as $s_0 = M_V^2 + Q^2$. While the energy dependence is fixed by the effective Pomeron trajectory, the function \mathcal{F} is unknown and should be fitted to the experimental data.

The cross section can be rewritten in terms of the nucleon structure function as

$$\frac{d\sigma}{dt} = \Phi(Q^2, M_V^2) F_2^x(x, Q^2) e^{\lambda(s)\omega}, \quad (2.86)$$

where the parametrization of F_2 is taken from [34]. This form of the cross section is suitable to apply QCD evolution equations at large values of Q^2 . The effective Pomeron trajectory determines the low x contribution of the sea quarks and gluons to the structure function and the latter equation is equivalent to equation 2.85 with $F_2 = F_2^{sea}$. For low energy production of vector mesons containing u and d quarks, one has also contributions from Reggeon exchange (ρ, ω, f, a_2) which are taken into account in equation 2.86 by the valence quark contribution to F_2 .

This model successfully describes the W dependence of both real and virtual photo-production of ρ^0, ω, ϕ and J/Ψ vector mesons, where for the latter two only Pomeron exchange contributes to the amplitude.

2.12 Perturbative QCD Models

Regge theory is a suitable way of describing vector meson production at low and high energies, but only at low momentum transfers. As soon as a hard scale in the scattering process sets in, one can turn to a perturbative quantum chromodynamics (pQCD) based model description of vector meson production. The hard scale can be introduced by going to high values of the momentum transfer Q^2 or $|t|$ or also by generating vector mesons containing heavy quarks (c or b quarks). The two collider experiments at HERA can access this kind of hard regime and provided a large amount of measurements allowing to test the variety of pQCD models.

When looking at exclusive vector meson production, one has to remember that the initial and final states in the scattering process cannot be described in a perturbative regime and therefore have to be separated from the short distance, hard interaction part. A general factorization theorem proven by Collins, Frankfurt and Strikman [37] states that at large values of $Q^2 \gg \Lambda_{QCD}^2$, for small $|t|$ and assuming that the meson mass can be neglected $M_V^2 \ll s$, the leptoproduction cross section $\gamma^* p \rightarrow V p'$ can be expressed as a convolution of a non-forward parton distribution function of the proton, a hard scattering function and a meson wave function.

In the proton rest frame, vector meson production at high energy can be seen to occur in three distinct steps ordered in time : the virtual photon breaks up in a quark-antiquark pair; the quark-antiquark pair interacts hard with the target; the scattered quark-antiquark pair forms the final state vector meson. The scattering process on the proton occurs on a much shorter timescale than the fluctuation of the photon in the $q\bar{q}$ pair or the vector meson formation time, allowing to treat the scattering as a perturbation.

The amplitude can thus be factorized in

$$A = \Psi_{\gamma^* \rightarrow q\bar{q}} \otimes A_{q\bar{q}+p \rightarrow q\bar{q}+p} \otimes \Psi_{q\bar{q} \rightarrow V}. \quad (2.87)$$

The first term represents the amplitude for the fluctuation of the virtual photon into a $q\bar{q}$ pair. The last term describes the recombination of the final, scattered hadronic state into the vector meson. The middle term corresponds to the short distance amplitude of the scattering of the hadronic state with the target. This latter term can be calculated in pQCD models and the exchanged color singlet system is at high energy (or small x) usually modeled as a gluon pair or a gluon Lipatov ladder. The obtained amplitude is proportional to the square of the gluon density in the proton ($xg(Q^2, x)$)². This makes hard vector meson production more sensitive to variations in the gluon distribution than the inclusive process, which depends only linearly on $xg(x, Q^2)$. Significant theoretical uncertainties arise due to the choice of the scale at which the gluon density is probed, the parametrization of the gluon distribution and the modelling of the vector meson wave function [42].

pQCD like calculations exhibit some general common features :

- The cross section for hard diffractive vector meson production is related to the square of the gluon density in the nucleon and therefore provides a sensitive probe of the gluon content in the target.
- The cross section should be dominated by production due to longitudinally polarized photons at high Q^2 , meaning that $R = \sigma_L/\sigma_T$ should increase with Q^2 to values above unity.
- At high Q^2 the longitudinal cross section goes like Q^{-6} .
- The vector meson production ratio $\rho : \omega : \phi : J/\Psi$ is predicted to be $9 : 1 : 2 : 8$ deduced from the naive SU(4) flavor symmetry quark counting rules taking the quark charges into account. At low Q^2 this ratio does not hold due the suppression of heavier quark flavors in ϕ and J/Ψ vector mesons, while for high Q^2 the production mechanism seems to become flavor independent resulting in a restoration of flavor symmetry.

2.12.1 The Ryskin Model

The model proposed by Ryskin in [38] was originally developed to describe diffractive J/Ψ electroproduction in the leading $\log(\frac{1}{x})$ approximation ($LLA(\frac{1}{x})^5$) of pQCD. Due to the high J/Ψ mass providing a large enough scale compared to the confinement scale Λ_{QCD} , a pQCD calculation becomes feasible, even at low Q^2 . In the Born approximation the two diagrams shown in figure 2.10 are taken into account. The vector meson production is described via the exchange of a colorless gluon ladder, which in the limit $t = 0$ can be modeled via the proton gluon distribution.

⁵leading $\log(\frac{1}{x})$: $\alpha_s(Q^2) \ln Q^2 \ll 1$ and $\alpha_s(Q^2) \ln \frac{1}{x} \sim 1$.

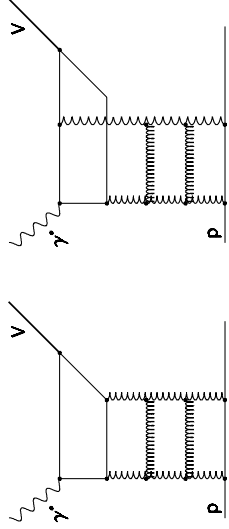


Figure 2.10: Lowest order diagrams taken into account in the Ryskin model. The exchanged virtual photon fluctuates into a $q\bar{q}$ pair which subsequently interacts with the proton via a gluon ladder.

The model uses a non-relativistic charmonium constituent quark wave function for the J/Ψ system with the quark and antiquark each having a momentum equal to half the meson momentum. The obtained cross section is

$$\frac{d\sigma}{dt}(\gamma^* p \rightarrow Vp) = [F_N^{2g}(t)]^2 \frac{\alpha_s^2(\bar{q}^2) \Gamma_{ee}^V M_V^3}{3\alpha_{em}} \pi^{-3} \left[\bar{x}g(\bar{x}, \bar{q}^2) \frac{2\bar{q}^2 - p_T^2}{(2\bar{q}^2)^3} \right]^2 \left(1 + \frac{Q^2}{M_V^2} \right). \quad (2.88)$$

The cross section is seen to be sensitive to the square of the proton gluon density probed at the effective photon virtuality and fractional gluon momentum

$$\bar{q}^2 = \frac{Q^2 + M_V^2 + p_T^2}{4}, \quad \bar{x} = \frac{4\bar{q}^2}{s}. \quad (2.89)$$

where p_T is the vector meson transverse momentum with respect to the virtual photon direction.

The newly introduced 2-gluon proton form factor $F_N^{2g}(t)$ (with $F_N^{2g}(0) = 1$) takes into account the t dependence of the amplitude and characterizes the correlations between two gluons inside the proton. This form factor remains unmeasured up to now and is usually approximated by the electromagnetic form factor.

The last term in equation 2.88 allows the production via longitudinal polarized photons with $\sigma_L/\sigma_T \approx Q^2/M_V^2$. The amplitude in this 2-gluon Pomeron exchange model conserves the initial photon helicity and for large $Q^2 \gg M_V^2$ one has that $\sigma_L \gg \sigma_T$.

The calculation was extended beyond the leading $\ln Q^2$ approximation in [39]. Several corrections, including relativistic effects in the vector meson wave function due to Fermi motion, rescattering and absorption of the quark-antiquark pair and next-to-leading order QCD radiative corrections, were estimated. These corrections partially compensate each other and become insignificant for $W \lesssim 20$ GeV; they leave the cross section basically unaltered, but do introduce large normalization uncertainties.

This approach followed in the Ryskin model is supported by the H1 measurements of the J/Ψ real photoproduction cross section [40]. The cross section exhibits a strong increase with energy, which is compatible with the strong rise of the proton structure function at low Bjorken x .

In principle the Ryskin model can also be applied to lepto-production of lighter vector mesons.

2.12.2 The Model of Brodsky *et al.*

A calculation similar to the Ryskin model, but suitable also for lighter vector meson states is given by Brodsky *et al.* in [41]. The forward differential cross section of diffractive vector meson lepto-production is calculated in pQCD in the double leading log approximation (DLLA)⁶. The model is valid in the kinematical region where $s/M_V^2 \gg 1$, $s/Q^2 \gg 1$ and $|t| \ll Q^2$. Furthermore, it is assumed that $Q^2 \gg \Lambda_{QCD}$ and $Q^2 \gg M_V^2$.

In the large s and large Q^2 limit, the process is expected to proceed predominantly via 2-gluon exchange. The lepto-production amplitude is predicted to be dominated by longitudinally polarized virtual photons coupling to longitudinal vector mesons with the leading forward longitudinal cross section given by

$$\left. \frac{d\sigma_L}{dt} \right|_{t=0}(\gamma^* p \rightarrow Vp) = \frac{12\pi^3 \Gamma_{ee}^V M_V \eta_V^2}{Q^6 \alpha_{em} N_c} \alpha_s^2(Q^2) \left[\left[1 + \frac{d}{2} \left(\frac{d}{d \ln x} \right) \right] xg(x, Q^2) \right]^2. \quad (2.90)$$

N_c is the number of colors (here equal to 3) and η_V is a moment of the vector meson distribution amplitude, which represents the integrated vector meson wave-function. The different parametrizations of the vector meson distribution amplitude introduce some theoretical normalization uncertainty on the cross section. As can be seen from equation 2.90 the model predicts a longitudinal cross section falling as $1/Q^6$. This large power is partially compensated by the Q^2 -dependence of the gluon distribution. Due to the rapid increase of $xg(x, Q^2)$ at small x and large Q^2 , the model predicts a substantial rise of the cross section with energy. The transverse cross section is predicted to fall as $1/Q^8$.

The t -dependence of the cross section is provided by a universal 2-gluon nucleon form factor, which is independent of the vector meson type. This leads to the prediction that at large Q^2 the t -slope becomes independent of the produced vector meson. The part of the amplitude corresponding to the $\gamma^* \rightarrow V$ depends only weakly on t for $|t| \ll Q^2$. This means that the cross section gets its t -dependence primarily from the gluon-nucleon part of the scattering amplitude. The slope of the t -dependence is expected to increase slowly with energy due to the Gribov shrinkage of the diffractive cone.

The model has some uncertainty on the evolution scale in equation 2.90. Note that here the scale of the gluon density is about a factor of 4 larger compared to the scale given by equation 2.89 in the Ryskin model.

Frankfurt, Koepf and Strikman [42] extended the model by calculating the process in the LLA approximation making it possible to use leading order gluon distributions in the cross section predictions to compare to experimental data. According to them equation 2.90 is valid when the coherence length $l_c = 1/(2M_N x)$ is large compared to the nucleon diameter $2r_N$, so that the virtual photon transforms into a hadronic component well before reaching the target and the final state vector meson is formed well past the target. This leads to an upper limit in x for the applicability of the model $x \ll 1/(4M_N r_N) \approx 0.06$. They find that taking into account transverse Fermi motion

⁶double leading log : $\alpha_s(Q^2) \ln Q^2 \ll 1$, $\alpha_s(Q^2) \ln \frac{1}{x} \ll 1$ and $\alpha_s(Q^2) \ln Q^2 \ln \frac{1}{x} \ll 1$.

of the quarks in the vector meson leads to a significant suppression of the cross section towards lower Q^2 , which slows down the Q^2 dependence. They claim that substantial next-to-leading order corrections should be present in diffractive vector meson production, which requires a rescaling of the photon virtuality Q^2 at which the gluon density is probed, to an effective value Q_{eff}^2 . For ρ production this results in a decrease of the cross section $Q_{eff}^2 < Q^2$, while for J/Ψ production where $Q_{eff}^2 > Q^2$ one obtains an increase.

The production ratio of various different vector mesons at large Q^2 is predicted according to equation 2.90 to be

$$\frac{\sigma_L(V_1)}{\sigma_L(V_2)} \Big|_{t=0} = \frac{M_{V_1} \Gamma_{ee}^{V_1} \eta_{V_1}^2}{M_{V_2} \Gamma_{ee}^{V_2} \eta_{V_2}^2}, \quad (2.91)$$

making the ratios closely related to the vector meson wave functions. All dependence on the quark masses is contained in the meson wave function and not in the scattering amplitude. Using experimental values of the leptonic decay widths and estimates of η_V [43] one has according to equation 2.91

$$\rho : \omega : \phi : J/\Psi = 9 : (1 \cdot 0.8) : (2 \cdot 1.0) : (8 \cdot 1.9), \quad (2.92)$$

predicting an approximate restoration of SU(4) flavor symmetry. At asymptotically large Q^2 all $q\bar{q}$ wave functions are expected to converge to a universal asymptotic wave function with $\eta = 3$ giving

$$\rho : \omega : \phi : J/\Psi = 9 : (1 \cdot 0.8) : (2 \cdot 1.2) : (8 \cdot 3.5), \quad (2.93)$$

resulting in a clear enhancement of heavy flavor resonance production. Due to the larger photon virtuality which enters the gluon distribution for heavy flavor production, an increase of the relative yield of heavy flavor production with decreasing x is predicted.

2.12.3 The Model of Martin *et al.*

It is suggested by Martin, Ryskin and Teubner in [44] that any description of vector meson production in terms of a convolution of the wave function of the $q\bar{q}$ pair (produced by the γ^*) with the one of the vector meson, yields a prediction for the longitudinal cross section consistent with the behavior of the data, while the transverse cross section is predicted much too small and falls too rapidly with increasing Q^2 .

The authors present an alternative pQCD approach to ρ electroproduction based on the production of open light $q\bar{q}$ pairs and the parton-hadron duality assumption, where the convolution with the ρ wave function is omitted. The parton-hadron duality hypothesis states that the total hadron (ρ, ω, \dots) production cross section averaged over a mass interval of typically 1 GeV^2 is well represented by the partonic cross section. In the low mass region containing the ρ meson, complicated partonic states (with e.g. additional gluon emission) are suppressed, while on the hadronic side one mainly has 2π and some 3π states. The cross section is therefore modeled according to

$$\sigma(\gamma^* p \rightarrow \rho p) \approx 0.9 \sum_{q=u,d} \int_{M_{low}^2}^{M_{high}^2} dM^2 \frac{d\sigma(\gamma^* p \rightarrow (q\bar{q})p)}{dM^2}, \quad (2.94)$$

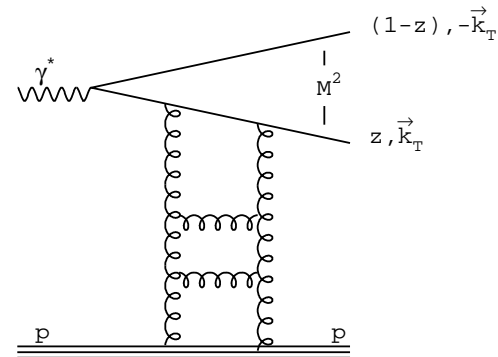


Figure 2.11: The diffractive production of an open light $q\bar{q}$ pair with invariant mass M , as used in the model of Martin *et al.* z and $(1-z)$ are the momentum fractions of the quark and antiquark relative to the virtual photon momentum. $\pm k_T$ denote the transverse momenta of the quark and antiquark.

where the integration limits are chosen to span the ρ invariant mass region (e.g. $0.6 < M < 1.05 \text{ GeV}$) with $M_{high}^2 - M_{low}^2 \sim 1 \text{ GeV}^2$ and where the factor 0.9 is introduced to allow for ω production. The basic diagram in their calculation is depicted in figure 2.11. The virtual photon fluctuates into a $u\bar{u}$ or $d\bar{d}$ pair, which then interacts hard with the proton via the exchange of a 2-gluon system or gluon ladder. A long time after the interaction the $q\bar{q}$ pair is distorted by confinement and has due to phase space restrictions little alternative but to hadronize into a ρ meson.

Both the longitudinal and transverse part of the cross section are found to be proportional to the square of the gluon density which is probed at a scale

$$K^2 = z(1-z)Q^2 + k_T^2, \quad (2.95)$$

where z and $1-z$ are the longitudinal momentum fractions of the quark and antiquark relative to the virtual photon momentum and $\pm k_T$ are the transverse momenta of the quark with respect to the direction of the virtual photon. This scale represents the typical transverse distance probed in the process $b_T \approx 1/K$.

The calculations are done under the assumption of s -channel helicity conservation and for $t = 0$. The model has no explicit dependence on t and therefore an exponential behavior $\exp(-b|t|)$ is added to the cross section with $b = 5.5 \text{ GeV}^{-2}$ as seen in experimental data for large Q^2 .

Their prediction for the R ratio may be written as

$$\frac{\sigma_L}{\sigma_T} = \frac{Q^2}{M^2} \left(\frac{\gamma}{\gamma+1} \right)^2, \quad (2.96)$$

with M the invariant mass of the $q\bar{q}$ pair and γ the effective anomalous dimension of the gluon as defined by $\gamma \equiv d \ln(xg(x, K^2))/d \ln K^2$. This anomalous dimension is seen to

decrease with increasing Q^2 and therefore slows down the strong increase with Q^2 of the R ratio at high Q^2 .

The model suffers from large normalization uncertainties on the predicted cross section. One problem is the choice of the width of the invariant mass interval over which the parton-hadron duality assumption has to be applied. Another one is the effect of virtual gluon corrections to open $q\bar{q}$ production, which lead to the so-called K factor enhancement $\exp(\alpha_s C_f \pi)$ with the color factor $C_f = 4/3$. The major ambiguity here is the choice of the scale for α_s . Nevertheless, the prediction of the R ratio is rather free of the above uncertainties and should therefore, according to the authors, provide a valuable probe of the gluon distribution $g(x, K^2)$ in the domain $x \approx Q^2/W$ and $K^2 \lesssim Q^2/4$.

2.12.4 The Model of Vanderhaeghen *et al.*

A calculation based on the OFPD framework for vector meson production in the valence region ($x \approx 0.3$) is presented in [45, 46] by Vanderhaeghen, Guichon and Guidal. The model is limited to the longitudinal cross section, as only there the factorization theorem holds.

The ξ -dependent parametrization of H^q was based on using the product of the unpolarized quark distribution (e.g. MRST98 [47]) with the appropriate form factor as in equation 2.75. Contributions from E^q are always multiplied with the momentum transfer Δ and can in the near-forward region be safely neglected. The dependence on the quark content of the vector meson is taken into account via appropriate combinations of H^q , so that different vector meson flavors probe different quark flavor combinations of unpolarized OFPD's. The leading order amplitude corresponding to the diagram in figure... (a) is found to behave as $1/Q$, resulting together with the kinematical phase factor going like $1/Q^4$, in a longitudinal cross section $d\sigma_L/dt$ varying like $1/Q^6$ for large Q^2 .

Corrections to the leading order amplitude due to the intrinsic transverse momentum of the quarks in the meson wave function and the nucleon were estimated and lead to a suppression of the cross section, especially at lower Q^2 . Also the contributions from soft overlap mechanisms, where the meson is formed without the exchange of a gluon between the quarks, were calculated as this can compete with the hard one-gluon exchange amplitude at leading order. The overlap contribution to the longitudinal cross section was found to drop approximately as $1/Q^8$ and was estimated to be an order of magnitude below the hard contribution in the valence region at $Q^2 \approx 3 \text{ GeV}^2$.

To allow comparison with experimental data at low x , a contribution due to perturbative 2-gluon exchange as modeled in [42] (see paragraph 2.12.2) was also implemented in their calculations. For small x the 2-gluon exchange mechanism will dominate as it probes the gluon distribution. The quark exchange mechanism dominates in the valence region as it is proportional to the quark distributions. This latter contribution also rises towards lower x due to the quark sea distribution. However it remains lower than the gluon exchange part.

The model predicts a ρ_L^0/ω_L ratio of about 5 : 1 in the valence region.

2.12.5 The Model of Royen *et al.*

The model presented by Royen *et al.* in [48] is a lowest order pQCD calculation and thus designed for high energy and Q^2 values. However, it also seems to describe the differential cross sections in the non-perturbative photoproduction region. The model uses the factorization approach, where the process is pictured via the exchange of a pair of gluons interacting with a $q\bar{q}$ pair emerging from the photon as shown in figure 2.12.

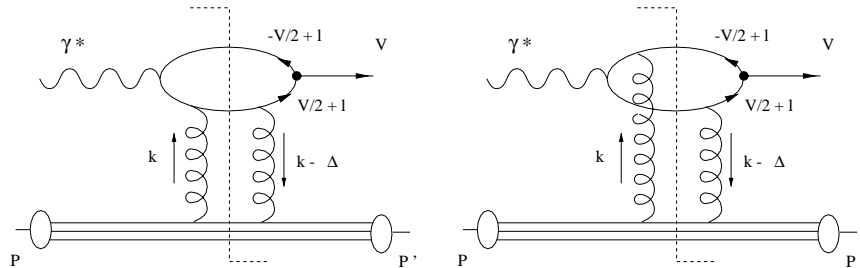


Figure 2.12: The two diagrams for exclusive VM production via 2 gluon exchange as implemented in the calculations of Royen *et al.*

In a first approach [49] the vector meson was modeled by its lowest Fock state ($q\bar{q}$) with no Fermi momentum, where the quark and antiquark each carried half of the meson four-momentum and had equal masses $m_q = M_V/2$. The proton was represented in a constituent quark model by a form factor based on the sum of two dipole form factors. The model could not predict any energy dependence, so that the latter was taken into account via a Regge factor, which was found to be independent of Q^2 and M_V . The diffractive slope was described in terms of a contribution coming from the proton form factor, the Regge factor (or Pomeron) and a part coming from the quark loop. This model was able to correctly reproduce the cross section ratios for ρ , ϕ and J/Ψ at both high and low Q^2 and to describe the dependence of the slopes on the mass of the vector meson. However, it produced a transverse cross section falling like $1/Q^8$ at high Q^2 , giving an R ratio rising linearly for all Q^2 , whereas experimental data indicates that the ratio reaches a plateau at high Q^2 .

The lower part of the diagram mainly controls the energy and t dependence of the process, whereas the upper loop is responsible for the helicity structure of the amplitude and the Q^2 dependence. Therefore, in a second approach the problem with the transverse amplitude was addressed by reconsidering the upper part of the diagram. Instead of the usual wave function formalism, the $q\bar{q} \rightarrow V$ transition was now modeled as a 3-point vertex function $\Phi(l^2)$ with l being the relative quark four-momentum. The quark and antiquark did no longer carry the same four-momentum and could now go off-shell. By doing so the vertex contained a pole in l , so that the integration over l^2 in the quark loop gave rise to two terms in the amplitude, one imaginary part coming from the discontinuity, which was analogous to the amplitude obtained with the wave function formalism, and one real contribution coming from the principle part of the amplitude. The latter behaved

like $A_L \propto 1/Q^3$ and $A_T \propto 1/Q^2$ at high Q^2 , while the imaginary parts like $A_L \propto 1/Q^3$ and $A_T \propto 1/Q^4$. Due to a suppression by the vertex function, this behavior only sets in for relatively large Q^2 . This approach resulted in an improved description of the R ratio in agreement with the data, where the linear behavior at lower Q^2 is seen to saturate as Q^2 increases above about 10 GeV².

2.13 Vector Meson Polarization

This section deals with the formalism used to study vector meson polarization states. The vector meson and the virtual photon have the same quantum numbers. The vector meson spin density matrix elements can be expressed in terms of helicity amplitudes describing the transfer of the virtual photon helicity to the vector meson. It is therefore useful to start with the derivation of the spin density matrix of the virtual photon to come to that of the vector meson itself. In the end the vector meson angular decay distribution is expressed as a function of these spin density matrix elements. A detailed and complete description of the formalism can be found in [50, 51]. The relevant features of the theory will be explained in the paragraphs below.

2.13.1 The Photon Spin Density Matrix

The differential cross section for vector meson V production in eN scattering reads

$$\frac{d\sigma_{eN \rightarrow eMV}}{dE' d\Omega' d\Phi dt} = \frac{1}{(2\pi)^5} \frac{E'}{E} \frac{m^2}{4\sqrt{t^2 + Q^2}} \frac{1}{4} \sum_{spins} |\mathcal{M}|^2, \quad (2.97)$$

where $d\Omega'$ is the volume element of the scattered lepton, Φ the angle between the scattering plane and the hadron production plane and \mathcal{M} the matrix element describing the scattering process. The matrix element is given by

$$\mathcal{M} = e^2 \langle l_2 | j_\mu | l_1 \rangle \cdot \langle n_2 v | j^\mu | n_1 \rangle, \quad (2.98)$$

with l_1, l_2, n_1, n_2 and v the spinors for the incoming and outgoing lepton and nucleon and vector meson respectively, e the electric charge and j the electromagnetic current operator.

For an unpolarized lepton beam $|\mathcal{M}|^2$ can be rewritten in terms of a known leptonic tensor $\tilde{L}_{\mu\nu}$ and a hadronic tensor $\tilde{T}^{\mu\nu}$

$$\frac{1}{4} \sum_{spins} |\mathcal{M}|^2 = \frac{1}{4} \tilde{L}_{\mu\nu} \tilde{T}^{\mu\nu}, \quad (2.99)$$

where both tensors are defined as

$$\tilde{L}_{\mu\nu} = \sum_{spins} m^2 \langle l_2 | j_\mu | l_1 \rangle \cdot \langle l_2 | j_\nu | l_1 \rangle^* \quad (2.100)$$

$$= m^2 \text{Tr} \left(\frac{l_2 + m}{2m} \gamma_\mu \frac{l_1 + m}{2m} \gamma_\nu \right), \quad (2.101)$$

$$\tilde{T}^{\mu\nu} = \sum_{spins} \langle n_2 v | j^\mu | n_1 \rangle \cdot \langle n_2 v | j^\nu | n_1 \rangle^*. \quad (2.102)$$

$\tilde{L}_{\mu\nu}$ is the virtual photon spin density matrix describing the spin state of the photon. One can evaluate this tensor in a coordinate system with the z -axis along the virtual photon direction $q = l_2 - l_1$ and with l_1 and l_2 in the x, z plane, where $\tilde{L}_{\mu\nu}$ in general has transverse (x, y) , longitudinal (z) and scalar (0) components. A Lorentz transformation along \vec{q} leaves the transverse components unchanged, but transforms the scalar and longitudinal components into each other. Just like the polarization of a physical spin 1 particle is Lorentz invariant, one can show that this also holds for the spin density matrix. It can thus be evaluated in the Breit frame, resulting in a matrix $L_{\mu\nu}(\epsilon, \delta)$ with ϵ the polarization parameter defined⁷ by $\frac{L_{11}}{L_{33}} = \frac{1-\epsilon}{1+\epsilon}$ and $\delta = \frac{2m^2}{Q^2} (1-\epsilon)$ the mass correction parameter. Finally $L_{\mu\nu}$ can be written in the hadron center of mass helicity frame by rotating it around the z -axis over an angle Φ between the leptonic and hadron production plane.

$$L_{\lambda\lambda'} = U_{\lambda\mu} L_{\mu\nu} U_{\lambda'\nu}^{-1}, \quad (2.103)$$

where λ, λ' denote the photon helicity ($\lambda, \lambda' = +1, 0, -1$) and $U_{\lambda\mu}$ describes the rotation. The end result is a spin density matrix $L_{\lambda\lambda'}$, which is a function of ϵ, δ and Φ .

In case of a polarized incident lepton beam with polarization vector P_μ , $\tilde{L}_{\mu\nu}$ has to be replaced by another matrix $\tilde{L}_{\mu\nu}$ given by

$$\tilde{L}_{\mu\nu} = \text{Tr} \left(\frac{l_2 + m}{2} \gamma_\mu \frac{l_1 + m}{2} (1 + \gamma_5 \not{P}) \gamma_\nu \right) \quad (2.104)$$

$$= \tilde{L}_{\mu\nu} + \frac{m}{4} \text{Tr} (\gamma_\mu \not{A} \gamma_5 \not{P} \gamma_\nu + \not{A} \gamma_\mu \gamma_5 \not{P} \gamma_\nu) \quad (2.105)$$

$$= \tilde{L}_{\mu\nu} + \tilde{S}_{\mu\nu}. \quad (2.106)$$

Just like $\tilde{L}_{\mu\nu}$, $\tilde{S}_{\mu\nu}$ is Lorentz invariant under a boost along \vec{q} and can be transformed into the helicity basis to $S_{\lambda\lambda'}$ which is a function of ϵ, Φ and the degree of polarization P .

The photon density matrix, normalized to a unit flux of transverse photons, then becomes

$$\rho(\gamma)_{\lambda\lambda'} = \frac{1-\epsilon}{Q^2} (L_{\lambda\lambda'} + S_{\lambda\lambda'}). \quad (2.107)$$

This density matrix can be decomposed into an orthogonal set of nine hermitian matrices Σ^α

$$\rho(\gamma) = \frac{1}{2} \sum_{\alpha=0}^8 \tilde{\Pi}_\alpha \Sigma^\alpha, \quad (2.108)$$

where $\tilde{\Pi}_\alpha$ is a known vector, function of ϵ, δ, Φ and the lepton polarization vector. Each of the nine hermitian matrices describes a different photon polarization state. The matrices $\Sigma^{0..3}$ describe transverse photons and correspond to the formalism used in the photoproduction formalism [50] : Σ^0 represents the unpolarized part, $\Sigma^{1..2}$ give the linear polarization and Σ^3 describes circular polarization. Σ^4 corresponds to longitudinal photons and $\Sigma^{5..8}$ provide transverse/longitudinal interference terms.

⁷When this expression is written in terms of lab system variables, one arrives at the second part of the previously given equation 2.10.

2.13.2 The Vector Meson Spin Density Matrix

The paragraphs above dealt with the lepton vertex only, leading to the spin density matrix of the virtual photon. To come to the spin density matrix of the vector meson, we now consider the hadron vertex corresponding to the scattering reaction $\gamma^* N \rightarrow VN$. The cross section for this process looks like

$$\frac{d\sigma_{\gamma^* N \rightarrow VN}}{dt d\Phi} = \frac{1}{32\pi^2(\nu^2 + Q^2)} \frac{2(1-\epsilon)}{Q^2} \frac{1}{4} \sum_{spins} |\mathcal{M}|^2, \quad (2.109)$$

where the factor $2(1-\epsilon)/Q^2$ is introduced to normalize to unit transverse photon flux. The cross section can be rewritten in terms of the helicity amplitudes of Jacob and Wick, describing the transfer of the photon helicity to the vector meson after summing over the nucleon helicities

$$T_{\lambda_V \lambda_{N'} \lambda_\gamma \lambda_N} = \langle \lambda_V \lambda_{N'} | j_{\lambda_\gamma} | \lambda_N \rangle, \quad (2.110)$$

with $j_{\lambda_\gamma = \pm 1} = j_x \pm ij_y$ and $j_{\lambda_\gamma = 0} = j_z$, resulting in

$$\frac{d\sigma_{\gamma^* N \rightarrow VN}}{dt d\Phi} = \frac{1}{32\pi^2(\nu^2 + Q^2)} \frac{1}{2} \text{Tr}(T\rho(\gamma)T^\dagger). \quad (2.111)$$

The vector meson spin density matrix is then

$$\rho(V) = \frac{1}{2} (T\rho(\gamma)T^\dagger) / \int \frac{d\Phi}{2\pi} \text{Tr}(T\rho(\gamma)T^\dagger), \quad (2.112)$$

where a summation over the nucleon helicities is understood and the integral is used to normalize the matrix. The density matrix can now also be decomposed into hermitian matrices in a similar way as for the photon density matrix

$$\rho(V) = \sum_{\alpha=0}^8 \Pi_\alpha \rho^\alpha, \quad (2.113)$$

with

$$\rho_{\lambda_V \lambda_V'}^\alpha = \frac{1}{2N_\alpha} \sum_{\lambda_{N'}, \lambda_N, \lambda_\gamma, \lambda_\gamma'} T_{\lambda_V \lambda_{N'} \lambda_\gamma \lambda_N} \Sigma_{\lambda_\gamma \lambda_\gamma'}^\alpha T_{\lambda_V' \lambda_{N'} \lambda_\gamma' \lambda_N}^*, \quad (2.114)$$

where the N_α are normalization constants and the vector Π_α is a known function of ϵ , δ , $R = \sigma_L/\sigma_T$, Φ and the lepton polarization vector. Each of these nine hermitian matrices ρ^α again represent production by different virtual photon polarization states. $\alpha = 0$ corresponds to unpolarized transverse photons, $\alpha = 1, 2$ to the two directions of linear polarization, $\alpha = 3$ represents circular photons and $\alpha = 4$ gives longitudinally polarized photon production. $\alpha = 5 \dots 8$ provide the transverse/longitudinal interference part, where only $\alpha = 5, 6$ contribute for an unpolarized lepton beam, while a polarized lepton beam gives the additional $\alpha = 7, 8$ terms.

Due to parity conservation the following symmetry relation for the helicity amplitudes holds

$$T_{-\lambda_V -\lambda_{N'} -\lambda_\gamma -\lambda_N} = (-1)^{(\lambda_V - \lambda_{N'}) - (\lambda_\gamma - \lambda_N)} T_{\lambda_V \lambda_{N'} \lambda_\gamma \lambda_N}. \quad (2.115)$$

One can prove that as a consequence of the previous relation and the symmetry properties of the Σ^α matrices, the vector meson spin density matrix elements defined by equation 2.114 obey the symmetry relation

$$\rho_{-\lambda -\lambda'}^\alpha = \begin{cases} (-1)^{\lambda - \lambda'} \rho_{\lambda \lambda'}^\alpha, & \alpha = 0, 1, 4, 5, 8, \\ -(-1)^{\lambda - \lambda'} \rho_{\lambda \lambda'}^\alpha, & \alpha = 2, 3, 6, 7. \end{cases} \quad (2.116)$$

2.13.3 Vector Meson Decay Angular Distribution

The ρ^0 or ω vector meson are spin-1 objects and hence in their rest frame they carry a total angular momentum $J = L + S = 1$. Due to angular momentum conservation, the decay meson system also has $J = 1$. When looking at the most common decay modes, $\rho^0 \rightarrow 2\pi$ and $\omega \rightarrow 3\pi$, the decay particles have spin 0, meaning that the angular momentum L of the decay system must be 1. When a vector meson decays, its spin-state will be reflected in the orbital angular momentum of the decay particles.

The decay distribution of the vector meson will be described in the vector meson rest frame using the so-called s -channel helicity system, in which the quantization axis (z -axis) is chosen opposite to the direction of the outgoing nucleon in the center-of-mass frame (see figure 2.13). The decay angles θ and ϕ are, in the case of the ρ^0 , defined as the polar and azimuthal angle of one of the decay pions, where usually the π^+ is taken. For a three particle decay, one takes the polar and azimuthal angle of the unit vector along the normal to the decay plane.

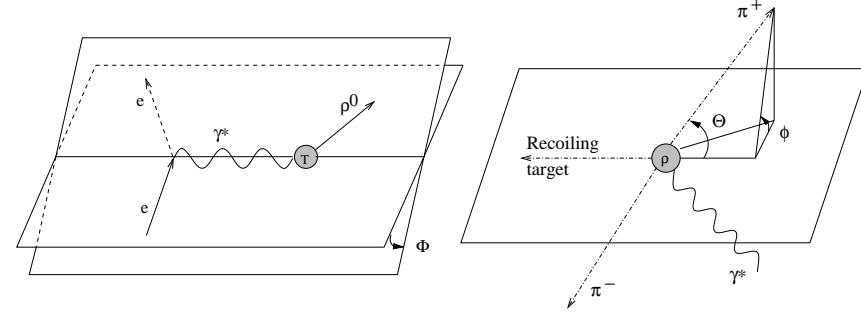


Figure 2.13: The definition of the angles used in the ρ^0 vector meson polarization analysis. Φ is the angle between the scattering plane and the hadron production plane. (θ, ϕ) are the polar and azimuthal angle of the decay π^+ in the vector meson rest frame in the s -channel helicity system.

In the vector meson rest frame the decay angular distribution for the decay into 2 or 3 pseudoscalar mesons is given by

$$\frac{dN}{d\cos\theta d\phi} \equiv W(\cos\theta, \phi) = \sum_{\lambda_V \lambda_V'} \langle \theta, \phi | M | \lambda_V \rangle \rho(V)_{\lambda_V \lambda_V'} \langle \lambda_V' | M^\dagger | \theta, \phi \rangle, \quad (2.117)$$

with M the decay amplitude. $\langle \theta, \phi | M | \lambda_V \rangle$ can be expressed as a function of the general Wigner D -functions $D_{mm'}^{(j)}(R)$ which give the probability that a quantum state $|j, m\rangle$ is transformed into the state $|j, m'\rangle$ after a rotation R . Here the D -functions are to be taken as $D_{\lambda_V, \lambda_V}^{S_V}(R)$ and they are given by

$$D_{10}^1(\phi, \theta, -\phi) = -\frac{1}{\sqrt{2}} e^{-i\phi} \sin \theta, \quad (2.118)$$

$$D_{00}^1(\phi, \theta, -\phi) = \cos \theta, \quad (2.119)$$

$$D_{-10}^1(\phi, \theta, -\phi) = \frac{1}{\sqrt{2}} e^{i\phi} \sin \theta. \quad (2.120)$$

The vector meson decay angular distribution in terms of the spin density matrix now reads

$$W(\cos \theta, \phi, \Phi) = \frac{3}{4\pi} \sum_{\lambda_V, \lambda_V'} D_{\lambda_V, 0}^1(\phi, \theta, -\phi)^* \rho(V)_{\lambda_V, \lambda_V'} D_{\lambda_V, 0}^1(\phi, \theta, -\phi), \quad (2.121)$$

where the explicit Φ dependence comes from the vector meson density matrix which Φ dependence arises in its turn from the virtual photon density matrix as can be seen from equation 2.112. Inserting equation 2.113 the above can be rewritten as

$$\begin{aligned} W(\cos \theta, \phi, \Phi) &= \sum_{\alpha=0}^8 \Pi_\alpha W^\alpha(\cos \theta, \phi, \Phi), \\ &= \sum_{\alpha=0}^8 \Pi_\alpha \left[\frac{3}{4\pi} \sum_{\lambda_V, \lambda_V'} D_{\lambda_V, 0}^1(\phi, \theta, -\phi)^* \rho_{\lambda_V, \lambda_V'}^{\alpha} D_{\lambda_V, 0}^1(\phi, \theta, -\phi) \right], \end{aligned} \quad (2.122)$$

This last equation can be split up into an unpolarized part and a beam polarization dependent term

$$W(\cos \theta, \phi, \Phi) = W^{unpol.}(\cos \theta, \phi, \Phi) + W^{pol.}(\cos \theta, \phi, \Phi), \quad (2.123)$$

where the beam polarization is either longitudinal or transverse.

With the symmetry relation 2.116 the total number of independent matrix elements appearing in equation 2.123 is 26. The unpolarized part turns out to be function of 18 ρ_{jk}^α with $\alpha = 0 \dots 2, 4 \dots 6$. However, in order to separate the contributions of ρ_{jk}^0 and ρ_{jk}^4 , the value of R has to be known and thus a separation of σ_T and σ_L is needed. For a longitudinal beam polarization the polarized term in equation 2.123 provides us with 8 additional ρ_{jk}^α with $\alpha = 3, 7, 8$. It is therefore sufficient to measure with a longitudinally polarized lepton beam to completely determine the full set of matrix elements entering equation 2.116 given the fact that R is known. Measurements with a transversely polarized lepton beam yield only the contributions of 6 ρ_{jk}^α with $\alpha = 7, 8$ and hence do not provide any additional information as compared to the longitudinal beam polarization case.

In the case no separation of σ_L and σ_T is done, the following combinations of the matrix elements ρ_{jk}^α can be determined

$$r_{jk}^{04} \equiv \frac{\rho_{jk}^0 + \epsilon R \rho_{jk}^4}{1 + \epsilon R}, \quad (2.124)$$

$$r_{jk}^\alpha \equiv \begin{cases} \frac{\rho_{jk}^\alpha}{1 + \epsilon R}, & \alpha = (1, 2, 3) \\ \frac{\rho_{jk}^\alpha}{\sqrt{R} + \epsilon R}, & \alpha = (5, 6, 7, 8). \end{cases} \quad (2.125)$$

With a longitudinally polarized lepton beam, as in HERMES, the decay angular distribution given by equation 2.123 becomes

$$W(\cos \theta, \phi, \Phi) = W^{unpol.}(\cos \theta, \phi, \Phi) + W^{long, pol.}(\cos \theta, \phi, \Phi). \quad (2.126)$$

The polarization independent term reads

$$\begin{aligned} W^{unpol.}(\cos \theta, \Phi) &= \frac{3}{4\pi} \left[\frac{1}{2}(1 - r_{00}^{04}) + \frac{1}{2}(3r_{00}^{04} - 1) \cos^2 \theta \right. \\ &\quad - \sqrt{2} \operatorname{Re} r_{10}^{04} \sin 2\theta \cos \phi - r_{1-1}^{04} \sin^2 \theta \cos 2\phi \\ &\quad - \epsilon \cos 2\Phi \left(r_{11}^1 \sin^2 \theta + r_{00}^1 \cos^2 \theta - \sqrt{2} \operatorname{Re} r_{10}^1 \sin 2\theta \cos \phi - r_{1-1}^1 \sin^2 \theta \cos 2\phi \right) \\ &\quad - \epsilon \sin 2\Phi \left(\sqrt{2} \operatorname{Im} r_{10}^2 \sin 2\theta \sin \phi + \operatorname{Im} r_{1-1}^2 \sin^2 \theta \sin 2\phi \right) \\ &\quad \left. + \sqrt{2} \epsilon (1 + \epsilon) \cos \Phi \left(r_{11}^5 \sin^2 \theta + r_{00}^5 \cos^2 \theta - \sqrt{2} \operatorname{Re} r_{10}^5 \sin 2\theta \cos \phi - r_{1-1}^5 \sin^2 \theta \cos 2\phi \right) \right. \\ &\quad \left. + \sqrt{2} \epsilon (1 + \epsilon) \sin \Phi \left(\sqrt{2} \operatorname{Im} r_{10}^6 \sin 2\theta \sin \phi + \operatorname{Im} r_{1-1}^6 \sin^2 \theta \sin 2\phi \right) \right]. \end{aligned} \quad (2.127)$$

This contribution contains 15 independent matrix elements, which in this work will be referred to as the 'unpolarized' elements. The term depending on the longitudinal beam polarization P_b is given by

$$\begin{aligned} W^{long, pol.}(\cos \theta, \phi, \Phi) &= \\ &= \frac{3}{4\pi} P_b \left[\sqrt{1 - \epsilon^2} \left(\sqrt{2} \operatorname{Im} r_{10}^3 \sin 2\theta \sin \phi + \operatorname{Im} r_{1-1}^3 \sin^2 \theta \sin 2\phi \right) \right. \\ &\quad \left. + \sqrt{2} \epsilon (1 - \epsilon) \cos \Phi \left(\sqrt{2} \operatorname{Im} r_{10}^7 \sin 2\theta \sin \phi + \operatorname{Im} r_{1-1}^7 \sin^2 \theta \sin 2\phi \right) \right. \\ &\quad \left. + \sqrt{2} \epsilon (1 - \epsilon) \sin \Phi \left(r_{11}^8 \sin^2 \theta + r_{00}^8 \cos^2 \theta - \sqrt{2} \operatorname{Re} r_{10}^8 \sin 2\theta \cos \phi \right. \right. \\ &\quad \left. \left. - r_{1-1}^8 \sin^2 \theta \cos 2\phi \right) \right], \end{aligned} \quad (2.128)$$

where P_b can be positive or negative depending on the helicity of the beam. The polarization dependent term is seen to contain 8 independent matrix elements, which will be referred to as the 'polarized' elements.

2.13.4 s-Channel Helicity Conservation

An important assumption in vector meson production concerns the helicity conservation in the s-channel (SCHC) at the $\gamma^* p$ vertex in the hadronic center of mass system, meaning that the helicity of the virtual photon would be retained by the vector meson. In terms of the helicity amplitudes this translates into

$$T_{\lambda_V, \lambda_V', \lambda_\gamma, \lambda_N} = T_{\lambda_V, \lambda_V', \lambda_\gamma, \lambda_N} \delta_{\lambda_V, \lambda_\gamma} \delta_{\lambda_V', \lambda_N}. \quad (2.129)$$

In that case all amplitudes corresponding to a helicity change become zero

$$T_{01} = T_{10} = T_{0-1} = T_{-10} = T_{-11} = T_{1-1} = 0, \quad (2.130)$$

where the nucleon helicities were omitted. Taking equation 2.115 into account leaves only three independent amplitudes T_{00} , T_{11} and T_{-1-1} . Using the relations between the helicity amplitudes and the matrix elements (see Appendix D) one finds that all matrix elements become zero except r_{00}^0 , r_{1-1}^1 , $\text{Im } r_{1-1}^2$, $\text{Re } r_{10}^5$, $\text{Im } r_{10}^6$, $\text{Im } r_{10}^7$ and $\text{Re } r_{10}^8$.

The decay angle distribution $W(\cos\theta, \phi, \Phi)$ given by equation 2.126 can in the case of SCHC be expressed as function of $\cos\theta$ and Ψ , where $\Psi = \phi - \Phi$ is called the polarization angle and represents the angle between the vector meson decay plane and the lepton scattering plane

$$\begin{aligned} W(\cos\theta, \Psi) = & \frac{3}{4\pi} \left[\frac{1}{2}(1 - r_{00}^0) + \frac{1}{2}(3r_{00}^0 - 1) \cos^2\theta \right. \\ & \left. + \epsilon r_{1-1}^1 \sin^2\theta \cos 2\Psi - 2\sqrt{\epsilon(1+\epsilon)} \text{Re } r_{10}^5 \sin 2\theta \cos \Psi \right. \\ & \left. + 2P_b \sqrt{\epsilon(1-\epsilon)} \text{Im } r_{10}^7 \sin 2\theta \sin \Psi \right]. \end{aligned} \quad (2.131)$$

The terms in r_{00}^0 which denote the contribution due to longitudinal vector mesons, depend only on $\cos\theta$. The term in r_{1-1}^1 represents the contribution from transverse vector mesons. The last two terms correspond to an interference between the longitudinal and transverse contributions.

2.13.5 Natural and Unnatural Parity Exchange

As was explained in previous sections the exclusive, diffractive production of vector mesons can be seen to proceed via exchange of particles through the t -channel. The exchanged particle could have natural parity $P = (-1)^J$ or unnatural parity $P = -(-1)^J$. Using yet another symmetry property of the helicity amplitudes

$$T_{-\lambda_V, -\lambda_V', -\lambda, -\lambda_N} = \pm(-1)^{(\lambda_V - \lambda_V')} T_{\lambda_V, \lambda_V', \lambda, \lambda_N}, \quad (2.132)$$

which is valid to leading order in s and where the $+(-)$ sign corresponds to natural (unnatural) parity exchange, one can show that both the helicity amplitudes and the spin density matrix elements can be split into a contribution from natural and unnatural parity exchange. A complete measurement of the spin density matrices ρ^{ss} even allows to separate both contributions and to determine the natural and unnatural parity exchange fractions of the transverse and longitudinal cross sections.

The Pomeron in diffractive interactions carries the quantum numbers of the vacuum and therefore has intrinsic parity equal to 1. Pomeron exchange thus corresponds to natural parity exchange (NPE) in the t -channel.

When assuming natural parity exchange in the t -channel together with SCHC, equation 2.132 leaves only two independent amplitudes, where usually T_{00} and T_{11} are chosen. The latter two denote the non-flip amplitudes for production by longitudinal and transverse photons respectively. A phase difference δ between these amplitudes is introduced according to

$$T_{00} T_{11}^* = |T_{00}| |T_{11}| e^{-i\delta}. \quad (2.133)$$

In that case equation 2.131 can be written as

$$\begin{aligned} W(\cos\theta, \Psi) = & \frac{1}{1 + \epsilon R 8\pi} \left[\sin^2\theta(1 + \epsilon \cos 2\Psi) + 2\epsilon R \cos^2\theta \right. \\ & \left. - \sqrt{2\epsilon(1+\epsilon)} R \cos\delta \sin 2\theta \cos \Psi + P_b \sqrt{2\epsilon(1-\epsilon)} R \sin\delta \sin 2\theta \sin \Psi \right], \end{aligned} \quad (2.134)$$

where the decay angle distribution is now determined by the R ratio and δ only.

2.13.6 Model Calculations

In most theoretical model calculations, the assumption of s -channel helicity conservation is made and the helicity flip amplitudes are neglected with respect to the dominating helicity conserving longitudinal and transverse amplitudes.

In [53] the model from Royen *et al.* as described in section 2.12.5, was used to calculate the amplitudes where the initial photon helicity is not retained by the vector meson. In this model the helicity properties of the amplitude are determined by the $\gamma^* \rightarrow V$ transition only. They find that for T_{λ_V, λ_V} with λ_V and λ_V the helicity of the photon and vector meson respectively that

$$|T_{00}| > |T_{11}| > |T_{01}| > |T_{10}| > |T_{1-1}|, \quad (2.135)$$

where $|T_{1-1}|$ is actually too small to be computed. In the HERA kinematical region⁸ the model predicts that $|T_{10}|$ is about 20 times smaller than $|T_{01}|$, which itself is a factor 30 smaller than $|T_{00}|$. They predict a ratio of helicity flip to non-flip amplitudes of 14 ± 0.8 at $|t| = 0.14 \text{ GeV}^2$. The spin flip amplitudes T_{01} and T_{10} vanish when the Fermi momentum is put to zero, indicating the importance of the non-zero Fermi momentum for these helicity non-conserving amplitudes. In the limit of $Q^2 \approx 0$, T_{00} and T_{10} reduce to zero, whereas T_{11} and T_{01} remain different from zero. For $|t| \approx 0$, all spin flip amplitudes cancel; the single flip amplitudes T_{01} and T_{10} are seen to reach their maximum at very small $|t|$. In general all amplitudes decrease with increasing $|t|$. For large Q^2 they predict that

$$\frac{T_{01}}{T_{00}} \propto \frac{\sqrt{|t|}}{Q}. \quad (2.136)$$

In the model from Ivanov *et al.* [54] the helicity amplitudes are calculated at large Q^2 in pQCD and are proportional to the gluon structure function of the proton. Also here, the single-helicity flip amplitudes require a longitudinal Fermi motion of the quarks and vanish in the non-relativistic limit. Similarly, the double-helicity flip amplitude needs transverse Fermi motion of quarks. The authors find the leading s -channel helicity non-conserving effect to be an interference between T_{00} and T_{01} . The calculations are also valid for heavy vector mesons and the authors claim that the conclusions concerning the substantial s -channel helicity non-conserving effects should hold beyond the pQCD approach and are also applicable to real photoproduction.

⁸HERA kinematics' means the region accessible for the collider experiments at HERA, being HI and ZEUS.

2.13.7 Double Polarized Formalism

So far we have only considered the case of a polarized lepton beam scattering on an unpolarized target. The formalism presented above can be extended in a similar fashion to the most general case of a polarized beam interacting on a polarized target [52]. In this case the expression for the (unnormalized) vector meson spin density matrix is (compare with equation 2.113 and 2.114)

$$\rho(V) = \sum_{\alpha=0}^8 \sum_{\beta=0}^3 \Pi_{\alpha} \xi_{\beta} \rho^{\alpha\beta}, \quad (2.137)$$

with

$$\rho_{\lambda_V, \lambda_V'}^{\alpha\beta} = \sum_{\lambda_N, \lambda_N', \lambda_N'', \lambda_N'''} e^{i\Phi(\lambda_V - \lambda_V')} T_{\lambda_V, \lambda_V', \lambda_N, \lambda_N'} \rho(N)_{\lambda_N, \lambda_N'}^{\beta} \rho(\gamma)_{\lambda_N'', \lambda_N'''}^{\alpha} T_{\lambda_N'', \lambda_N''', \lambda_N}^* \quad (2.138)$$

Φ is the angle between the lepton and hadron plane, $\rho(N)$ and $\rho(\gamma)$ are the nucleon and virtual photon spin density matrix respectively and Π_{α} and ξ_{β} are known functions. Just like before we have nine different polarization states α for the photon. For the nucleon we have four : unpolarized $\beta = 0$, transverse polarization in the production plane $\beta = 1$, polarization normal to the production plane $\beta = 2$ and longitudinal polarization $\beta = 3$.

The formalism indicates that in case of the ρ^0 a longitudinally polarized target does not yield any extra information as compared to an unpolarized target. A transversely polarized target may help to study unnatural parity exchange, which in the limit of low momentum transfer $|t|$ can be identified with one-pion exchange. A polarized lepton beam yields only additional information for natural parity exchange processes. Considering these conclusions, we shall not pursue this double polarized formalism any further in this work.

2.14 Measurements of Vector Meson Production

Exclusive light vector meson production has been studied experimentally in the past by many different groups. A detailed overview of the experimental data taken before 1978 is given in [128]. References to more recent vector meson experiments can be found in [55].

Photoproduction measurements with photon energies between 2 and 18 GeV on hydrogen fixed targets were conducted at DESY, SLAC, Cornell and the Cambridge Electron Accelerator. Electro- and muoproduction of light vector mesons was investigated up to Q^2 values of about 2 GeV² at DESY, SLAC and Cornell. High energy muoproduction of ρ^0 mesons was studied by the CHIO collaboration at FNAL, by EMC and NMC at CERN. More recently, the E665 collaboration at FNAL studied ρ^0 production with muon-proton scattering at the Fermilab Tevatron in the kinematical domain $0.15 < Q^2 < 20$ GeV² and $9.5 < W < 24$ GeV.

The main common features of light vector meson production found by these past measurements can be summarized as follows :

- At small values of t , the cross section exhibits an exponential behavior $d\sigma/dt \propto e^{-|t|}$.

- At low energy, the cross section is seen to decrease with energy, while at high energy the cross section remains nearly constant or shows a small rise.
- The data satisfy the s -channel helicity conservation assumption to a large extent. Only small fractions of helicity non-conserving amplitudes have been found in photoproduction measurements.

Today vector meson production is intensively studied by the ZEUS and H1 collaboration at DESY. They report results spanning the kinematical domain from photoproduction up to Q^2 values of about 50 GeV² and $20 < W < 180$ GeV. HERMES measures vector meson production at DESY on different light and heavy nuclei in a fixed target in the energy range of about $4 < W < 6$ GeV with photon virtualities going from quasi-real up to roughly 5 GeV².

The latter one was initiated in 1995 to study CP violation in B-meson systems and uses the halo of the HERA proton beam to scatter on target wires. HERMES became operational in 1995 and utilises only the HERA lepton beam to scatter on an internal gas target, while the proton beamline passes through the detector without interaction.

Chapter 3

The HERMES Experimental Setup

In this chapter the HERMES experimental setup is presented. This includes a description of the HERA storage ring with the polarized lepton beam, the HERMES internal gas target, the different components of the HERMES detector and the data acquisition system.

3.1 The HERA Storage Ring Facility

The lepton beam used in the HERMES experiment is provided by the HERA storage ring, which is part of the DESY (Deutsches Elektronen Synchrotron) accelerator complex located in Hamburg (Germany). HERA, depicted in figure 3.1, is an underground storage ring facility which became operational for particle physics research in 1992. The HERA tunnel has a circumference of 6.3 kilometers and lies about 10 to 25 m under the ground. In the tunnel there are two separate accelerators; one beamline is used to circulate 27.5 GeV electrons or positrons in one direction, while the other ring contains the 820 GeV protons¹ going the opposite way. The lepton ring magnets contain normal conductors, while for the proton ring superconducting magnets are needed which operate at 4.4 K. Both HERA beams are fed by the PETRA (Positron-Electron Tandem Ring Accelerator) facility which has a circumference of 2.3 kilometer and nowadays mainly serves as a preaccelerator². PETRA itself is filled by the two smaller DESY rings and two linacs. In each of the four straight sections along the HERA tunnel an experimental hall with an interaction zone was build, each housing a different experiment. Two of them, ZEUS and H1, use the HERA storage ring in collider mode. Both experiments came online in 1992 and study high energy deep-inelastic electron-proton scattering and photoproduction processes in a very broad kinematical range. The other two, HERMES and HERA-B, are fixed-target experiments.

¹As of 1998 HERA was able to ramp the proton beam up to 920 GeV after some modifications to the ring system.

²When PETRA was still used as an electron-positron collider, experimental evidence for the existence of gluons was given in 1979 by the MARK-J, PLUTO, TASSO and JADE collaborations with the discovery of 3-jet event topologies [56].

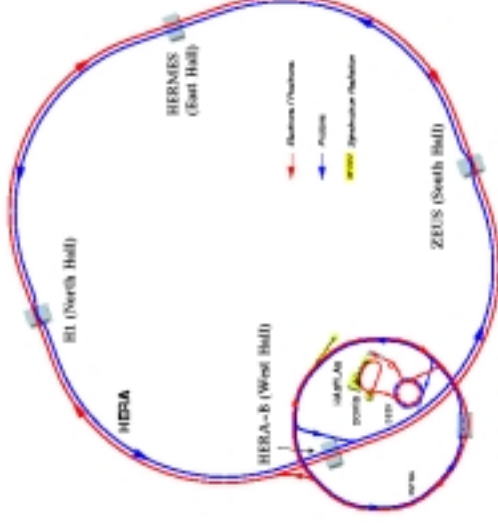


Figure 3.1: The DESY accelerator complex. Shown is the HERA collider with the proton and electron/positron storage rings and the four experimental halls, where the HERMES detector is located in the East Hall. Also shown are the smaller booster rings together with the synchrotron radiation facilities (DORIS/HASYLAB).

The HERA ring was started up as an electron-proton collider. However, the negatively charged electron beam tends to attract positively ionized dust in its path and the lifetime of the beam is severely limited due to Bremsstrahlung losses. During the 1995-97 running the machine was therefore operated with positrons. Improvements in the vacuum system allowed to switch back to electron running from 1998 on. At HERMES energies most scattering processes are dominated by one-photon exchange in lowest order and the charge of the beam makes no difference³. On the contrary electro-weak processes which can be probed at higher energies like for the ZEUS and H1 experiment, are sensitive to the lepton beam charge.

The positrons in the HERA lepton beam were stored in 189 individual bunches which had a 96 ns (29 m) separation and were arranged in 3 bunch trains. HERA ran 174 colliding bunches and 15 non-colliding or so-called pilot lepton bunches, which were used in background studies for the collider experiments. Each lepton bunch was 27 ps (8 mm) long and contained about $2.9 \cdot 10^{10}$ particles. The average lifetime of the positron beam

³An example where the charge of the lepton beam plays a role is deep virtual Compton scattering.

	p-ring	e-ring	Unit
Nominal energy	820	30 (27.5)	GeV
c.m.s. energy	314 (300)		GeV
Maximum momentum transfer	98400 (90200)		GeV ²
luminosity	1.5 (1.4) · 10 ³¹		cm ⁻² s ⁻¹
Number of interaction zones	4		
Crossing angle	0		°
Circumference	6336		m
Bending radius	588	608	m
Magnetic field	4.65	0.165	T
Energy range	300-820	10-33	GeV
Injection energy	40	12	GeV
Average injected current	163 (76)	58 (36)	mA
Number of bunch buckets	220		
Number of stored bunches	210 (180)	210 (189)	
Number of particles per bunch	10 (7.7)	3.6 (2.9)	10 ¹⁰
Bunch length	11	0.8	cm
Time between collisions		96	ns

Table 3.1: The main HERA design parameters. The numbers in brackets give the attained values for the 1995-97 running.

was around 10 hours. The main characteristics of the HERA storage ring are summarized in table 3.1.

3.2 Beam Polarization at HERMES

In this section we discuss the build-up of the HERA lepton beam polarization together with the most important depolarization effects. A short description is given of the HERA spin rotators which rotate the lepton beam spin from the transverse into the longitudinal direction for the HERMES experiment. The section is concluded with a discussion of the two lepton beam polarimeters.

3.2.1 Spontaneous Polarization in Storage Rings

Electrons or positrons in a storage ring emit synchrotron radiation under the influence of the magnets in the accelerator. Ternov, Lostukov and Korovina [57] discovered that this radiation process slightly depends on the initial spin state of the lepton. It contains a small asymmetric spin-flip amplitude that enhances the polarization state where the spin of the positron (electron) is parallel (anti-parallel) to the magnetic field of the ring. This phenomenon results in a natural build-up of transverse polarization in storage rings.

The lepton beam transverse polarization P is defined as

$$P = \frac{N^{\downarrow} - N^{\uparrow}}{N^{\downarrow} + N^{\uparrow}}, \quad (3.1)$$

where $N^{\uparrow} (N^{\downarrow})$ stands for the number of leptons with spin parallel (anti-parallel) to the magnetic field in the ring. Sokolov and Ternov [58] calculated the rate of photon emission in a constant, uniform magnetic field for an electron with given initial and final spin state in the direction parallel or anti-parallel to the magnetic field. The radiation process accompanied by a spin-flip is suppressed by about 10 orders of magnitude as compared to the non-flip radiation. However, the asymmetry in the small spin-flip amplitude is quite large and leads to a build-up of the polarization. The resulting transverse degree of polarization for an ideal planar ring can then be computed, which leads to the exponential law for the rise of the polarization in time

$$P(t) = P_{ST} \cdot \left(1 - e^{-\frac{t}{\tau_{ST}}}\right), \quad (3.2)$$

with P_{ST} the Sokolov-Ternov asymptotic degree of polarization equal to $8\sqrt{3}/15 \approx 92.4\%$, corresponding to the asymmetry in the spin-flip amplitude, and the characteristic polarization risetime

$$\tau_{ST} = \frac{8m_e}{5\sqrt{3}r_e \hbar c^2 \gamma^5} \rho^3 \quad (3.3)$$

with r_e the classical electron radius, $\gamma = E/m_e$ with E the beam energy and ρ the bending radius in the magnetic field. For the HERA storage ring this gives a polarization risetime of about 40 minutes.

The results given above can be generalized for more realistic rings where the spin vectors are not always vertical and the magnetic fields can be inhomogeneous. The spin dynamics in such magnetic fields can be described by the Thomas-Bargmann-Michel-Telegdi (T-BMT) equation [59]

$$\frac{d\vec{S}}{dt} = \Omega_{T-BMT} \times \vec{S} = \frac{e}{m_e \gamma} \vec{S} \times \left[(1 + a\gamma) \vec{B}_{\perp} + (1 + a) \vec{B}_{\parallel} \right], \quad (3.4)$$

where $\vec{B}_{\perp} (\vec{B}_{\parallel})$ is the transverse (longitudinal) component of the induction \vec{B} relative to the particle velocity and $a = 1.16 \cdot 10^{-3}$ the gyro-magnetic anomaly. As the revolution frequency for relativistic particles is given by $\Omega_e = e\vec{B}_{\perp}/m_e\gamma$ it follows that for each particle revolution the spin precesses $a\gamma$ times around the vertical field with respect to the orbit frame, i.e. the frame attached to the particles trajectory. This latter quantity is called the spin tune

$$\nu_s = a\gamma = \frac{g-2}{2} \frac{E}{m_e}, \quad (3.5)$$

which for a HERA lepton energy of 27.5 GeV gives $\nu_s = 62.5$.

Several depolarizing mechanisms [60] will compete with the Sokolov-Ternov effect. Small misalignments of the magnets in the ring, beam-beam interactions between the lepton and proton beam in the interaction zones at HERA, spin diffusion and depolarizing resonances all decrease the maximum reachable polarization. The condition for the depolarizing resonances is given by

$$\nu_s = k + k_x Q_x + k_y Q_y + k_s Q_s, \quad (3.6)$$

with the k 's being integers, Q_x, Q_y the horizontal and vertical betatron tunes and Q_s the synchrotron tune. As the spin tune is energy dependent it can be chosen as far away as possible from these resonances by making slight adjustments to the beam energy giving e.g. a half-integer value for the spin tune.

All depolarization effects competing with Sokolov-Ternov effect can be combined and characterized phenomenologically by a single time constant τ_D . The asymptotic polarization and effective risetime constant are then given by

$$P_\infty = P_{ST} \frac{\tau_D}{\tau_{ST} + \tau_D}, \quad (3.7)$$

$$\tau_{eff} = \tau_{ST} \frac{\tau_D}{\tau_{ST} + \tau_D}. \quad (3.8)$$

The depolarization effects thus lead to a lower asymptotic polarization, which is attained with a shorter risetime constant. Note that the asymptotic polarization is directly related to τ_{eff} , so that determination of the latter can be used for calibration of polarization measurements.

The transverse polarization can in the end be improved in several different ways. For example the quadrupole magnets alignment can be optimized and the lepton beam tilt can be corrected for around the ring. An empirical optimization of the harmonic spin-orbit correction bumps also proves to be quite effective [61]. Transverse polarization values of about 70% have been achieved in the HERA lepton ring.

3.2.2 The HERA Spin Rotators

To accomplish its spin physics program [62] HERMES needs a longitudinally polarized lepton beam at the interaction point. As the Sokolov-Ternov effect induces transverse lepton polarization in HERA, two 90° spin rotators were installed in front of and behind the experiment as depicted in figure 3.2. They turn the vertical spin into the longitudinal direction before the interaction with the target and put it back vertical afterwards, without changing the degree of polarization of the beam.

As shown by the T-BMT equation, every angular deflection ϕ of the beam direction due to a transverse magnetic field will result in a spin rotation over an angle equal to $a\gamma\phi$. A net rotation of the spin from the transverse to the longitudinal direction can thus be achieved using a certain combination of horizontal and vertical dipole magnets. The design of the HERA spin rotators [63], which was derived from the Siberian Snake of the first kind⁴, is schematically shown in figure 3.3. The horizontal bending of the rotators is incorporated into the arc of the ring. The rotators produce a vertical closed bump of about 20 cm and are 56 m long. The helicity of the lepton can actually be inverted by reversing the direction of the vertical bump.

⁴These are straight units which rotate the spin 90° around the longitudinal direction [64]. The concept of these Snakes is transformed into the rotator by changing the sign of the last horizontal bending magnet, which gives the rotator its bend structure in the horizontal plane.

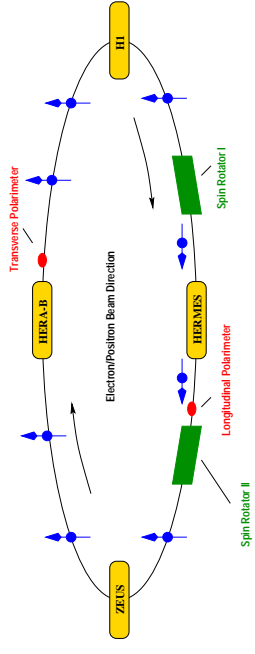


Figure 3.2: Polarization in the HERA electron/positron ring. The transverse lepton beam polarization induced by the Sokolov-Ternov effect is modified into a longitudinal polarization for the HERMES experiment with the use of two spin rotators positioned right in front of and behind the HERMES experimental area.

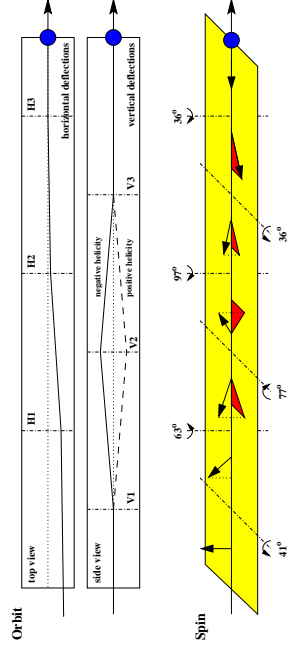


Figure 3.3: Principle of the HERA spin rotators. Using the correct sequence of horizontal and vertical dipole magnets, the transverse spin direction can be turned into the longitudinal direction.

3.2.3 The HERMES Polarimeters

The HERA lepton polarization was measured independently by the transverse and longitudinal Compton polarimeter positioned in the HERA tunnel as shown in figure 3.2.

The transverse polarimeter (TPOL) exploited the fact that the Compton scattering cross section for circularly polarized photons on transversely polarized leptons has a spin-dependent azimuthal distribution [65]. The vertical (transverse) polarization P_y was extracted by measuring for a given photon energy the shift in the mean vertical coordinate of the backscattered photons for opposite light helicities

$$\Delta y(E_\gamma) = \frac{\langle y \rangle(E_\gamma)|_{L^-} - \langle y \rangle(E_\gamma)|_{R^-}}{2} = \Delta P_{circ} P_y \Pi(E_\gamma), \quad (3.9)$$

where $\Delta P_{circ} = (P_{circ|L^-} - P_{circ|R^-})/2$ is the difference of the circular photon polarization in each helicity state and $\Pi(E_\gamma)$ the analyzing power indicating the expected shift when both

the photons and leptons are 100% polarized. The linearly polarized photon beam provided by an argon ion laser delivering continuous green light at 514.5 nm, was converted by a Pockels cell to a circularly polarized beam. During the measurements the polarization helicity was flipped at 83.3 Hz. A system of remotely controllable mirrors transported the photon beam over about 200 m to the interaction point in the HERA tunnel, where a set of lenses focussed the photons onto the lepton beam with a crossing angle of 3.1 mrad. The backscattered photons, which could have energies up to about 13.8 GeV, were measured in a position sensitive tungsten-scintillator calorimeter positioned about 65 m away from the interaction point. It consisted of two optically decoupled halves symmetric around the lepton beam plane. The polarimeter was operated in the single-photon method meaning that the laser intensity was chosen low enough to detect only single photons. The measured asymmetry of the shower development in the two halves and the total energy deposit can be related to the vertical impact position and energy of the photon giving access to the lepton polarization according to equation 3.9. The analyzing power of the measurement was optimized by selecting the backscattered photon energy range where the asymmetry is largest.

In 1997 the second HERMES polarimeter became fully operational, measuring directly the longitudinal polarization in the region between the two spin rotators. The polarimeter used the energy asymmetry of the Compton cross section on longitudinally polarized leptons for circularly polarized photons. A pulsed Nd:YAG laser produced, with a Pockels cell, circularly polarized photons at 532 nm. The photons were transported in an optical system, similar to that of the transverse polarimeter, to the lepton beam interaction point about 52 m downstream of the HERMES experiment. The backscattered photons were detected in a calorimeter which was positioned about 54 m away from the interaction point and consisted of 4 NaBi(WO₄) Čerenkov crystals. As the Bremsstrahlung background in the area downstream of the HERMES target was too large, the polarimeter operated in the multi-photon regime where over 10³ backscattered photons may be generated per laser pulse. One of the differences with the transverse polarimeter was e.g. that the longitudinal one could measure the polarization of the individual lepton beam bunches.

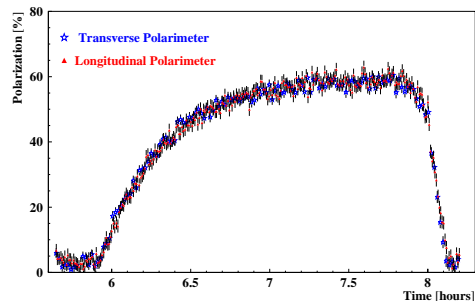


Figure 3.4: The rise time curves of the HERA lepton beam polarization as measured by both the transverse and longitudinal Compton polarimeter.

The exponential rise of the polarization to its asymptotic value can be seen in figure 3.4, where a comparison between measurements of the transverse and longitudinal polarimeter is given. In the analysis the beam polarization was smoothed by a fit of an exponential, so that the statistical uncertainty on the measurements could be neglected. The systematic uncertainty on the measured beam polarization was 5.5 % in 1995, while 3.4 % for 1996-97.

3.3 The HERMES Internal Gas Target

Since the insertion of a liquid or solid target into the lepton beam is incompatible with the running conditions of HERA, HERMES uses an internal gas target. This type of target gives a high degree of nuclear polarization with at the same time a low dilution of spectator nuclei. Moreover, the direction of the target polarization can be flipped rapidly, reducing systematic uncertainties in the experiment. The target area is schematically drawn in figure 3.5.

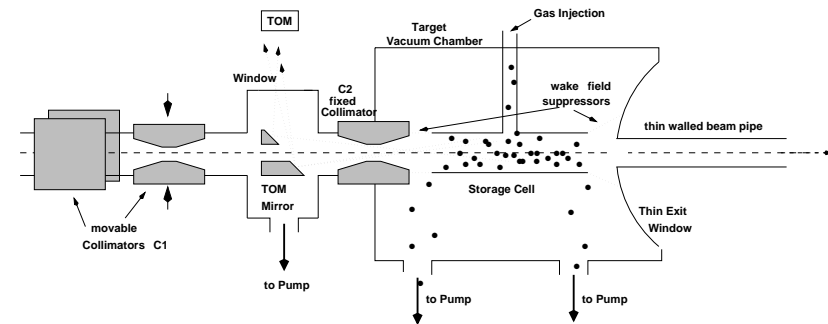


Figure 3.5: Diagram of the HERMES target region during the 1995 running period. Shown is the target storage cell inside the vacuum chamber together with the target optical monitor (TOM) and the collimator systems.

The HERMES target consisted of a windowless internal storage cell, where the lepton beam passed through coaxially. The cell was a 29 × 9.8 mm elliptical cylinder with a length of 550 mm made of about 100 micron aluminum. Only 400 mm of the tube was included in the target region and the remaining 150 mm forms an extension on the spectrometer side to ensure that particles leaving the target under small angles pass through the same amount of material. The target gas was injected via a gas inlet tube in the central part of the cell which confines the injected particles around the beam line. The chances of interaction with the beam is increased by the high number of wall bounces of the target gas particles before they leave the cell at the open ends. The resulting target thickness was about two orders of magnitude larger than for a free gas jet crossing the beam [66]. As the target density increases with decreasing cell temperature, the cell could be cryogenically cooled down to 15 K by flowing cold helium gas through the cell support structure. The

equilibrium target density profile along the cell obtained by the injection of the gas in the central part of the cell and the gas diffusion towards both ends, had a triangular shape as shown in figure 3.6.

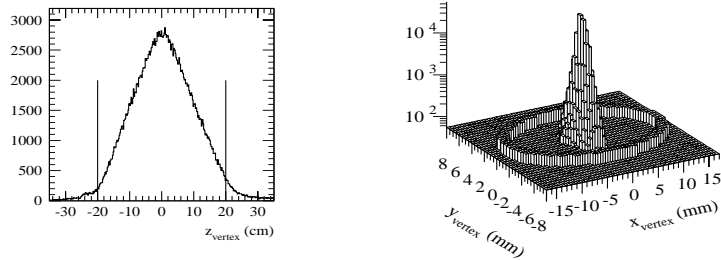


Figure 3.6: The event scattering vertex distribution in the target cell. Shown is the longitudinal vertex position, where the triangular shape is clearly visible, and the transverse vertex distribution. The boundaries of the target cell are drawn on both figures.

The cell was mounted within an aluminum vacuum chamber with a 0.3 mm stainless steel exit window. A differential vacuum pumping system removed the target gas to prevent degradation of the lepton ring vacuum. Two turbomolecular pumps maintained a pressure level of $1.5 \cdot 10^{-7}$ mbar in the target region. Three additional pump stations, two upstream and one downstream, reduced the pressure to the level of the ring vacuum of about $5 \cdot 10^{-9}$ mbar.

A set of two collimators positioned upstream of the target protected the target cell from synchrotron radiation emitted by the lepton beam. The first collimator C1 located 2 m upstream of the target consisted of a horizontal and a vertical movable piece and shielded direct radiation. Collimator C2 which was slightly larger than C1, was fixed and located just upstream of the cell. It was the smallest fixed aperture in the ring and blocked secondary scattered radiation from the C1 collimator.

As the target cell had an open geometry it formed a discontinuity in the beam pipe which could generate wake fields causing energy loss in the beam with subsequent heating in the target chamber [66]. Therefore thin-walled metallic meshes, so-called wake field suppressors, were used to create a smoothly varying bore between the cell and the beam pipe on the downstream end and the C2 collimator on the other end.

The target cell could basically hold any gas type. The maximal allowed target density was restricted by the impact the target gas had on the lepton beam lifetime, where the limit was set to 45 hours.

The polarized target systems actually consisted of a polarized gas source, the internal target storage cell, a magnetic holding field and a target polarimeter. In 1995 the HERMES polarized ^3He target was used, while for the 1996-97 running the system was

exchanged with the polarized H-D target. Both systems had the possibility to introduce unpolarized gas into the storage cell through a direct unpolarized gas feed system (UGFS). In this way measurements on unpolarized H_2 , D_2 , ^3He , N_2 and Kr_2 have been performed with areal target gas densities up to about 10^{15} nucleons/ cm^2 . Both target systems will be discussed in the following sections.

3.3.1 The Polarized ^3He Target

The polarized ^3He target actually served as an effective polarized neutron target since about 90% of the ^3He wavefunction is in the S-state where the proton spin states compensate each other and the total spin is generated by the neutron [67].

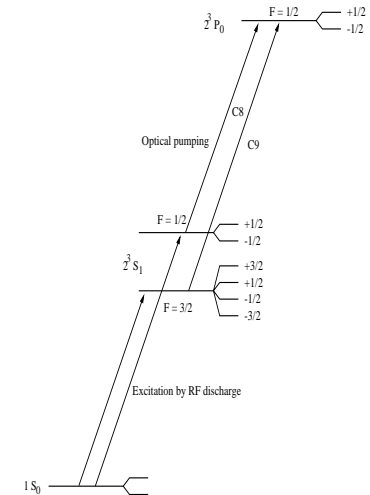


Figure 3.7: The atomic energy levels of ^3He relevant for the optical pumping. The metastable 2^3S_1 is populated by RF discharge, while circularly polarized light induces the C8 and C9 transitions to the 2^3P_0 state.

The ^3He gas was polarized via metastability-exchange optical pumping [68] in a cubic quartz pumping cell with a volume of 705 cm^3 and 0.635 cm thick walls. Figure 3.7 shows the relevant electron energy level structure in ^3He . A small fraction (10^{-6}) of the ^3He atoms is excited from the ground state 1^1S_0 into the long-lived metastable 2^3S_1 state by a radio-frequency (RF) discharge from two square electrodes on opposite sides of the cell. An infrared laser system with a $\text{La}_{.85}\text{Nd}_{.15}\text{MgAl}_{11}\text{O}_{19}$ (LNA) crystal lasing medium provided circularly polarized light at $1.083 \mu\text{m}$ to induce transitions between the 2^3S_1 and 2^3P_0 state. The angular momentum of the polarized photons is transferred to the metastable atoms which become polarized. Right-handed (left-handed) circularly polarized light incident upon the ^3He gas along a weak applied magnetic field induces

transitions with the $\Delta m_F = +1$ ($\Delta m_F = -1$) selection rule and thus excites atoms from the metastable $m_F = -\frac{1}{2}, -\frac{3}{2}$ ($m_F = +\frac{1}{2}, +\frac{3}{2}$) hyperfine levels to the 2^3P_0 state. The latter level will decay back with equal probability to all 2^3S_1 sublevels via the emission of unpolarized light. This results in a net enhancement of the population in the 2^3S_1 hyperfine levels $m_F = +\frac{1}{2}, +\frac{3}{2}$ ($m_F = -\frac{1}{2}, -\frac{3}{2}$). Hyperfine interactions may mix the electron and nuclear spins, which produces a net polarization in the ^3He nuclei. The majority of the atoms in the gas are in the ground state. The nuclear polarization of the metastable atoms is transferred to the ground state ^3He atoms through metastability-exchange collisions



In these collisions the electron clouds of the colliding atoms are exchanged, without changing the polarization of the nuclei or the electrons.

The polarized ^3He gas flows through an exit capillary from the pumping cell to the storage cell as shown in figure 3.8. A small holding field of 3.4 mT determines the quantization axis of the polarization. A target spin flip can be accomplished by reversing the sense of the circular laser light polarization and takes less than a minute.

The ^3He target polarization was measured in both the pumping cell and the storage cell by observation of the circular polarization of light emission from electronic de-excitation. The pumping cell polarimeter (PCP) used the 667 nm transition between the 3^1D-2^1P level, which occurs coincidentally due to the RF excitation of the ^3He gas. The degree of circular polarization is measured in an optical system consisting of a rotation quarter-wave plate, a linear polarizer, a 667 nm filter and a photomultiplier (PMT). The calibration in terms of nuclear polarization was done in [69]. As the ^3He nuclear depolarization is very low, the polarization measured in the pumping cell is approximately equal to the one in the storage cell. The polarization in the storage cell was directly measured by the target optical monitor (TOM) which looked at radiation coming from atoms excited by the Coulomb interaction with the HERA lepton beam.

Typical target polarization values were around 50% with a relative error of about 5%. The target spin had a flipping period of 10 minutes. The nominal areal target density was 10^{15} nucleons/cm 2 with a source intensity of $1.2 \cdot 10^{17}$ atoms/s. The target storage cell temperature typically was 25 K.

3.3.2 The Polarized H-D Target

During 1996-97 the polarized H-D target as shown in figure 3.9, was run with ^1H . The system mainly consisted of the atomic beam source, the target analyzer and the Breit-Rabi polarimeter.

The polarized gas was provided by an atomic beam source (ABS) which made use of Stern-Gerlach spin separation by multipole magnets. The molecular H_2 gas was dissociated by a 13.56 MHz RF discharge into H atoms. A cooled nozzle and skimmer formed an atomic thermal velocity beam, which was fed through a system of five sextupole magnets. Figure 3.10 shows the hyperfine states (hfs) of hydrogen. The upper lfs $|1\rangle$ and $|2\rangle$ were focussed by the magnets, while states $|\beta\rangle$ and $|4\rangle$ were deflected. The electron

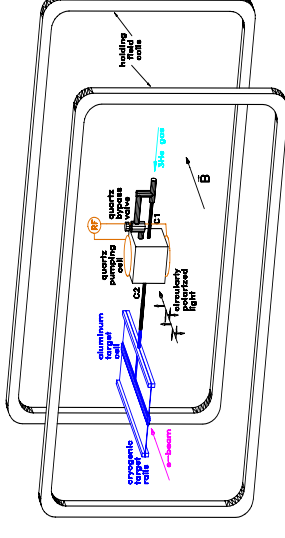


Figure 3.8: Schematic drawing of the ^3He target. Unpolarized ^3He gas is injected into the pumping cell where it becomes polarized. The polarized gas flows from the pumping cell to the target storage cell. The holding field coils are needed to define the polarization axis.

polarization of the atomic beam was transferred to the protons by means of adiabatic RF transitions, induced by units at the end of the magnet system. When the transition units were switched off, the atomic beam was electron polarized only. A transition from state $|1\rangle$ to $|\beta\rangle$ provided negative nuclear polarization, while the $|2\rangle$ to $|4\rangle$ transition gave positive polarization. The polarized atomic beam was focussed by the sextupole magnets into the entrance tube of the storage cell.

A superconducting magnet produced a 335 mT holding field providing the quantization axis for the target polarization. The storage cell was coated with Drifilm or a layer of ice in order to minimize randomization of the nucleon spins or molecular recombination through interactions with the cell walls. The cell temperature was kept at 100 K which is the lowest temperature possible without causing substantial degradation of polarization and increased recombination, while maximizing the target gas density [71].

The target polarization was monitored by the Breit-Rabi polarimeter (BRP). A gas sample from the middle of the storage cell diffused into an extraction tube, which fed the sample through a system of transition units and sextupole magnets. The sextupoles removed the states with negative electron spin projection, $|\beta\rangle$ and $|4\rangle$, from the gas sample, while states $|1\rangle$ and $|2\rangle$ remained in the beam and were seen by the atomic beam detector consisting of a chopper and a quadrupole mass spectrometer. Switching on a certain RF transition would therefore change the beam flux. The four hyperfine states defining the nuclear and electron polarization could be determined from combining measurements with different RF transition units switched on [72].

Part of the extracted gas sample from the storage cell went to the target gas analyzer (TGA) which used a chopper and a quadrupole mass spectrometer to measure the fraction of atomic and molecular hydrogen in the gas sample.

The value of the target polarization was calculated according to

$$P_T = \alpha_0 (\alpha_r + (1 - \alpha_r)\beta) P_T^{atom}. \quad (3.11)$$

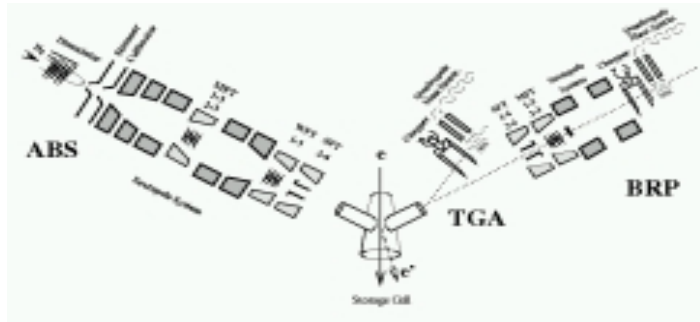


Figure 3.9: The polarized H-D target consisting of the atomic beam source (ABS), Breit-Rabi polarimeter (BRP) and the target gas analyzer (TGA).

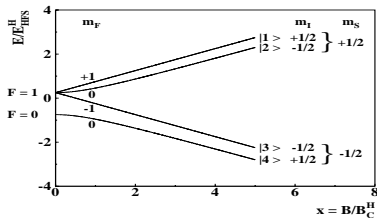


Figure 3.10: Hyperfine splitting of hydrogen. The energy is plotted in units of the hyperfine splitting energy $E_{HFS}^H = 1420.4$ MHz versus the magnetic field strength in units of the critical field $B_C^H = 50.7$ mT.

Here $1 - \alpha_0$ is the initial fraction of protons which enter the cell in molecules with $\alpha_0 = 0.99 \pm 0.01$. The dominant source for these molecules are the residual gas in the target chamber and the flow of undissociated hydrogen in the ABS. $1 - \alpha_r$ represents the fraction of atoms that recombine to molecules in the cell, where $\alpha_r = 0.88 \pm 0.03$ during 1996 and $\alpha_r = 0.93 \pm 0.04$ for 1997. β specifies the nuclear polarization of these recombined molecules relative to the atomic nuclear polarization given by P_T^{atom} . This molecular polarization is basically unknown and leads to a systematic uncertainty of the target polarization value. Additional information on the molecular polarization was obtained by performing an inclusive asymmetry $A_{||}$ measurement sensitive to the nucleon polarization for a high and low value of α_r^{TGA} . This constrained the range for the molecular polarization to $0.25 \leq \beta \leq 1.0$ for a nominal cell temperature of 100 K [70].

In general the quantities α_r^{TGA} and P_{BRP} for the gas sample as measured by the TGA and BRP respectively, differ from the actual quantities which are seen by the lepton beam. During the atomic diffusion spin relaxation by wall and spin exchange collisions

and recombination will change the atomic fraction and the polarization of the target gas. Therefore one needs to introduce sampling corrections as defined by

$$\alpha_r = c_\alpha \alpha_r^{TGA}, \quad (3.12)$$

$$P_T^{atom} = c_P P_{BRP}. \quad (3.13)$$

which can be estimated by means of Monte Carlo simulations [70, 72]. The luminosity monitor (see section 3.4.4) can be used to measure a large spin dependent Bhabba scattering asymmetry of polarized beam positrons on polarized target electrons when electron polarized atoms are injected in the cell. This asymmetry can be related to the electron polarization as measured by the BRP and the α_r^{TGA} as seen by the TGA, which further constrains the Monte Carlo models [73].

The proton polarization could be reversed on a timescale of a second, however during data taking it was flipped every 45 s. The average nuclear polarization was 82 ± 6.3 % in 1996 and 88 ± 4.5 % during 1997. The systematic uncertainty on the 1996 target polarization was high due to the low value of α_r . The average areal target density was about $7 \cdot 10^{13}$ nucleons/cm² for an ABS atomic flux of $6.4 \cdot 10^{16}$ nucleons/s.

3.4 The HERMES Spectrometer

The HERMES spectrometer was designed to measure both inclusive and semi-inclusive scattering to study the nucleon spin structure functions. Apart from detecting scattered leptons it also had to be able to measure hadronic particles formed in the various scattering processes.

Figure 3.11 shows the sideview diagram of the HERMES spectrometer. The system consisted of two identical halves located symmetrically above and below the HERA lepton beamline. The proton beam pipe also passes in between the two halves, at a horizontal distance of 72 cm from the lepton beam. The entire apparatus was mounted on a movable platform which allowed the experiment to move out of the beamlines completely during major HERA shutdown periods, when large service equipment and material had to enter the tunnel in the East Hall.

The spectrometer was divided in three parts. The front region contained only tracking devices which identify the scattering angles and trajectories of charged particles. The big spectrometer magnet in the center bent these particles according to their momenta and contained extra tracking chambers to match the tracks reconstructed in the front and back region. The back region itself contained more tracking chambers and some trigger and particle identification detectors.

The HERMES coordinate system has the z -axis along the lepton beam direction, the y -axis pointing vertically upwards and the x -axis pointing horizontally towards the outside of the ring, which from the lepton beam point of view means to the left.

The different components of the spectrometer will be discussed in the following paragraphs. A more detailed description of the system can be found in [74] and references therein.

by studying track residuals in the analysis of data taken with the spectrometer magnet off causing all particle trajectories to be straight lines. The relative alignment was also continuously monitored by the laser alignment system (see paragraph 3.4.2).

	Vertex	Drift Vertex	Front	Magnet	Back
Detector	VC1	DVC	FC1	MC1	BC1/2
Cell design	VC2	horizontal drift	FC2	MC2	BC3/4
mm from target	731	1100	1530	proportional	horizontal drift
Active area	965		1650	2725	3047
hor. (mm)	323	474	660	996	1210
vert. (mm)	137	290	180	263	306
Cell width (mm)	0.193	6	7	Ar/CO ₂ /CF ₄	Ar/CO ₂ /CF ₄
Chamber gas	DME/NE	Ar/CO ₂ /CF ₄	Ar/CO ₂ /CF ₄	65/30/5	90/5/5
Gas mix (%)	50/50	90/5/5	90/5/5	1	1
Number of modules	1	1	1	1	2
Module config.	VUX	XXUUVV ⁷	UU ⁷ XXVV ⁷	UXV	UU ⁷ XXVV ⁷
Channels/module	6014	544	576	1520	1824
Wires in X plane	1674	80	96	496	608
Wires in U,V plane	2170	96	96	512	608
Rad. len./mod. (%)	0.8	0.25	0.75	0.29	0.26
Resol./plane (μm)	65	220	225	700	275
Readout	digital (APC)	TDC	TDC	digital (PCOS)	TDC

Table 3.2: Relevant properties of the tracking chambers

The main properties of the chambers are listed in table 3.2. All tracking devices will be discussed briefly in the following sections. The momentum resolution obtained with this tracking system was around 1 % over the entire kinematic range of the experiment, while the uncertainty on the reconstructed scattering angle was below 0.6 mrad. The resolution for the kinematic variables x and Q^2 was of the order of 4-8 % and 2 % respectively.

3.4.1.1 The Vertex Chambers

The vertex chambers had to provide a high-precision measurement of the scattering angle and the vertex position over the full acceptance of the spectrometer. The chambers were positioned directly behind the target exit window, which imposed severe geometrical constraints, and they were demanded to operate in the presence of a high background flux. These requirements could be met with microstrip gas chamber (MSGC) technology.

Each VC plane consisted of a 200 μm thick glass substrate at a distance of 3 mm from a planar cathode. On the substrate were etched alternating aluminum 7 μm anode strips and 85 μm cathode strips, where the distance between two anode lines was 193 μm. The cathode planes were kept at 1800 V, whereas a voltage difference of 580 V was applied between the anode and cathode strips. Ionisation electrons created by particles traversing the chamber gas moved under influence of the drift field away from the cathode plane towards the substrate, where gas multiplication occurred in the vicinity of the anode. To get a high gas amplification at 580 V a 50/50 dimethyl-ether(DME)/Ne mixture was used a chamber gas.

The upper and lower VC assemblies each contained six MSGC planes grouped into two modules with plane configurations VUX (VC1) and XUV (VC2). The U and V planes were made of five substrates, while the X planes consisted of three substrates, where

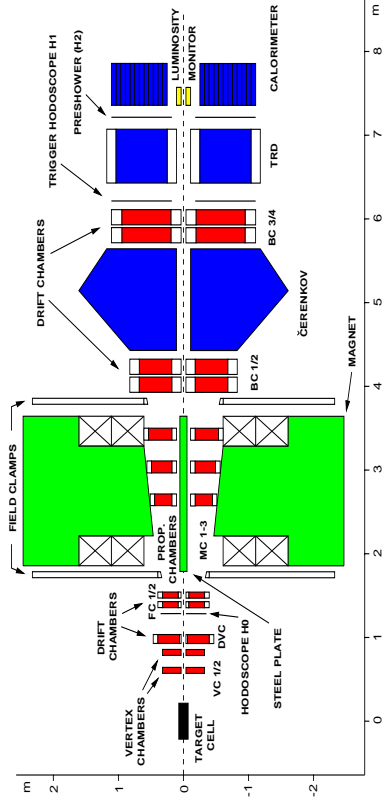


Figure 3.11: Schematic drawing of the HERMES spectrometer. One can see the target cell, the tracking chambers, the spectrometer magnet in the center and the trigger and particle identification detectors in the back region.

3.4.1 Tracking Detectors

The HERMES tracking system consisted in the front region of the vertex chambers (VC), drift vertex chambers (DVC) and the front chambers (FC). These detectors provided the charged particles scattering angles, the event vertex positions and possible displaced particle decay vertices. The main spectrometer magnet in the center produced a deflecting power of $\int B dl = 1.3$ T-m bending the charged particles in the horizontal plane, which was used for the particle momentum determination. A horizontal septum plate with compensator coils was mounted in the middle of the magnet in the beam plane to avoid distortions of the HERA beams by the magnetic field. Inside the spectrometer magnet were the magnet tracking chambers which helped to match the charged particle trajectories in the front region and the back region after deflection in the dipole field. The back region contained the back chambers which measured the deflected particle trajectories behind the magnet. These backward tracks were used to associate hits in the particle identification detectors to the reconstructed particle trajectories and to measure the deflection of the trajectories in the magnet yielding the particles momenta.

The angular acceptance in the front region was $40 \text{ mrad} < |\theta_y| < 140 \text{ mrad}$ and $|\theta_x| < 170 \text{ mrad}$, where the latter was increased behind the magnet to 270 mrad.

The tracking chambers determine the track positions using wire planes in which the position sensitivity is along the coordinate perpendicular to the direction of the wires and the beam. The horizontal x coordinate was measured using vertical wire planes, while planes with wires tilted 30° right and left defined u and v coordinates respectively. A combination of planes with different wire orientations yields trajectory space points.

The relative positioning of the tracking detectors was determined during installation with conventional optical measurements. A fine tuning of the alignment could be done

the outer two were tilted by ± 120 mrad with respect to the $x - y$ plane to increase the detection efficiency and resolution for tracks at large angles. The digital readout of the strips was based on the Analog Pipeline Chip (APC).

The vertex chambers suffered from readout problems in 1995 and in 1996 only the upper half was functioning. Therefore the VC were only used for tracking from 1997 on. The attained resolution per plane was about $65 \mu\text{m}$, which is close to the calculated resolution of $193 \mu\text{m}/\sqrt{12} = 56 \mu\text{m}$.

3.4.1.2 The Drift Chambers

The drift vertex chambers, the front chambers and the back chambers were conventional horizontal drift chambers. A drift cell layer was made of a plane of alternating anode and cathode wires between a pair of cathode foils. The cathode wires and foils were run at negative high voltage with the anode sense wires kept at ground potential. Each chamber module consisted of six drift cell layers in three coordinate doublets UU', XX' and VV'. The X', U' and V' planes were staggered by half a cell size with respect to their partner planes in order to resolve left-right position ambiguities. The chamber gas was a mixture of Ar/CO₂/CF₄ (90/5/5), which was both non-flammable to avoid hazards in the HERA tunnel environment and fast to limit the drift cell occupation time. The position of a particle trajectory in the drift cell was deduced from the space drift time relation (SDTR) using the time difference between the detector trigger signal and the sense wire pulse measured with a TDC.

The front chambers FC1 and FC2 were positioned right in front of the spectrometer magnet and each chamber above and below the beam line consisted of one module. Their drift cell size was 7 mm and they had to provide good spatial resolution for the front region tracking. The single-plane efficiency was above 97 % with a resolution per plane of about $225 \mu\text{m}$.

The drift vertex chambers were located in between the VC and FC and each chamber also consisted of a single module. They were introduced in 1997 to ensure redundancy in the front region tracking. Their drift cell design was similar but slightly smaller than the one of the FC. The DVC acceptance however, ranged from ± 35 to ± 270 mrad vertically and covered ± 200 mrad horizontally to provide front tracking after future spectrometer upgrades to allow muon detection beyond the HERMES standard acceptance. The DVC readout system was identical to that of the FC, giving a similar performance.

The back chambers sets BC1/2 and BC3/4 provided the tracking in the region behind the spectrometer magnet. Their design was again similar to that of the FC. However, due to the large distance from the target and the enlarged spectrometer acceptance after the magnet the active area of the modules was much larger. Due to this large size special care was required in the design to ensure uniform wire tension and alignment. Each set of BC contained two modules of six planes, where BC1/2 was positioned in between the spectrometer magnet and the Čerenkov detector and BC3/4 right behind the latter. The separation of the two sets provided a good lever arm to reconstruct the trajectory angle and allowed, together with the lower track density in the back region, a wider drift cell size of 15 mm. The average plane efficiency was around 97 %, while the attained resolution per plane for BC1/2 and BC3/4 was about $275 \mu\text{m}$ and $300 \mu\text{m}$ respectively.

3.4.1.3 The Magnet Chambers

The magnet chambers were multi-wire proportional chambers (MWPC) mounted above and below the septum plate in the gap of the spectrometer magnet. Their original purpose was to help matching the reconstructed tracks in the front and back region for high multiplicity events. It turned out that the low background made this unnecessary and that the MC could be used to determine the partial tracks and momenta of low energy particles that were deflected into the iron yoke of the spectrometer magnet before they could enter the back region.

Each magnet chamber consisted of three modules containing three submodules with wire orientations UXV. Each submodule contained two cathode planes made of $90 \mu\text{m}$ wires at a 0.5 mm pitch with common negative high voltage, typically 2850 V, and a plane of anode wires at ground potential with a wire distance of 2 mm. The distance between the anode and cathode planes was about 4 mm. The chamber gas had the same constituents as for the drift chambers but with different proportions Ar/CO₂/CF₄ (65/30/5) to optimize it for multi-wire proportional chamber application. The digital readout of the wires was accomplished with the Lecroy PCOS IV system.

The MC suffered from electronics failure in 1995. After a redesign of part of the readout electronics the chambers started working reliably from 1996 on with a typical plane efficiency of 98-99%. The attained resolution per plane was about $700 \mu\text{m}$, whereas the calculated resolution is $2 \text{ mm}/\sqrt{12} = 577 \mu\text{m}$.

3.4.2 The Laser Alignment System

To continuously monitor the relative alignment of the tracking detectors a laser alignment system (LAS) was implemented monitoring the chamber positions online. Each detector module was equipped with two optical targets at $x = \pm 45$ cm. The optical targets were 24.5 mm diameter Fresnel zone plates mounted on a remotely controllable system which could move the targets into the path of a laser beam. A He-Ne laser together with a semi-transparent mirror provided two 2 cm diameter laser beams parallel to and on either side of the beam pipe in the beam plane. Only one target was moved into the laser beam at a time. The diffraction pattern was recorded by a CCD camera, where any shift in the detector or target was detected as a corresponding shift in the focal pattern at the camera. The laser alignment system reached a precision of about $30\text{-}50 \mu\text{m}$.

3.4.3 Particle Identification Detectors

The HERMES particle identification (PID) system was designed to identify scattered leptons with high efficiency and low hadronic contamination. This was accomplished by a Čerenkov counter, a transition radiation detector, a preshower detector and a lead glass calorimeter. All PID detectors were positioned in the back region and the detector responses were assigned to the reconstructed tracks with the help of the trajectories found in the back chambers.

A measure of the performance of a PID detector is given by its pion (hadron) rejection

factor (PRE), which in this case is defined at a certain positron PID efficiency as the ratio of the total number of pions (hadrons) to the number of pions (hadrons) misidentified as positrons. The response of a PID detector can be studied with clean positron and hadrons samples selected by putting stringent cuts on the responses for the samples in the other PID detectors.

3.4.3.1 The Čerenkov Detector

In between the two sets of BC a single-gas radiator threshold Čerenkov counter was installed to provide pion identification. A particle traversing a medium with refractive index n will emit electromagnetic (Čerenkov) radiation on a cone around the direction of its momentum if its velocity $v = \beta c$ is larger than the phase velocity of light in that medium $v_{ph} = c/n$, where c is the speed of light in vacuum. The angle under which the Čerenkov photons are radiated is given by

$$\theta_c = \arccos\left(\frac{v_{ph}}{v}\right) = \arccos\left(\frac{1}{\beta n}\right) \quad (3.14)$$

whereas the threshold momentum for Čerenkov radiation for a particle with rest mass m is

$$p_{thr} = m\gamma_{thr}\beta_{thr}c = \frac{mc}{\sqrt{n^2 - 1}}, \quad (3.15)$$

with threshold speed parameter $\beta_{thr} = 1/n$ and Lorentz factor $\gamma_{thr} = (1 - \beta_{thr}^2)^{-\frac{1}{2}}$. As in the experiment the momentum of the particle was determined by tracking, limited information on the particles mass was given by whether or not at the given momentum Čerenkov photons were detected along the track.

The HERMES Čerenkov counter is depicted in figure 3.12. The radiator box was made of aluminum and had a depth of 1.17 m. The entrance and exit windows consisted of a composite foil of 100 μm mylar and 30 μm tedlar separated by a 1 cm gap from a second identical composite foil. In this gap dry nitrogen was continuously flowing to avoid diffusion of atmospheric gas through the windows into the radiator volume. Particles entered the radiator volume from the left. The produced Čerenkov light was reflected from an array of 2×10 spherical mirrors, which focussed the photons onto corresponding phototubes mounted on top of the detector outside the acceptance of the spectrometer. The mirrors were coated with aluminum and magnesium fluoride and had a reflectivity of 90 % at 400 nm. The phototubes had 12.7 cm diameter photocathodes and were fitted with aluminum coated Hunter-berger-Winston light cones to improve the light collection. The radiator gas, which was kept at atmospheric pressure, was pure nitrogen in 1995 for which the Čerenkov momentum thresholds were about 5.6, 19.8 and 37.6 GeV/c for pions, kaons and protons respectively, while in 1996-97 the detector ran with a mixture of 70 % nitrogen and 30 % perfluorobutane (C_4F_{10}) which gave corresponding thresholds of about 3.8, 13.6 and 25.8 GeV/c.

The Čerenkov counter could cleanly identify leptons with momenta below the pion threshold, while the latter could be identified for momenta between the pion and kaon threshold when the remaining PID detectors were used to separate them from the leptons. The response of the Čerenkov counter for positrons and hadrons is shown in figure 3.13

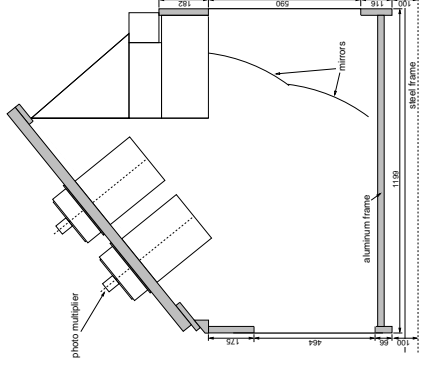


Figure 3.12: Side view of the Čerenkov counter. Particles entered the detector from the left and the produced Čerenkov photons were reflected on the mirrors onto the photomultipliers on top.

in terms of number of photoelectrons N_{pe} produced by the Čerenkov photons in the photomultipliers. The response for positrons above and below the pion threshold was almost identical and the mean number of photoelectrons for a $\beta = 1$ particle was measured to be slightly less than 3. Below the pion threshold the hadron signal was always close to zero photoelectrons, while above threshold hadrons produced a response quite similar to positrons, however with a higher peak at zero photoelectrons mainly due to kaons in the sample.

In 1998 the threshold Čerenkov counter was upgraded to a ring imaging Čerenkov counter (RICH) which would allow a cleaner pion and kaon identification over a larger kinematic range. The design of the RICH is further discussed in chapter 4.

3.4.3.2 The Transition Radiation Detector

Relativistic charged particles crossing a boundary between materials with different dielectric constants ϵ will emit transition radiation in the forward direction under an angle proportional to $1/\gamma$ where γ is the Lorentz factor. The mean energy of the radiation scales with γ and is for ultra-relativistic particles ($\gamma > 1000$) in the X-ray range (several keV). As in the HERMES kinematic range leptons have a much higher ($\gamma \gtrsim 10^4$) Lorentz factor than hadrons ($\gamma < 200$), transition radiation can be used to distinguish leptons and hadrons.

The HERMES TRD as depicted in figure 3.14, consisted of six modules per detector half, where each module was built of a radiator and a multi-wire proportional chamber to detect the X-rays. The radiators were loosely packed arrays of 17-20 μm diameter

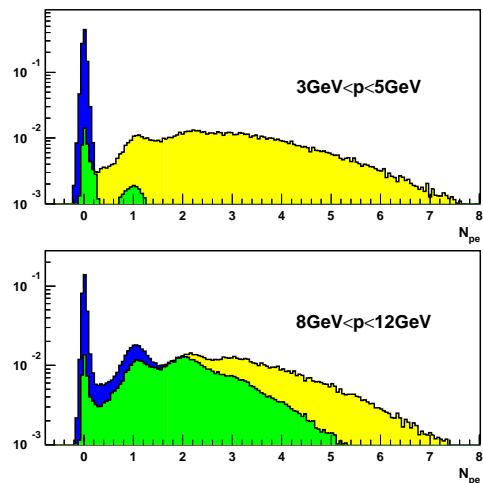


Figure 3.13: The response, normalized to 1, of the Čerenkov counter in 1995 for positrons (light) and hadrons (dark). The top graph gives the response below the pion threshold, while the response above the pion threshold is shown in the bottom graph.

polyethylene/polypropylene fibers arranged in layers. They had a density of 0.059 g/cm^3 and a thickness of 6.35 cm which corresponded to about 300 layers. The MWPC were 2.54 cm thick and had 256 vertical gold coated Be-Cu anode wires of $75 \mu\text{m}$ with a spacing of 1.27 cm between two cathode foils. A 3100 V potential was applied to the anodes, while the cathode foils remained at ground potential. The chambers ran a gas mixture of Xe/CH_4 (90/10), where Xe was chosen for its high X-ray absorption factor and CH_4 served as quenching gas to absorb secondary photons. On either side of the chambers were 6.35 mm flush gaps through which CO_2 flowed, reducing the diffusion of oxygen and nitrogen into the wire chamber.

Both hadrons and leptons deposited energy in the TRD due to the ionization of the chamber gas. Leptons however, produced on average much larger signals than hadrons due to the additional emitted transition radiation. The TRD signals were calibrated using the peak of minimum ionizing particles and by studying spectra of electrons and pions that were recognized in the calorimeter or the Čerenkov. The response of the TRD, normalized to 1, for hadrons and positrons is shown in figure 3.15. The upper graph displays the response in a single module, where both response functions are rather broad and show large overlap, indicating that several modules had to be combined to provide good PID. Therefore the TRD response was analyzed using the truncated mean method, which implies that the largest signal from the six modules is discarded and the average is taken of the remaining five modules. This procedure reduced the size of the long hadron tail which was mainly caused by energetic δ -ray electron production, and resulted in a well separated positron and hadron distribution as shown in the lower graph of the figure.

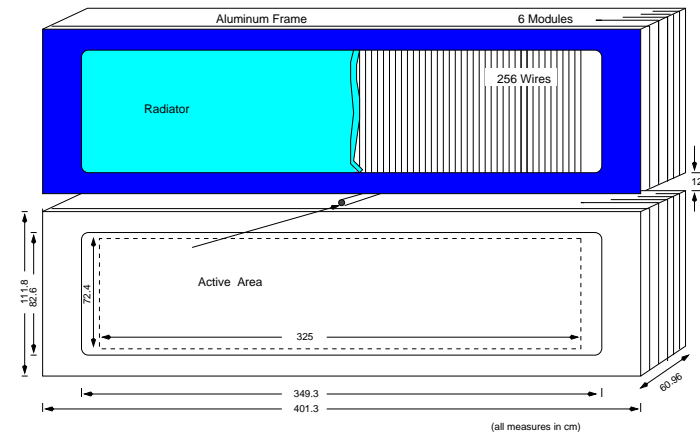


Figure 3.14: Schematic view of the TRD. One can see for both detector halves the six modules each consisting of a radiator and a proportional chamber.

This method gave for a 90 % positron efficiency an energy averaged pion rejection factor of 150. Using a probability based analysis similar to the one described in section 5.4, a PRF of about 1500 was obtained.

3.4.3.3 The Hodoscopes

The HERMES spectrometer contained two hodoscope walls in the back region providing both particle identification information and trigger signals. In each detector half the counters were built of 42 vertical 1 cm thick (2.3% radiation length) scintillator paddles with an area of $9.3 \times 91 \text{ cm}^2$. The paddles were staggered with an overlap of $2\text{-}3 \text{ mm}$ to maximize detection efficiency and each one was coupled via a light guide at the outside end with respect to the beam to a 5.2 cm diameter photomultiplier detecting the scintillation light.

Hodoscope H1, positioned in between BC3/4 and the TRD, served as trigger device and provided time-of-flight information. The hodoscope wall H2 was located behind the TRD and was used as a preshower counter allowing discrimination between leptons and hadrons. This was accomplished (see figure 3.16) by putting in front of the paddles a passive radiator made of an 11 mm (2 radiation lengths) thick Pb layer sandwiched in between two 1.3 mm stainless-steel sheats. While hadrons hardly produced any electromagnetic showering in the radiator and thus only gave minimum ionizing signals, leptons do shower and deposit much more energy in the scintillators. The hodoscope paddles were calibrated using the signals from minimum ionizing particles. The preshower response to positrons and hadrons is plotted in figure 3.17. Hadrons deposited about 2 MeV in the preshower almost independent of their energy, while positrons produced a broad response distribution with

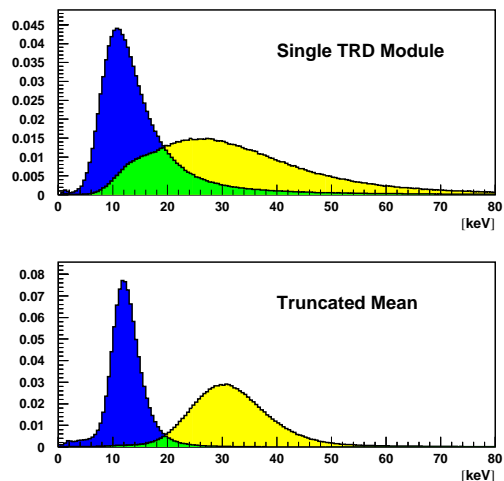


Figure 3.15: The TRD response, normalized to 1, for hadrons (dark) and positrons (light) integrated over all momenta. The top graph shows the response for a single module, while the bottom graph gives truncated mean.

an energy deposit roughly proportional to $\log E$. A pion rejection factor of about 10 was possible with 95 % efficiency for positron identification.

In 1996 a forward trigger hodoscope (H0) was implemented right in front of the FC. Its purpose was to improve the suppression of background coming from the proton beam pipe (see paragraph 3.4.6). Each detector consisted of a single sheet of 3.2 mm thick (0.7 % radiation length) plastic scintillator. The scintillation light was detected with two 5.08 cm phototubes on the side edges.

3.4.3.4 The Calorimeter

The calorimeter was intended to provide a first-level trigger and particle identification and to perform a coarse position measurement. As shown in figure 3.16 it consisted in each detector half of an array of 42×10 radiation-resistant F101 lead-glass blocks with a length of 50 cm (about 18 radiation lengths) and an area of 9×9 cm². To provide light insulation the blocks were polished, wrapped with 51 μ m thick aluminized mylar foil and covered with a 127 μ m thick tedlar foil. Each block was coupled at the rear end with a silicone glue to a 7.62 cm Philips XP3461 photomultiplier surrounded by a μ -metal magnetic shield and an aluminum tube to provide the light seal. To avoid radiation damage of the lead-glass blocks during injection of the HERA beams or when a beam dump was foreseen, both calorimeter halves were mounted on movable platforms which could be retracted vertically away from the beam pipe by 50 cm. To monitor radiation

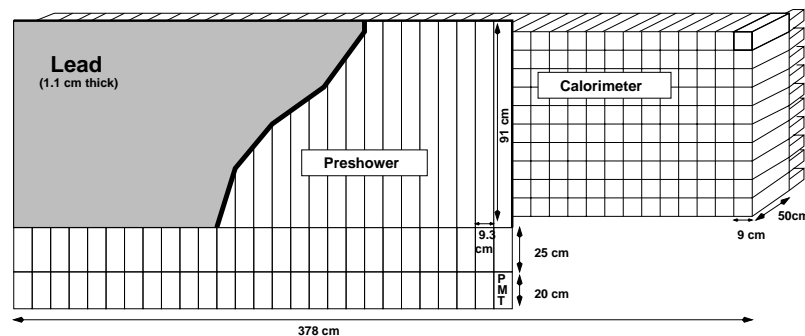


Figure 3.16: Schematic view of the preshower counter and the calorimeter. The paddles of the former were aligned with the corresponding columns of the calorimeter and were preceded by a Pb sheet.

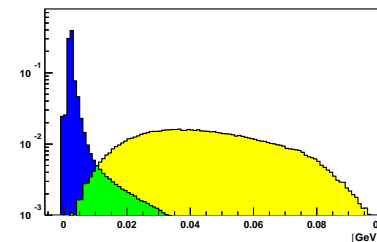


Figure 3.17: The response of the preshower detector, normalized to 1, for positrons (light) and hadrons (dark) integrated over all momenta.

damage indirectly TF1 blocks were placed behind the calorimeter. That material is much more sensitive to radiation damage than F101, so that a degradation of their response caused by showers from proton beam losses could be noticed much sooner.

The choice of the size of the blocks was driven by the requirement that the shower of an axially incident electron was developed for 80 % inside the block, which imposed a minimum cell size. This implied that more than 95 % of the deposited energy would be contained within two columns of blocks, which made the calorimeter suitable for trigger purposes (see paragraph 3.4.6). The maximum cell size was determined by the requirement that the cell occupancy was less than 1 for most triggers as it is impossible to separate tracks showering in the same block.

The length of the lead-glass blocks was large enough to ensure that incident leptons would lose practically all their energy, while hadrons would deposit only a fraction of their

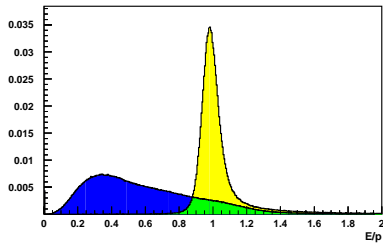


Figure 3.18: The response of the calorimeter, normalized to 1, for positrons (light) and hadrons (dark) integrated over all momenta.

energy in the calorimeter. This resulted in the fact that the ratio of the summed energy deposit in the preshower and calorimeter and the reconstructed momentum from tracking would be approximately equal to unity for leptons, while much smaller than one for hadrons. In this way the calorimeter could be used for particle identification purposes, where the reconstructed tracks in the back region could be extrapolated to match the energy clusters. The lead-glass calibration constants were known from testbeam data. The response of the calorimeter, normalized to 1, for positrons and hadrons is depicted in figure 3.18. The high energy tail above $E/p = 1$ could be explained partially by pre-magnet Bremsstrahlung, where particles losing energy before entering the spectrometer magnet had a lower measured momentum, while the emitted photons could be detected in the same calorimeter cluster as the particle itself provided that its deflection in the spectrometer magnetic field was small. Most of the electromagnetic showers already started in the preshower and they give the dominant contribution to the $E/p = 1$ peak. However, part of the showers only started inside the lead-glass blocks. These showers could still deposit all their energy in the calorimeter, but the produced light suffered less attenuation in the lead-glass blocks before its detection, which resulted in large E/p values. The E/p ratio for positrons can be used for additional calibration of the calorimeter response.

From CERN testbeam measurements with 1-30 GeV electrons the energy resolution of the calorimeter was found to be

$$\frac{\Delta E}{E} [\%] = (1.5 \pm 0.5) + \frac{(5.1 \pm 1.1)}{\sqrt{E[\text{GeV}]}} \quad (3.16)$$

with a linear energy response to within 1 % and a spatial resolution of about 0.7 cm. When combined with the preshower detector a pion rejection factor of about 2500 was found for a 95 % electron detection efficiency.

Apart from PID information and trigger generation (see paragraph 3.4.6), the calorimeter was also used to measure the energy deposit of photons produced in the lepton scattering process. The overall calibration of the calorimeter could actually be cross-checked by the reconstruction of $\pi^0 \rightarrow 2\gamma$ decays.

3.4.4 The Luminosity Monitor

The HERMES luminosity monitor was based on the detection of elastic Bhabha scattering ($e^+e^- \rightarrow e^+e^-$) of beam positrons from the target gas electrons and their annihilation into photon pairs ($e^+e^- \rightarrow \gamma\gamma$). The cross sections for these processes including radiative corrections are precisely known from Quantum Electrodynamics.

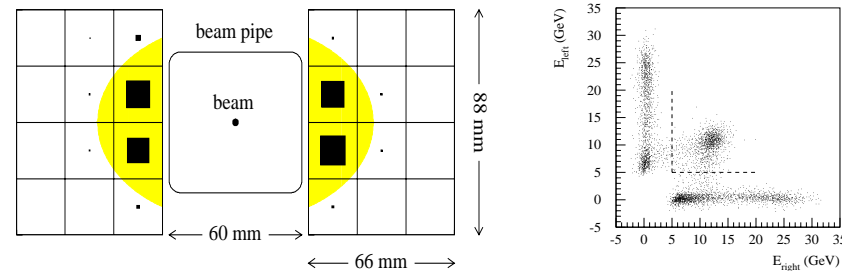


Figure 3.19: The picture on the left shows a schematic view of the luminosity monitor together with the hit distribution indicated by boxes where the size is proportional to the number of hits per channel. The shaded area shows the beam pipe acceptance. The scatter plot on the right indicates the deposited energy in the left versus right luminosity detector half, where the dashed line shows the trigger threshold of 5 GeV in both halves for Bhabha events.

The detector consisted of two calorimeter modules flanking the beam pipe horizontally at a distance of 7.2 cm from the target cell. They had a horizontal acceptance of 4.6-8.9 mrad and were small enough to be placed inside the gap of the lead-glass calorimeter. With a 27.5 GeV beam the symmetric scattering angle is 6.1 mrad, where both particles have half of the beam energy. As depicted in figure 3.19 each calorimeter was a 3×4 array of $22 \times 22 \times 200$ mm³ NaBi(WO₄)₂ Čerenkov crystals, which were very radiation hard to withstand the high radiation background in the region near the beam pipe and had a small radiation length and Molière radius allowing a compact design. Each crystal was wrapped in aluminised mylar foil and coupled to a 1.9 cm diameter photomultiplier. The calibration of the crystals was done in test beams. During beam injection and before dumping, the luminosity monitor was moved away from the beam pipe horizontally by about 20 cm.

Bhabha and annihilation events were separated from background by requiring a coincident signal with an energy threshold of 5 GeV in each calorimeter module. A plot of the deposited energy is shown in figure 3.19. In 1995 a coincidence rate of about 130 Bq was measured with a beam current of 20 mA and a ³He areal target density of 10¹⁵ nucleons/cm². When after 1997 HERA started running electrons the luminosity monitor used the Møller scattering process ($e^-e^- \rightarrow e^-e^-$) instead.

3.4.5 The Gain Monitoring System

To monitor the gain and ageing effects every detector component equipped with photomultipliers (hodoscopes, calorimeter, Čerenkov and luminosity monitor) was connected to a light source via glass fibres. A dye laser at 500 nm was used to send pulses of various intensities through the fibers to every PMT and to a reference counter photodiode. The intensity variations were produced by a rotating wheel with several attenuation plates. As the photodiode had a stable gain, the comparison of the PMT signal to that in the photodiode was used to monitor relative gain changes over time and to find dead channels.

3.4.6 The Trigger

The first level trigger system must produce a fast readout signal for the entire spectrometer whenever it finds an event of possible interest for physics analysis. The main physics trigger was therefore designed to detect deep-inelastic scattering events by looking for scattered positrons in fast detector components.

Trigger Number	Trigger Logic
17	$(H0 \cdot H1 \cdot H2)_T + (H0 \cdot H1 \cdot H2)_B$
18	$(H1 \cdot H2 \cdot Calo)_T + (H1 \cdot H2 \cdot Calo)_B$
19	$(H0 \cdot H1 \cdot Calo)_T + (H0 \cdot H1 \cdot Calo)_B$
20	$(H0 \cdot H2 \cdot Calo)_T + (H0 \cdot H2 \cdot Calo)_B$
21 (standard)	$(H0 \cdot H1 \cdot H2 \cdot Calo)_T + (H0 \cdot H1 \cdot H2 \cdot Calo)_B$
28 (photoprod.)	$(H0 \cdot H1 \cdot H2)_T \cdot (H0 \cdot H1 \cdot H2)_B \cdot (2 \leq H0 \leq 8 \cdot 2 \leq H1 \cdot 2 \leq H2 \cdot 2 \leq BC1) (1996)$ $(H0 \cdot H1 \cdot H2 \cdot BC)_T \cdot (H0 \cdot H1 \cdot H2 \cdot BC)_B \cdot (H0 \leq 8) (1997)$

Table 3.3: The trigger logic of the HERMES standard physics and photoproduction trigger together with several subtriggers allowing to determine efficiencies of individual trigger components.

Various triggers existed for different physics studies and also some technical triggers were implemented to measure trigger efficiencies or background. The trigger logic of the most common triggers is listed in table 3.3. The conditions for the HERMES main physics trigger were the following:

- *A high energy calorimeter cluster was found in the calorimeter.* To test this condition the energies of all 10 blocks in each calorimeter column were summed. The calorimeter trigger signal was formed by adding the signals in two neighbouring calorimeter columns and this segment sum was required to be above a certain threshold. To cover the full calorimeter these segment sums were overlapping. In 1995 the threshold was set at 3.5 GeV, which was equivalent to selecting events with $y < 0.87$. As of 1996 the calorimeter threshold during polarized target running was lowered to 1.4 GeV to be able to access events with higher y . By doing so the trigger purity dropped drastically since hadronic showers could then also reach the threshold. Most of this background was seen to come from scattering on the collimators in front of the target.

- *A preshower signal above the minimum ionizing level was found.* This requirement reduced the background from hadronic showers above threshold in the calorimeter.

- *A signal in hodoscope H1 was present.* This condition suppressed the background coming from photons which could produce large signals in the calorimeter and preshower detector.

- *All signals fulfilled timing conditions.* The timing of the signals was compared to the lepton beam bunch signal (HERA clock) which indicated the time at which positron bunches passed the target and thereby could define a time window for all trigger detector signals to arrive. The main background came from the HERA proton beam, where protons leaving the orbit and hitting the beam pipe could produce hadronic showers entering the spectrometer from the backside. As these protons produced mostly out-of-time signals with the HERA clock, this background was suppressed by imposing the narrow time window. Protons moving out of a bunch into so-called satellite bunches were out of time with the main proton bunches and could therefore still cause considerable background. From 1996 on the additional scintillator H0 was incorporated into the trigger to suppress this proton background even more by distinguishing forward and backward going particles using the time of flight between the scintillators in the front and back region. A particle at light-speed takes about 18 ns to traverse all trigger detectors, so that a backward going particle would be displaced in time by about 36 ns from normal trigger conditions.

To monitor the background coming from the proton beam, a veto scintillator counter was installed around the proton beam pipe behind the calorimeter. This device was however not included into the trigger scheme.

Another important physics trigger was the photoproduction trigger designed to detect hadrons (e.g. K_S^0 , ρ , ω , Λ^0 , $J/\Psi \dots$) produced at low Q^2 and decaying into a least two charged particles. For these events the positron was scattered into low angles and disappeared into the gap between the two spectrometer halves without producing a standard trigger. Therefore a new trigger which did not include the calorimeter was introduced in 1996. The trigger scheme demanded at least one charged particle track in each spectrometer half where a track was defined using hits in all three hodoscopes and in the BC1 wire chamber. The usage of multiplicity cuts in the wire chamber and hodoscopes reduced the trigger background rate significantly. In 1996 only one BC1-x plane per detector half was included in the trigger, where a cluster multiplicity of at least 2 in every hodoscope and the BC was required with an upper limit of 8 clusters in H0. In 1997 two BC planes per detector half could be used in the trigger, so that the requirement for the BC was then at least one cluster in either one of the two planes per half, which improved the trigger efficiency. A second photoproduction trigger was implemented with a similar trigger scheme as the first one, however without requiring the two tracks to be in separate detector halves. Due to its high rate, this trigger had to be prescaled and is therefore not used in this analysis presented in this work.

The first-level trigger system decided within 400 ns whether an event was usable or not. The trigger logic was implemented using programmable logic units (PLU) to allow easy modification if needed. The signals from all trigger detector components were processed and collected into a signal bus providing the input to the PLU. The outputs from the PLU were collected after prescaling into the Master Event OR. This Master Event was gated by the non-busy signal from the data acquisition and produced after retiming by the HERA clock the Master Trigger which initiated the event digitization and readout.

3.4.7 Data Acquisition

The data acquisition (DAQ) backbone was based on Fastbus technology and contained front-end crates to digitize the data from each detector, an event collector crate and an event receiver crate which was connected to an online workstation cluster via SCSI interfaces. The Fastbus masters were CERN Host Interfaces (CHI) equipped in most places with Struck Fastbus Readout Engines (FRE) to enhance their readout performance. The frontend electronics were located in a trailer close to the experiment, where the event collector was connected via a fibre optical link to the event receiver crate in the HERMES counting room. All collected event information from the detectors was processed and reduced typically by almost a factor 2 by the FRE before it was transmitted to an Alpha 3000X online workstation. The event collection was done in parallel with the readout of the following event. Apart from the standard detector readout several asynchronous independent events were implemented for e.g. the luminosity monitor and equipment calibration or monitoring. Additional VME and CAMAC branches were connected to the event collector crate to handle special data acquisition tasks and slow control.

The incoming data was written as run files in EPIO⁵ format to staging disks. In between two HERA machine fills all run files were copied to a taping robot in the DESY computer center and to a local tape backup system. The maximal DAQ throughput as determined by the CPU and I/O bandwidth of the distributing online workstation, was 1.5 MB/s corresponding to an event rate of about 150 Eq. In 1997 this event rate was doubled after an upgrade of the 175 MHz workstation to a 266 MHz Alpha 5/266.

3.4.8 Online Monitoring

An online monitoring system is needed for several reasons. First of all the status of the experiment has to be accessible permanently to the shift crew, which has to spot and if possible to cure problems with any component of the experiment. Second, all this status information has to be recorded for usage in the offline analysis afterwards.

The data structure of the monitoring system was just like for the measured physics data (see section 5.2) based on the ADAMO (Aleph DAta MOdel) [76] entity relationship model for data handling. Data were stored in ADAMO objects called dataflows, which combine several smaller objects like e.g. tables and relationships between them. A client/server based Distributed ADAMO Database (DAD) [77] was developed to improve the accessibility of the ADAMO information for multiple processes or for different computing platforms, by introducing information providers (servers) between every ADAMO database file and the data processing tasks (clients). Graphical user interfaces (GUIs) were a particular kind of DAD-clients written in PINK [78], which is a TCL/TK⁶ interface to ADAMO and DAD objects. These GUIs were used as permanent displays in the HERMES counting room and monitored virtually every detector component and the status of the HERA machine. Hardware clients reported the detector status to DAD servers and sent commands from servers to hardware, while monitoring clients looked into the

⁵Experimental Physics Input Output Package [75]

⁶Tool Command Language/Tool Kit, more information can be found at for example <http://www.tcltk.com/>

contents of a DAD server to produce status messages. A taping client collected the slow control information from all servers to write it to disk and tape for further usage in the physics analysis.

Chapter 4

The HERMES Ring Imaging Čerenkov Detector

particle, this information restrains its mass and hence allows a more precise PID.

The main physics analysis topic considered in the RICH upgrade program is the study of the nucleon spin structure. Precise inclusive polarized DIS experiments indicate that quarks only generate about 30 % of the nucleon spin. In order to determine the various contributions of the individual quark flavours, one has to perform polarized semi-inclusive measurements ($e, e'/hX$), where preferably a distinction can be made between detected pions, kaons and protons. Combining the results for inclusive asymmetries and semi-inclusive charged hadron asymmetries (without hadron identification) on different targets during the 1995-97 running yielded a good determination of the polarized u and d quark distributions ($\Delta u + \Delta \bar{u}$)/($u + \bar{u}$) and $(\Delta d + \Delta \bar{d})/(d + \bar{d})$ and of the sea quark distribution $\Delta q_s/q_s$ [2]. Implementing a RICH into the HERMES spectrometer would not only allow a precise determination of the semi-inclusive charged pion asymmetry, but also for the first time yield a measurement of charged kaon asymmetries. With kaons being strange mesons a good determination of the nucleon strange quark sea $\Delta s/s$ would become feasible and combining the pion and kaon asymmetry results would make the picture of the quark contributions to the nucleon spin complete.

The origin of the remaining part of the nucleon spin may lie with the gluons. Determining the gluon polarization ΔG is a non-trivial issue. One possible way of accessing ΔG is by measurement of the spin asymmetry of high- p_T hadron pairs [3]. Another method may be the detection of open charm production in polarized scattering, which is believed to proceed predominantly via photon-gluon fusion making the asymmetries sensitive to $\Delta G/G$. Signals of open charm production in the D^0 ($= c\bar{u} \rightarrow K^- + \pi^+$) and \bar{D}^0 have been found in the HERMES data [79], however with low statistical significance due to the large combinatorial background mainly from pions. With a clean pion and kaon identification this background could be largely suppressed, enabling a measurement of the asymmetries in open charm production and ΔG .

Another HERMES analysis topic that would benefit from the presence of a RICH, is the production of Λ ($= uds \rightarrow p + \pi^-$) and $\bar{\Lambda}$. A clean proton identification would result in virtually backgroundless, high statistics samples of Λ events. Just like for kaons, the Λ baryon spin asymmetries may provide access to the nucleon strange sea polarization. Moreover the Λ is self-analyzing allowing a measurement of the polarization transfer to the baryon from its angular decay distribution.

Also the analysis of vector meson production may benefit from a RICH detector, where pion and kaon identification would improve the detected signals especially for ϕ ($\rightarrow K^+ + K^-$) mesons.

4.2 General Design of the RICH

Monte Carlo studies indicate that about 95 % of all hadrons (π, K and p) in the HERMES acceptance are produced with momenta between 2 and 15 GeV. To cover this momentum range a dual radiator system is used in the HERMES RICH : a C_4F_{10} gas radiator and a clear silica aerogel radiator wall. The Čerenkov angles for both radiators are shown in figure 4.1 as function of the particle momentum. The gas, with an index of refraction of 1.00137, covers the PID in the higher momentum range above about 10 GeV and gives a

During the HERA shutdown in the summer of 1998 the existing threshold Čerenkov counter was replaced by a ring imaging Čerenkov (RICH) detector. The HERMES Gent group was involved in the design of the data acquisition software and setup of the photomultiplier test bench, the assembling and testing of the photomultiplier matrix and the final implementation of the detector into the HERMES spectrometer. In this chapter an overview will be given of the design, the used particle identification algorithms and some first results of the RICH.

4.1 Physics Motivation of the RICH

During the 1995-97 data taking period the PID detectors in the spectrometer allowed only a limited level of particle identification. The system was mainly designed to separate leptons from hadrons, while the hadron identification itself was rather poor. In the momentum range of roughly 4 to 14 GeV the Čerenkov provided pion identification capabilities, while only at low momenta (≈ 1 GeV) the time of flight information from the hodoscopes could be used to distinguish pions, kaons and protons. In view of the extensive semi-inclusive physics program of HERMES a good pion/kaon separation over the entire momentum range (≈ 1 to 20 GeV) is needed.

To accomplish this sort of improvement in the HERMES hadron PID capabilities, the existing threshold Čerenkov counter was upgraded to a ring imaging Čerenkov counter. The main difference with a threshold counter is that in a RICH one detects full rings of light originating from the emission of Čerenkov radiation in a cone around the direction of the momentum of incident particles. This means that one does not only have threshold information, deduced from the presence of Čerenkov light or not, but one can also determine the Čerenkov angle of the emitted light. For a given momentum of an incident

pion, kaon and proton threshold of 2.7, 9.4 and 17.9 GeV respectively. The aerogel has to take up the PID in the low momentum region between roughly 2 to 10 GeV and to this end the index of refraction for the aerogel was chosen to be about $n = 1.03$, leading to a pion, kaon and proton threshold of 0.6, 2.0 and 3.8 GeV respectively.

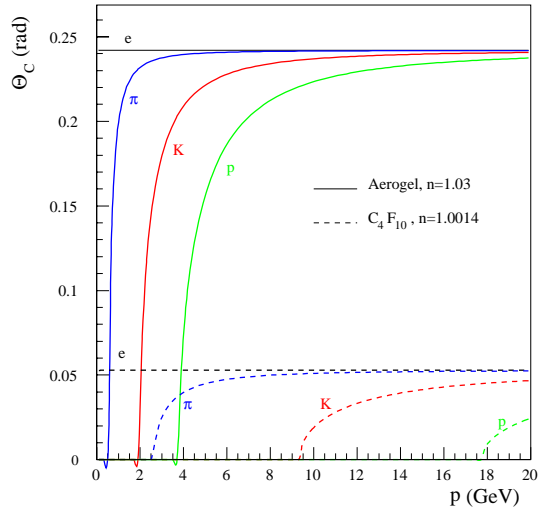


Figure 4.1: The Čerenkov angle as function of the particle momentum for e , π , K and p for the aerogel and gas radiators.

The particle identification capability of a RICH detector is usually quantified [80] in terms of the maximum separation momentum p_{max} defining the maximum momentum for which the average Čerenkov angle of two particle types (masses m_1 and m_2) is separated by a number of standard deviations n_σ

$$p_{max} = \sqrt{\frac{m_2^2 - m_1^2}{2k_f n_\sigma}}, \quad (4.1)$$

with $k_f = \tan \theta \sigma_\theta / \sqrt{N}$ the RICH detector constant, N the number of detected photons, θ the Čerenkov angle and σ_θ the standard deviation of its distribution. In the design n_σ was taken to be 4.652, corresponding to a misidentification of 1 % if one assumes equal particle fluxes and detector responses and no background.

The RICH consists of two symmetric halves located above and below the HERA beamline. A drawing of one half of the detector is displayed in figure 4.2. It shows the detector body containing the aerogel radiator directly behind the entrance window, a reflecting mirror system and a photomultiplier (PMT) matrix on top.

The geometrical design of the RICH counter was largely constrained by the requirement that the detector had to fit into the spectrometer at the position of the old Čerenkov

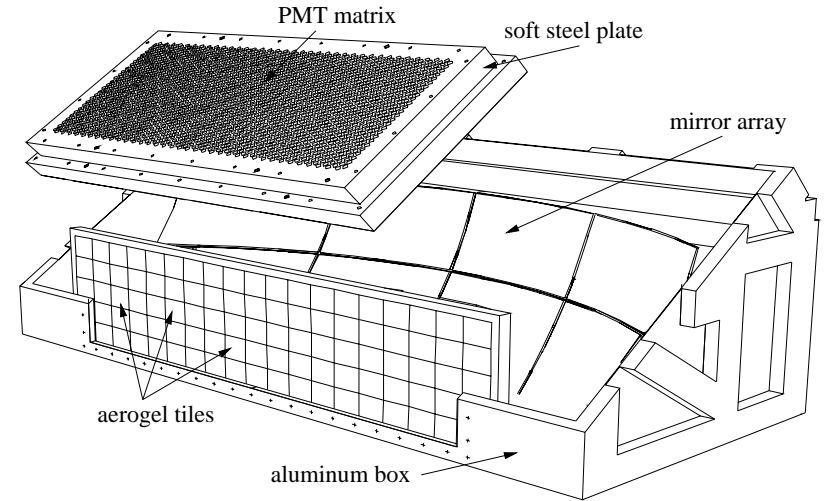


Figure 4.2: A cutaway drawing of the RICH. One can see the aerogel radiator box at the entrance of the detector, the segmented spherical mirror in the back and the photomultiplier matrix mounted on top.

counter, which meant it could have a length of about 1.25 m. The detector body is constructed of aluminum and has a volume of about 4000 l. The entrance and exit windows are made of 1 mm thick aluminum. The main volume is filled with C_4F_{10} radiator gas, which is recirculated through the box and kept at a pressure slightly above the atmospheric level by a gas control system. The inside of the box is blackened to reduce light reflections from the walls. The aerogel radiator is an assembly of individual tiles covering the entire entrance window of the detector. The radiation length of the detector material in the path of the particles traversing the detector volume has to be as low as possible, which imposed large constraints on the mirror design. The segmented mirror system is built out of 8 parts (2 rows of 4) and has a radius of curvature of 2.20 m. The segments are constructed with a graphite fiber composite backing which is coated with an epoxy film to obtain an optically smooth surface. The surface is also aluminized and gives reflectivity above 85 % in the 300 to 600 nm range. The mirror system contributes less than 1 % to the radiation length, the radiator gas 5 %, the entrance and exit windows 3 % and the aerogel 2.8 %.

The resolution on the reconstructed Čerenkov angle for a single photon is estimated to be about 7 mrad for both radiators. This includes for the gas and the aerogel the uncertainty in the point of emission along the particle track in the radiator, the pixel size of the detector and (for the aerogel only) the chromatic aberration due to the variation of the index of refraction with the photon wavelength. The high end of the considered hadron momentum range fixes the number of PMT hits one needs to be able to perform

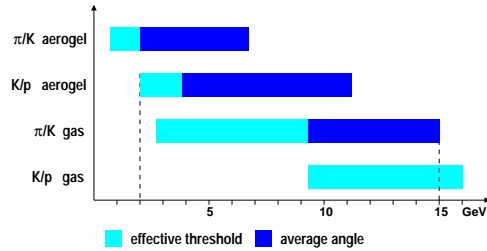


Figure 4.3: Momentum ranges for the hadron identification for the two radiators.

a full hadron identification. From equation 4.1 one gets for $p_{max}(\pi, K) = 15$ GeV that N should be 12 for the gas. Assuming that $N = 10$ for the aerogel, one can deduce the momentum ranges for hadron identification with both radiators as displayed in figure 4.3. The dashed lines correspond to the limits on the momenta for hadron separation. The lightly colored regions indicate the momentum ranges where identification is possible based on the presence of a ring or not. The dark regions indicate the ranges where the identification is based on the measured average Čerenkov angle.

4.3 The PCOS4 System

The readout of the PMT matrix is done via the Lecroy PCOS4 system, which was basically designed for MWPC readout purposes. The system was updated for application in the HERMES magnet chambers by Lecroy and INFN-Sanita [81]. It consists of three main parts : the front-end readout cards, the VME/CAMAC control modules and interfaces called backplanes between the latter two.

The front-end cards amplify and digitize the input signals, which are then delayed for a certain amount of time. This delay has to be remotely calibrated and varies between 300 ns and 1 μ s. If after this delay an external trigger gate signal arrives, then the processed signals are stored in a data register on each card (if not, then the signal is lost and the system is immediately ready for the next event). Afterwards the data acquisition has to initiate, via a read signal from the VME control modules, a data transfer from the cards to the backplane electronics or has to give a clear signal to the cards to allow new data to come in. Each card holds 4 preamplifiers and 2 programmable Lecroy MDL108 chips, which need 3 different low voltage levels and a common ground. Each preamplifier can handle 4 detector channels and each MDL chip gets input from 2 preamplifiers. The threshold for the discriminators varies between roughly 0 and 1.3 V and can be set via two 6-bit registers (one for positive and one for negative values) which are common to 4 channels. Every chip contains an 8-bit data register and also holds 8 16-bit configuration registers used to store their remotely given configuration. Data are sent and received by the cards over a high speed serial readout line.

The PCOS4 backplanes serve on the one hand as a simple interface between the front-

end cards and the VME/CAMAC control modules and on the other hand as mechanical and electrical support for the cards, where one side of each card is connected to the chamber wires and the other side fits into the backplane. Each backplane can hold up to 16 cards. The design of the backplanes is based on the Xilinx 4005 FPGA¹ chip, which can be configured by software and serves as a buffer between the VME modules and the MDL chips on the cards. The cards are read by the FPGA in parallel over their serial line at a rate of 10 MHz, after which the data is sent to the VME modules serially at a rate of 20 MHz. Serial configuration data coming in from the VMD modules, is written by the FPGA to each MDL chip in parallel via their serial line at a rate of 0.6 MHz.

The control and readout of the PCOS4 system is basically performed by the Lecroy VME2748 and VME2749 modules. Each 2748 module can be connected to up to 4 backplanes via 4 8-channel flat cables. The modules handle the reading and writing of the processed signals from the front-end cards via the backplanes and can also transfer the proper configuration data and test signals to the MDL chips. The 2749 module is mainly used to distribute the read signal to the 2748 modules and to calibrate the delay of the cards. For this delay calibration, the 2749 has to send a series of two separated 50 ns pulses. These pulses resemble the measured data signal and the subsequent delayed readout gate signal and are used by the MDL chips to adjust their internal delay lines according to the time difference between them, which can be set in steps of 50 ns. The 2749 can also generate test pulses used for various card tests. The backplane FPGAs are controlled by a Lecroy CAMAC PLM2366 module via a fan-out board. The 2366 handles the needed control signals for the initial FPGA configuration after a power-up and the FPGA mode selection during readout. It receives the read signal from the trigger logic and passes it on after a delay to the 2749 module. The 2366 also provides the FPGA with the 0.6-10 MHz clock pulses for the readout of the cards.

The PCOS4 system has several advantages. The configuration, e.g. threshold and delay setting, of the system can be done fully remotely. It has a compact design and requires only a small amount of electronics and detector cabling. The system provides a high gain of about $4.3 \mu V/e$ with a low noise level below 3000e, has a high input sensitivity with a threshold of 3000e and has a high data transfer rate. One of the drawbacks of the system is that it needs three different low voltage levels and a common ground for the front-end cards.

4.4 The PMT Testbench

The selection of a suitable photomultiplier tube for the HERMES RICH was based on several tests. The PMT sensitivity was checked and compared to the spectral light emittance of the aerogel and gas radiators. As can be seen from the curves in figure 4.4, the C_4F_{10} gas radiates predominantly in the UV-region, which favors PMTs with a UV-entrance window, while the aerogel requires a good sensitivity in the blue-green-red visible light region.

The PMT responses were tested using blue and red light emitting diodes (LED) coupled with an optical fibre to the PMTs mounted in a light-tight, black box. The LEDs

¹Field Programmable Gate Array

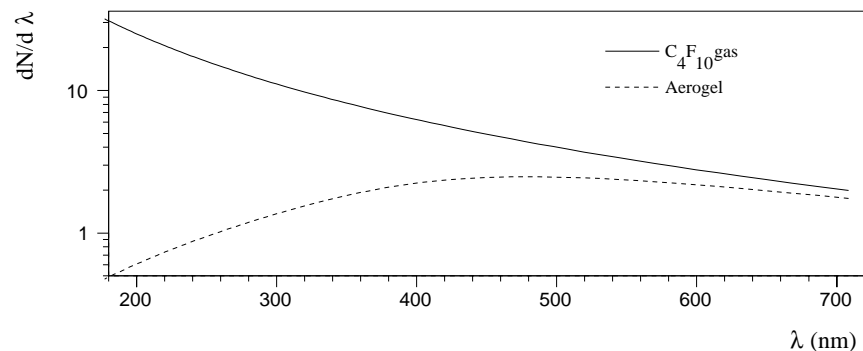


Figure 4.4: Light emittance spectra for the RICH radiator gas and aerogel.

were flashed using a custom-made LED driver, firing at a rate of 30 Hz to 1 MHz with an adjustable amplitude. PMTs from different manufacturers were evaluated using the same negative high-voltage bleeder. Test measurements included several items :

- The capability of the tube to resolve the one photo-electron (PE) peak with a standard 50 fC/chan. charge sensitive ADC was determined using a 100 ns gate. Measurements at a fixed LED amplitude (corresponding to the 2 PE peak) with varying HV level and vice versa were performed.
- The PMT plateau curve was measured where the PMT signal was fed via an amplifier into a discriminator, which provided the stop signal for a TDC. The start signal of the TDC was provided by the firing of the LED and the threshold was set between 10 and 30 mV for an amplification factor of 10. The number of non-overflow TDC events versus HV for a fixed number of LED triggers yields the PMT plateau curve.
- The dark rate was checked as function of the applied high voltage with a fixed threshold using the same method as for the plateau curve measurements.

The finally selected tube was the Philips 3/4" green enhanced XP1911/UV. This tube provides an excellent resolution and has a high quantum efficiency in the blue and red region. Due its high sensitivity the PMT does suffer from a relatively high noise level. This however, decreases strongly after a few hours of warm-up and being kept in the dark.

Before the PMTs were installed into the photodetector matrix, nearly all 4000 PMTs were tested to judge their quality and to determine best individual working conditions. To accomplish this task an automated testing set-up was built. Two black, light-tight metal boxes were constructed as shown in figure 4.5, where the PMTs were put into a wooden matrix capable of holding 49 tubes. The PMT matrix was flashed by a single 470 nm LED, where the individual PMT holes were covered with transparent foil depending on their position to ensure a uniform illumination of the matrix. To monitor the stability of the test bench, each box contained one reference tube which remained there for the entire

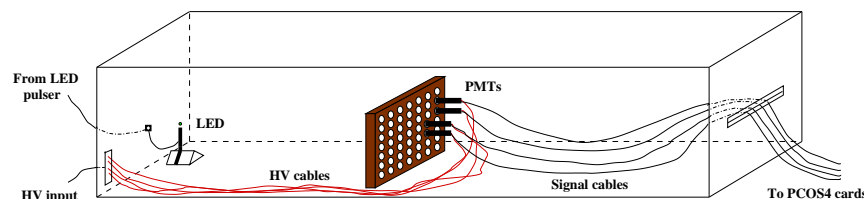


Figure 4.5: Schematic drawing of the black box in the PMT test bench. A wooden matrix holding the PMTs inside a metal lighttight box is lighted uniformly by a pulsed LED. The PMT signals are read out by the PCOS4 system.

testing period. During the measurements the plateau curve for each tube was determined together with the noise rate. The HV was raised from 600 to 1900 V in steps of 50 V, while the PCOS 6-bit threshold value was varied from 0 to 50 in steps of 10. The noise level of the tubes was required to be below 5 kHz at a threshold of 0.2 PE. While the measurements were going on for the PMTs stored in one box, the next PMT batch to be tested was kept in the dark in the second black box. About 60 PMTs could be tested in 8 hours.

The readout of the testbench was partially² based on the PCOS4 system as shown in figure 4.6. Per measurement 32 PMTs connected to 2 PCOS cards in a single backplane and to a single HV channel were tested. The calibration and triggering of the system was performed using an output register (Jorway 41). Six outputs of the output register were connected to the PCOS backplane to control the readout. One output generated the overall system trigger forming the PCOS gate puls, the LED puls and the DAQ trigger for the event collection in a CHI (STR330), which had a SCSI connection to a DEC workstation. The LED puls could be disabled using another output on the register. Two more outputs were used to generate the dual pulses for the delay calibration of the PCOS cards and in the meantime to veto the system trigger. The positive HV (see section 4.5 for the PMTs was supplied by a CAEN SY527 board which was controlled by software using a CAMAC CAENET controller C117B module.

4.5 The Photon Detector

The choice of dimensions of the photon matrix was based on Monte Carlo simulations, indicating that a 120 × 60 cm planar surface is enough to contain about 95 % of the ring centers and about 90 % of all produced photons. These measures serve as a lower limit of the final design. Both photon detectors contain a hexagonally closed packed matrix of 1934 PMTs arranged in 73 columns of alternately 26 and 27 tubes, where the area covered by PMTs was about 147 × 63 cm. The 0.75 inch XP1911 tube has a guaranteed minimum active photocathode diameter of 15 mm. Each hole in the matrix has a light-

²At the time of the set-up of the testbench some modules like the CAMAC 2366 and VME 2749 were not available at DESY yet.

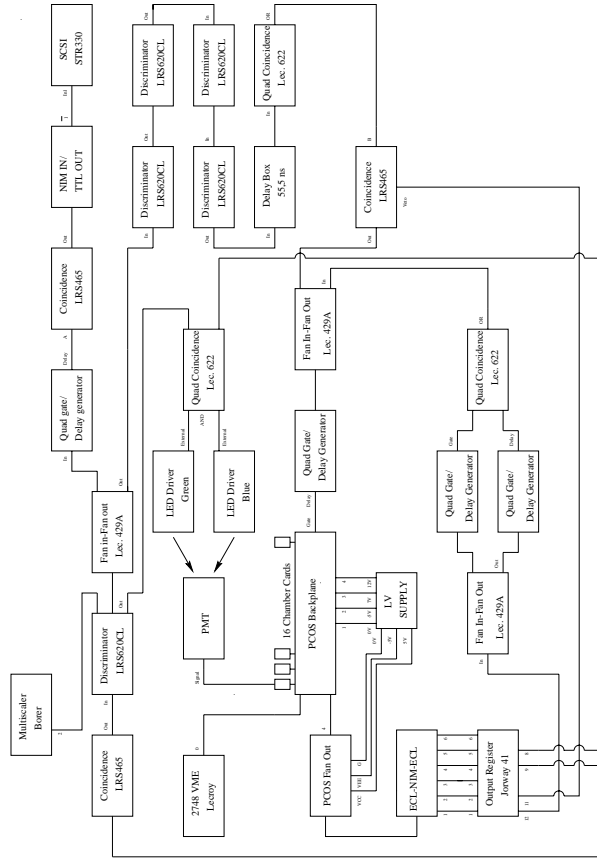


Figure 4.6: Schematic drawing of the PMT test bench electronics set up. An output register is used to generate the trigger for the readout and the LED puls to flash the PMTs (output 9), to en/disable the LED puls (output 8), to perform the delay calibration of the PCOS cards (output 12) and to control their readout (output 1-6).

cattering come reducing the inactive space between the photocathodes to increase the photon collection. The distance between adjacent photocathodes centers is 23.27 mm. As only 37.7 % of area of the focal plane filled with PMTs is covered by photocathodes additional aluminumized mylar foil funnels were inserted into each cone. The funnels have an opening diameter of 23.27 mm leading to a coverage of the photon detector of 90.7 %. They have a high reflectivity for wavelengths above 200 nm. Monte Carlo simulations indicate that photons do not reflect much more than twice on the funnels before entering the photocathode. The stray fields generated by the dipole magnet in the spectrometer may reach up to 90 G perpendicular and 25 G parallel to the PMT matrix. Shielding of the tubes is therefore needed and provided by a 100 μ m thick μ -metal wrapping around each tube and by the matrix itself and the cone inserts, both fabricated from soft steel. A schematic view of a section of the PMT matrix design is shown in figure 4.7.

Due to the specific layout of the PCOS4 system, the tubes were divided into groups of 16 PMTs which were connected to a single PCOS4 card. As the PCOS backplanes can house up to 16 cards, a total of 8 backplanes holding 121 cards was needed to cover an entire matrix. The ideal high voltage of each PMT was chosen based on the results of the testbench to ensure that the tube operated well inside its plateau. To avoid sparking

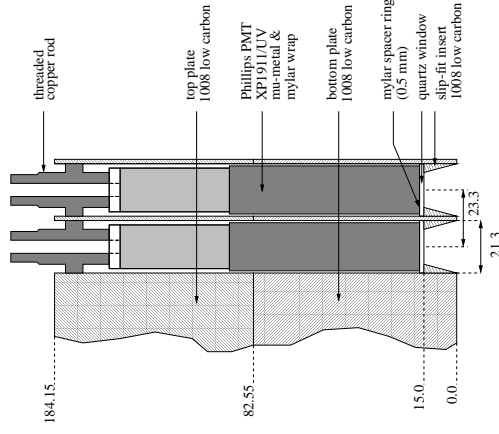


Figure 4.7: Drawing of the photon matrix design.

between the PMT cathodes and the metal of the matrix, positive HV is used at the anode and the cathode is grounded. PMTs with a similar ideal HV setting were put together in groups of 32, divided over 2 PCOS cards and could be supplied from a single HV channel, which was possible with the use of a low current high voltage divider (40 μ A at 1300 V). Each PMT matrix therefore contains 61 HV-groups. The high voltage settings for all PMT groups correspond to an average gain of about $3 \cdot 10^6$. The gain stability of the PMTs can be checked via LED flashes, where each detector half contains 9 LEDs distributed in 3 rows of 3, one row at the bottom of the mirror, one in the middle and one on top, to illuminate the entire matrix. To monitor the LED intensity itself, 2 PMTs in each detector half were connected to an ADC which is read out after each LED puls. The photon detector is read out with a threshold of 0.1 photo-electrons. Special care has been taken during the installation of PMTs to minimize the noise introduced by the large amount (6 km) of cables connecting the tubes with the PCOS cards and the HV system. All cables have an equal length to assure that each PMT has the same timing. A noise level of 1 kHz was measured after the implementation of the RICH into the HERMES detector, which given a readout gate of 100 ns, corresponds to 1 random tube firing in each half of the detector every 5th event. The PCOS electronics mounted on each side of both matrices and the tubes were cooled using a closed cooling air stream integrated in the copper PMT RF-shielding and electronics enclosure. The transferred heat is removed by a water-cooled heat exchanger.

4.6 The Aerogel Radiator

The clear hydrophobic aerogel (SiO_2) used in the RICH consists of silica particles in a porous netlike structure. It was manufactured by Matsushita Electric Works in the form of tiles with average dimensions of $11.4 \times 11.4 \times 11.3 \text{ cm}^3$. The aerogel radiator is made up of stacks of individual tiles, where the wall is 5 tiles thick and contains 5 rows and 15 columns. Opaque black tedlar sheets placed between the aerogel stacks reduce the distortion effects due to reflection of Čerenkov light crossing the stack boundaries. The aerogel wall is contained in an aluminum frame with a 1 mm thick aluminum entrance window and a 3.2 mm UV transmitting lucite exit window. Black plastic spacers between the tiles and the frame hold the aerogel in place when the detector is moved. The container is sealed gas tight and is continuously flushed with dry nitrogen to avoid possible aerogel degradation due the C_4F_{10} gas.

Important parameters of the aerogel tiles are their light transmission, their index of refraction, the density and the quality of the surface. These properties were measured for each tile and the latter three were used to determine the location of every tile in the radiator wall. The average index of refraction of the tiles is 1.03040 with a spread of $3.6 \cdot 10^{-4}$. Tiles with similar refractive indices were put together into one stack to assure that particles traversing the stack emit Čerenkov light under similar angles giving the best possible ring resolution. Variations in the refractive index between different stacks could be corrected for in a calibration procedure using relativistic electrons. Due to the specific manufacturing process of the aerogel tiles in a mold, the surface of the tiles is not entirely flat, but rises steeply close to (at $\sim 5 \text{ mm}$ of) the edges of the tile giving differences in height between the center and the edges of a tile up to 2 mm.

Čerenkov light produced in the aerogel may scatter diffusely throughout the material due to Rayleigh scattering which is nearly isotropic. This scattered light poses no problem for threshold applications, but becomes a problem for a RICH where the unscattered light yield is important. The transmittance of light with wavelength λ through material with thickness L is given in the long wavelength limit by the Hunt formula as [82]

$$T = Ae^{-\frac{C\lambda}{\lambda^4}}, \quad (4.2)$$

where C and A are called Hunt parameters (C is the clarity coefficient) characterizing the light attenuation due to isotropic Rayleigh scattering in the material and the absorption effects independent of the wavelength respectively. Measurements done for the HERMES RICH tiles give $C \cdot L = 0.0094 \mu\text{m}^4$ and $A = 0.964$, indicating that the aerogel is highly transparent. Due to the λ^{-4} dependence of the Rayleigh scattering cross section the scattered light is found predominantly at lower wavelengths than the unscattered light. The UV transmitting lucite exit window was chosen to suppress this background of Rayleigh scattered light as this material has an absorption cutoff around 290 nm. Most of the Čerenkov light produced in the lucite itself, which has a refractive index of about $n = 1.5$, is emitted at such high angles that it is internally reflected at the lucite-gas border. The total thickness of the radiator wall was chosen to optimize the yield of unscattered photons with respect to the amount of scattered photons.

4.7 The Readout System

The readout system of the HERMES RICH is based on the PCOS4 system which was described in paragraph 4.3. A schematic drawing of the RICH electronics is shown in figure 4.8.

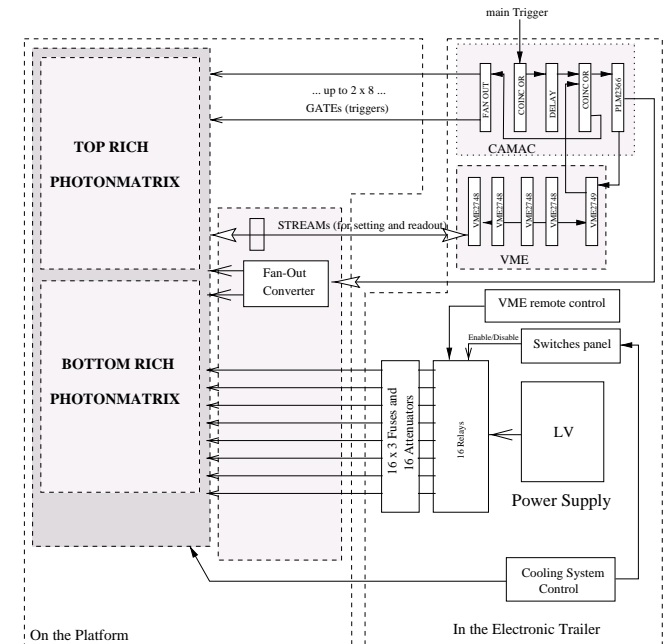


Figure 4.8: Schematic diagram of the RICH readout electronics.

The HERMES electronics trailer contains the RICH trigger electronics, the high and low voltage power supplies and the cooling system control units. The entire detector is readout using four 2748 (two for each detector half), one 2749 VME module and one 2366 CAMAC module. Each 2748 module is connected via 4 long flat cables to 4 backplanes which are mounted onto the photon detector on the HERMES detector platform. The 2366 module is connected via a splitted 16-channel flat cable to 2 fan-outs (1 for each detector half) which are mounted on the detector platform, where each fan-out is connected via 4 splitted 16-channel flat cables to 8 backplanes. The 3 low voltage levels needed for the backplanes come from 2 supplies (1 for each detector half) for each level. The entire PMT matrix gets its HV from 8 16-channel HV boards mounted in a single CAEN crate. Cables going between the electronics trailer and the detector platform are roughly 40 m long.

The RICH trigger logic is schematically drawn in figure 4.9. It must be a multipurpose

The particle type assignment cannot be done with certainty, which implies that a probability has to be assigned to each particle type hypothesis. To treat hit-pattern overlap in a consistent way, one should if possible consider all tracks in each event simultaneously, yielding a combined particle type hypothesis. The PID algorithms are then used to compute the likelihood of each hypothesis, leading eventually to the one with the highest probability. To get a measure of the reliability of the highest probability hypothesis, a quality parameter is introduced

$$Q_p = \log_{10} \left(\frac{L_1}{L_2} \right), \quad (4.3)$$

where L_1 and L_2 are the most and second most likely hadron type hypothesis respectively. This parameter varies between roughly 0 and 13 and can be used to reduce the contamination in a certain hadron sample. It should be noted that the other PID detectors in the spectrometer have a high efficiency to separate electrons and positrons from hadrons and hence the RICH only considers the identification of the hadron tracks.

4.8.1 Inverse Ray Tracing Based Algorithm

This method makes use of the inverse ray tracing (IRT) technique similar to that in [83]. The Čerenkov photon emission angles under which a photon had to be emitted from a given track to produce an observed hit in a certain PMT are calculated. Both the polar and azimuthal Čerenkov angles are determined, since the latter can be an indicator of ring overlap or localised noise. To compute the angles one has to make an assumption of the emission vertex of the photon as the photon could have been produced in the aerogel or the gas radiator. The angles are therefore determined for each radiator hypothesis and due to the rather different index of refraction, one can clearly identify the correct radiator assumption as can be seen from figure 4.10. However, an uncertainty in the emission vertex remains due to the length of both radiators. This shows up as a contribution to the single photon resolution. For photons generated in the aerogel an extra correction is needed to account for refraction at the aerogel-gas border.

The calculated Čerenkov angles are then accumulated in histograms for each track assuming all hits were produced by photons emitted from the track in one of the two radiators. A window can then be imposed on the spectrum at the position of the theoretically expected angle θ_h , where the width of the window is taken to be 4 times ($\pm 2\sigma$) the single photon resolution (a setting that could be optimized if wanted). From the reconstructed angles within this window, the average Čerenkov angle can be determined. The measured distribution of the average angles for a given particle type and momentum will be Gaussian shaped and can be normalized to form a conditional probability or a likelihood to observe an average angle $\langle \theta \rangle$ assuming that the particle is of the considered type

$$L(\langle \theta \rangle) = \exp \left[- \frac{(\theta_h - \langle \theta \rangle)^2}{2\sigma_{\langle \theta \rangle}^2} \right]. \quad (4.4)$$

Here the average angle resolution can be computed from the single photon resolution as $\sigma_{\langle \theta \rangle} = \sigma_\theta / \sqrt{N}$ with N the average expected number of the PMT hits. The likelihoods for both radiators can be combined by multiplication to come to an overall likelihood. The

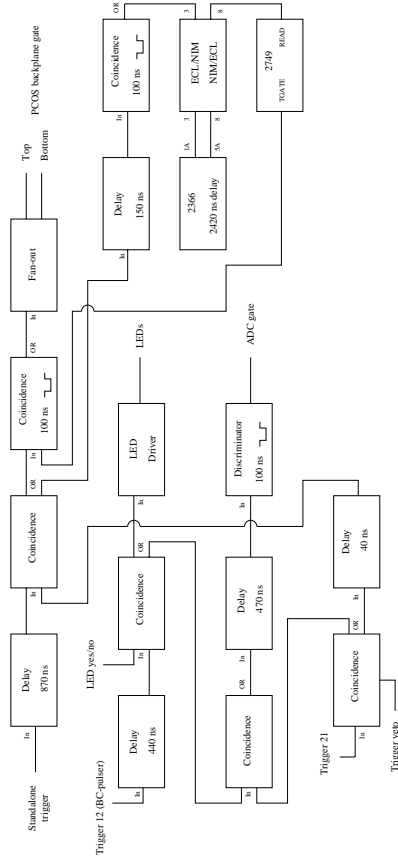


Figure 4.9: Schematic diagram of the RICH trigger logic.

logic, which should facilitate the PCOS electronics initialization, the handling of the standard HERMES trigger for data-taking and of a standalone trigger for detector testing and it should accommodate the pulser signal (BC-pulser) which is used to generate tube maps and also read the signals from the ADC connected to the 4 PMTs monitoring the LED intensity. The standard HERMES physics trigger (trigger 21) is split up into two separate signals, where one is used to generate the 100 ns ADC gate, while the other one goes into a coincidence unit which initiates the PCOS card readout by providing on the one hand the 100 ns gate for the backplanes and on the other hand the triggering via the 2366 module for the readout of the cards in the 2749 VME module. Trigger 21 can be vetoed to inhibit all readout during initialization or delay calibration of the PCOS electronics and to allow test measurements using a standalone trigger which is generated via an output register. The PCOS cards have a delay setting of 16·50 ns = 800 ns. Pulses to flash the LEDs inside the RICH can be triggered via the BC-pulser firing at a rate of about 0.6 Hz or via an output register when using the standalone trigger during detector tests.

4.8 Particle Identification Algorithms

The underlying idea of the RICH PID is to determine the type of particle leaving a track in the detector. As input to the PID algorithms we have the PMT hit configuration and the track 3-momentum information from the tracking detectors in the spectrometer, where the track trajectories are extrapolated to the PMT matrix as if each particle would be reflected from the spherical mirror, thereby predicting the ring centres. Due to the fact that the flat photon detector does not coincide with the true mirror focal surface, the detected images of the Čerenkov light are not really rings, but rather asymmetrically distorted ellipses.

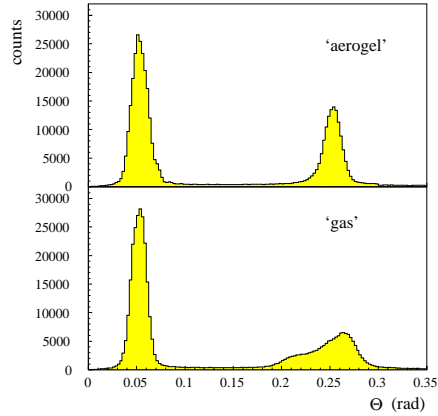


Figure 4.10: Reconstructed angle spectra under the assumption that the photons were emitted in the aerogel (top) or in the gas (bottom) for single track, low background electron events with momenta above 5 GeV.

hadron type giving the highest likelihood is then assigned to the particle. This algorithm can be extended to incorporate the threshold aspects of the RICH and also to take into account a certain level of background (due to e.g. electronic noise or Rayleigh scattered photons) in the hit patterns.

4.8.2 Direct Ray Tracing Based Algorithm

Another PID approach relies on the direct ray tracing technique where a Monte Carlo algorithm is used to generate a sample of Čerenkov photons from each track under a certain particle type hypothesis, which are propagated to their impact points on the PMT matrix after reflection from the mirror. This technique can be used to calculate the relative probability $P^{(h,t,r)}(i) = N^{(h,t,r)}(i)/N^{(h,t,r)}$ that a certain PMT i will be hit by photons from a particular track t by generating a number $N^{(h,t,r)} = \sum_i N^{(h,t,r)}(i)$ of photons for radiator r under the hypothesis h . The total number of photoelectrons in each PMT under hypothesis h can be evaluated as

$$N_{pe}^h(i) = \sum_{t,r} n^{(h,t,r)} \cdot P^{(h,t,r)}(i) + B_{pe}^h(i), \quad (4.5)$$

where n is the expected number of photoelectrons in the ring and B is an additional background term. A Poisson distribution yields the probability not to fire or to fire PMT i , $\bar{P}_{PMT}^h(i) = \exp(-N_{pe}^h(i))$ and $P_{PMT}^h(i) = 1 - \bar{P}_{PMT}^h(i)$. Finally the hypothesis likelihood is then defined as

$$L^h = \prod_i [P_{PMT}^h(i)C_{PMT}(i) + \bar{P}_{PMT}^h(i)(1 - C_{PMT}(i))] \quad (4.6)$$

where C is 1 or 0 depending on whether the PMT did or did not fire. The hypothesis yielding the highest likelihood is assumed to be the true one. The drawback of this particular method is the large number of Monte Carlo calculations which have to be performed for each track, particle hypothesis and radiator, which makes this algorithm several times slower than the IRT based method.

4.8.3 First Results of the RICH

A RICH event display is depicted in figure 4.11 showing some typical aerogel and gas rings in the photon detector. The asymptotic (towards high particle momenta) number of PMT hits for the aerogel and the gas is about 8 and 12, respectively for hadrons, which is in rough agreement with the design values. About half of the tracks is affected by acceptance effects due to the tile structure of the aerogel radiator. Roughly one third of the particles producing clear rings cannot be assigned to a full track in the spectrometer (e.g. δ -rays) and these rings represent background to the rings which can be associated with tracks. Other background sources include Rayleigh scattered photons, Čerenkov light produced in the lucite window, radiator gas scintillation, proton beam induced showers hitting the tubes directly and a small amount of electronic noise.

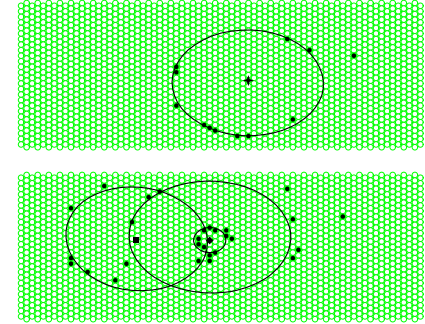


Figure 4.11: A view of the RICH photon detector for an event containing a gas and aerogel ring for a 14.6 GeV electron and an aerogel ring corresponding to a 5.5 GeV K^+ in the top half. The solid dots mark the hit PMTs, while the markers in the ring centers indicate the extrapolated positions of the tracks if they would be reflected from the spherical mirror. The lines show a fit to some simulated photon hits generated using the known track parameters and particle types.

Apart from the effects mentioned in paragraph 4.2 the experimental single photon resolution contains some more contributions. For the aerogel one has to include a tile contribution due to refraction of light near the edges of the tiles where the surface is sharply curved, one has to account for the variation of the index of refraction between the tiles and one must include a forward scattering contribution [84]. For the gas angles there

is an effect due to the pressure and temperature fluctuations changing the gas density and the index of refraction. A contribution due to the non-sphericity of the mirror array and an amount of diffuse reflection on its surface also has to be considered. The experimental single photon resolution for high energy lepton tracks that are not affected by tile or mirror acceptance effects nor by any atmospheric pressure fluctuations or event background is about 7.5 mrad for both radiators. The dominant contribution to the resolution comes from the photon detector pixel size.

Monte Carlo based predictions for hadron identification using the IRT algorithm yield pion, kaon and proton efficiencies of typically 0.95, 0.74 and 0.54 with purities of 0.95, 0.63 and 0.86. Clean hadron samples extracted from the measured data are not available as no other detectors can be used to select them. However, one can use samples of decaying particles like ρ , ϕ , K_s mesons and Λ hyperons to determine identification efficiencies, yielding momentum integrated values of about 0.90, 0.75 and 0.73 for pions, kaon and protons respectively. Currently, a lot of development and optimization is still going on to improve the RICH PID scheme.

also the smallest timescale on which the slow control information corresponding to the events taken at that time was available.

The bursts were grouped into runs where the amount of data collected in each run was determined by the tape size of the central storage system. A run typically lasted about 10 minutes depending on the beam current and trigger rates and contained roughly about 50 bursts.

Each run belonged to a certain fill defined as a beam fill of the HERA machine which typically lasted for about 8 hours. At the beginning of a fill after injection, as soon as the beam conditions (e.g. background rates, beam positions and tune ...) allowed it, the HERMES spectrometer was switched on to take data in parallel with the other experiments at the HERA ring. Data taking usually continued until the lepton beam current reached down to about 9 mA, at which moment all detectors were brought to a stand-by level and the lepton beam was dumped. Depending on the beam quality, the proton beam was sometimes kept in the ring during 2 subsequent lepton beam fills.

The HERMES data was further characterized by the data taking year during which it was collected. Each of these periods had a unique polarized target and spectrometer configuration. Major detector upgrades were normally done during the longer HERA shutdown and maintenance periods in between the different data taking years.

5.2 Data Production

Before the recorded raw detector and slow control information could be accessed in data analysis it first had to pass through the data production software chain designed to perform the necessary event reconstruction and synchronization of the slow control data and to transfer the output into smaller and manageable files formatted in a suitable, logical way.

The software production chain is schematically shown in figure 5.1. The HERMES Decoder (HDC) read the raw event run files in EPIO format and converted the data from each subdetector into its specific quantities, e.g. hit positions in wirechambers, energy depositions or timing information. The output format was based on the tabular structure of the ADAMO package and the data was written to GAFs (Generic Adamo Files). The HDC output was fed into the HERMES Reconstruction Code (HRC) (see section 5.3) which basically took care of reconstructing the recorded particle trajectories in the spectrometer and the clustering in the calorimeter. Tracking chamber efficiencies and calibrations were calculated from the HRC GAF output files by the ACE (Alignment, Calibration, Efficiency) program. Several DAD servers contained the detector geometries and mapping and calibrations of various detector responses, as needed by the previously mentioned packages. The HDC/HRC/ACE part of the production could actually be iterated to account for improved knowledge of the detector alignment and calibration.

The slow control information was provided partially by 'fill files' of the taping client and by HDC and included also some external data coming from offline studies performed by subsystem experts. All this information was combined into one enhanced and time-ordered slow control data file for each fill.

Chapter 5

Event Reconstruction and Data Analysis

Here we discuss how the several Terabytes of raw detector information accumulated each year was converted offline into quantities which were more suitable for usage in physics analysis. We shortly present the HERMES data organization and production chain. The tracking and clustering and particle identification algorithms were two items in the data production of particular importance for the analysis and are therefore described in some more detail. A major part of the analysis presented in this work uses Monte Carlo codes, simulating different types of scattering processes, and detector geometry and responses. The last section of this chapter provides a short description of the HERMES Monte Carlo program used in the analysis.

5.1 The HERMES Data Organization

The vast amount of collected data demands some sort of simple organization in order to be manageable in physics analysis.

The basic unit of data was a single event containing all detector information as recorded by the data acquisition system when it received a single trigger (or multiple different triggers at the same time). Each event corresponded to a scattering process of the HERA lepton beam on the target.

The event stream was bundled online by the DAQ into bursts, which typically lasted for 10 seconds as defined by the scaler readout. From 1996 on the polarized target spin was reversed much more frequently than in 1995. As the target polarization during a flip was undefined, bursts belonging to a target spin flip were unusable for any asymmetry analysis. To avoid the loss of a large amount of such data, the spin flip bursts were split into different polarization records in which the target still had a well-defined polarization state and records where the target polarization was undefined. The burst or record was

Finally a filter program extracted the relevant data for physics analysis from the HRC output and combined it with the corresponding information from the slow control fill files to produce compact run files called μ DSTs (Data Summary Tapes). These μ DSTs form the basis for all further physics analysis.

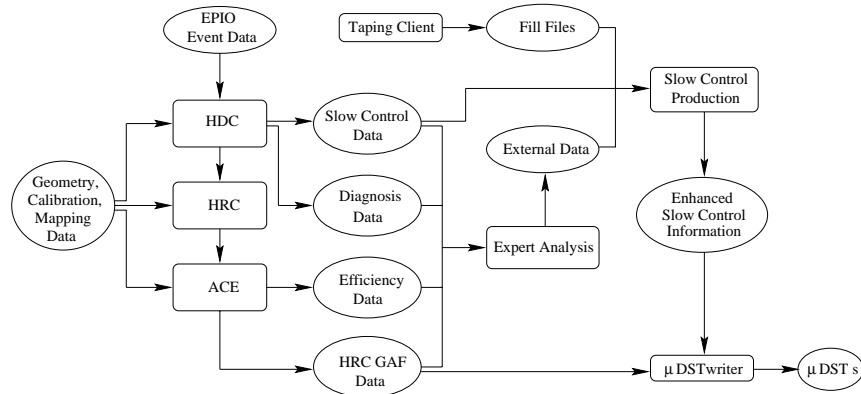


Figure 5.1: Diagram of the HERMES data production chain. Boxes represent software packages handling the data stored on disks or tape depicted by elliptical shapes.

5.3 Tracking and Clustering

Data coming from the HERMES decoder or from the HERMES Monte Carlo were analyzed by the HERMES Reconstruction Code which used a pattern recognition algorithm to reconstruct the charged particle trajectories from the information recorded by the tracking chambers. Tracking was done separately for the front and back region, resulting in the reconstruction of partial tracks. A bridging algorithm identified the backward and forward partial tracks belonging to a single trajectory yielding full tracks for each event.

The tracking algorithm started by combining the detector hits in each of the three wire directions (U, X, V) to reconstruct track projections, called tree-lines, in each of these three planes. This was accomplished by a pattern recognition routine which matched the detector information against a pattern database representing all possible tracks in the spectrometer. As depicted in figure 5.2 a recursive tree-search algorithm started in a first step with an artificial detector resolution of two bins. The hit pattern obtained in this way was matched against a first-level database pattern. In each successive step the resolution was doubled and the hit patterns were compared to all physically possible child patterns deduced from the matching parent pattern found in the previous step. This procedure was repeated until the bin size was of the order of the spatial resolution of the tracking chambers. The algorithm was able to tolerate a certain number of missing hits in the patterns to account for possible detector inefficiencies.

Over a 100 million possible patterns for particle trajectories exist for the HERMES spectrometer given the chamber resolutions. The database contained only straight tracks as the magnetic fields in the forward or backward regions were negligible. The number of possible patterns to be stored in the database could be reduced by symmetry arguments and the size of the database could be compressed even more using pattern scaling and shifting properties.

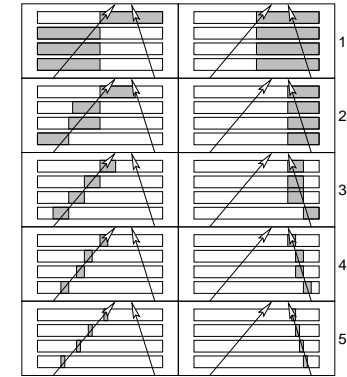


Figure 5.2: The tree-line search algorithm recursively matches the detected hit pattern against a database with increasing resolution.

When a trajectory was identified by the algorithm the track parameters (e.g. the slope) were calculated from a straight line fit to the detector hits along the trajectory where the detector resolutions were applied as weights in the χ^2 fit. Once all tree-lines in the U, X, V projections were found, they were combined into 3-dimensional partial tracks by combining a U and V tree-line and comparing this to the reconstructed X tree-lines.

The reconstructed partial tracks in the two spectrometer regions then had to be connected to form full tracks. This could be done by comparing the projected position of the forward and backward partial tracks in the middle of the spectrometer magnet ($z = 275$ cm). Deviations for true particle trajectories were below 1.0 cm. This type of tracking includes the information coming from the vertex chambers and is referred to as ‘standard tracking’. In 1995-96 the VC performance was too low to be included into the tracking and only the FC information was available to reconstruct the forward partial tracks. This resulted in a high uncertainty for the forward track and limited the performance of the tracking system. The problem was dealt with by the concept of forced bridging, where the matching point of the backward track in the center of the magnet was used as an extra space point in an iterative recalculation of the parameters of the forward partial track. This tracking method is referred to as ‘NOVC tracking’. When the magnet chamber were operational their information could be incorporated into the bridging using a so-called Kalman filter. In this algorithm the backward partial tracks were extrapolated into the magnet and defined a region where hits in the chambers should be present given

the magnetic field information and the maximal possible deflection of a particle above a certain momentum.

Once a full track was found the momentum of the particle was determined using a lookup table, generated beforehand by tracking a large amount of particles through a Monte Carlo model of the setup with a parametrization of the accurately measured field map of the spectrometer magnet. The table contained, among other things, the change of the angle in the x -direction as function of discrete values of the scattering angles in the x and y direction and the momentum. The forward partial track position and angles at the magnet entrance, together with the known deflection, were used to find the momentum of the particle by interpolation in the table. The momentum and angular resolution attained was better than $\Delta p/p = 0.5\%$ and 1 mrad respectively.

For each track the minimal distance of approach to the beamline was calculated, which provided a good indication whether the particle originated from an interaction with the target or not.

Particle showers in the calorimeter were usually larger than the cell size of the calorimeter, so that signals were produced not only in the block that was hit, but also in the surrounding blocks. This resulted in the formation of so-called calorimeter clusters. Test beam measurements reported cluster widths of $\sigma_d = 4.5$ cm. The determination of the calorimeter energy of charged particles was important for the particle identification. Also neutrals, especially photons, produced calorimeter clusters whose energy and position represented the only source of information on these particles as they were not seen by the tracking chambers.

The cluster search algorithm in HRC was based on finding local energy maxima in the calorimeter plane. A cluster was then defined as the group of 3×3 cells centered around the block with the largest energy signal. The energy of the cluster was calculated by summing over its member cells and the (x, y) -position of the cluster was defined as the energy weighted mean position of the centers of the blocks in the cluster. Partial cluster overlap was taken into account by distributing the energy of overlapping cells proportional to the energy sums of the non-overlapping cells.

For each reconstructed backward partial track, HRC tried to find the corresponding calorimeter cluster by extending the partial track to the calorimeter and locating the cluster whose center fell within $2\sigma_d$ of the impact point. Particles emitting Bremsstrahlung in the chambers or target exit window could also generate a cluster around the extension of the forward partial track. If the bending of the particle's trajectory was large enough the two clusters could be well separated.

A detailed description of the HERMES reconstruction code and the tracking algorithms can be found in [85].

5.4 Particle Identification

As discussed in the previous chapter 3, the spectrometer contained four particle identification detectors, each with a different response to different types of particles. The main aim of the HERMES PID system was to provide a reliable method to allow separation of

leptons and hadrons.

One way to accomplish this was to use the responses of the individual detectors directly in the analysis and to impose hard cuts to select clean lepton or hadron samples.

Another way was to combine all four detector responses into a logarithmic likelihood ratio method. In this method the response of a detector D was converted into a conditional probability \mathcal{L}_i^D that the observed signal was due to the passage of a particle of type i . This was done using the different response of each PID detector to leptons and hadrons, determined from test beam measurements, Monte Carlo simulations or by using clean samples obtained with restrictive cuts on the other PID detectors in the spectrometer. The detector responses for a certain particle type were actually momentum and angle dependent. The response distributions were used directly or were fitted with analytical functions. To obtain the conditional probabilities \mathcal{L}_i^D (referred to as parent distributions), the response distributions to a certain type of particle were normalized to one. The combination of several detectors D yielded the overall conditional probability for particle type i

$$\mathcal{L}_i = \prod_D \mathcal{L}_i^D. \quad (5.1)$$

These conditional probability distributions could be converted into true probabilities \mathcal{P}_i that the observed responses were due to a particle of type i , by taking into account the different particle fluxes ϕ_i . These fluxes were in general again momentum and scattering angle dependent. Bayes' theorem shows that this probability is given by

$$\mathcal{P}_i = \frac{\phi_i \mathcal{L}_i}{\sum_j \phi_j \mathcal{L}_j}. \quad (5.2)$$

For positron-hadron separation this becomes

$$\mathcal{P}_e = \frac{\mathcal{L}_e}{\Phi \mathcal{L}_h + \mathcal{L}_e}, \quad (5.3)$$

$$\mathcal{P}_h = \frac{\Phi \mathcal{L}_h}{\Phi \mathcal{L}_h + \mathcal{L}_e}, \quad (5.4)$$

where Φ is the flux ratio ϕ_h/ϕ_e . A PID parameter was defined in the analysis by taking the logarithm of the ratio of these positron and hadron probabilities

$$PID = \log_{10} \left(\frac{\mathcal{P}_e}{\mathcal{P}_h} \right) = \log_{10} \left(\frac{\mathcal{L}_e}{\Phi \mathcal{L}_h} \right) = \log_{10} \left(\frac{\mathcal{L}_e}{\mathcal{L}_h} \right) - \log_{10} \Phi. \quad (5.5)$$

When a particle was equally likely to be a positron or a hadron the PID parameter was zero, while positive (negative) values indicated the particle was more likely to be a positron (hadron). Similarly, a PID parameter for each individual detector could be introduced as follows

$$PID_D = \log_{10} \left(\frac{\mathcal{L}_e^D}{\mathcal{L}_h^D} \right), \quad (5.6)$$

such that equation 5.5 becomes

$$PID = \sum_D PID_D - \log_{10} \Phi. \quad (5.7)$$

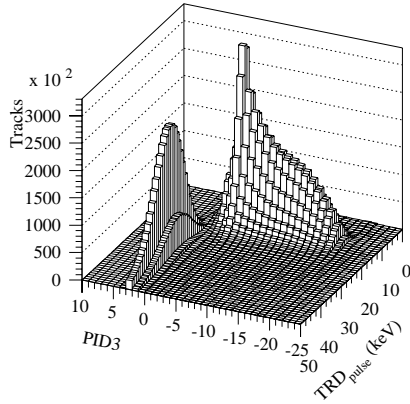


Figure 5.3: Correlation of PID3 and truncated mean TRD response for 1995 data. A clean separation of leptons and hadrons is visible.

The flux ratio Φ could be neglected provided it was not a strong function of momentum and angle. This simply shifted the PID distribution.

In 1995 the probability analysis of the TRD was not yet fully finished. Instead one relied on the truncated mean response of the TRD modules and parent distributions were generated from the TRD puls spectra without any momentum dependence. The calorimeter, preshower and Čerenkov counter were combined to form a log-likelihood quantity given by

$$PID3 = PID_{cal} + PID_{pre} + PID_{\check{C}er} = \log_{10} \left(\frac{\mathcal{L}_e^{cal} \mathcal{L}_e^{pre} \mathcal{L}_e^{\check{C}er}}{\mathcal{L}_h^{cal} \mathcal{L}_h^{pre} \mathcal{L}_h^{\check{C}er}} \right). \quad (5.8)$$

A similar quantity PID2 was defined using only the calorimeter and preshower and also PID4 was constructed including the TRD with parent distributions as mentioned above. The more commonly used PID parameter in 1995 was a combination of PID3 and the TRD mean response. The correlation plot of both quantities is given in figure 5.3 which shows a clean separation between positrons and hadrons. The optimal PID quantity was derived from a valley cut whose position was determined in a 2-dimensional fitting procedure finding the cut which had the smallest number of particles close to it, resulting in

$$PID_{95} = PID3 + 0.31 \cdot TRD_{pulse} - 5.48. \quad (5.9)$$

If the Čerenkov performance was limited a similar cut in the PID2-TRD plane gave

$$PID_{95} = PID2 + 0.51 \cdot TRD_{pulse} - 9.0, \quad (5.10)$$

whereas if the TRD failed then

$$PID_{95} = PID3. \quad (5.11)$$

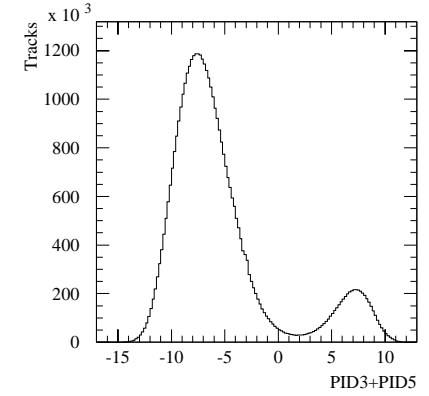


Figure 5.4: Distribution of PID3+PID5 used as PID parameter for the 1996-97 data.

In 1996-97 the full probability analysis for the TRD was done and a quantity

$$PID5 = PID_{TRD} = \log_{10} \left(\frac{\prod_{m=1}^6 \mathcal{L}_e^{TRD,m}}{\prod_{m=1}^6 \mathcal{L}_h^{TRD,m}} \right) \quad (5.12)$$

was introduced based on the responses of the six individual TRD modules. The commonly used PID quantity was then simply

$$PID_{96-97} = PID3 + PID5, \quad (5.13)$$

as shown in figure 5.4.

The contamination of the lepton or hadron samples and the efficiencies of the applied cuts were estimated by fitting e.g. Gaussian curves to the lepton and hadron PID parameter distributions in the region around the cut. An overall positron efficiency of better than 97 % with a hadronic contamination level of less than 1 % was achieved with this PID method.

A more detailed description of the HERMES PID can be found in [86].

5.5 The HERMES Monte Carlo

Monte Carlo simulations of a particle physics experiment are usually needed to study the influence of the experimental apparatus on the detected physics events. The spectrometer has a finite geometrical acceptance which allows detection of only a fraction of the induced physics events. Detection systems have a certain finite resolution and efficiency and can also influence measurements due to e.g. multiple scattering, energy

losses, Bremsstrahlung or particle showering. This will lead to smearing effects in the reconstructed event quantities with respect to their real values. After the reconstruction each event has to pass a certain analysis software chain, which also has a certain intrinsic efficiency. All these effects have to be estimated and corrected for using a full Monte Carlo simulation of the measurement. Apart from that Monte Carlo studies can also be used to estimate e.g. event count rates or to perform studies of background processes.

The HERMES Monte Carlo (HMC) program [87] was able to simulate several different scattering processes using different, appropriate physics event generators. The default parameters were set to use LEPTO [88] which is a leptoproduction event generator for the simulation of deep-inelastic scattering. LEPTO contains the parton level interactions based on the standard model leading order electro-weak cross sections. Due to the relatively low energy scale at HERMES no higher order QCD radiation effects leading to parton showers were included. To simulate polarized deep-inelastic scattering at HERMES an extension of LEPTO called PEPSI [91] was used. The (un)polarized quark-parton distribution functions serve as input to the Monte Carlo to describe the target partonic substructure. The fragmentation and decay of unstable primary hadrons was governed by JETSET [89] based on the LUND string model [90]. HMC also contained other event generators like e.g. PYTHIA [89], capable of generating hard and soft processes in collisions between photons, leptons and hadrons, and AROMA [92], a generator for heavy-flavor processes in leptoproduction.

The tracking and modelling of the detector responses was implemented using the GEANT¹ detector description and simulation tool [93]. Using experimental resolutions and efficiency functions, the generated detector signals were finally digitized into more realistic responses. The entire output of HMC was stored in ADAMO formatted GAF files which were readable by the HERMES reconstruction program, so that Monte Carlo data could be treated just like actual measured data.

The Monte Carlo studies of vector meson production were performed with some standalone generators (see chapter 7), where the event output was redirected into specific GAF files. The HERMES Monte Carlo had the feature that it could read these special user generated GAF files and feed each event through the GEANT tracking and digitization chain without performing any event generation itself. This had the advantage that basically any physics event generator could be coupled to HMC to make a simulation of the entire experiment feasible.

Figure 5.5 displays a HMC simulated $e^-p \rightarrow e^- \omega p$ event generated with DIPSI (see section 7.2) where the ω decays into $\pi^+ \pi^- \pi^0$. All components of the HERMES spectrometer can be seen from the top and from the side. The picture includes the particle trajectories and the produced hits in the different detectors. Also the bending of the charged particles in the spectrometer magnet was simulated.

¹Generation of Events AND Tracks

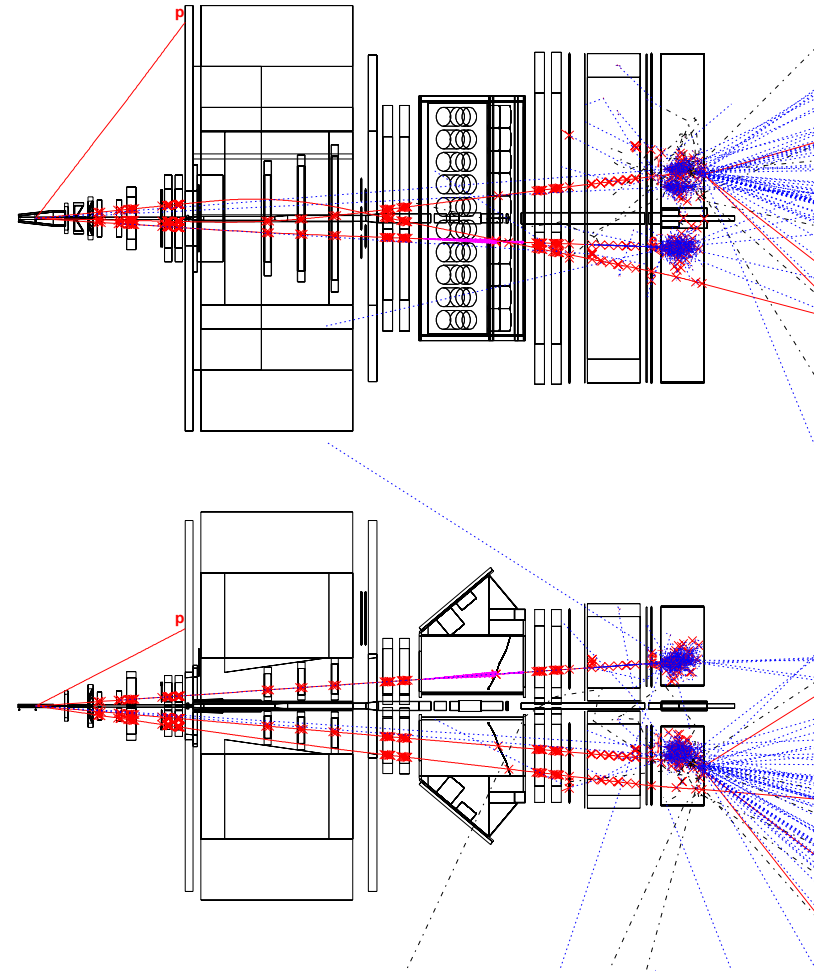


Figure 5.5: A picture of a simulated $e^-p \rightarrow e^- \omega p$ event with the DIPSI generator coupled to HMC. The plot on top shows a detector view from the top, while the bottom picture gives a side view. One can clearly see the recoiling proton (which is not detected) and the tracks of the scattered lepton and the two charged pions. Only the electron produces Čerenkov light and a calorimeter shower in the top right half. One also notices the two π^0 decay photons indicated by the dashed lines, which also induce large calorimeter showers in the bottom left half. The bending of the charged tracks in the spectrometer magnet is also visible.

distributions. In general one has to take care not to impose tight data selection criteria on physical quantities related to considered physics processes, e.g. particle yields, as this may introduce biases in the final result.

Chapter 6

Data Quality and Event Selection

In this chapter the different data quality requirements for each data taking year covered in this work are presented in detail. Furthermore the selection criteria are described for the ρ^0 and ω events which are to be used for further analysis.

6.1 Data Quality

One important aspect of the event selection is the quality of the data sample with respect to the detector performance. The HERMES spectrometer consists of several subdetector systems which all have to be fully operational to assure a reliable data analysis. As soon as a single component is not working properly or performs unstable in time, part of the recorded data sample has to be skipped. Apart from that, one also has to require good beam conditions and a high quality target performance. The general idea behind the data quality selection procedure is to try to minimize systematic uncertainties coming from the experimental conditions. 1995 was the HERMES commissioning year and thus the performance and operation of the detector was not always optimal. Hence a huge amount of time was spent on a detailed study of the recorded data to understand the behaviour of each detector component and to determine the quality of the recorded data. For the subsequent running periods all data quality studies were conducted in a similar fashion based on the results and the experience gained from the 1995 data taking.

Data quality selection was done on the fill, run and burst level. A first pass in the selection process removed the fills and runs dedicated to detector calibrations or detector and machine studies. In the next step the information stated in the official HERMES logbooks was used to remove those runs which suffered obvious problems. Runs where the necessary slow control information was missing were also discarded. Table 6.1 lists the final run statistics for the 1995-97 data taking periods. The further evaluation of the data sample on the run and burst level was based on the offline study of the recorded slow control information, the detector responses, the actual event yields and kinematical

Data Taking Year	Physics Runs on μ DSTs
1995	3191
1996	7845
1997	12986

Table 6.1: Run statistics for the 1995-97 data taking

The data quality selection criteria used in this analysis are adopted from the results of the HERMES inclusive g_1 analysis [95]. As opposed to the inclusive asymmetry analysis where results can be obtained for each detector half independently, we require both spectrometer halves to be working stable at the same time, since the scattered positron and the vector meson decay products may end up in different halves of the detector. Some of the inclusive analysis selection criteria, e.g. for the beam and target polarization, can be relaxed or even omitted for some parts of the analysis.

Tables 6.2 and 6.3 list all selection criteria as used for the inclusive analysis and indicate which of these criteria were applied in the analysis reported in this work. The final results of the data quality selection on the burst level are summarized in Appendix A, where the effect of the different cuts on the amount of useful data is quantified. In the following sections all data quality selection criteria for the inclusive asymmetry analysis will be described in detail.

6.1.1 Beam and Target Criteria

The degree of polarization of the lepton beam in HERA and the target polarization are important quantities in measurements of spin asymmetries. Moreover, the beam polarization can also play a role in the analysis of the vector meson decay angle distributions. Periods of low polarization do not contribute much to the measured asymmetries and are consequently removed from the data set. The smoothed beam polarization value was required to be within a certain upper and lower limit. The lower limit cuts away periods of low polarization or periods when the polarimeter measurements were unreliable and also removes data taken at the beginning of each fill when the polarization value was still rising. The target was required to be in a well-defined nuclear polarization state parallel or anti-parallel to the beam direction, which is not the case while the direction of the target polarization is being switched. For data taken with the ABS only nuclear polarization states are used in the analysis, since residual electron polarization could introduce asymmetries in the luminosity measurement. For the ^3He target the values of the target polarization measured with either the pumping cell polarimeter or the target optical monitor were required to be within a certain range, while for the ^1H running the polarization value from the BRP was demanded to be within acceptable limits. The lower boundaries on the target polarization cut away those bursts where the polarization did not yet reach its maximum value after a spin-flip. The upper boundaries on both the beam and target

polarization reflect the maximum measured values and are used to remove periods with an unphysically high polarization measurement.

For the ^3He running the target density was required to stay within a reasonable operating range. As there were no direct measurements of the target density with the ABS, this kind of cut was not possible for the ^1H data. For the latter data the atomic fractions α_0 and α_R were restricted to positive values and a regular update of the α measurement was required. Bursts which suffered from target related hardware problems were discarded.

6.1.2 Luminosity

The luminosity measurement is very important for several analysis topics. First of all the spin asymmetry measurements have to be normalized with the (relative) luminosity value because of the permanently changing beam current and the relatively long time in between the target spin flips. Luminosity measurements are also necessary for the absolute and relative normalization of the data sets, which is needed for e.g. cross section or nuclear transparency determinations.

The luminosity monitor rates were restricted to a nominal range. For the 1995 data these rates were cross-checked by comparing them to the product of the beam current and target density values, where the latter two quantities were also limited to reasonable values to ensure a reliable comparison.

From 1996 on, the luminosity monitor calorimeter blocks were also monitored by the gain monitoring system. The requirement was made that all blocks of the calorimeter were functioning optimally.

6.1.3 Data Acquisition

Since the data acquisition controls the recording of the incoming data, one must ensure that this system is operating stably.

An important DAQ related quantity is the deadtime or equivalently the live time τ_{live} , which basically indicates the fraction of time the DAQ system is able to accept and record new incoming data without being blocked due to the processing of the previously accepted data. This fraction can be estimated from the total number of generated triggers and triggers accepted by the DAQ per burst

$$\tau_{\text{live}} = \frac{T_{\text{acc}}}{T_{\text{gen}}}. \quad (6.1)$$

For the 1997 data quality studies this quantity was also calculated separately for trigger 21, $\tau_{T_{21}}$. Also, a correction factor for the total live time was computed to account for missing events in the data stream, yielding an artificial live time τ_{Art} . The live time together with the burst length, which is the length in time during which the data in that burst was collected, enter the luminosity normalization and are therefore restricted to certain ranges. For 1997 cuts were also imposed on the trigger 21 live time and on the total artificial live time. In 1995 the burst length was restricted to be close to the nominal

value of 10 seconds, while for 1996-97 this value could be lower due to the shorter records during the much more frequent target spin flips.

To avoid DAQ problems during the beginning or termination of a run, when the DAQ has to perform several clean-up and initialization tasks, the first and last bursts from each run were removed from the data.

Furthermore, any bursts exhibiting problems with timing or synchronization with the slow control data, which occurred mostly during 1996-97, were cut out from the data.

6.1.4 Tracking Chambers

The detection and reconstruction of the charged particle trajectories depends on the tracking detectors in the spectrometer so that the stability and efficiency of these devices should be monitored to ensure good tracking performance.

In 1995 the tracking efficiency was monitored using the ACE¹ code [96] that is able to calculate the individual tracking chamber plane efficiencies per burst from the reconstructed tracks in the burst. As in that data taking year the detector high voltage information was not yet recorded in the slow control data stream, these efficiency values were the only available source of information to identify chamber trips. Cuts were imposed on the total tracking efficiency of the front and back drift chambers. Whenever a burst failed the efficiency cut, both the burst preceding and following burst were also removed to ensure that the entire affected period was removed.

From 1996 on the high voltage information was recorded so that for the FC's and BC's cuts on HV trips could be made directly. For the 1997 data taking these cuts were also applied to the VC's and DVC's as they were included in the standard tracking method used for the reconstruction of the polarized target runs. Apart from that, bursts which showed specific problems related to the VC's were also excluded from the data reconstructed with standard tracking. In 1996 an entire period of data taking was affected due an accidentally misplaced VC plate covering part of the acceptance of the bottom detector.

6.1.5 Trigger and Particle Identification Detectors

Because the trigger efficiency and particle identification performance is influenced by the H1 hodoscope, the preshower and the calorimeter, it is imperative to monitor these detectors.

In 1995 the information from the gain monitoring system for the calorimeter and the preshower was accessible only on a run by run basis, since the statistics of the measurements was insufficient to evaluate the performance at the burst level. The stability of each detector module was checked offline by comparing its average gain to its nominal gain. A calorimeter block was declared unstable if the measured gain differed by more than 10% from its nominal value, while preshower blocks were allowed to have a gain within 20% of the nominal value. Cuts were imposed on the maximum allowed number of GMS bad blocks in the top and bottom half of the spectrometer. Due to the forward nature of the

¹Alignment, Calibration, Efficiencies

scattering process the edges of the spectrometer were not hit as often as the central part around the beam pipe. Therefore for the 1995 data both the top and bottom calorimeter and preshower were split into an inner and outer part, where the inner part was taken as the central thirty columns of calorimeter blocks and the central thirty hodoscope scintillators. Cuts on the maximum number of bad channels are applied separately for the inner and outer region of the top and bottom detector half, where the cuts on the inner region are more stringent. This kind of far-reaching requirements were not necessary for the 1996-97 data taking, so that for these data sets simple cuts on the total number of dead blocks as seen by the GMS were made.

For both the HI hodoscope and the preshower the number of scaler counts per channel per burst was used to identify malfunctioning modules in 1995, where a module was marked bad if zero counts were measured.

The particle identification performance is also affected by the TRD and Čerenkov counter. Due to the limited amount of statistics both detectors were checked at the run level.

The total number of tracks in the top and bottom detector producing a TRD signal and the amount of tracks without a TRD response were recorded together with the simple mean values M of the pulse-height distributions. For each run the TRD response to a sample of pions and positrons as defined by the calorimeter and preshower was determined for each detector half separately. The peaks in the pulse-height spectra were then fitted with Gaussian functions to determine their mean value m and standard deviation σ . For pions this fitted mean value $m(\pi)$ will usually differ from the simple mean value $M(\pi)$ of the spectrum due to the Landau-tail of the distribution, making the ratio $m(\pi)/M(\pi)$ smaller than 1. The number of tracks was used to check whether the TRD was operational during the run. The calibration of the detector was monitored by checking the stability of the mean and sigma of the pion peak, while the ratio $m(e^+)/m(\pi)$ of the positron and pion peak positions indicated the linearity of the TRD. Trip detection was accomplished by examining the $m(\pi)/M(\pi)$, where the ratio becomes larger than 1 when a trip occurs.

For the Čerenkov data quality studies a sample of positrons as defined by the calorimeter and preshower was taken for each run. A cut was imposed on the efficiency of the detector ϵ_{cer} , which was calculated from the ratio of the number of positrons recognized by the Čerenkov and the total number of positron tracks. Also the mean number of photoelectrons for high momentum positrons was limited to an acceptable range to ensure stable operation.

6.1.6 Overall Stability

In the 1995 inclusive asymmetry analysis it was found that, in spite of all the data quality requirements listed above, the data still showed instabilities. Hence, the amount of remaining good bursts per run and per fill was examined after the application of the criteria mentioned above. To avoid possible systematic errors due to changing detector behaviour the asymmetry was calculated on a fill by fill basis. Therefore a minimum amount of good bursts per fill for each detector half was required in order to use the fill in the analysis. Also on the run level a minimum fraction of good bursts per run was demanded and an upper limit was placed on the amount of gaps defined as the change

from good to bad data quality, as these quantities are a measure of the instability of the experiment.

The instabilities in the data as seen in 1995 did not appear in the 1996-97 running, making this kind of requirements superfluous for these data taking years.

6.2 Event Selection

After the application of the different data quality criteria clean and stable data samples are obtained suitable for further analysis. As the HERMES spectrometer detects a large variety of different processes, additional cuts have to be imposed to select the type of events one wants to study and to remove those events which one is not interested in and form the 'background' in the sample. In general the selection criteria are chosen to diminish the contamination due to background in each sample, while keeping the statistical precision of the event signal under study as high as possible. In this section all applied event selection cuts will be listed and explained in detail.

The analysis presented here covers the HERMES polarised data taking on a ^3He target in 1995 and on ^1H in 1996-97 and also the data collected during periods of unpolarised target running in 1996-97 on a ^1H , ^2H , ^3He and ^{14}N target. The data samples from the short periods of unpolarised target running in 1995 on ^1H , ^2H contain only a negligible amount of usable vector meson events and were therefore not considered in this analysis. Most of the results obtained in this work comprise the analysis of the HERMES main physics trigger events where scattered positrons were detected in the final state together with (a fraction of) the particles produced in the scattering process. Part of the analysis was also done using the data collected with the photoproduction trigger, where the information of the scattered positron was missing.

The ρ^0 and ω vector mesons are unstable short-lived particles that will decay immediately after formation² before they reach the spectrometer so that only their final decay products could be detected. The main decay channels of the ρ^0 and ω meson are listed in table 6.4. The ρ^0 will be analysed in the $\rho^0 \rightarrow \pi^+\pi^-$ decay channel, while for the ω the $\omega \rightarrow \pi^+\pi^-\pi^0$ and $\omega \rightarrow \pi^0\gamma$ decay modes will be considered.

The HERMES spectrometer had no means of detecting the recoil particles from any scattering process in general³. In particular in the case of exclusive vector meson production the recoiling proton (or nucleus) remained undetected and the event information and reconstruction was based on the detection of only the meson decay products and possibly the scattered positron. For those events where the scattered positron track could be reconstructed together with all final state decay particles of the vector meson, it was possible to calculate the necessary event kinematics and to select exclusive, diffractive events. For the photoproduction trigger events, part of the event kinematics could not be determined and no selection on exclusivity was feasible.

²Using $\tau = \hbar/\Gamma$ one can estimate the lifetime of the ρ^0 and ω to be $\tau_{\rho^0} = 4.4 \cdot 10^{-24}$ s and $\tau_{\omega} = 7.8 \cdot 10^{-23}$ s respectively (see table 6.4). The distance these particles will travel before decaying can be approximated by $c\tau$ with c being the speed of light, which gives $c\tau_{\rho^0} = 1.3$ fm and $c\tau_{\omega} = 23$ fm, which is roughly the scale of the nucleon size.

³Plans to install a recoil detection system do exist [97].

Nr.	Quantity	Criterion	Applied
0	Target polarization	$\left\{ \begin{array}{l} \text{well defined state} \\ 30 < P_{\text{target}} < 60 \% \end{array} \right.$	-
1	Beam polarization	$40 < P_{\text{beam}} < 70 \%$	-
2	First burst	reject first 3 bursts in run	✓
3	Last burst	reject last burst in run	✓
4	Live time	$50 < \tau_{\text{live}} < 100 \%$	✓
5	Burst length	$9 < t_{\text{burst}} < 11 \text{ s}$	✓
6	Beam current	$8 < I_e < 32 \text{ mA}$	✓
7	Target density	$0.85 < n < 1.4 (10^{15} \text{ nucl./cm}^2)$	✓
8	Luminosity rate	$40 < N_{\text{lumi}} < 210 \text{ Bq}$	✓
9	Lumi./curr./dens.	$5 < \frac{N_{\text{lumi}}}{I_e n} < 7.2 (10^{-15} \text{ cm}^2\text{s/mA nucl.})$	✓
16	FC efficiency	$80 < \epsilon_{\text{front}} < 100 \%$	✓
17	BC efficiency	$94 < \epsilon_{\text{back}} < 100 \%$	✓
18	GMS calorimeter	$\left\{ \begin{array}{l} \text{top inner : } \leq 3 \\ \text{bottom inner : } \leq 4 \text{ bad blocks} \\ \text{outer : } \leq 8 \end{array} \right.$	✓
19	GMS preshower	$\left\{ \begin{array}{l} \text{inner : } \leq 1 \text{ bad blocks} \\ \text{outer : } \leq 5 \end{array} \right.$	✓
20	H1 scaler	$\left\{ \begin{array}{l} \text{top : } \leq 1 \text{ bad channels} \\ \text{bot : } 0 \end{array} \right.$	✓
21	Preshower scaler	$\left\{ \begin{array}{l} \text{top : } 0 \text{ bad channels} \\ \text{bottom : } 0 \end{array} \right.$	✓
22	Čerenkov & TRD	reject burst if both bad	✓
23	Logbook	reject data marked bad	✓
29	Gap / good bursts	$\left\{ \begin{array}{l} n_{\text{gaps}}/n_{\text{bursts}} < 0.10 \text{ per run} \\ n_{\text{goodbursts}}/n_{\text{bursts}} > 0.40 \text{ per run} \end{array} \right.$	-
30	Short fill	$\left\{ \begin{array}{l} n_{\text{goodbursts}}^{\uparrow\uparrow} \geq 100 \text{ per fill} \\ n_{\text{goodbursts}}^{\downarrow\downarrow} \geq 100 \text{ per fill} \end{array} \right.$	-
31	Previous / next burst	skip if burst fails nr. 16/17	✓

Table 6.2: The 1995 data quality cuts. The last column indicates whether a particular criterion was applied in this analysis or not.

Nr.	Quantity	Criterion	1996	1997
0	Target spin state	well defined	-	-
1	Beam polarization	$30 < P_{\text{beam}} < 80 \%$	-	-
2	Live time	$\left\{ \begin{array}{l} 50 \leq \tau_{\text{live}} < 100 \% \\ 0 < \tau_{\text{Trt1}} \leq 100 \% \\ 95 \leq \tau_{\text{Aprt}} \leq 100 \% \end{array} \right.$	✓	✓
3	Burst length	$0 < t_{\text{burst}} \leq 11 \text{ s}$	✓	✓
4	Beam current	$8 < I_e < 50 \text{ mA}$	✓	✓
5	Luminosity rate	$5 \leq N_{\text{lumi}} \leq 1000 \text{ Bq}^{(a)}$	✓	✓
6	First burst	reject first burst in run	✓	✓
7	Last burst	reject last burst in run	✓	✓
8	μ DST problems	reject bad timing bursts	✓	✓
9	Logbook data quality	$\left\{ \begin{array}{l} \text{reject 'VC plate period' } \\ \text{reject bad logbook bursts} \end{array} \right.$	✓	✓
10	Logbook ABS mode	reject unpolarized	-	-
11	Logbook gas type	reject non-hydrogen	-	-
12	Beam pol. data quality	reject bad polarim. DQ bursts	-	-
13	Target type	reject unpolarized	-	-
15	UGFS setting	reject non-ABS	-	-
16	Target data quality	reject bad target DQ bursts	-	-
17	GMS Calorimeter	$\left\{ \begin{array}{l} \text{top: } 0, \text{ bot: } \leq 1 \text{ bad blocks} \\ \text{top: } 0, \text{ bot: } 0 \end{array} \right.$	✓	✓
18	GMS H2 & lumi. mon.	0 bad blocks	✓	✓
19	TRD data quality	reject bad TRD DQ bursts	✓	✓
20	HV trips	reject $\left\{ \begin{array}{l} \text{FC \& BC} \\ \text{FC, BC, VC \& DVC} \end{array} \right.$ trips	✓	$\checkmark^{(b)}$ $\checkmark^{(b)}$
23	α_0	$\alpha_0 > 0$	-	-
24	α_R	$\left\{ \begin{array}{l} \alpha_R > 0 \\ \text{regular } \alpha \text{ update} \end{array} \right.$	-	-
25	Čerenkov data quality	reject bad Čer. DQ bursts	✓	✓
26	VC data quality	reject bad VC DQ bursts	✓	$\checkmark^{(b)}$
27	Target polarization	$\left\{ \begin{array}{l} 50 \leq P_{\text{target}} \leq 150 \% \\ \text{regular target update} \end{array} \right.$	-	-
28	Beam polarization fit	regular polarim. update	-	-

^(a) For polarized data analysis one uses $5 \leq N_{\text{lumi}} \leq 60 \text{ Bq}$ due to the lower target density.

^(b) Only for the standard tracking reconstruction method.

Table 6.3: The 1996-97 data quality cuts. The last two columns indicates whether a criterion was applied in this analysis or not; an empty box means that a criterion was not defined for that particular data taking year.

Particle Type	Mass (MeV)	Full Width (MeV)	Main Decay Modes
$\rho^0(770)$	770.0 ± 0.8	150.7 ± 1.1	$\pi^+\pi^-$ (100%)
$\omega(782)$	781.94 ± 0.12	8.41 ± 0.09	$\pi^+\pi^-\pi^0$ (88.8%) $\pi^0\gamma$ (8.5%) $\pi^+\pi^-$ (2.21%)

Table 6.4: ρ^0 and ω main particle properties [94]

It was attempted to perform the analysis on the ρ^0 and ω in a consistent way as much as possible. The selection criteria of events in both analysis are thus rather similar. However, due to the much larger statistics in the ρ^0 data sample and the different final states in the main decay channels of the two vector mesons, some cuts can differ a little.

6.2.1 Selection of Scattered Positrons, Hadrons and Photons

The identification of scattered positrons and charged hadrons was done using the PID parameters as defined in section 5.4. For the chosen cuts, the contamination of misidentified hadrons in the scattered positron sample or of misidentified leptons in the hadron sample is negligible.

Additional cuts were imposed on the reconstructed positron vertex quantities z_{vertex} and r_{vertex} , being the position along the z axis and the perpendicular distance from the z axis of the vertex defined by the track and the beamline respectively, to select only tracks originating from the target cell indicating that the positrons interacted with the target gas. To ensure that the positron had deposited all its energy in the calorimeter, a fiducial volume for the tracks was defined using the position of the track at the calorimeter. This removes the tracks at the edges of the spectrometer where the positron identification efficiency goes down. To avoid the region of the septum plate in the magnet a cut on the vertical scattering angle was imposed. A kinematical cut on y was introduced to make sure that the positron had enough energy to generate a trigger and also to limit the events to a region where the radiative corrections are not too high. Finally a minimum value of W was required to remove the events from the nucleon resonance region and the data below threshold for ρ^0 and ω production⁴.

For the charged hadron tracks one did not need as stringent cuts as for the positron since the hadrons were used to reconstruct the vector meson which effectively identified useful events for the analysis.

Photons were identified as calorimeter clusters where no full particle trajectory pointed to. Photons assigned to forward partial tracks were considered to be generated due to Bremsstrahlung and were accordingly discarded. The photons used in the ω analysis were required to have a minimum energy to remove the large background at low energy. The

⁴Note that this cut is slightly above the ρ^0 and ω -production threshold $W_{\text{thres}} = M_p + M_{\pi^0}$, being 1.71 GeV and 1.72 GeV respectively. However, as the detector acceptance for exclusive ρ^0 and ω production is negligible around this W value (see figure 7.1 and 7.2) this cut does not remove any useful data.

Quantity	Charged Track Selection	Criterion
Particle Identification Cuts		
positron identification	$\left\{ \begin{array}{l} \text{charge}=+1 \\ \text{PID}_{95} > 0 \text{ (1995)} \\ \text{PID}_{96-97} > 2 \text{ (1996-97)} \\ \text{PID}_{95} < 0 \text{ (1995)} \\ \text{PID}_{96-97} < 2 \text{ (1996-97)} \end{array} \right.$	
hadron identification		
Geometry Criteria		
horizontal fiducial cut (positron)		$ x_{\text{calo}} < 175 \text{ cm}$
vertical fiducial cut (positron)	$ y_{\text{calo}} > 30 \text{ cm}$	
magnet septum plate	$ \theta_y > 40 \text{ mrad}$	
Target region (positron)		
reconstructed vertex inside target	$ z_{\text{vertex}} < 20 \text{ cm}$	
transverse vertex offset	$r_{\text{vertex}} < 0.75 \text{ cm}$	
Kinematics		
non-resonance region	$W > 2.0 \text{ GeV}$	
small radiative corrections	$y < 0.85$	
Photon Selection		
remove low energy background	$E_\gamma > 0.8 \text{ GeV}$	

Table 6.5: The track and photon selection criteria.

photon emission angles in the lab frame were calculated assuming that the ω decay vertex coincided with the positron scattering vertex, which, in view of the short lifetime of the ω meson, was certainly a good enough approximation.

All requirements for the positron and hadron charged tracks and the photons are listed in table 6.5.

6.2.2 Selection of Exclusive, Diffractive Events

Since we are interested in exclusive vector meson production we rejected every event containing additional tracks or trackless calorimeter clusters other than the ones associated with the scattered positron and the meson decay products, as this indicated that other particles were created through e.g. target break-up or photon radiation. In the case of the ρ^0 , events were selected with exactly three tracks, where one was identified as the scattered positron and the other two corresponded to the two charged hadrons. For the ω analysis in the 3-pion decay mode, events with exactly three tracks and two photon clusters associated with the decayed π^0 were selected, while for the pion-gamma decay channel, events with one positron track and three additional photon clusters were used.

Eventually the production of vector mesons was identified as a peak in the invariant mass distribution M_V of the reconstructed candidate vector mesons. These candidates were formed by combining the measured assumed decay particles, which in four-vector

language translates into adding up the four-momenta.

Since non-exclusive events could also exhibit the same event topology as an exclusive event when part of the produced particles escaped the detector acceptance, another measure of whether the event was exclusive or not, was needed. Therefore the following quantity

$$\Delta E = \frac{M_x^2 - M_{Iarg}^2}{2M_{Iarg}} = \nu - E_V + \frac{t}{2M_{Iarg}} \quad (6.2)$$

was introduced, with the rest mass of the recoiling baryonic system $M_x^2 = p^2$ in semi-inclusive $A(c, e'V)$ given by

$$M_x = \sqrt{(p+q-p_V)^2}. \quad (6.3)$$

For exclusive events, M_x will be equal to the initial target rest mass, giving $\Delta E = 0$ GeV, while for non-exclusive events it will be larger and result in $\Delta E > 0$ GeV. With t given by equation 2.9 for exclusive events, one can also see that the second part of equation 6.2 reduces to zero and simply denotes energy conservation in case of exclusive scattering. For scattering on ^1H we have $M_{Iarg} = M_p$, the mass of the proton. For scattering on composite nuclei one can have either incoherent scattering from individual nucleons inside the target nucleus or coherent scattering from the entire nucleus. In the former case one can also assume $M_{Iarg} = M_p$, while for coherent scattering one ought to take $M_{Iarg} = M_A$, the target nucleus mass. However, as the experimental resolution was limited, one could not distinguish the two different types of scattering processes and M_{Iarg} was chosen to be equal to the proton mass throughout the entire analysis. In this case exclusive coherent events occur at slightly negative values of ΔE as can be easily seen from the second part of equation 6.2. The coherent process is also expected to have a much smaller non-exclusive contribution than the incoherent one [98]. Other experiments sometimes use $z = E_V/\nu \approx 1$ [99] or $I = (M_x^2 - M_p^2)/W^2 \approx 0$ [100] as measure for exclusivity. ΔE has the advantage that it includes the recoil nucleon kinetic energy correction $-t/2M_p$ and that the threshold value for inelastic scattering $\Delta E = M_\pi + M_\pi^2/2M_p$ is independent of kinematics.

Parameter	ρ^0 ($\rightarrow 2\pi$)	Requirement	ω ($\rightarrow 3\pi, \pi\gamma$)
Invariant mass	$0.6 \text{ GeV} < M_{2\pi} < 1.0 \text{ GeV}$	$0.72 \text{ GeV} < M_{3\pi}, M_{\pi\gamma} < 0.88 \text{ GeV}$	
Exclusive events	$\Delta E < 0.6 \text{ GeV}$	$\Delta E < 1.0 \text{ GeV}$	
Diffraction events	$-t' < 0.4 \text{ GeV}^2$	$-t' < 0.5 \text{ GeV}^2$	
2-kaon mass	$M_{2K} > 1.06 \text{ GeV}$	-	

Table 6.6: Requirements for exclusive, diffractive ρ^0 and ω candidate events.

Diffraction interactions have their main contribution at small values of t , the squared four-momentum transfer to the target, and their cross section in that region exhibits an exponential dependence on t . In the hadron center-of-mass frame one can derive from equation 2.8 that

$$t = (v_{cm} - E_{v,cm})^2 - (|\vec{q}_{cm}| - |\vec{p}_{v,cm}|)^2 - 4|\vec{q}_{cm}||\vec{p}_{v,cm}|\sin^2(\theta_{cm}/2) \quad (6.4)$$

$$= t_0 - 4|\vec{q}_{cm}||\vec{p}_{v,cm}|\sin^2(\theta_{cm}/2) \quad (6.5)$$

with θ_{cm} the angle between the vector meson and the virtual photon and t_0 the value t would attain if the vector meson was emitted along the direction of the virtual photon at fixed ν , Q^2 , M_V and M_x . The variable t_0 is not Lorentz invariant and was calculated in the hadron center-of-mass frame using

$$\nu_{cm} = \frac{W^2 - Q^2 - M_p^2}{2W}, \quad (6.6)$$

$$E_{v,cm} = \frac{W^2 + M_V^2 - M_x^2}{2W}, \quad (6.7)$$

$$|\vec{q}_{cm}| = \sqrt{\nu_{cm}^2 + Q^2}, \quad (6.8)$$

$$|\vec{p}_{v,cm}| = \sqrt{E_{v,cm}^2 - M_V^2}. \quad (6.9)$$

In the analysis one often uses the quantity t' defined by

$$t' = t - t_0. \quad (6.10)$$

In the relativistic metric used $t, t_0, t' \leq 0$ GeV², which makes t_0 the maximum kinematically allowed value of t . Since the t_0 subtraction removes the longitudinal component of the momentum transfer, t' is a measure of the transverse momentum transfer. Also, $-t' \gtrsim p_t^2$, where p_t is the vector meson transverse momentum with respect to the virtual photon direction. For exclusive, diffractive processes in the forward region t_0 is small and $t' \approx t$.

Data Taking Year	Target	$\#\rho^0$	$\#\omega$ ($\rightarrow 3\pi$)	$\#\omega$ ($\rightarrow \pi\gamma$)
1995	^3He	5649	136	44
1996	^1H	3334	80	45
	^2H	3689	99	34
	^3He	1221	35	16
1997	^1H	4935	142	70
	^2H	3689	113	49
	^{14}N	3913	79	39

Table 6.7: The number of exclusive, diffractive ρ^0 and ω events remaining after the application of all the cuts described in the text, given for each data taking year and target. The data sets taken on polarized and unpolarized target are added together. Note that in case of the 1997 ^{14}N data, the number of ω events seems lower than expected from the number of ρ^0 events in comparison with the other data samples. This has to do with the fact that on heavy targets the dominant mechanism is coherent production at low $-t'$, whereas the detector acceptance for ω production in the considered decay modes decreases towards low $-t'$ while it remains nearly constant for ρ^0 production over the entire $-t'$ range.

The following paragraphs will deal with the specific selection of exclusive, diffractive ρ^0 and ω event samples. All cuts are summarized in table 6.6. Unless otherwise stated, the events shown in the plots below correspond to the HERMES 1996-97 running on ^1H , where the polarized and unpolarized target data samples were added together. Note

however, that all selection criteria described below are applicable to every HERMES data set and have qualitatively the same impact. Table 6.7 lists the final number of events after the selection cuts for the different targets and data taking years considered in this work.

6.2.2.1 Selection of ρ^0 Events

In the ρ^0 analysis one assumes that the detected hadrons are actually pions and the true resonant ρ^0 production events should appear as a peak in the 2-pion invariant mass distribution

$$M_{2\pi} = \sqrt{(p_{\pi^+} + p_{\pi^-})^2}, \quad (6.11)$$

with p_π the four-momenta of the hadrons assumed to be pions. The 2-pion invariant mass distribution is depicted in figure 6.1. The ρ^0 events show up clearly in the wide bump around the expected mass value. The narrow peak in the lower mass region corresponds to K_S^0 mesons which have a mass of 497.672 ± 0.031 MeV and also decay into $\pi^+\pi^-$ with a branching ratio of 68.61 ± 0.28 % [94]. The ρ^0 events were filtered out in a first step by imposing a mass window $0.6 < M_{2\pi} < 1.0$ GeV on the event sample. As can be seen on the plot, the majority of the events selected within the mass window did not correspond to resonant ρ^0 production, but rather to e.g. hadron pairs produced in fragmentation processes, production of other particles decaying into hadrons or exclusive $\pi^+\pi^-$ production without resonant formation of an intermediate ρ^0 meson.

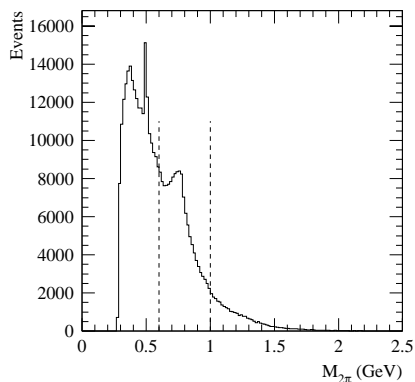


Figure 6.1: The reconstructed $M_{2\pi}$ distribution without any additional cuts. The ρ^0 events clearly show up around the right mass value. The narrow peak in the lower mass region corresponds to K_S^0 production. The dashed lines indicate the invariant mass window to select ρ^0 events.

To restrict the event sample further to exclusive and diffractive production in the

forward region cuts on ΔE and $-t'$ were used. Figure 6.2 (a) shows the ΔE distribution of the sample with the ρ^0 mass window. The narrow peak at $\Delta E \approx 0$ GeV indicates the exclusive event candidates, while the majority of the events is non-exclusive and is contained in the wide structure at higher ΔE . Exclusive event candidates were selected using $\Delta E < 0.6$ GeV. The correlation of ΔE with $-t'$ is plotted in figure 6.2 (b), where a pile-up of exclusive event candidates occurs at very low $-t'$. This is a clear sign of a diffractive production mechanism. Diffractive events were selected using $-t' < 0.4$ GeV².

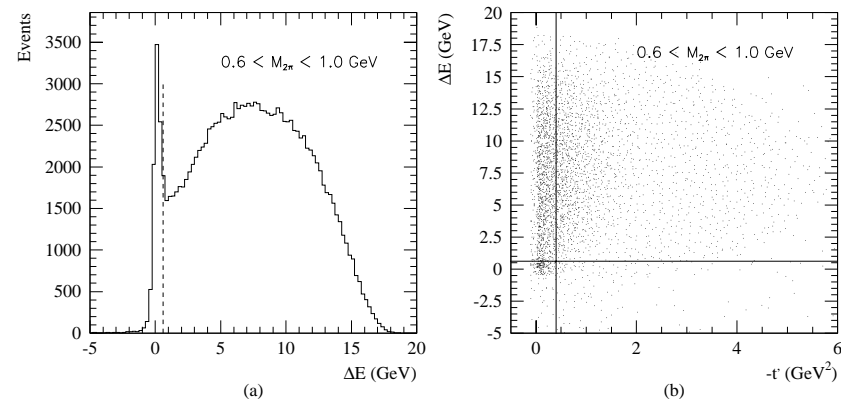


Figure 6.2: (a) The ΔE distribution of the event sample within the ρ^0 mass window. The peak at $\Delta E \approx 0$ GeV corresponds to exclusive events. The dashed line indicates the cut used in the analysis. (b) The correlation between ΔE and $-t'$ for the same event sample. The exclusive events at very low $-t'$ correspond to diffractive production. The lines indicate the cuts used in the analysis.

The ρ^0 event candidates were reconstructed under the assumption that both charged hadrons were actually pions. As the pion identification capability of the threshold Čerenkov counter was limited to a certain momentum range, this information was not used in the ρ^0 analysis to avoid loss of event statistics. The sample of hadron pairs was therefore contaminated with e.g. kaons and protons. An important source of background events may come from production of ϕ vector mesons which have a mass of 1019.413 ± 0.008 MeV and decay into K^+K^- pairs with a branching ratio of 49.1 ± 0.8 % [94]. To look for ϕ production events in the sample, one must examine the 2-kaon invariant mass distribution given by

$$M_{2K} = \sqrt{(p_{K^+} + p_{K^-})^2}, \quad (6.12)$$

with p_K the 4-momenta of the hadrons assumed to be kaons. The 2-kaon invariant mass spectrum is plotted in figure 6.3 (a), where the distribution is shown using the cuts mentioned above on ΔE and $-t'$. A narrow peak at the expected mass can be seen,

corresponding to exclusive, diffractive ϕ production⁵. The correlation between $M_{2\pi}$ and M_{2K} is depicted in figure 6.3 (b), where the lines correspond to the cuts given above. As the plot demonstrates, all ϕ events were clearly outside the ρ^0 event sample when the 2-pion invariant mass window was imposed. However, to clean up the invariant mass spectrum of the ρ^0 event candidates (see figure 6.4), all ϕ production events were removed from the sample by the additional requirement that $M_{2K} > 1.06$ GeV.

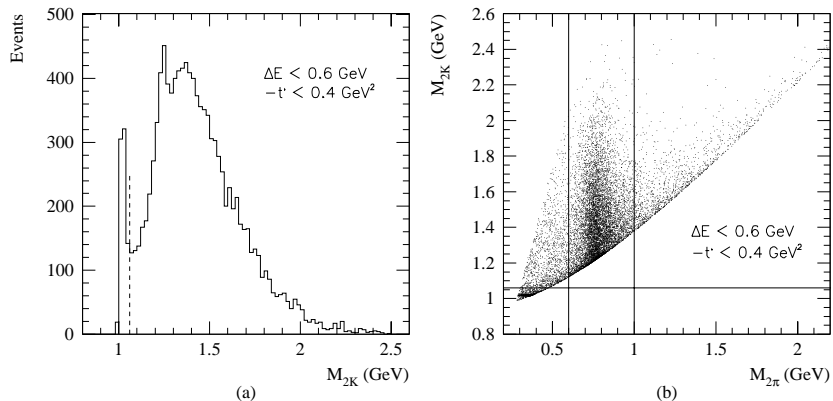


Figure 6.3: (a) The 2-kaon invariant mass distribution, where a signal of exclusive, diffractive ϕ production is present at the expected mass value. The dashed line indicates the cut used in the analysis. (b) Correlation between $M_{2\pi}$ and M_{2K} , where the lines indicate the cuts as outlined in the text. The plot demonstrates that all ϕ events were outside the ρ^0 event candidate sample when the 2-pion invariant mass window was imposed.

All other sources of background in the event sample defined above, were not handled on the event selection level, but will be discussed and corrected for further on in the analysis.

The influence of the cuts given above on the invariant mass distribution of the ρ^0 event sample is shown in figure 6.4.

⁵Apart from the signal at about 1.02 GeV corresponding to ϕ production, one sees another peak around 1.25 GeV on the lower mass end of the bump in the distribution. As the plot shows, the events in that region mostly corresponded to ρ^0 production and the small peak in the distribution was found to be due to a geometrical acceptance effect.

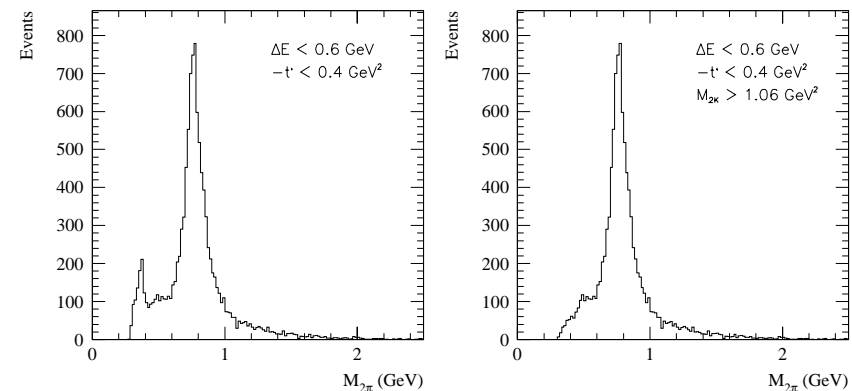


Figure 6.4: The effect of the cuts mentioned in the text on the 2-pion invariant mass spectrum for the exclusive, diffractive ρ^0 event candidate sample.

6.2.2.2 Selection of ω Events

For both decay modes of the ω considered in the analysis one has to start with the reconstruction of the π^0 from its two decay photons

$$M_{2\gamma} = \sqrt{(p_{\gamma_1} + p_{\gamma_2})^2} = 2\sqrt{E_{\gamma_1}E_{\gamma_2}} \sin\left(\frac{\theta_{\gamma_1\gamma_2}}{2}\right), \quad (6.13)$$

where p_γ are the four-momenta of the photons and $\theta_{\gamma_1\gamma_2}$ is the angle between the two photons in the lab frame. The $M_{2\gamma}$ distribution for events in the 1997 data with exactly two good photon clusters as defined in section 6.2.1, is shown in figure 6.5 (a), where a prominent signal from π^0 mesons is present. A fit to the distribution with a Gaussian function plus a 4th order polynomial respectively describing the π^0 peak and the background underneath the resonance, yields a π^0 mass of $M_{\pi^0} = 134.98 \pm 0.03$ MeV, in agreement with the PDG value [94]. The width of the π^0 peak was 12.13 ± 0.03 MeV which serves as a measure for the spectrometer resolution for photons.

The fact that the π^0 mass is reconstructed so well is not a coincidence, but merely a consequence of an extra calibration of the photon energy, which is needed as the calorimeter response is calibrated using the positron E/p ratio⁶, whereas photons have slightly different showering characteristics leading to a small miscalibration of their energy. To correct for this effect an E_γ scaling factor was determined from a π^0 invariant mass fit using a semi-inclusive π^0 production event sample for each data taking year. The ratio of the PDG M_{π^0} value to the measured one gives according to equation 6.13 the needed photon energy scale factor, which varies between 0.95 and 0.98 for the 1995 to '97 data.

⁶ E/p is the ratio of the measured calorimeter energy E and the momentum p as determined by the tracking through the spectrometer dipole magnet.

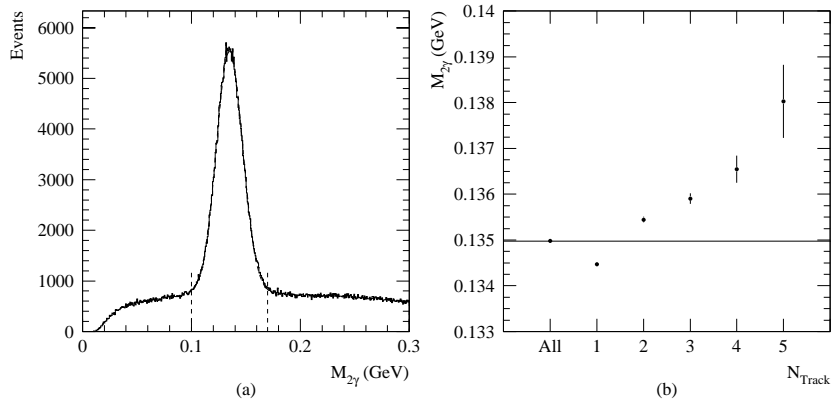


Figure 6.5: (a) The reconstructed $M_{2\gamma}$ invariant mass for the entire '97 data set. The prominent π^0 peak shows up on top of some combinatorial background. The distribution in the region of the π^0 resonance can be perfectly described by a Gaussian plus a 4th order polynomial function, where the fit matches the distribution so well that it is hardly visible on the plot. (b) The fitted π^0 mass for the '97 data as function of the number of reconstructed charged tracks per event. Only events with at least one single track (identified as the scattered positron) were considered.

Another small effect on M_{π^0} which can be taken into account is displayed in figure 6.5 (b) where the fitted π^0 mass is shown as a function of the number of reconstructed tracks in the event taken from the semi-inclusive production sample mentioned above. The higher the charged particle multiplicity in a π^0 event is, the larger the probability becomes for a photon calorimeter cluster or shower to (partially) overlap with the one of a charged particle, which explains the observed rise of M_{π^0} with the number of tracks per event. For the 3-pion decay ω analysis, where events are considered containing three charged tracks, this effect was corrected for with another E_γ scaling factor varying between 0.99 and 1.00 for the 1995 to '97 data. For the $\pi^0\gamma$ decay mode no correction of this kind is needed.

In the ω analysis, π^0 mesons were selected by imposing a cut on the 2-photon invariant mass $0.10 < M_{2\gamma} < 0.17$ GeV.

For the ω 3-pion decay mode, one has to examine the 3-pion invariant mass

$$M_{3\pi} = \sqrt{(p_{\pi^+} + p_{\pi^-} + p_{\pi^0})^2}, \quad (6.14)$$

with p_π the four-momenta of the hadrons assumed to be pions. The 3-pion invariant mass distribution is shown in figure 6.6 (a). The spectrum reveals a clear resonance around 780 MeV corresponding to ω production and also a second peak around 550 MeV corresponding to the production of pseudoscalar η mesons which have a small branching

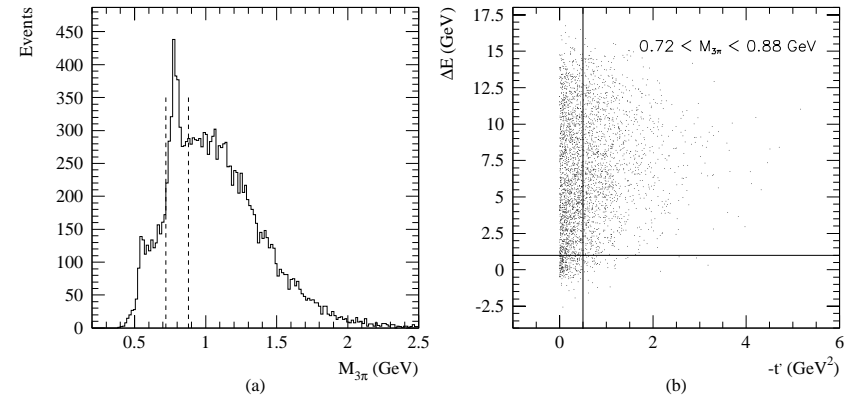


Figure 6.6: (a) The 3-pion invariant mass distribution. A clear peak corresponding to ω meson production shows up around the expected invariant mass. The dashed lines indicate the invariant mass window used in the analysis. A second peak appears around 550 MeV which indicates the production of pseudoscalar η mesons. (b) The $(-t', \Delta E)$ correlation for the sample in the selected ω invariant mass region. A small pile-up of exclusive, diffractive production events at small ΔE and $-t'$ can be seen. The lines indicate the applied cuts in the analysis.

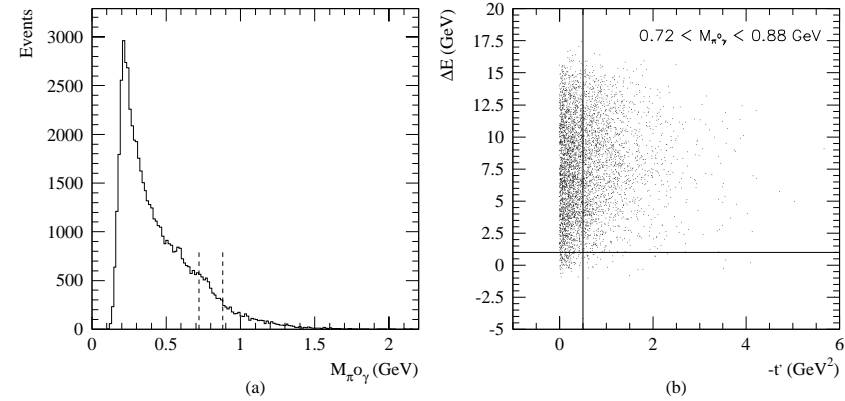


Figure 6.7: (a) The $\pi^0\gamma$ invariant mass distribution where a slight hint of ω production is given by the bump around the expected invariant mass. The dashed lines indicate the invariant mass window used in the analysis. (b) The $(\Delta E, -t')$ correlation for the $\pi^0\gamma$ event sample in the selected ω invariant mass region. The lines indicate the cuts used to select the exclusive, diffractive ω event signal.

ratio into the 3-pion mode [94] (see also paragraph 6.4). Figure 6.6 (b) shows the $(-t', \Delta E)$ correlation for 3-pion decay events in the selected mass range, where again a small pile-up of exclusive, diffractive ω events can be spotted at low $-t'$.

In the case of the ω pion-gamma decay mode one has to examine

$$M_{\pi\gamma} = \sqrt{(p_{\pi^0} + p_{\gamma})^2}, \quad (6.15)$$

which is shown in figure 6.7 (a) giving only a slight hint of ω production in this mode with a shoulder visible around the ω invariant mass. The $(-t', \Delta E)$ correlation for the events in the same ω invariant mass region as for the 3-pion mode is given in figure 6.7 (b).

For both decay modes ω events were in a first step selected using $0.72 < M_{3\pi} < 0.88$ GeV.

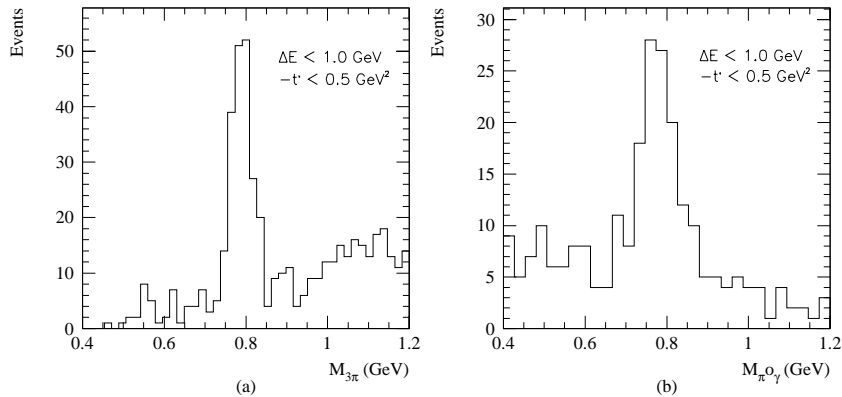


Figure 6.8: The ω invariant mass distribution after application of the exclusive, diffractive event cuts for the 3-pion sample (a) and the $\pi^0\gamma$ event sample (b).

To select exclusive, diffractive ω production in the low momentum transfer region we apply, just like for the ρ^0 analysis, limits on the ΔE and $-t'$ range. In this case however, the cuts are chosen a little wider to be $\Delta E < 1.0$ GeV and $-t' < 0.5$ GeV², which is done for two reasons. First, as can be seen from the plots in figure 6.6 (a) and 6.7 (a) the ω statistics in the samples are much lower than for the ρ^0 , which means we cannot afford as tight cuts here as in the ρ^0 analysis. This will result in a somewhat lower signal-to-background ratio in the exclusive ω sample, but that can be corrected for when needed. Second, as the ω decay modes used in this analysis contain a π^0 , or even a π^0 and a γ , the resolution on e.g. ΔE will be worse. This causes a broader ΔE peak for exclusive ω events as compared to the exclusive ρ^0 case and calls for a wider cut on ΔE . The resulting invariant mass distributions in the ω analysis after the cuts described above are displayed in figure 6.8.

6.2.3 Selection of Quasi-real ω Photoproduction Events

As mentioned in paragraph 3.4.6, a special trigger scheme was implemented in 1996 to detect processes at low Q^2 where the scattered positron disappears along the beam pipe into the gap of the spectrometer and thus cannot generate a standard trigger. The trigger required at least one charged track in each of the detector halves. This imposed the additional geometrical constraint that the minimum angle between the two charged tracks, usually corresponding to decay products of some primary produced hadron, had to be about 80 mrad.

In the ω analysis events were selected containing exactly two charged tracks corresponding to hadrons of opposite charge and two photon clusters associated with the decayed π^0 . A photon energy calibration factor of the same order of magnitude as for the standard trigger data was applied to correct for the difference in the calorimeter response between leptons and photons and for the presence of other overlapping clusters from charged particles as explained before.

In the ω analysis, π^0 mesons were selected by imposing $0.10 < M_{2\gamma} < 0.17$ GeV and $0.02 < \theta_{\gamma_1\gamma_2} < 0.15$ rad, where the latter cut provides additional combinatorial background suppression.

The 3-pion invariant mass distribution for the 1997 ¹H quasi-real photoproduction trigger data is displayed in figure 6.9, where a huge peak corresponding to ω production and a small signal of ϕ production is found near the expected masses. Due to the lack of kinematical event information, it is not possible to select exclusive, diffractive production events or to suppress the combinatorial background underneath the ω resonance.

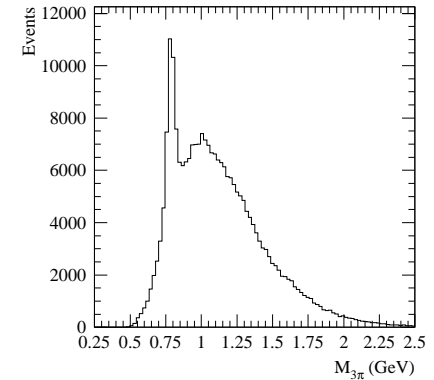


Figure 6.9: The 3-pion invariant mass distribution for the 1997 ¹H photoproduction trigger data. A signal of ω production is seen at the expected mass and also a small indication of ϕ production shows up around 1.02 GeV.

6.3 Addendum 1: Charged ρ Production

The ρ^0 is actually part of an isotriplet, where the other two members are the ρ^+ and ρ^- . As some theoretical interest in terms of OFPD's is attached to the exclusive production of longitudinal ρ^+ (see section 2.10), a signal of charged ρ 's was sought in the HERMES data. The $\rho^{+(-)}$ vector mesons have a nearly 100 % branching ratio into the $\pi^{+(-)}\pi^0$ decay channel [94]. Due to their charge, the exclusive channels for production of both mesons on ^1H differ

$$\gamma^* + p \rightarrow \rho^+ + n, \rho^+ + \Delta^0 \quad (6.16)$$

$$\gamma^* + p \rightarrow \rho^- + \Delta^{++}. \quad (6.17)$$

The reconstructed $\pi^{+/-}\pi^0$ invariant mass distributions extracted from the 1997 ^1H data are shown in figure 6.10 (a,b), where one can see a signal for both mesons around the ρ mass. Events were selected with one positron, one charged hadron and exactly two photons adding up to a neutral pion as described above. Both invariant mass distributions were fitted with a Gaussian signal curve and a third order polynomial background function. The fitted invariant masses were $M_{\rho^+} = 772 \pm 5$ MeV and $M_{\rho^-} = 765 \pm 5$ MeV, compatible with the PDG value [94], with a width of about 60 MeV. Roughly estimated about 1850 ρ^+ and 1250 ρ^- events were contained in the sample, giving a ratio of ρ^+ to ρ^- similar to the observed production ratio of semi-inclusive π^+ to π^- .

The majority of the reconstructed charged ρ mesons came from fragmentation processes. A rough selection of exclusive events could be done using a cut on $\Delta E < 1.0$ GeV as shown in the lower panels of figure 6.10 (a,b). Less than 10 % of the charged ρ events in the original sample satisfied this requirement. For ρ^- however, the exclusive events should appear around⁷ $\Delta E \approx 0.34$ GeV, resulting in a small but visible upward shift in the ΔE distribution as compared to the ρ^+ case. The ratio of the number of exclusive ρ^+ to ρ^- production events was roughly 1.7.

Further analysis on charged ρ mesons was not pursued here, as this was beyond the scope of the present work.

6.4 Addendum 2: η Production

The invariant mass spectrum displayed in figure 6.6 (a) revealed a signal for the pseudoscalar η meson. Just like with vector mesons, the exclusive production of pseudoscalar mesons like π^0 and η can e.g. provide access to OFPD's (see section 2.10). Also the π^0/η production ratio in deep-inelastic scattering offers a nice test of the SU(6) (SU(3) combined with spin) quark model symmetry [101], where the HERMES data are compatible with an SU(6) violating s quark suppression of order $\lambda \approx 1/3$ [102].

Figure 6.11 (a) displays the 3-pion invariant mass distribution for the entire 1997 data set in the η production region. The η resonance, which has a 23.0 ± 0.4 % branching ratio in this mode [94], is fitted with a Gaussian, while the background is described by a 3rd order polynomial. The measured invariant mass was $M_\eta = 550.9 \pm 1.8$ MeV, in agreement

⁷See equation 6.2 with M_x being $M_\Delta \approx 1.232$ GeV [94]

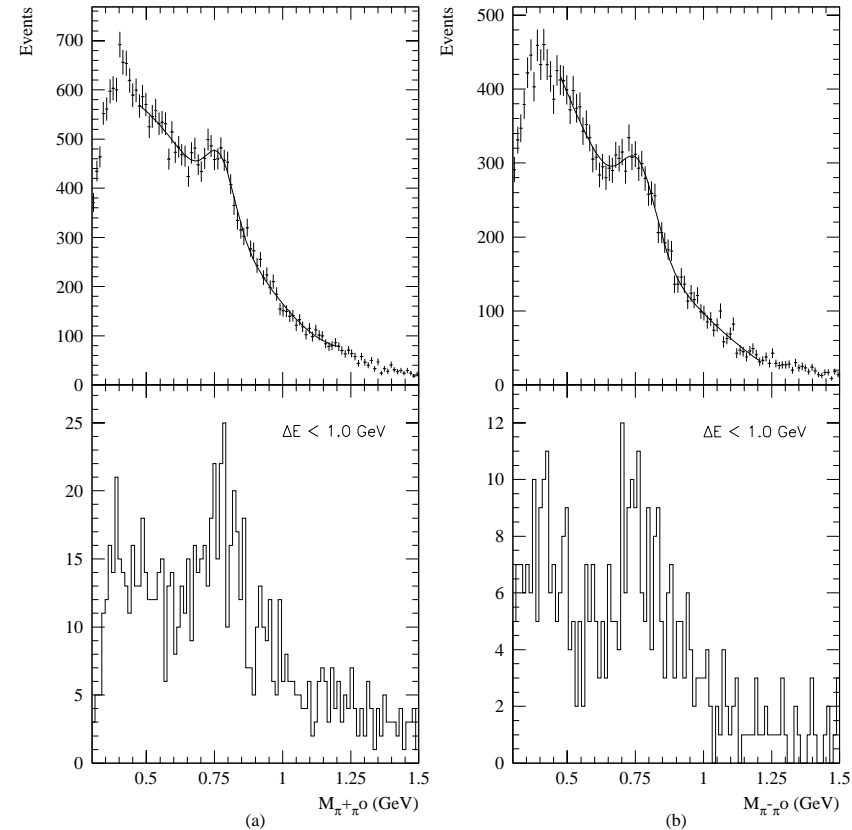


Figure 6.10: The $\pi^+\pi^0$ and $\pi^-\pi^0$ invariant mass distributions with a signal of ρ^+ and ρ^- production in (a) and (b) respectively. The fit in the upper panels is a Gaussian signal curve added to a third order polynomial for the background description. The lower panels have a cut on ΔE to select exclusive events.

with the PDG value of $M_\eta = 547.30 \pm 0.12$ MeV [94]. The width of the resonance was about 14 MeV. The η peak for this decay mode contained roughly 250 events for the entire 1997 data set.

The η meson also has a 39.33 ± 0.25 % branching ratio into the 2-photon mode. Figure 6.11 (b) shows the 2-photon invariant mass for the entire 1997 data set in the η mass region. Additional cuts on the photon energy and the angle between the two photons were applied to suppress the large background diluting the large η signal. The distribution was again fitted with a Gaussian plus 3rd order polynomial, yielding an η mass of $M_\eta = 535 \pm 1$ MeV with the width of the peak being about 38 MeV. The fact that here the η mass is about 10 MeV off the PDG value is due to the additional cuts applied to the distribution distorting the slightly energy dependent calorimeter calibration. The η peak in the figure contained roughly 9000 events obtained from the entire 1997 data set.

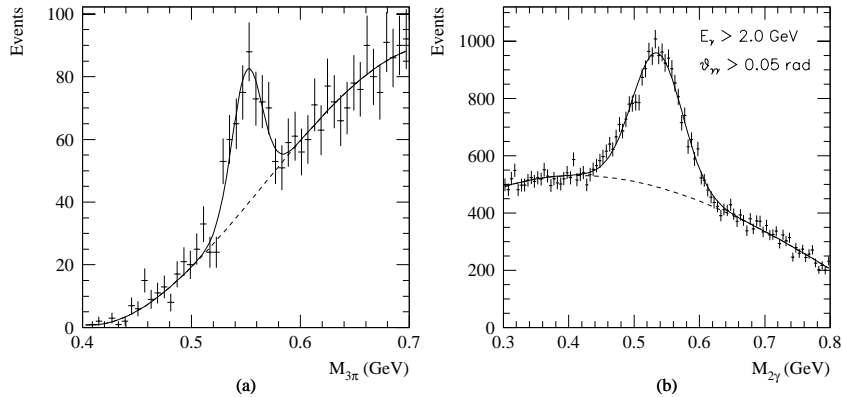


Figure 6.11: Signals in the HERMES data of η production in the 3-pion decay channel (a) and in the 2 photon decay channel (b), where for the latter plot more restrictive cuts were applied to suppress low energy background. Both fits are Gaussians to describe the η resonance plus 3rd order polynomials (dotted lines) to parametrize the background. The plots were generated for the entire 1997 data set.

Figure 6.12 depicts the 1997 2-photon invariant mass distribution with a cut on z , which is the fractional energy of the 2-photon system with respect to the virtual photon $z = E_{2\gamma}/\nu$, removing a large part of low-energy non-exclusive background from the event sample. The figure clearly shows signals of π^0 , η and also ω production. For the latter only one of the two π^0 decay photons in the $\pi^0\gamma$ mode is detected, causing a broadening of the resonance in the distribution.

Also for η production no further analysis of this topic was pursued, as this was beyond the scope of the present work.

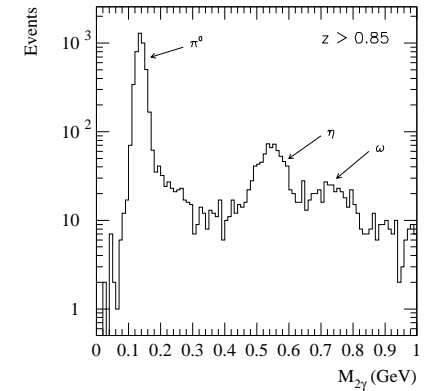


Figure 6.12: The 2-photon invariant mass distribution for the entire 1997 data set with a cut on z to remove a large portion of the low-energy, non-exclusive background events in the sample. Prominent signals of π^0 and η production can be seen and also a hint of exclusive ω production. As the latter meson decays in fact into $\pi^0 + \gamma$, where in this case one of the π^0 decay photons was not included, the invariant mass peak is smeared out.

Chapter 7

Monte Carlo Studies

Most of the results presented in this work rely on the use of Monte Carlo methods. Monte Carlo codes can simulate the scattering processes and the detector geometry and responses. This kind of simulation is usually needed e.g. to compute acceptance or detector smearing corrections to the actual measured data, to make background estimates, to test analysis algorithms or to make predictions for count rates. In this chapter we discuss the vector meson production generators applied in the analysis and compare their predictions with the data. We describe some results and procedures for using Monte Carlo data in the physics analysis, in particular for acceptance corrections and background subtractions.

7.1 The VDM ρ^0 Generator

The Monte Carlo simulations in the ρ^0 analysis were all performed using a generator [103] based on the vector meson dominance model. It applies the commonly used ‘hit and miss’ technique [104] to generate events according to a VDM based cross section with the free variables being Q^2 , the energy of the scattered lepton E' and the azimuthal scattering angle ϕ . The cross section for exclusive, diffractive ρ^0 electroproduction is modelled as

$$\frac{d\sigma}{dQ^2 dE' d\phi} = \frac{1}{2EE'} \Gamma_T(\cos\theta, \phi, E') \sigma_{\gamma^*p}(Q^2), \quad (7.1)$$

where $\sigma_{\gamma^*p}(Q^2)$ represents the virtual photoproduction cross section $\gamma^*p \rightarrow \rho^0p$ and Γ_T the transverse photon flux factor given by

$$\Gamma_T(\cos\theta, \phi, E') = \frac{\alpha}{4\pi^2} \frac{W^2 - M^2}{2M} \frac{1}{Q^2} \frac{E'}{E} \frac{2}{1 - \epsilon}. \quad (7.2)$$

The virtual photoproduction cross section is modelled with a VDM-like Q^2 -dependence

$$\sigma_{\gamma^*p}(Q^2) = \frac{1}{(1 + Q^2/M^2)^2} \sigma_{\gamma p}, \quad (7.3)$$

where the real photoproduction cross section $\sigma_{\gamma p} = \sigma_{\gamma^*p}(Q^2 = 0)$ is given by

$$\sigma_{\gamma p}(Q^2 = 0) = A_\gamma \frac{2M}{W^2 - M^2} + B_\gamma, \quad (7.4)$$

with $A_\gamma = 29.4 \mu\text{b-GeV}$ and $B_\gamma = 9.5 \mu\text{b}$ as determined from a fit to the data given in reference [105]. To speed up the sample-and-reject method, the sampling of high Q^2 events, where the cross section becomes relatively low, is somewhat suppressed by generating events uniformly in a variable K given by e.g. $K \propto (1/Q^2)^2$, rather than in Q^2 itself.

The invariant mass was generated according to a skewed Breit-Wigner distribution (see also section 8.1.4)

$$\frac{dN}{dM_{2\pi}} \propto \frac{M_{2\pi} \Gamma_\rho M_\rho}{(M_{2\pi}^2 - M_\rho^2)^2 + M_\rho^2 \Gamma_\rho^2} \left(\frac{M_\rho}{M_{2\pi}} \right)^{n_{\text{skew}}}, \quad (7.5)$$

where the skewing parameter $n_{\text{skew}} = 2$ and $\Gamma(M_{2\pi})$ is given by

$$\Gamma(M_{2\pi}) = \Gamma_0 \left(\sqrt{\frac{M_{2\pi}^2 - 4M_\pi^2}{M_\rho^2 - 4M_\pi^2}} \right)^3 \frac{M_\rho}{M_{2\pi}}, \quad (7.6)$$

with $\Gamma_0 = 0.1507 \text{ GeV}$ and $M_\rho = 0.7700 \text{ GeV}$, the ρ^0 width and mass [94].

The forward diffractive peak of the cross section as function of t' was modelled according to

$$\frac{dN}{dt'} \propto e^{-b|t'|}, \quad (7.7)$$

with $b = 6.0 \text{ GeV}^{-2}$ following the data in [105].

The generation of the decay angular distributions was implemented in several ways where the user can choose the desired method. One model assumes s -channel helicity conservation and natural parity exchange in the t -channel. The decay angles are then generated according to

$$\frac{dN}{d\cos\theta d\Psi} \propto 2\epsilon R \cos^2\theta + \sin^2\theta(1 + \epsilon \cos 2\Psi) - \sqrt{2\epsilon R(1 + \epsilon)} \cos\delta \sin 2\theta \cos\Psi. \quad (7.8)$$

The ratio $R = \sigma_L/\sigma_T$ is computed according to $R = \frac{1}{2} \frac{r_{00}^{04}}{1 - r_{00}^{04}}$, where the matrix element is given by $r_{00}^{04} = 0.28015(Q^2)^{0.45080}$ as taken from [106]. In another scenario, one can generate the decay angles according to the full blown equation 2.126. In that case all 23 SDME and the beam polarization have to be given by the user as input. A third possibility exists where the decay angles are simply isotropically generated.

Some more information on the generator can also be found in [107].

7.2 The DIPSI Generator

The DIPSI generator [108] is based on the Ryskin model as described in section 2.12.1. It simulates the process of exclusive vector meson production ($\rho, \phi, \omega, J/\Psi, \dots$) via pomeron

exchange. The Ryskin model assumes that the virtual photon fluctuates into a $q\bar{q}$ pair which then interacts with the proton via a gluon ladder. The kinematical dependence of the model on W and t can be fixed by providing the strong coupling constant α_s , the two-gluon proton form factor and the gluon momentum density in the proton.

The generator uses input data cards to allow the user to set some options or parameters, like the lepton beam type (electron¹, muon), lepton and proton beam momenta, kinematical limits, the type of vector meson, its decay mode and invariant mass distribution, α_s , the proton gluon density and the proton form factor. The 2-gluon form factor of the proton can be set to a dipole shape or to an exponential one. The gluon density can be defined by the user or may be taken from the PDFLIB [109].

DIPSI is a weighted generator, meaning that each event is assigned a weight equal to its cross section. This has two main advantages. First of all, kinematical regions where the cross section is rather low can be easily populated by generating events according to a more uniform distribution then the cross section. Each event gets a weight according to the cross section together with a correction factor to account for the way in which the kinematical variables were generated. Second, if desired by the user, one can reweight every event to implement some modifications to the cross section model, e.g. a different gluon density or slope parameter, without having to redo the entire event generation. The use of an event weight has some implications on the error analysis. The statistical error on a sum $n = \sum_{i=1}^N w_i$ of N weighted events with weight w_i is given by

$$\delta n = \sqrt{\sum_{i=1}^N w_i^2}. \quad (7.9)$$

One can define an equivalent number of events \tilde{n} , which is the number of unweighted events having the same relative error as the weighted sum $\delta\tilde{n}/\tilde{n} = \delta n/n = 1/\sqrt{\tilde{n}}$

$$\tilde{n} = \frac{(\sum_i w_i)^2}{\sum_i w_i^2}. \quad (7.10)$$

The generator includes the decay angular distributions according to the s -channel helicity conservation assumption. We added an extra feature to the generator enabling the user, if needed, to generate events with isotropic decay distributions.

7.3 Data to Monte Carlo Comparison

Both generators described above were linked to the HERMES Monte Carlo code as described in paragraph 5.5 to be able to feed the generated event samples through the HERMES detector simulation and through the reconstruction software chain. The statistical precision of a useful Monte Carlo event sample should be at least of the same order of magnitude or preferentially much higher than that of the measured data sample, so that the statistical uncertainty of the generated sample is negligible as compared to that of the data. A full simulation of the experiment however, requires a large amount of

¹The charge of the lepton does not play a role here.

CPU time to perform all the necessary particle tracking and digitization of the detector responses. Moreover, such a simulation also takes up an enormous amount of disk space to store all the event, tracking and digitized detector information. To limit the amount of needed disk space and CPU time, the event generation could be done on two separate levels : generation in 4π solid angle and generation inside a geometrical box. The event generation in 4π was done without interfacing to HMC, while the generation inside the box was coupled to HMC afterwards. The box was chosen to match the HERMES spectrometer acceptance as much as possible where however, the outer geometrical limits were taken to be somewhat wider than the ones of the actual detector to avoid any fake edge effects due to the introduction of such an intermediate, artificial box geometry. The box model imposed the following criteria :

- All particles had to have a positive momentum in the z -direction and an energy of at least 0.5 GeV. In case of a standard trigger event simulation, the scattered positron had to have an energy of at least 3.5 GeV corresponding to the calorimeter threshold for the trigger.

- All particles (charged particles and photons) were required to satisfy

$$\arctan \left| \frac{p_x}{p_z} \right| < 180 \text{ mrad}, \quad 38 \text{ mrad} < \arctan \left| \frac{p_y}{p_z} \right| < 180 \text{ mrad} \quad (7.11)$$

- Low momentum charged particles will be deflected quite heavily by the spectrometer dipole magnet and some of them can even be kicked out of the backward detector acceptance. The influence of the magnetic field on the acceptance was taken into account by requiring that charged particles with momenta less than 4 GeV hit the calorimeter leading to

$$p > \frac{(z_{calo} - z_{magnet}) \int B dl}{w_{calo} + z_{calo} \frac{p_x}{p_z}}, \quad (7.12)$$

where $z_{calo} = 720$ cm and $z_{magnet} = 272.5$ cm are the positions in the z -direction of the calorimeter and the spectrometer magnet, $w_{calo} = 180$ cm is the half-width of the calorimeter and $\int B dl = 0.40$ GeV is the spectrometer magnet field integral²

Figure 7.1 and 7.2 show a comparison between measured data on ^1H and Monte Carlo simulated kinematical distributions for exclusive ρ^0 and ω production respectively. The ρ^0 events were generated using the VDM generator, while the ω events were simulated with DIPSI. Both event samples were generated in the geometrical box and then fed through HMC and the entire reconstruction and offline analysis chain. In both cases the Monte Carlo generators gave a good description of the measured data distributions.

7.4 Acceptance and Reconstruction Efficiency

Each event generated in a 4π solid angle was checked to see whether it was contained in the geometrical box or not and was marked accordingly. This defined an acceptance

²The magnetic field integral is actually 1.3 T-m=0.39 GeV. However here, this value was treated as an effective parameter and was optimized [110] to match the data using equation 7.12.

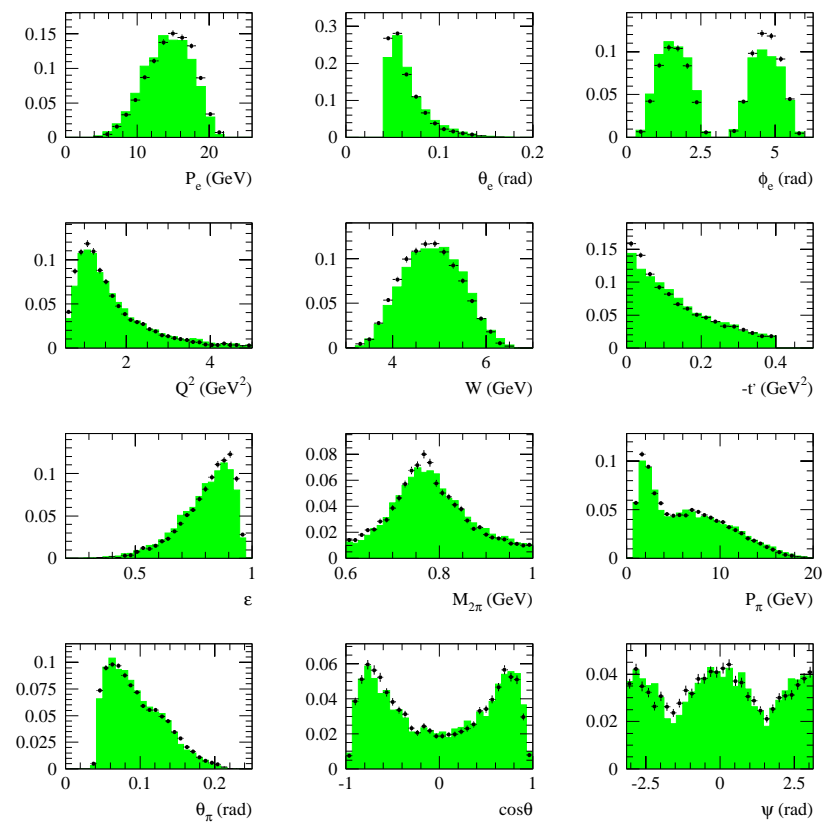


Figure 7.1: Comparison of the VDM Monte Carlo generated ρ^0 events with the measured data on ^1H as a function of several kinematical variables. The histograms are the results of the simulation, the dots represent the ρ^0 data. To facilitate the comparison all the distributions were normalized to unity.

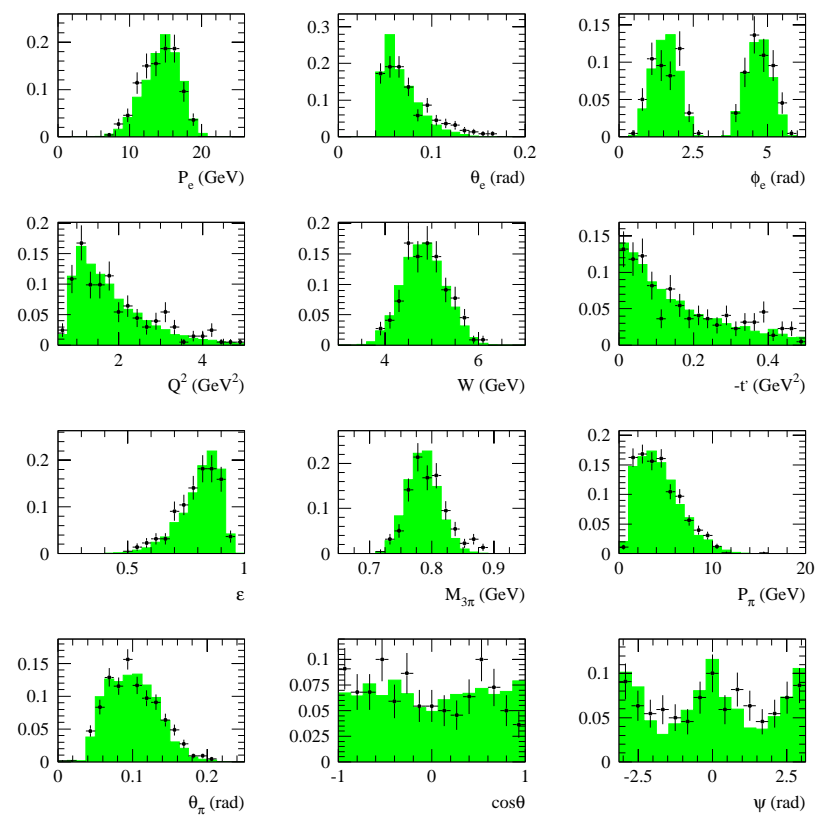


Figure 7.2: Comparison of the DIPSI Monte Carlo generated ω events with measured data on ^1H as a function of several kinematical variables. The histograms are the results of the simulation, the dots represent the ω data. To facilitate the comparison all the distributions were normalized to unity.

for 4π events going to the box geometry. In a second step, where events were generated inside the box geometry and then fed through HMC, the reconstruction code and the offline analysis chain, another acceptance could be defined for ‘box’ events going to the HERMES spectrometer. The final acceptance to be used in the analysis, is the product of the latter two. This acceptance value not only accounts for the detector geometry, but also for the reconstruction efficiencies, detector smearing and offline analysis cuts. The acceptance in a particular kinematical bin was computed according to

$$\epsilon = \frac{\sum_{acc} w_i}{\sum_{gen} w_i}, \quad (7.13)$$

where the summation runs over the event weights w_i of all accepted and generated events³ in the considered bin. The statistical error on the acceptance is given by [111]

$$\sigma_\epsilon = \frac{\sqrt{\sum_{gen} w_i^2 \cdot \epsilon \cdot (1 - \epsilon)}}{\sum_{gen} w_i}. \quad (7.14)$$

Results for the computed acceptance as function of different kinematical variables for ρ^0 and ω production will be given later on in this work.

7.5 Resolution

The Monte Carlo generators can be used to determine the experimental resolution on all kinematical variables. The absolute deviation between the generated and reconstructed value for some of the inclusive event kinematics as determined with the VDM generator is shown in figure 7.3. The resolution on the energy transfer ν is driven by the measurement of the scattered lepton momentum via the tracking through the spectrometer magnet. The energy transfer tends to be a little overestimated, which is due to energy loss of the lepton while travelling through the detector. The resolution on the photon virtuality Q^2 is somewhat worse as there also the scattering angle determined from the tracking comes in. The effect of additional energy of the scattered lepton in the detector results in this case in an underestimation of Q^2 . As x and W are determined from Q^2 and ν , their resolutions are correlated to the ones of the latter two variables.

Fitting a Gaussian shape to the relative deviation between the generated and reconstructed variables gives relative resolutions on ν , Q^2 , x and W of about 2 %, 2.5 %, 4 % and 1 % respectively.

Figure 7.4 shows the absolute resolution for some of the relevant exclusive ρ^0 and ω event kinematics as obtained using the VDM and DIPSI generators. The resolution on the 2-pion invariant mass is determined by the measurement of two charged pion tracks, while for the 3-pion invariant mass one includes on top of that a large contribution from the π^0 whose 2-photon decay is detected by the calorimeter. The detection of the third pion in the ω analysis also results in a worse resolution on ΔE as compared to the ρ^0 analysis. The resolution on $|t'|$ turns out to be similar for both vector meson channels, indicating that it is dominated by the resolution on inclusive variables.

³For an unweighted Monte Carlo generator the weights are to be taken equal to 1.

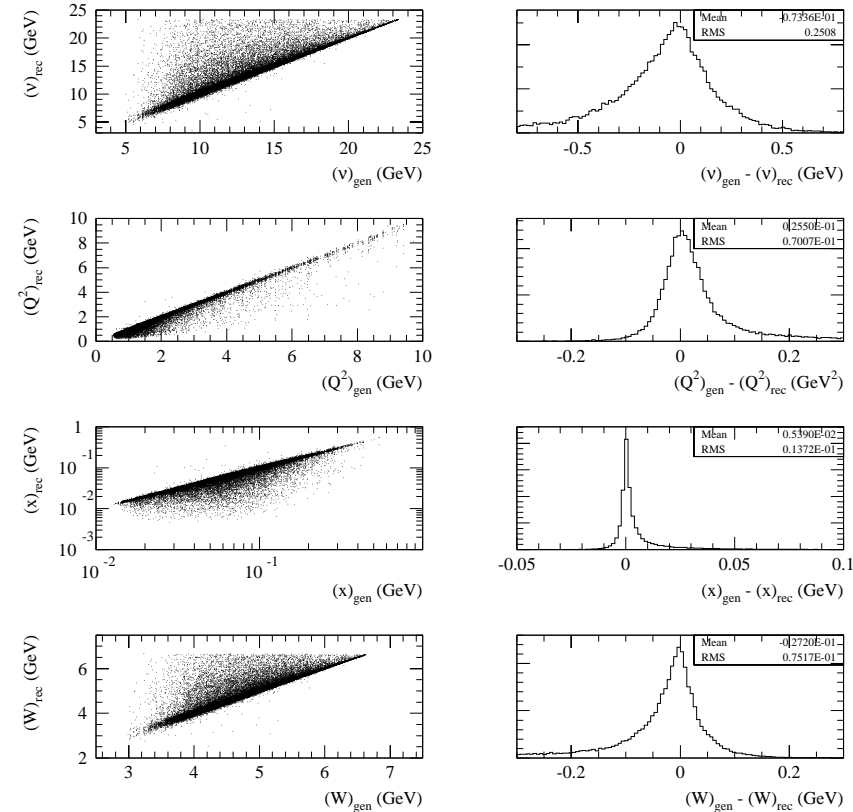


Figure 7.3: The obtained resolution on the most common inclusive event kinematics determined from the scattered lepton.

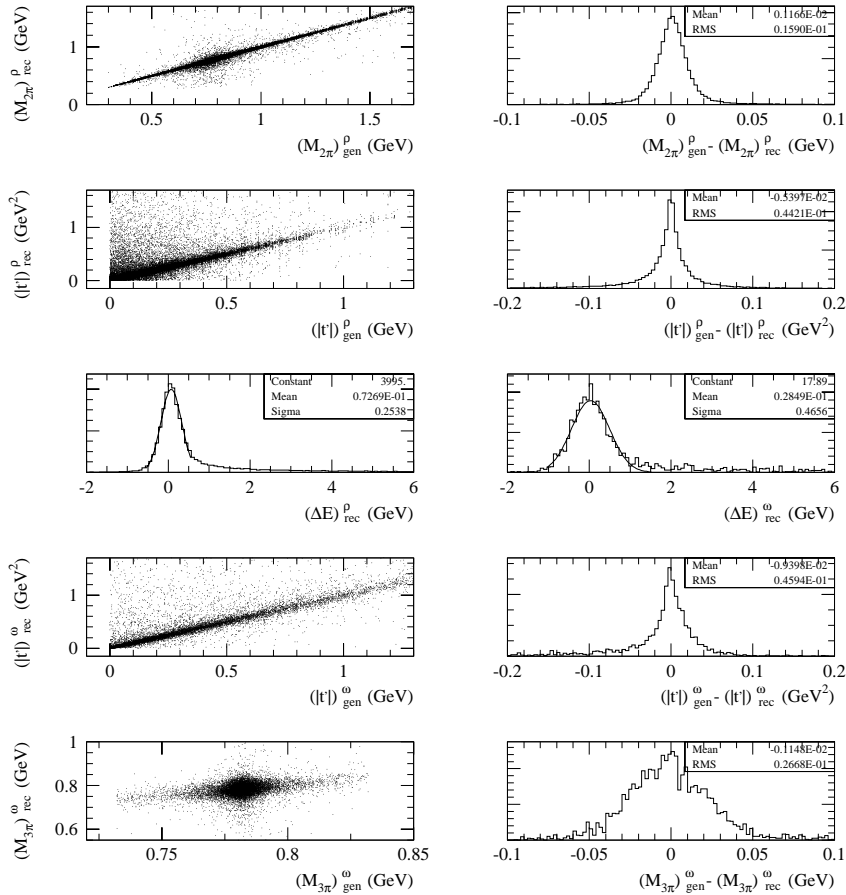


Figure 7.4: The obtained resolution on the relevant event kinematics for exclusive ρ^0 (first five plots) and ω (last five plots) production. Note that the ω plots were made with a weighted Monte Carlo, which may distort the correlation scatter plots somewhat. The reconstructed ΔE distributions were fitted with a Gaussian to estimate the resolution.

Note that in the generators used to compute the resolutions presented above no radiative corrections were applied, which results in slightly overoptimistic values compared to the ‘true’ resolutions.

7.6 Monte Carlo DIS Background Studies

When studying a particular physics channel, one always has to think about possible sources of background diluting the signal. Whenever possible one should try to estimate the amount of background and correct the results accordingly. Here we are looking into exclusive, diffractive production of vector mesons. The most important background contamination in that case comes from deep-inelastic scattering fragmentation events. To correct the signal this deep-inelastic scattering (DIS) background was estimated with a Monte Carlo simulation based on the LEPTO generator (see section 5.5). The generated event sample contained hadrons from fragmentation processes (which also includes hadrons from non-diffractive vector meson production events). No generation of exclusive, diffractive vector meson production was included. The generated event sample was tracked through the GEANT simulation of the detector, reconstructed and subjected to the same offline analysis procedure as the measured data.

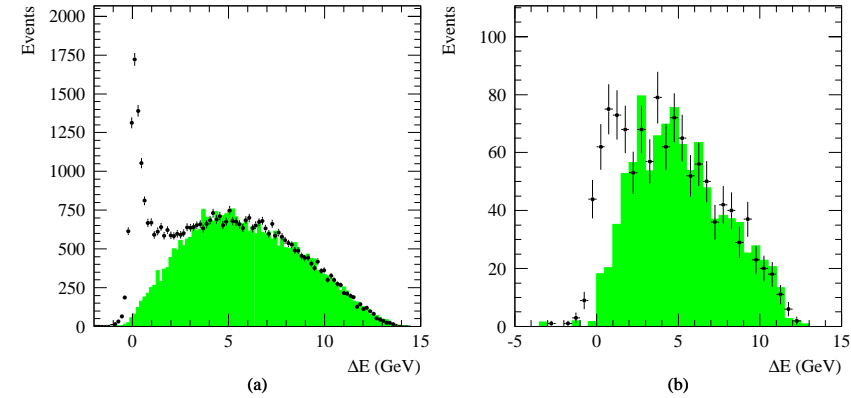


Figure 7.5: Estimation of the DIS background to the exclusive, diffractive (a) ρ^0 and (b) ω signal with the DIS Monte Carlo using the ΔE distribution. The Monte Carlo ΔE distributions (histograms) are normalized to the data (dots) in the region $\Delta E > 3.0$ GeV. These normalized distributions then provide the amount of background in the ΔE region of the exclusive signals.

As was explained in section 6.2.2 the variable ΔE was used as a measure of the exclusivity of the events : exclusive events have $\Delta E \approx 0$ GeV, while DIS events appear at higher ΔE values. The shape of the measured ΔE distribution outside the region of

the peak corresponding to exclusive events, should in principle be described well by a DIS Monte Carlo simulation. A Monte Carlo simulated sample obviously has to be normalized to the measured data. This should be done outside the exclusive, diffractive region where the Monte Carlo data is expected to match the measured data. Figure 7.5 shows the ΔE spectra of the measured ρ^0 and ω data on ^1H together with the obtained Monte Carlo distributions for the background events. Both the data and Monte Carlo event samples have all cuts used in the exclusive, diffractive analysis except the cut on ΔE . The latter distributions were normalized to the measured data in the ΔE region above 3.0 GeV. In both cases the Monte Carlo generator clearly gave a suitable description of the DIS background in the measured event samples.

Chapter 8

ρ^0 and ω Invariant Mass Distribution

In this chapter the ρ^0 and ω invariant mass distributions are presented. The ρ^0 invariant mass distribution first needs a correction for acceptance effects and for possible background contributions, e.g. from deep-inelastic scattering fragmentation processes. The final distribution is fitted with several different parametrizations which can account for the observed skewing and for $\rho^0 - \omega$ interference effects. The Q^2 -dependence of the Ross-Stodolsky and Söding lineshape for the ρ^0 is measured.

8.1 ρ^0 Invariant Mass Distribution

After applying all off-line cuts as described in section 6.2, the invariant mass distribution $M_{2\pi}$ was obtained as shown in figure 8.1 for the ρ^0 candidate events. The data were selected in the W range between 4.0 and 6.0 GeV and Q^2 between 0.7 and 5.0 GeV². No dependence of the invariant mass distribution on the target mass A was seen when no distinction was made between coherent and incoherent scattering events¹. The data shown in the plot were therefore summed over all data sets for the different targets and data-taking years considered in this analysis.

This distribution has to be corrected for DIS background events and for possible contamination by other meson decay channels, e.g. from the ω or ϕ meson. Unlike the ω or ϕ vector meson, the ρ^0 is a relatively wide resonance, which makes an acceptance correction as a function of invariant mass necessary. One should also consider a possible mass-dependence of the width of the resonance.

¹Very preliminary studies performed after the completion of this work indicate that the ρ^0 resonance peak for coherent scattering events on a composite target may have a somewhat smaller width compared to the peak for incoherent production events. However, this finding requires more study to be confirmed and the effect it would have on the results presented in this chapter is negligible.

8.1.1 Background Treatment

The amount of contamination in the ρ^0 invariant mass distribution due to deep-inelastic scattering fragmentation events was estimated with the DIS Monte Carlo method as described in section 7.6. The Monte Carlo background distribution was scaled according to the measured signal-to-background ratio and subtracted from the data, where the statistical error on the Monte Carlo distribution was taken into account. For the studies of kinematical dependence of the invariant mass distribution, this background correction was done for each kinematical bin individually. The estimated background contribution for the invariant mass distribution at average kinematics is shown in figure 8.1.

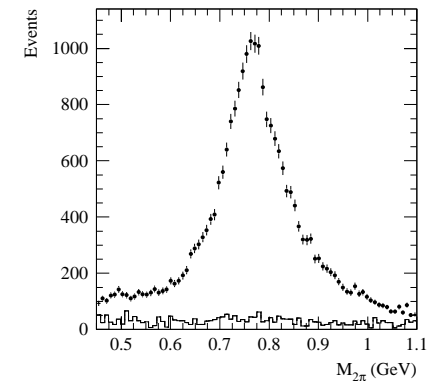


Figure 8.1: The 2-pion invariant mass distribution. The dots represent the measured distribution summed over all 1995-97 data sets. The histogram is the Monte Carlo estimated background contribution from deep-inelastic scattering fragmentation events.

The ρ^0 signal can also receive contributions from the two other light vector mesons, the ω and the ϕ , which both have decay modes containing two oppositely charged hadrons. The ω meson has two main decay channels which can contribute to the ρ^0 event sample

$$\omega \rightarrow \begin{cases} \pi^+ + \pi^- + \pi^0 & (88.8\%) \\ \pi^+ + \pi^- & (2.21\%), \end{cases} \quad (8.1)$$

while the ϕ meson could contribute via three different channels

$$\phi \rightarrow \begin{cases} K^+ + K^- & (49.1\%) \\ \rho + \pi & \\ \pi^+ + \pi^- + \pi^0 & (15.5\%). \end{cases} \quad (8.2)$$

To estimate the amount of contamination these branching ratios have to be folded with the $\rho^0 : \omega : \phi$ cross section ratio, which is here taken to be roughly 1 : 0.20 : 0.075 in the

HERMES energy region. This makes the ω 3-pion channel the largest possible background source. This type of background was examined by performing a ρ^0 -like analysis on a $\omega \rightarrow 3\pi$ sample generated with the DIPSI generator. The reconstructed $M_{2\pi}$ -distribution for ω events turns out to be centered around about 0.45 GeV with a Gaussian width of about 0.075 GeV. This means that the majority of these events is outside the relevant ρ^0 invariant mass window. Moreover, the tight cut on ΔE (and $-t'$) in the ρ^0 analysis effectively suppresses the entire $\omega \rightarrow 3\pi$ background completely. The ω 2-pion decay mode is however indistinguishable from the ρ^0 events and is therefore kept in the sample. This contribution actually produces a visible $\rho^0 - \omega$ interference effect (see paragraph 8.1.6). The ϕ 2-kaon decay channel is removed entirely by the M_{2K} cut used in the ρ^0 analysis. The remaining ϕ 3-pion and $\rho\pi$ decay mode can also be safely neglected. In view of the considerations made above, no additional corrections for ω or ϕ contributions were made.

8.1.2 ρ^0 Invariant Mass Acceptance

The acceptance for the ρ^0 invariant mass as determined using the VDM generator is depicted in figure 8.2 (a). The error bars reflect the statistical precision of the Monte Carlo simulation. The acceptance function shows an enhancement at lower invariant mass corresponding to a smaller opening angle between the two decay pions. This effect, combined with the rapid decrease of the cross section for higher invariant mass, results in the observed bump at the left side of the ρ^0 resonance peak in figure 6.4.

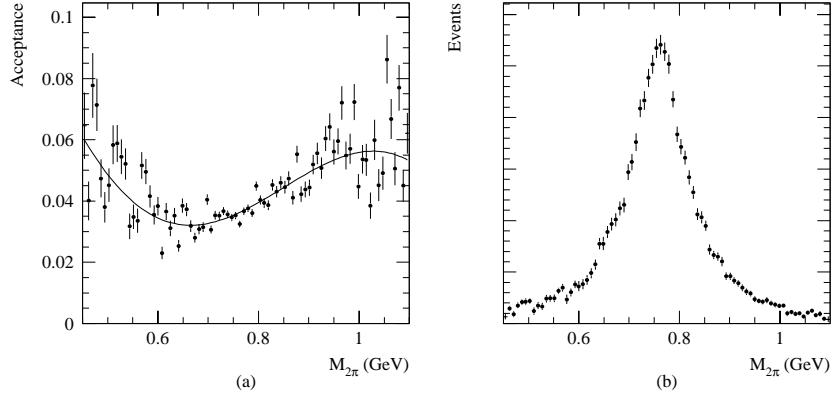


Figure 8.2: (a) The ρ^0 invariant mass acceptance as computed with the VDM Monte Carlo generator. The acceptance was parametrized with a 5th order polynomial function. (b) The final 2-pion invariant mass distribution after the Monte Carlo background subtraction and acceptance correction.

To avoid too much distortion of the shape of the data due to fluctuations in the Monte

Carlo acceptance distribution, the acceptance correction was smoothed with a simple 5th order polynomial function which is also shown in figure 8.2 (a). The resulting function was used to correct the data distribution, leading to the spectrum shown in figure 8.2 (b). No errors on the acceptance correction were taken into account.

8.1.3 The Breit-Wigner Lineshape

The simplest function to fit to a resonance is a non-relativistic Breit-Wigner curve given by

$$\frac{dN}{dM_{2\pi}} = \frac{\Gamma_\rho}{4(M_\rho - M_{2\pi})^2 + \Gamma_\rho^2}. \quad (8.3)$$

Here M_ρ and Γ_ρ represent the mass and the width of the ρ^0 resonance.

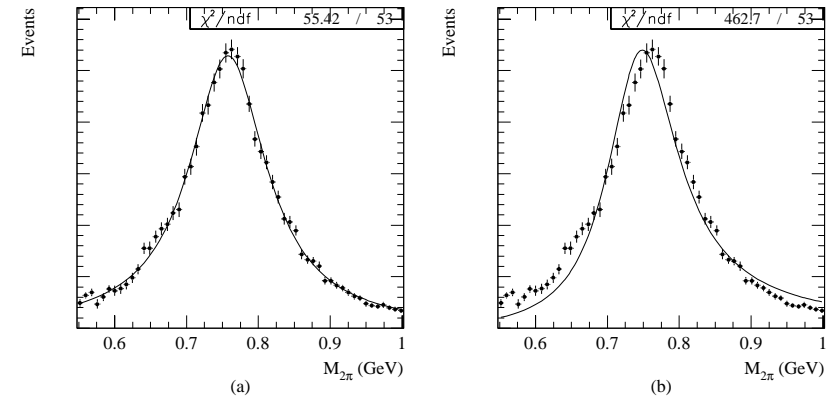


Figure 8.3: The 2-pion invariant mass distribution fitted with (a) a non-relativistic Breit-Wigner curve given by equation 8.3 and (b) a relativistic p -wave Breit-Wigner function given by equation 8.4.

However, at high energy one often uses [112, 113] a relativistic p -wave Breit-Wigner shape describing a spin-1 object decaying into two spin-0 objects

$$\frac{dN}{dM_{2\pi}} \equiv BW(M_{2\pi}) = \frac{2}{\pi} \frac{M_{2\pi} M_\rho \Gamma(M_{2\pi})}{(M_\rho^2 - M_{2\pi}^2)^2 + M_\rho^2 \Gamma^2(M_{2\pi})}. \quad (8.4)$$

Here the width of the resonance $\Gamma(M_{2\pi})$ is energy dependent as given by lowest order perturbation theory for a $J^P = 1^- \rightarrow 0^-0^-$ particle decay [112]

$$\Gamma(M_{2\pi}) = \Gamma_\rho \left(\frac{q}{q_0}\right)^{2l+1} \frac{M_\rho}{M_{2\pi}}, \quad (8.5)$$

with $l = 1$ for the p -wave Breit-Wigner. q is the decay pion momentum in the $\pi^+\pi^-$ center of mass frame and q_0 is the value of q for $M_{2\pi} = M_\rho$

$$q = \frac{\sqrt{M_{2\pi}^2 - 4M_\pi^2}}{2}, \quad q_0 = \frac{\sqrt{M_\rho^2 - 4M_\pi^2}}{2}. \quad (8.6)$$

Note that other parametrizations for the width of the resonance exist in literature [115, 116, 105]

$$\Gamma(M_{2\pi}) = \Gamma_\rho \left(\frac{q}{q_0}\right)^3 \frac{2}{1 + (q/q_0)^2}, \quad (8.7)$$

$$\Gamma(M_{2\pi}) = \Gamma_\rho \left(\frac{q}{q_0}\right)^3. \quad (8.8)$$

The first one is an empirical width proposed in [114]

The lowest χ^2 -values were obtained when using equation 8.5 or equation 8.7 as the parametrization for the width of the resonance, while equation 8.8 always gave the worst results. For the fits presented in the following paragraphs equation 8.7 will be used to describe the resonance width.

Figure 8.3 shows the results of the Breit-Wigner fits to the 2-pion invariant mass distribution. The free parameters were M_ρ and Γ_ρ . The results of the fit are listed in table 8.1. The non-relativistic Breit-Wigner (equation 8.3) gave a satisfactory result. However, the mass and width of the resonance were far off the PDG values given in table 6.4. The relativistic p -wave Breit-Wigner function (equation 8.4) was completely unable to describe the 2-pion invariant mass distribution. Including additional arbitrary functions to describe other possible background effects did not improve the quality of the fit. This result clearly shows that the 2-pion invariant mass around the ρ^0 resonance region is skewed as compared to a simple relativistic Breit-Wigner shape. One sees an enhancement of events on the low mass side, while the high mass side seems to be suppressed.

8.1.4 The Ross-Stodolsky Lineshape

As was shown in the previous paragraph, the relativistic Breit-Wigner shape could not describe the data very well. To account for the observed skewing, the following parametrization was proposed in a phenomenological model by Ross and Stodolsky [117]

$$\frac{dN}{dM_{2\pi}} = BW(M_{2\pi}) \left(\frac{M_\rho}{M_{2\pi}}\right)^{n_{skew}}. \quad (8.9)$$

Here n_{skew} is the skewing parameter. Their model predicted $n_{skew} = 4$ for ρ^0 photoproduction, however, as will be discussed in paragraph 8.1.7, this skewing parameter turns out to be Q^2 - and t -dependent.

The result of the fit of equation 8.9 to the 2-pion invariant mass distribution is shown in figure 8.4. The free parameters were M_ρ , Γ_ρ and n_{skew} , and the fitted values are given in table 8.1. Clearly this skewed shape provides a much better description of the data as compared to the simple Breit-Wigner curve.

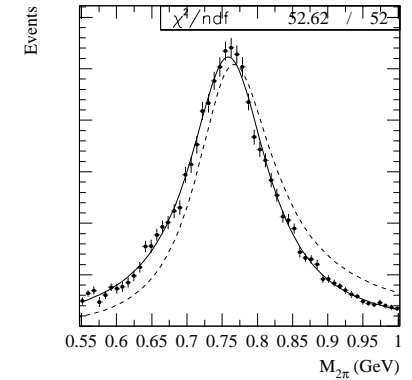


Figure 8.4: The 2-pion invariant mass distribution fitted with the Ross and Stodolsky parametrization given by equation 8.9. The dashed line represents the contribution of the Breit-Wigner.

8.1.5 The Söding Lineshape

Another phenomenological approach to the apparent ρ^0 mass shift problem was made by Söding [118]. There the skewing was explained as an interference effect between resonant ρ^0 production and $\pi\pi$ Drell-type background processes [119] in which a virtual photon diffractively scatters on the target as shown in figure 8.5.

This non-resonant background has an amplitude proportional to the pion-proton cross section $\sigma_{\pi p}$ and can actually be used to estimate the size of this cross section at high energies above the region of the existing direct measurements [120]. This background also leads to a nontrivial dependence of the ratio $R = \sigma_L/\sigma_T$ on the 2-pion invariant mass $M_{2\pi}$, where the variation becomes less steep for higher Q^2 [120]. Note that in the experimental data this type of background cannot be distinguished from the exclusive resonant ρ^0 production diagram and thus cannot be subtracted from the signal like e.g. the DIS background.

The invariant mass distribution parametrization often used to take this interference into account was [121, 116, 122]

$$\frac{dN}{dM_{2\pi}} = A_{reso} BW(M_{2\pi}) + A_I I(M_{2\pi}) + A_{nr}, \quad (8.10)$$

where we have a sum of a contribution A_{reso} of resonant ρ^0 production with a Breit-Wigner shape, a contribution A_{nr} of non-resonant pion pair production and a contribution A_I of

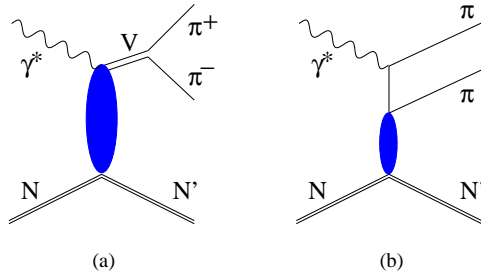


Figure 8.5: Diagrams of (a) resonant vector meson (ρ^0) production and (b) non-resonant $\pi^+\pi^-$ pair production.

the interference between the two processes given by

$$I(M_{2\pi}) = \frac{M_\rho^2 - M_{2\pi}^2}{(M_\rho^2 - M_{2\pi}^2)^2 + M_\rho^2 \Gamma^2(M_{2\pi})}. \quad (8.11)$$

Note that the non-resonant term is expected to give a smooth and rather flat background and was here taken to be constant. No constraints were imposed on the relative normalization between the different terms in equation 8.10. However, the normalization constants were all restricted to positive values. Here the ratio of the interference to the resonant normalization constant A_I/A_{reso} , in units of GeV, is taken as the measure of the skewing of the ρ^0 peak.

Figure 8.6 (a) shows the result of the fit to the 2-pion invariant mass spectrum with equation 8.10. Free parameters were M_ρ , Γ_ρ , A_{reso} , A_I and A_{nr} . Table 8.1 gives the fitted values. The fit looks reasonable, but the χ^2 -value was somewhat higher than for the Ross and Stodolsky fit. The non-resonant background contribution was negligible. Removing this term from the fits did not change any of the other parameters or the χ^2 of the fit.

The fit using equation 8.10 leaves the interference term independent of the resonant and non-resonant terms. This is not really physically correct as the two diagrams in figure 8.5 should be added coherently. Therefore, the following fit function was preferred over equation 8.10

$$\begin{aligned} \frac{dN}{dM_{2\pi}} &= \left| A_{reso} \frac{\sqrt{M_{2\pi} M_\rho \Gamma(M_{2\pi})}}{M_{2\pi}^2 - M_\rho^2 + i M_\rho \Gamma(M_{2\pi})} + A_{nr} \right|^2, \\ &= A_{reso}^2 \frac{M_{2\pi} M_\rho \Gamma(M_{2\pi})}{(M_{2\pi}^2 - M_\rho^2)^2 + M_\rho^2 \Gamma^2(M_{2\pi})} \\ &\quad + 2A_{reso}A_{nr} \frac{\sqrt{M_{2\pi} M_\rho \Gamma(M_{2\pi})} (M_{2\pi}^2 - M_\rho^2)}{(M_{2\pi}^2 - M_\rho^2)^2 + M_\rho^2 \Gamma^2(M_{2\pi})} + A_{nr}^2, \end{aligned} \quad (8.12)$$

where the non-resonant amplitude A_{nr} was taken to be constant and real. In this case the skewing of the ρ^0 resonance is determined by the ratio of the non-resonant to the resonant

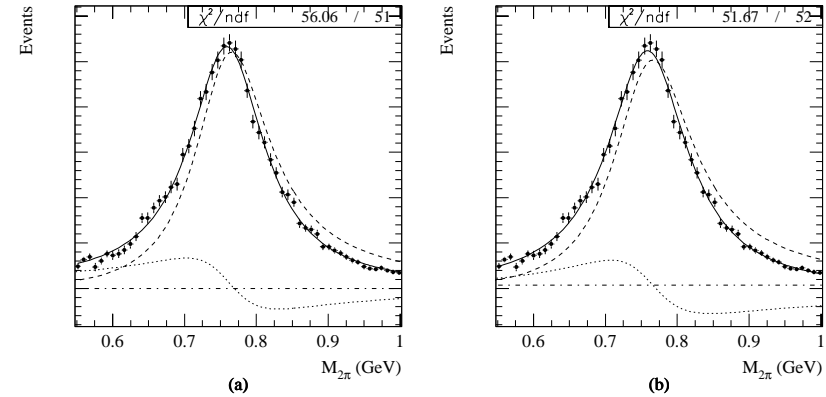


Figure 8.6: The 2-pion invariant mass distribution fitted with the Söding parametrization as given by (a) equation 8.10 and (b) equation 8.12. The dashed lines give the Breit-Wigner contributions, the dotted lines represent the interference terms and the dash-dotted lines show the non-resonant parts.

contribution $|A_{nr}/A_{reso}|$, expressed in units of $\text{GeV}^{-1/2}$. When comparing equation 8.12 to equation 8.10, one expects the value for $|A_{nr}/A_{reso}|$ to be roughly a factor 2 higher than the corresponding A_I/A_{reso} ratio.

The result of the fit using equation 8.12 is presented in figure 8.6 (b). The values of the fitted free parameters M_ρ , Γ_ρ , A_{reso} and A_{nr} are listed in table 8.1. Using equation 8.12 instead of 8.10 to fit the invariant mass distribution clearly resulted in a better χ^2 value. Modifying A_{nr} in equation 8.12 to $A_{nr}e^{i\alpha}$ to account for a possible phase difference between the two processes did not improve the quality of the fit or change the other parameters. Moreover, the fitted value of α was compatible with zero in support of our initial assumption that the non-resonant amplitude is real. One also notices from figure 8.6 that the non-resonant contribution is no longer negligible as was the case for the fit using equation 8.10.

8.1.6 ρ^0 - ω Interference

The ω meson (isospin 0) has a G -parity violating decay mode into a $\pi^+\pi^-$ pair (isospin 1) with a branching ratio of 2.21 ± 0.30 %. As the ω has a mass close to that of the ρ^0 meson, a $\rho^0 - \omega$ interference can be observed in e.g. the $e^+e^- \rightarrow \pi^+\pi^-$ reaction. This interference can be modelled as a $\rho^0 - \omega$ mixing, $\omega \rightarrow \rho^0 \rightarrow 2\pi$, and a possible intrinsic decay $\omega \rightarrow 2\pi$. A good overview of the history and present developments in the theory on $\rho - \omega$ mixing is given in [123].

The interference effect was taken into account with the following modification of the

Fitted function	M_ρ (GeV)	Γ_ρ (GeV)	n_{skew}	A_I/A_{reso} (GeV)	$ A_{nr}/A_{reso} $ (GeV $^{-1/2}$)	χ^2/ndf
non-relat. BW	0.7577 ± 0.0007	0.1310 ± 0.0017				55.42/53
p-wave relat. BW	0.7519 ± 0.0007	0.1226 ± 0.0016				462.7/53
Ross & Stodolsky	0.7708 ± 0.0012	0.1390 ± 0.0020	2.67 ± 0.13			52.62/52
Söding (8.10)	0.7693 ± 0.0011	0.1298 ± 0.0019		0.163 ± 0.009		56.06/51
Söding (8.12)	0.7702 ± 0.0012	0.1383 ± 0.0020			0.315 ± 0.016	51.67/52

Table 8.1: The fitted values of the free parameters for the different functions used to describe the 2-pion invariant mass distribution. For each of the skewed shapes the fitted ρ^0 mass agreed with the PDG value (see table 6.4), while the width of the resonance seemed to be somewhat underestimated. The result for the width seemed to improve a little when the $\rho^0 - \omega$ interference was taken into account (see paragraph 8.1.6). In general the χ^2 values increased when the range of the invariant mass in the fit was enlarged a bit more. The χ^2 of the fits also became worse when an additional arbitrary curve was included to describe possible uncorrected background contributions.

Ross and Stodolsky parametrization [124, 125]

$$\frac{dN}{dM_{2\pi}} = \frac{2}{\pi} M_{2\pi} M_\rho \Gamma(M_{2\pi}) \left(\frac{M_\rho}{M_{2\pi}} \right)^{n_{skew}} \left| \frac{1}{M_{2\pi}^2 - M_\rho^2 + i M_\rho \Gamma(M_{2\pi})} + \frac{\xi e^{i\alpha}}{M_{2\pi}^2 - M_\omega^2 + i M_\omega \Gamma_\omega} \right|^2, \quad (8.13)$$

where ξ is the strength of the interference and α the phase difference between the interfering processes.

Given the fact that the ω is a rather narrow resonance, that the $\gamma - \omega$ coupling is much smaller than the $\gamma - \rho^0$ coupling and that the branching ratio for $\omega \rightarrow 2\pi$ is only a few percent, the $\rho^0 - \omega$ interference is a small effect and one needs a high statistics sample to obtain a reasonable measurement of its size. As the statistical significance of the weighted DIS Monte Carlo sample was limited, this background was, unlike for the results above, not subtracted from the signal in order not to disturb the shape around the interference region. Instead, an arbitrary function was added to the fit to describe the shape of the background underneath the ρ^0 resonance peak. This combinatorial background was parametrized according to

$$f_{bg}(M_{2\pi}) = c_1 M_{2\pi}^{c_2} e^{-c_3 M_{2\pi}}. \quad (8.14)$$

The use of this shape to describe the background was justified by examining the 2-pion invariant mass distribution outside the exclusive, diffractive ρ^0 signal region, i.e. at high ΔE and high $-t'$, and the background shape as produced by the DIS Monte Carlo. Several other background parametrizations were tried in the fitting procedures, including a simple polynomial shape. However, the functional form given above seemed to give the most stable results. Furthermore, to be able to get a better description of the shape of the background the invariant mass range used in the fit was somewhat extended as compared to the previous paragraphs.

Figure 8.7 shows the result of the fit of the 2-pion invariant mass spectrum with the sum of equation 8.13 and equation 8.14. The fitted free parameters of the resonance shape were

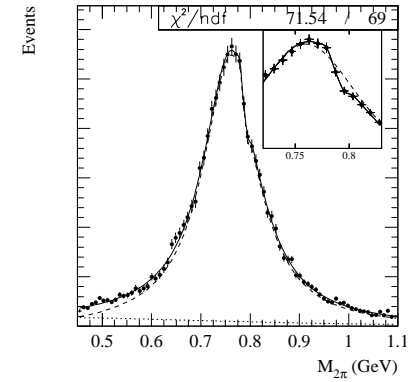


Figure 8.7: The 2-pion invariant mass distribution fitted with a skewed Breit-Wigner function modified to include $\rho^0 - \omega$ interference. The dashed line gives the skewed Breit-Wigner contribution according to equation 8.13, while the dotted line represents the background contribution according to equation 8.14. The small panel shows the fit to the invariant mass distribution near the interference region, where the dashed line gives the Breit-Wigner curve with the interference effect turned off.

$M_\rho = 0.7727 \pm 0.0014$ GeV, $\Gamma_\rho = 0.1404 \pm 0.0029$ GeV, $M_\omega = 0.7881 \pm 0.0024$ GeV, $\Gamma_\omega = 0.0069 \pm 0.0017$ GeV, $n_{skew} = 2.70 \pm 0.17$, $\xi = 0.0064 \pm 0.0032$ and $\alpha = 132 \pm 24$ deg. The ρ^0 and ω mass and width are in agreement with the PDG values and the observed skewing is compatible with the skewing of the Ross and Stodolsky shape without interference effects. The size and the phase of the interference are close to the results from previous experiments [124, 125]. The χ^2/ndf value was 71.54/69 which makes equation 8.13 one of the best functional shapes to describe the 2-pion invariant mass distribution.

A different approach to describe the $\rho^0 - \omega$ mixing was proposed by Niesler *et al.* [126]. They described the diffractive production of low mass pion pairs in a generalized vector meson dominance model. The invariant mass distribution of the pion pairs was determined by the 2-pion contribution to the photon spectral function, where the latter expresses the probability that a photon fluctuates into a pion pair in the presence of a target. This 2-pion contribution Π was related to the pion form factor F_π using

$$\Pi(M_{2\pi}^2) = \frac{1}{48\pi^2} \Theta(M_{2\pi}^2 - 4M_\pi^2) \left(1 - \frac{4M_\pi^2}{M_{2\pi}^2} \right)^{3/2} |F_\pi(M_{2\pi}^2)|^2, \quad (8.15)$$

where Θ is the Heavyside step function. The pion form factor was represented as

$$F_\pi(q^2) = \left(1 - \frac{g_{\rho\pi\pi}}{g_\rho(q^2)} \frac{q^2}{q^2 - M_\rho^2 + iM_\rho\Gamma_\rho(q^2)} \right) \left(1 + \frac{g_\rho(q^2)}{g_\omega} \frac{z_{\rho\omega}}{q^2 - M_\omega^2 + iM_\omega\Gamma_\omega} \right), \quad (8.16)$$

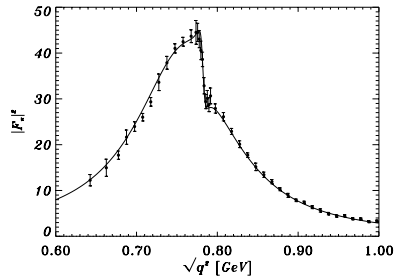


Figure 8.8: The pion form factor as used in the 2-pion invariant mass distribution fit using equation 8.19. The data come from reference [127], while the fitted function is given by equation 8.16. Picture taken from reference [126].

where the first part describes the ρ^0 contribution and the second factor accounts for the $\rho^0 - \omega$ mixing. The width of the ρ^0 resonance was parametrized as

$$\Gamma_\rho(q^2) = \frac{g_{\rho\pi\pi}^2}{48\pi M_\rho \sqrt{q^2}} (q^2 - 4M_\pi^2)^{3/2}, \quad (8.17)$$

with the coupling of the ρ^0 to the pion pair $g_{\rho\pi\pi} = 6.05$. The effective $\gamma\rho$ coupling was taken to be

$$g_\rho(q^2) = \left(\frac{1}{\dot{g}_\rho} - \frac{M_\rho^2 - \dot{M}_\rho^2 - iM_\rho\Gamma_\rho(q^2)}{g_{\rho\pi\pi}q^2} \right)^{-1}, \quad (8.18)$$

with $\dot{M}_\rho = 0.81$ GeV being the bare ρ^0 mass and $\dot{g}_\rho = 5.44$ the bare $\gamma\rho$ coupling. The $\gamma\omega$ coupling was taken to be $g_\omega = 17.0$, the ω resonance width was fixed at the PDG value $\Gamma_\omega = 8.41$ MeV and the interference strength $z_{\rho\omega} = -4.52 \cdot 10^{-3}$ GeV². The parametrization of the pion form factor as described above is depicted in figure 8.8. The agreement with the measured data is excellent. The 2-pion invariant mass distribution was then described by

$$\frac{dN}{dM_{2\pi}} = \frac{\Pi(M_{2\pi}^2)}{M_{2\pi}} \left(1 + c \frac{M_\rho^2 - M_{2\pi}^2}{M_{2\pi}^2} \right) \left(\frac{M_{2\pi}^2}{M_{2\pi}^2 + Q^2} \right)^2 \left(1 + \epsilon \xi^2 \frac{Q^2}{M_{2\pi}^2} \right), \quad (8.19)$$

where the second factor quantifies a possible mass dependence of $\sigma_{\pi\pi N}$ or inelastic contributions, while the last two factors describe the Q^2 dependence according to the vector meson dominance model.

The result of the fit of equation 8.19 together with the background described by equation 8.14 to the 2-pion invariant mass distribution is shown in figure 8.9. The fitted free parameters of the resonance shape were $M_\rho = 0.7750 \pm 0.0010$ GeV, $M_\omega = 0.7861 \pm 0.0004$ GeV, $c = 1.00 \pm 0.06$, $\xi^2 = 0.015 \pm 0.033$. The χ^2/ndf value of the fit was 88.40/72. The magnitude of the background contribution seems to be somewhat underestimated

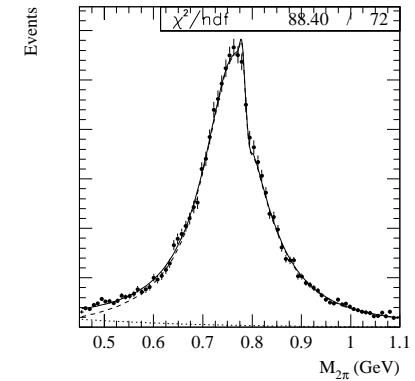


Figure 8.9: The 2-pion invariant mass distribution fitted with the Niesler parametrization given by equation 8.19. The dashed line gives the Niesler contribution, while the dotted one represents the background according to equation 8.14.

as compared to the background seen in e.g. figure 8.1 and 8.7, although this has little influence on the description of the interference effect. The fit clearly shows that the model based on the behaviour of the pion form factor can effectively reproduce our measured $\rho^0 - \omega$ interference effect.

8.1.7 Kinematical Dependence of the Invariant Mass Distribution

As suggested in [117] the observed skewing of the ρ^0 invariant mass peak is expected to disappear at high $-t$. Photoproduction experiments and low- Q^2 data indeed indicate that the skewing decreases with $-t$ [128, 129]. Leptoproduction experiments also show that the skewing is Q^2 -dependent and disappears with increasing Q^2 [128, 99, 130]

The ρ^0 invariant mass distribution was studied as function of Q^2 and $|t|$. The acceptance correction was performed separately for each kinematical bin. The DIS background contribution to the invariant mass spectra was estimated and corrected for in each Q^2 and $|t|$ bin. For the latter distributions the background estimation method described in section 7.6 cannot be applied as function of $|t|$ due to the strong correlations between ΔE and t (t') in our data. Therefore the Monte Carlo normalization factor was assumed to be constant as function of $|t|$ and equal to the normalization factor at average Q^2 . It was checked that the average Q^2 was nearly constant over the bins in $|t|$. The ρ^0 invariant mass distribution was corrected for acceptance in each Q^2 and $|t|$ bin. As an example, the acceptance as function of Q^2 is shown in figure 8.10. The resulting 2-pion invariant mass distributions were fitted with equation 8.9, 8.12 and 8.10 and the Q^2 -dependence

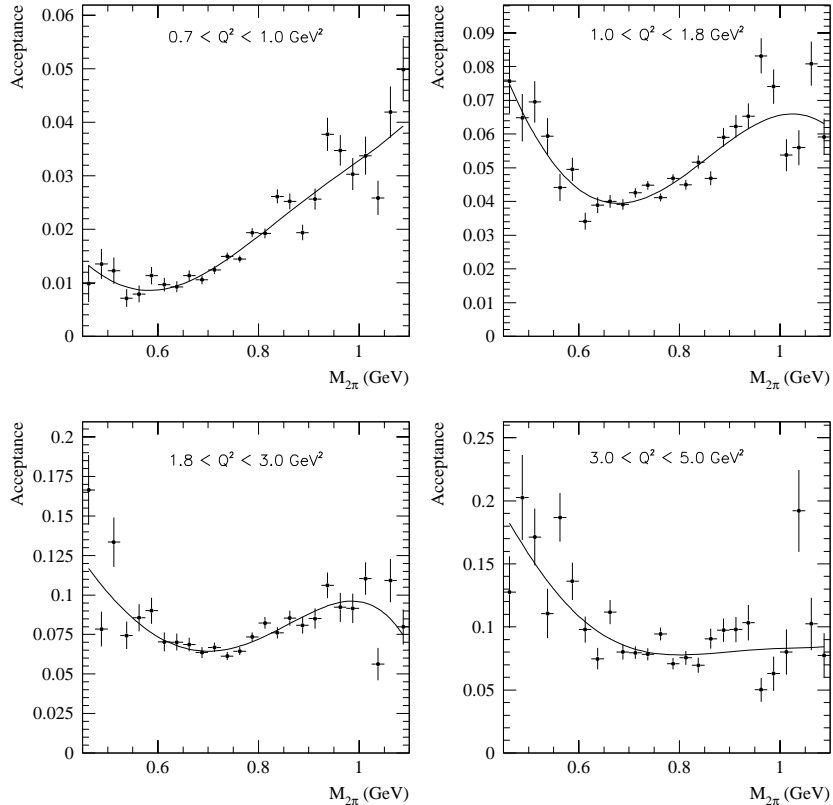


Figure 8.10: The acceptance as function of the 2-pion invariant mass computed with the VDM generator for the different Q^2 regions.

of the former two is illustrated in figure 8.11 and 8.12 respectively. As the statistical significance of the distributions in the individual Q^2 and $|t|$ bins is much lower than for the total invariant mass spectrum, no $\rho^0 - \omega$ interference effects were considered in these fits.

Systematic studies of the kinematical dependence of the skewing included the following items :

- The acceptance correction was not done using the fitted polynomial function, but was performed bin by bin without any fit.
- The width of the ρ^0 resonance was parametrized with equation 8.5 instead of equation 8.7.
- The DIS background was not subtracted from the signal, but was instead described using the shape given in equation 8.14.
- The number of bins used in the histograms for the invariant mass distributions was varied.
- The fits were performed for a more extended range of $M_{2\pi}$.

Each of the above items lead to more or less similar systematic changes of the result, where the contribution of each item to the systematic error varied in general from roughly 2 to 5 % up to about 15 to 30 %. To catch possible target mass effects, the results were also computed for an event sample restricted to H data only. No target mass dependence was found within the systematical error presented above. Due to the limited statistical precision of the results for H data as compared to the values for the full data set, this item was not included into our estimate of the systematic error.

Figure 8.13 shows the measured Q^2 dependence of the skewing of the ρ^0 resonance peak as parametrized by equation 8.9, 8.12 and 8.10. The error bars represent the total error where the statistical and systematical errors were added in quadrature and the horizontal lines indicate the contribution of the statistical error. Also shown on the plot are results from previous experiments (E665, ZEUS and H1) which all measured at much higher energies. The results clearly indicate that the skewing diminishes for increasing Q^2 and tends to disappear completely at high Q^2 . Moreover, when comparing the HERMES data points with the other experimental data, one can see that the agreement is very good in the overlapping Q^2 range, which proves that the skewing of the ρ^0 resonance shows only very little or no energy dependence at all. By comparing the results presented in figure 8.13 (b) and (c), one can see that, as expected, the values for $|A_{nr}/A_{reso}|$ are systematically about a factor 2 higher than the corresponding A_I/A_{reso} results. The results of the Q^2 -dependence analysis are summarized in table B.1.

The measured t -dependence of the ρ^0 resonance skewing is depicted in figure 8.14. Here the dependence of the fit with equation 8.10 was not considered as it contains no additional physics information as compared to the fit with equation 8.12. The data reveal only a weak dependence on t , where the skewing decreases for increasing $|t|$. This result agrees with the observation made by H1 [130] where also no significant t dependence was seen in their electroproduction data for Q^2 above 1 GeV^2 . However, a strong t -dependence of the skewing at $Q^2 \approx 0$ was reported by ZEUS [129] and by several low

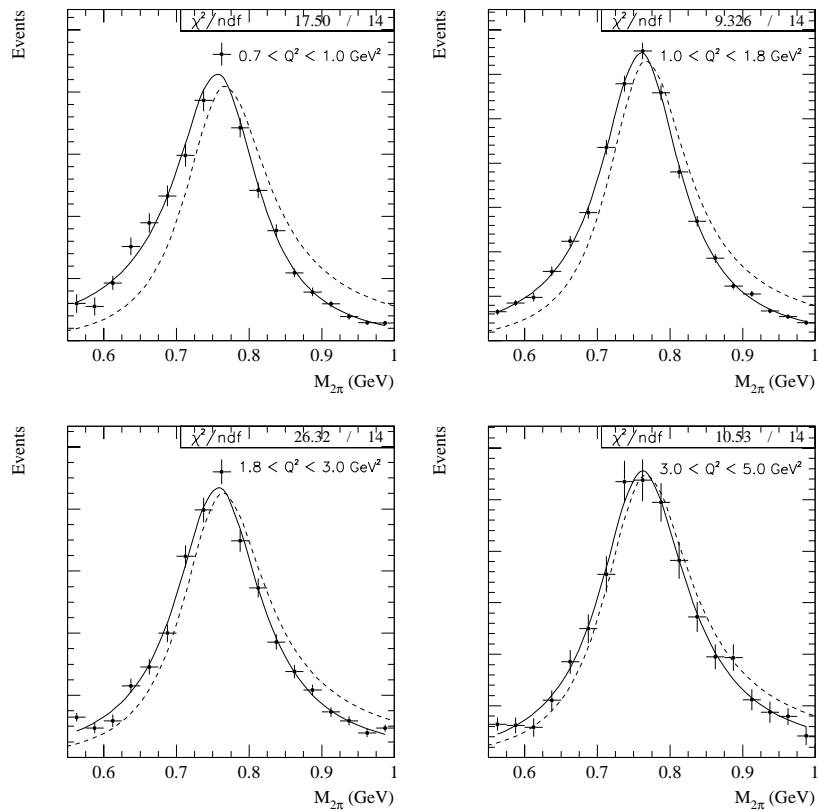


Figure 8.11: The acceptance and background corrected 2-pion invariant mass distribution for the different Q^2 intervals fitted with the Ross and Stodolsky parametrization. The dashed lines show the Breit-Wigner contributions.

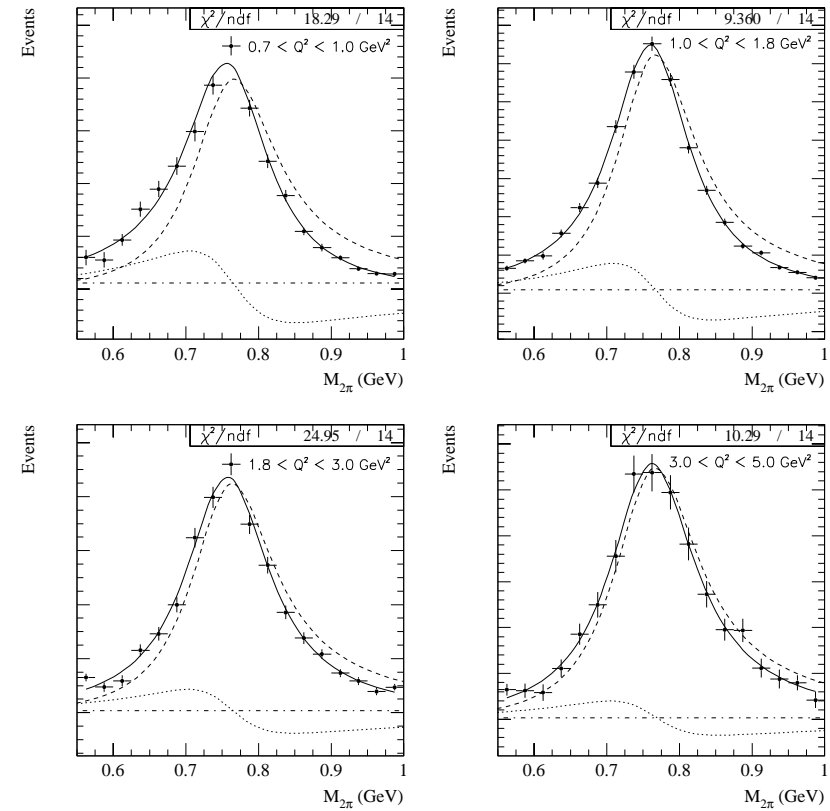


Figure 8.12: The acceptance and background corrected 2-pion invariant mass distribution for the different Q^2 intervals fitted with the Söding parametrization. The dashed lines give the Breit-Wigner contributions, the dotted lines represent the interference terms and the dashed-dotted lines show the non-resonant parts.

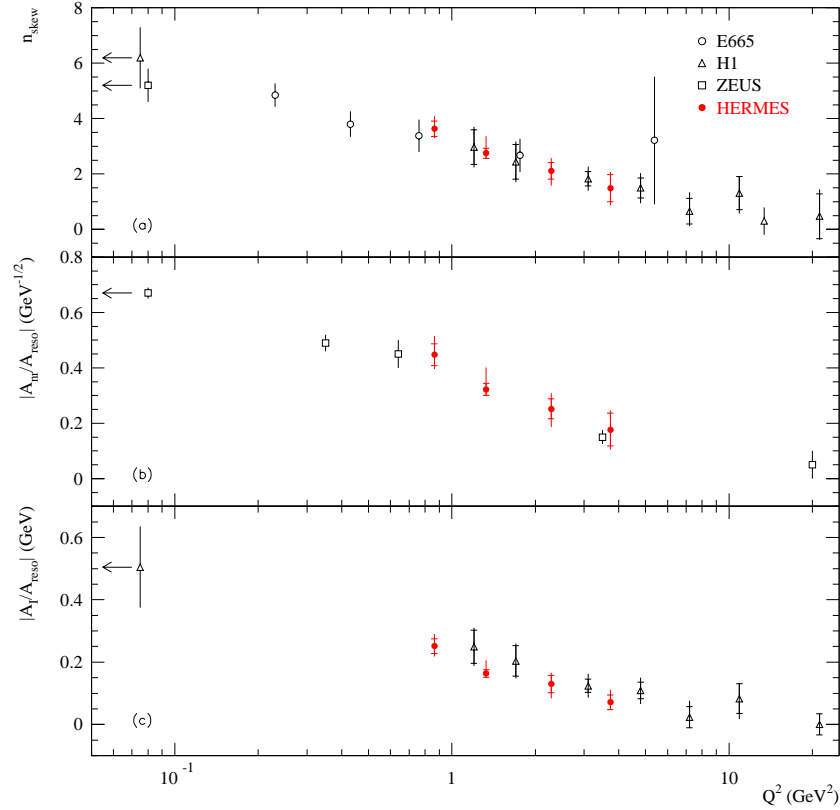


Figure 8.13: The measured Q^2 -dependence of (a) the Ross and Stodolsky shape given by equation 8.9, and the Söding function given by (b) equation 8.12 and (c) equation 8.10. The photoproduction data points (marked with arrows) are results from ZEUS [129] and H1 [132], while the electroproduction data come from E655 [99], H1 [133, 130] and ZEUS [131].

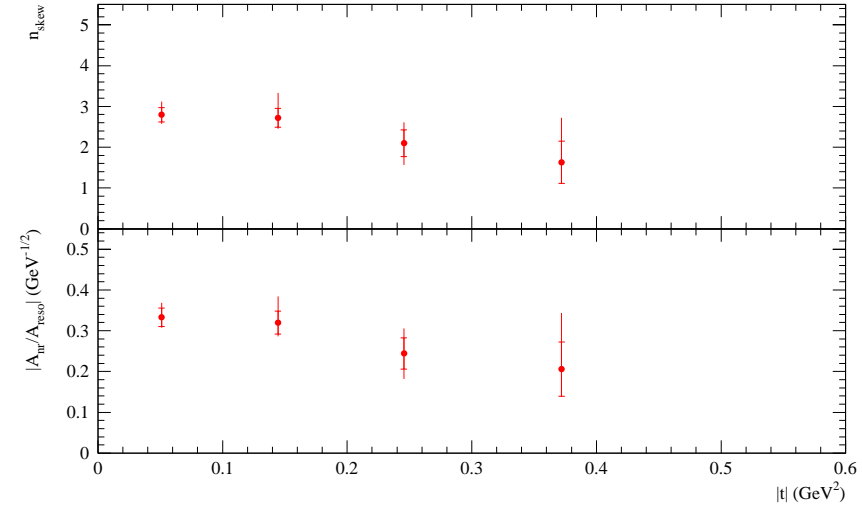


Figure 8.14: The measured t -dependence of (a) the Ross and Stodolsky shape given by equation 8.9 and (b) the Söding function given by equation 8.12.

energy ρ^0 photoproduction experiments [128]. This would lead to the conclusion that the ρ^0 resonance skewing becomes less t -dependent for increasing Q^2 . The results of the fits as function of $|t|$ can be found in table B.2.

8.2 ω Invariant Mass Distribution

The reconstructed invariant mass distribution of the $\pi^+\pi^-\pi^0$ decay channel obtained after all offline cuts as described in section 6.2.2 is shown in figure 8.15 (a). All data from the different standard trigger data sets considered in this analysis were added together. The data were selected in the W -range between 4.0 and 6.0 GeV and Q^2 between 0.7 and 5.0 GeV². The ω resonance peak clearly shows up in the expected mass region. Apart from the ω signal one also notices some hints of production of η and ϕ mesons, which both have a small branching ratio for the 3-pion decay channel.

In contrast with the ρ^0 meson the ω meson is a rather narrow resonance. Therefore the influence of acceptance effects on the shape of the invariant mass distribution turns out to be negligible and therefore the acceptance corrections were not applied in this case. Also no correction for any kind of background contributions was considered.

The ω invariant mass peak was fitted with a simple non-relativistic Breit-Wigner curve.

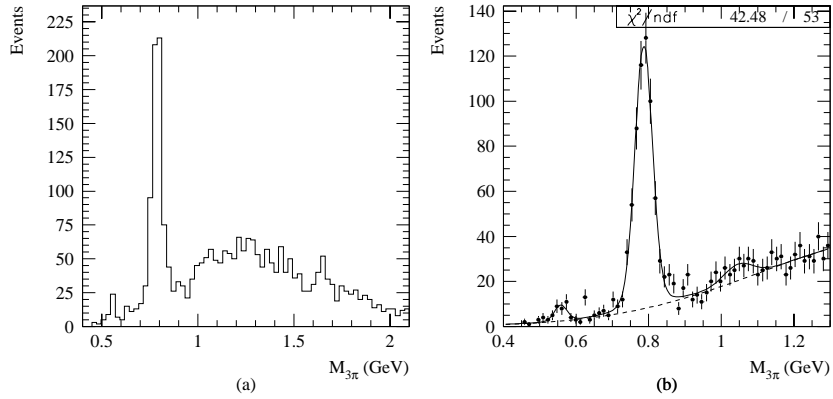


Figure 8.15: The ω invariant mass distribution. (a) The 3-pion invariant mass distribution obtained after all offline cuts for the combined data sample. A clear mass peak shows up at the mass of the ω meson. (b) The fitted ω invariant mass distribution, with the peak being the convolution of a non-relativistic Breit-Wigner function with a Gaussian function. The two Gaussian shapes on the left and right side of the ω resonance represent production of η and ϕ mesons respectively. The dotted line represents the combinatorial background described by a 4th order polynomial.

However, due to the finite detector resolution, especially on the reconstructed π^0 , the ω invariant mass peak will be broadened. To take this effect into account the Breit-Wigner was convoluted with a Gaussian function. The fitted function was then

$$\frac{dN}{dM_{3\pi}} = \int_{-\infty}^{+\infty} \frac{\Gamma_{\omega}}{4(x - M_{\omega})^2 + \Gamma_{\omega}^2} \cdot e^{-\frac{1}{2}\left(\frac{M_{3\pi}-x}{\sigma}\right)^2} dx. \quad (8.20)$$

In the fit the width of the Breit-Wigner Γ_{ω} was kept constant at the PDG value (see table 6.4) so that the width of the convoluted Gaussian function provided an estimation of the detector resolution. The η and ϕ resonances were described using simple Gaussian functions, while the shape of the combinatorial background could be parametrized with either a 4th order polynomial or also with a simple Gaussian function.

The fitted ω mass was 786.5 ± 1.2 MeV, in reasonable agreement with the PDG value, and the convoluted Gaussian width was 22.3 ± 1.2 MeV with χ^2/ndf of the fit equal to 42.48/53. The fitted η mass and width were 557 ± 6 MeV and 17 ± 5 MeV, while the fitted ϕ mass and width values were 1.046 ± 20 GeV and 40 ± 20 MeV respectively. Both the η and ϕ mass are in reasonable agreement with the PDG values [94]. The width of the convoluted Gaussian of the ω resonance and of the two Gaussians describing the η and ϕ peaks were clearly driven by the reconstructed π^0 invariant mass peak, which had a width comparable to the values obtained here.

Due to the limited statistical significance of the standard trigger ω sample no fur-

ther investigation of the kinematical dependence of the invariant mass distribution was undertaken.

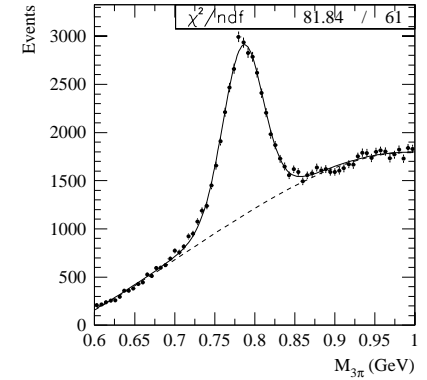


Figure 8.16: The 3-pion invariant mass distribution obtained from 1997 photoproduction trigger data on ^1H , where the fitted function is a convolution of a non-relativistic Breit-Wigner function with a Gaussian function, describing the ω resonance, plus a 5th order polynomial (dotted line) to model the combinatorial background underneath the peak.

For the photoproduction trigger data a similar ω invariant mass fit was performed. The result for the 1997 ^1H data is displayed in figure 8.16. The fitted function was the sum of equation 8.20 and a 5th order polynomial describing the combinatorial background underneath the ω resonance. The fitted ω invariant mass and the width of the convoluted Gaussian were 785.3 ± 0.3 MeV and 23.6 ± 0.3 MeV respectively, with a χ^2/ndf of 81.84/61. Both fitted parameters are fully compatible with the results obtained for the standard trigger data set.

here, the term proportional to m_e^2 in the expression for Γ_T in equation 2.30 can be safely neglected. This leads after some algebra to the following relation between the electro- and virtual photoproduction cross section

$$\sigma^{\gamma^*p \rightarrow \gamma p} = \frac{1}{\Gamma_T(Q^2, W)} \frac{d^2 \sigma^{\rho^0 \rightarrow \epsilon p \gamma}}{dW dQ^2}, \quad (9.2)$$

with the transverse photon flux given by

$$\Gamma_T(Q^2, W) = \frac{\alpha}{2\pi} \frac{W}{M} \frac{W^2 - M^2}{2M} \frac{1}{Q^2} \frac{1}{E^2} \frac{1}{1 - \epsilon}, \quad (9.3)$$

and the ratio of the fluxes

$$\epsilon = \frac{1 - y - Q^2/4E^2}{1 - y + y^2/2 + Q^2/4E^2}, \quad (9.4)$$

where the term $Q^2/4E^2$ can actually be neglected. When summing over the individual flux factors computed for each event we get

$$\sum_i \frac{1}{\Gamma_T(Q^2, W)} = \mathcal{L} \int_{\Delta Q^2} \int_{\Delta W} \frac{1}{\Gamma_T(Q^2, W)} \frac{d^2 \sigma^{\rho^0 \rightarrow \epsilon p \gamma}}{dW dQ^2} dQ^2 dW \quad (9.5)$$

$$= \mathcal{L} \sigma^{\gamma^*p \rightarrow \gamma p} \Delta Q^2 \Delta W, \quad (9.6)$$

where we made use of equation 9.2 and where \mathcal{L} represents the total integrated luminosity. To extract an absolute cross section value from the measured data several corrections to the previous equation are needed leading to the following final expression

$$\sigma^{\gamma^*p \rightarrow \gamma p} = \frac{1}{\mathcal{L}} \frac{1}{\Delta W \Delta Q^2} \frac{1}{1 + s/b} \frac{1}{Acc \cdot B \cdot \eta} \sum_i \frac{1}{\Gamma_T(Q^2, W)}, \quad (9.7)$$

where s/b is the signal to background ratio for exclusive events, Acc is the total acceptance, B is the total branching ratio for the analyzed decay mode (equal to $B = B_{\omega \rightarrow 3\pi^0} \cdot B_{\rho^0 \rightarrow 2\gamma} = 0.877$ for the ω and $B = B_{\rho^0 \rightarrow 2\pi} \approx 1$ for the ρ^0) and η is the radiative correction factor.

9.2 Luminosity Determination

As shown in section 9.1 a measure of the integrated absolute luminosity is needed for the absolute normalization of the extracted cross section values. In the analysis two independent ways to determine the total absolute luminosity were pursued as explained below.

The HERMES luminosity monitor (as described in paragraph 3.4.4) measures a relative luminosity using the detected coincidence rate N_{lumi} of e^+e^- pairs from Bhabha scattering. This rate is measured on the burst scale and has thus to be multiplied by the length in time of the burst t_{burst} . To convert the measured number of Bhabha events to a value for the integrated absolute luminosity a calibration factor C_{lumi} is needed which relates the measured Bhabha rate to the well-known Bhabha cross section by accounting

Chapter 9

The γ^*p Cross Sections

This chapter deals with the determination of absolute cross sections for exclusive, diffractive ρ^0 and ω production in the HERMES kinematic range. The different ingredients which enter the extraction and the applied corrections are described. The absolute cross section part ends with an evaluation of the ω/ρ^0 production ratio and a comparison to existing data and some theoretical models. Next, the measured slope factors for both vector mesons are discussed and compared to world data. Finally we present a study of nuclear attenuation for exclusive vector meson production on composite nuclei.

9.1 Extraction of Absolute γ^*p Cross Section

The cross section for exclusive ρ^0 production was evaluated as function of Q^2 and W . The chosen range in these two variables was taken as wide as possible, while however those regions where the detector acceptance became too low were avoided. Given the limited region in W covered by the experiment only two bins for this kinematical variable ($4.0 < 5.0 < 6.0$ GeV) were chosen, whereas four bins in Q^2 were taken ($0.7 < 1.0 < 1.8 < 3.0 < 5.0$ GeV²). Due to the limited statistics of the exclusive ω event sample the cross section was evaluated in either two bins in Q^2 ($0.7 < 1.8 < 5.0$ GeV²) or two bins in W ($4.0 < 5.0 < 6.0$ GeV), where the binning was deliberately chosen similar to the one used in the ρ^0 analysis.

Our measured count rate for exclusive ρ^0 or ω production is in fact proportional to an electroproduction cross section. To facilitate comparison with other experimental results one usually takes the known flux factor of virtual photons emitted by the initial beam particle to convert this former quantity into a virtual photoproduction cross section σ^{γ^*p} , which starting from equation 2.22 is defined according to

$$\frac{d^2 \sigma^{\rho^0}}{dW dQ^2} = \Gamma_T \sigma_T^{\rho^0} + \Gamma_L \sigma_L^{\rho^0} = \Gamma_T \left(\sigma_T^{\rho^0} + \epsilon \sigma_L^{\rho^0} \right) = \Gamma_T \sigma^{\gamma^*p}, \quad (9.1)$$

where the ratio of the fluxes is given by $\epsilon = \Gamma_L/\Gamma_T$. In the kinematic region considered

for e.g. the luminosity monitor acceptance and efficiency. This correction factor was computed [73] for the 1996 data to be $0.448 \mu\text{b}^{-1}$ with a systematic uncertainty of 6.3 %. The dominant contribution to the error came from the uncertainty in the detector geometrical acceptance determination. In the end also a target dependent factor C_{targ} is necessary to correct for the ratio of the number of electrons to the number of nucleons in the target atoms. This factor is equal to 1 for ^1H (and H_2) targets, 1.5 for ^3He and 2 for D_2 and N_2 targets. The final expression for the integrated absolute luminosity on a target T derived from the HERMES luminosity monitor is then

$$\begin{aligned} \mathcal{L}_{\text{lumi}}(T) &= C_{\text{lumi}} \cdot C_{\text{targ}}(T) \cdot \left(\sum_{\text{bursts}} N_{\text{lumi}} \cdot t_{\text{burst}} \right), \\ &= 0.448 \cdot 10^{-6} \cdot \begin{cases} 1 & (^1\text{H}, \text{H}_2) \\ 1.5 & (^3\text{He}) \\ 2 & (\text{D}_2, \text{N}_2) \end{cases} \cdot \left(\sum_{\text{bursts}} N_{\text{lumi}} \cdot t_{\text{burst}} \right) \text{ pb}^{-1}. \end{aligned} \quad (9.8)$$

Note that the statistical uncertainty on this measured total luminosity (integrated Bhabha rate) is very small and essentially negligible.

A second method to determine the integrated luminosity was based on a data-Monte Carlo comparison [134] of the measured unpolarized deep-inelastic scattering cross section to the theoretical value calculated from the known world data on the F_2 structure function. This kind of analysis yielded a calibration factor C_{DIS} which could then be used to compute the integrated luminosity for a data sample by counting the total number of DIS positrons it contained. The number of DIS positrons in each data sample was counted burst by burst using the following criteria :

- A lepton was defined as a particle with $PID4 > 1$.
- The lepton with the highest momentum was selected.
- The track had to fulfil the following kinematical and geometrical constraints :
 - $Q^2 > 1 \text{ GeV}^2$ (DIS regime),
 - $W > 2 \text{ GeV}$ (non-resonance region),
 - $y < 0.85$ (small radiative corrections),
 - $|\theta_x| < 170 \text{ mrad}$ and $40 < |\theta_y| < 140 \text{ mrad}$ (detector geometrical acceptance).

The number of positrons N_{e^+} per burst obtained in this way was corrected for background from charge symmetric processes by subtracting the number of electrons N_e passing the same criteria as mentioned above. The efficiency of the data acquisition system ϵ_{DAQ} , which is here given by the DAQ live time defined by equation 6.1, was also folded burstwise into the corrected number of DIS positrons $N_{e^+}^{\text{corr}}$. The calibration constant was determined from the 1996 data taken on an unpolarized ^3He target to be $C_{\text{DIS}} = 21.8 \cdot 10^{-6} \text{ pb}^{-1}$ with a systematic uncertainty of 4 % [134]. Here one has to assume that the reconstruction efficiency for DIS positrons in the acceptance remains the same for all different targets over the different data taking years and for all track reconstruction methods. Since the DIS cross section depends on the used target, a correction

factor was needed to compensate for the difference. The integrated luminosity for a data sample taken on target T was then finally computed according to

$$\begin{aligned} \mathcal{L}_{\text{DIS}}(T) &= C_{\text{DIS}} \cdot \left(\sum_{\text{bursts}} N_{e^+}^{\text{corr}} \cdot \frac{1}{\epsilon_{\text{DAQ}}} \right) \cdot \frac{\sigma_{\text{DIS}}(^3\text{He})}{\sigma_{\text{DIS}}(T)}, \\ &= 21.8 \cdot 10^{-6} \cdot \left(\sum_{\text{bursts}} N_{e^+}^{\text{corr}} \cdot \frac{1}{\epsilon_{\text{DAQ}}} \right) \cdot \left. \begin{matrix} 56.15 \\ \left\{ \begin{matrix} 60.90 & (\text{H}) \\ 53.82 & (\text{D}) \\ 56.15 & (^3\text{He}) \\ 54.50 & (\text{N}) \end{matrix} \right\} \end{matrix} \right\} \text{ pb}^{-1}, \end{aligned} \quad (9.9)$$

where $\sigma_{\text{DIS}}(T)$, expressed in nb, denotes the total deep-inelastic cross section per nucleon for a target T , including radiative effects. The values were computed with world data on F_2 and were integrated over the entire HERMES kinematic range. They have a systematic error of 3 % related to the normalization uncertainty of the F_2 data. σ_{DIS} for ^3He and N were calculated using the HERMES results on F_2 [135]. It should be noted that as the count rate of deep-inelastic positrons is much less than the measured luminosity monitor coincidence rate, the statistical error of this DIS normalization method will be somewhat larger as compared to the first method, but still negligible.

Target	Data Taking Year	$\mathcal{L}_{\text{lumi}}$ (pb^{-1})	\mathcal{L}_{DIS} (pb^{-1})	$\mathcal{L}_{\text{DIS}}/\mathcal{L}_{\text{lumi}}$
H	'96	49.21	51.11	1.04
	'97	81.91	80.28	0.98
D	'96	54.40	56.37	1.04
	'97	62.27	61.48	0.99
^3He	'95	75.35	93.85	1.25
	'96	16.79	17.45	1.04
N	'97	56.49	54.24	0.96

Table 9.1: The integrated absolute luminosity values for all '95-97 HERMES targets suitable for vector meson analysis. The polarized and unpolarized periods for ^3He in '95 and H in '96-97 have been added together.

Table 9.1 summarizes the calculated integrated absolute luminosity values after the data quality selection outlined in section 6.1 for the different HERMES targets in '95-97 which were used in vector meson analysis. The statistical errors for $\mathcal{L}_{\text{lumi}}$ are of the order of 1 to $2 \cdot 10^{-2}$, whereas the errors on \mathcal{L}_{DIS} are about a factor of 1.5 to 2.5 larger, which agrees with the average count rate of DIS events being roughly a factor of 3 to 6 times smaller than the luminosity monitor coincidence rate. The ratio of the luminosity values obtained with the two different methods explained above is also indicated, where the statistical error of the order of 10^{-3} is neglected. This ratio should be unity for all targets, which is in most cases true within the systematic errors, except for the 1995 ^3He data where the ratio amounts to 1.25. This deviation is related to the exchange of the photomultipliers of the luminosity monitor after the '95 data taking period. As the C_{lumi} calibration factor was only determined from the '96 data, this constant was not valid

for the '95 data and hence an extra correction factor of 1.25 for the luminosity monitor is needed. For an unknown reason there seems to be a tendency towards smaller ratios for the '97 data as compared to '96. One should also be aware of the fact that the DIS normalization method depends on the tracking efficiency. Due to the inefficiencies in the vertex chambers, this reconstruction efficiency is slightly lower for the tracking method with the vertex chambers included than for the method without VC's. This will somewhat affect the ratio for the '97 H data as this sample is reconstructed partially with the VC included tracking method. In this work, the luminosity calculation will be based on the DIS-normalization scheme.

9.3 Acceptance Correction

The acceptance correction for the ω and ρ^0 cross section analysis was computed as outlined in section 7.4 using the DIPSI and VDM generator respectively. The correction factor was evaluated as function of W and Q^2 in the binning given in paragraph 9.1. Due to the event weighting procedure with the transverse virtual photon flux in the extraction of the absolute cross section, also the generated and reconstructed Monte Carlo events had to be weighted in a similar fashion. The acceptance, depending on the kinematical bin, varied between 0.32 % and 0.84 % for ω production and between 1.2 and 7.4 % for ρ^0 production. Note that these correction factors also include the effect of the offline analysis cuts.

The systematic error on the acceptance correction comprises several things. In the case of the ω analysis the uncertainty on the acceptance correction due to the DIPSI generator was estimated by varying the input gluon distribution to the pQCD model. The MRS A94, MRSA low Q^2 , CTEQ41Q, GRV'HO, GRV94HO and GRV pol. HO [109] quark-parton distribution sets were tried, where it was checked whether the reconstructed MC distributions were in agreement with the data. Also the sensitivity of the acceptance correction to the vector meson decay angle distributions was included into the systematics by generating the angles isotropically instead of assuming SCHC. In the case of the ρ^0 analysis, the sensitivity to the generator model was checked by changing the t' slope factor by 0.3 GeV⁻², by changing the exponent n in the Q^2 dependence of the VDM propagator $1/(1 + Q^2/M_\rho^2)^n$ from 2.0 to 2.5 and by varying the c_0 and c_1 parameters in the Q^2 dependence of the $R(Q^2) = c_0 \cdot (Q^2/M_\rho^2)^{c_1}$ ratio. The uncertainty due to the geometrical acceptance was estimated by shifting the box representing the spectrometer acceptance towards and away from the beamline resulting in changes of the vertical minimum scattering angle of 1 mrad. The total fractional systematic uncertainty found in this way due to the MC model dependence ranged from 13 to 25 % for the ω analysis and from 2 to 19 % for the ρ^0 , while the fractional uncertainty due to the detector geometry varied between roughly 1 and 5 %.

The Monte Carlo statistical error on the total acceptance was ranging from 10⁻² to 10⁻¹ % over the bins in case of the ρ^0 analysis and was about 10⁻² % for the ω analysis. In both cases the statistical error on the acceptance correction was negligible in comparison to the systematic uncertainty and was therefore not taken into account.

The average kinematics in e.g. Q^2 and W which one assigns to the center of each bin are calculated taking the shape of the kinematical data distributions into account.

However, the detector acceptance modifies the kinematical dependence of the data, so that one cannot derive the bin averages directly from the reconstructed events. As the reconstructed Monte Carlo kinematical distributions are seen to match the measured spectra, we assume that the bin averages computed with the 4 π Monte Carlo provide a good estimate of the true bin averages.

9.4 DIS Background Subtraction

In exclusive vector meson production on the nucleon, the target particle remains intact. Here, the recoiling nucleon is not detected and hence, given the experimental resolution a certain amount of non-exclusive events will slip through the exclusive, diffractive event cuts and will show up as background underneath the ΔE peak around zero as can be seen in e.g. figure 7.5.

The majority of these background events comes from deep-inelastic scattering fragmentation processes, where the final state contains at least e.g. a pair of pions or other hadrons, a vector meson or other particles decaying into vector mesons or pions ... A large portion of this background is already removed by the ΔE and $-t'$ cuts. To correct for the remaining fraction, several independent approaches were considered as discussed below.

The correction for the DIS background was performed via an estimated signal-to-background ratio s/b .

$$N_{corr} = N_{tot} \frac{s/b}{1 + s/b}, \quad (9.10)$$

where N_{tot} and N_{corr} are the total and background corrected flux weighted number of events respectively. The statistical error on the s/b ratio is usually non-negligible and always contains a contribution due to the statistical precision of the measured data sample itself. In some cases this contribution actually dominates the statistical uncertainty on the ratio, which then leads to the argument that the latter error should be propagated into the uncertainty on the corrected number of events. In that case one gets

$$\sigma(N_{corr}) = \sqrt{\left(\frac{s/b \cdot \sigma(N_{tot})}{(1 + s/b)}\right)^2 + \left(\frac{N_{tot} \cdot \sigma(s/b)}{(1 + s/b)^2}\right)^2}, \quad (9.11)$$

where $\sigma(N_{tot})$ and $\sigma(s/b)$ represent the statistical error on the total number of flux weighted events and s/b respectively. The former error is given by

$$\sigma(N_{tot}) = \sqrt{\sum_i (1/\Gamma_i^2)}, \quad (9.12)$$

with the sum running over the events in the considered kinematical bin and Γ_i the eventwise computed transverse photon flux factor. However, in case that the statistical error on the s/b ratio is dominated by e.g. some Monte Carlo sample, then this error should be included into the systematic uncertainty of the final result.

To take into account any possible variation of the DIS background as a function of Q^2 or W , the background estimation and correction was performed for each (Q^2, W)

bin individually. The resulting signal to background ratios for the different methods considered below are listed in table 9.2 and 9.3.

9.4.1 DIS Monte Carlo Method

This method relies on the Monte Carlo technique as outlined in section 7.6. A signal to background ratio s/b for exclusive, diffractive sample could be determined by counting the total number of data N_{tot} and normalized background events N_{back} passing the full set of analysis cuts

$$\frac{s}{b} = \frac{N_{tot} - N_{back}}{N_{back}}, \quad \sigma\left(\frac{s}{b}\right) = \sqrt{\frac{N_{tot}}{N_{back}^2} + \frac{\sigma(N_{back})^2 N_{tot}^2}{N_{back}^4}}, \quad (9.13)$$

where the error on the ratio includes the statistical error on the number of data and Monte Carlo events and the Monte Carlo normalization factor. The signal-to-background ratio was determined for each individual (Q^2, W) bin, where the resulting distributions are shown in figure C.2 and C.1. The Monte Carlo gave a satisfactory description of the background in the considered kinematic range of the bins.

The systematic uncertainty on the s/b ratio determined with this method was estimated by varying the lower ΔE limit of the Monte Carlo normalization region. In case of the ω analysis this gave a relative error of about 3.4 % on average, while for the ρ^0 analysis an average of about 3.5 % and 0.8 % was found for the bins at low and high W respectively.

9.4.2 Zone Method

Another background subtraction method relies on the use of measured data only. As the majority of the HERMES standard trigger events actually corresponds to deep-inelastic scattering events, this data can serve as a background measurement for our exclusive, diffractive event sample instead of a Monte Carlo generated background sample. Just like in the previous method the s/b measurement is based on the form of the ΔE -distribution, where the background ΔE -spectrum is now determined using events with $-t' > 0.8 \text{ GeV}^2$. This latter distribution is then normalized to the ΔE -spectrum of the events with $-t' < 0.4 \text{ GeV}^2$ in the region of $\Delta E > 3.0 \text{ GeV}$, where we expect to have only deep-inelastic scattering events.

The zone method can also be explained quantitatively using the $(\Delta E, -t')$ plot for e.g. the ρ^0 events in figure 9.1. The exclusive diffractive events are contained in zone 1, while the background events are taken from zone 2. The background events are normalized using the ratio of the number of events in zone 3 and 4, i.e.

$$N_{back} = N_2 \cdot \frac{N_4}{N_3}. \quad (9.14)$$

As can be seen in figure 9.2 the assumed background shape does not quite match the data as good as the Monte Carlo generated background distribution from the previous section. Moreover, the ΔE -shape of the background slightly depends on the chosen

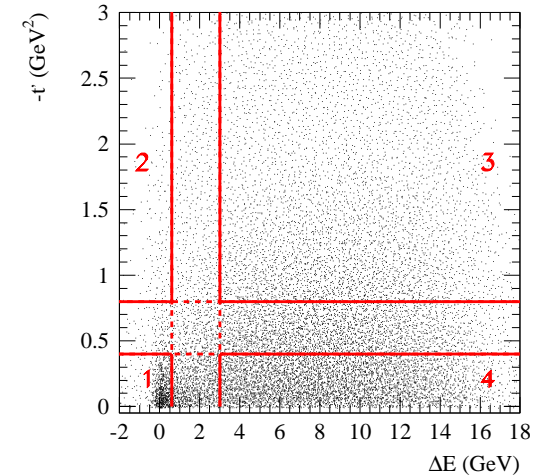


Figure 9.1: The different zones in the $(\Delta E, -t')$ plot used in the DIS background Zone Method. Zone 1 is the exclusive, diffractive region. The background events are taken from zone 2, while the background normalization is done using zone 3 and 4.

minimum value of $-t'$ for the background events, whereas the method assumes that this shape is in reality independent of $-t'$. Part of this dependence is possibly related to the geometric acceptance of the detector. Also, a tiny fraction of exclusive events at high $-t'$ may enter the obtained background ΔE -spectra with this method, leading to a slight overestimate of the size of the background.

The resulting background distributions obtained with this method for the different bins are illustrated in figure C.4 and C.3. The signal-to-background were calculated according to equation 9.13, where the error on the number of background events included the statistical error on the number of events in the different zones appearing in equation 9.14.

9.4.3 Fit Method

In the third and last DIS background estimation method one tries to fit the ΔE spectrum outside the exclusive region as depicted in figure 9.3. The extrapolation of the fitted function inside the exclusive region then serves as a background measurement. In this way the possible dependence of the ΔE shape on $-t'$, which was the drawback of the previous method, is avoided. In case of the ρ^0 the ΔE distribution was fitted with a 7th order polynomial function where the region $[-0.6, 3.0]$ was excluded from the fit, while for the ω a 5th order polynomial was taken outside the region $[-0.75, 3.0]$.

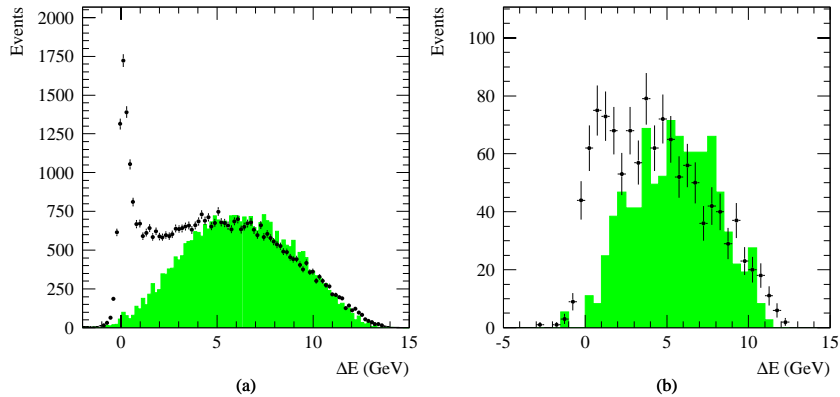


Figure 9.2: The DIS background Zone Method applied to the (a) ρ^0 and (b) ω sample. The dots represent the data, while the histograms are the DIS background distributions measured at $-t' > 0.8 \text{ GeV}^2$ and normalized to the data in the region $\Delta E > 3.0 \text{ GeV}$.

The background fits performed for the different bins are shown in figure C.6 and C.5. The signal-to-background ratios were calculated using equation 9.13, where now the number of background events was determined by integrating the fitted function in the exclusive region. The errors on the fit parameters were propagated in the integral and provided the error on the total number of background events.

This method turns out to be the least stable one of the three different approaches. The drawbacks are that the shape of the background underneath the exclusive ΔE peak cannot be determined exactly from the shape outside the exclusive region. The fits presented here tend to overestimate the amount of background in the exclusive sample. Moreover, especially for the ω analysis, the fits are not really stable when the fit region is varied or when higher or lower order polynomial functions are used, producing very large systematic uncertainties on the s/b values. As the shape of the background seems to vary over the different kinematical bins, it is hard to find a more specific functional shape instead of a simple polynomial to parametrize every bin at the same time.

9.5 Double Dissociative Background

Another possible source of background to our exclusive event samples is double-diffraction dissociation (DD), where the proton is excited into a multiparticle state Y with $M_Y > M_p$. As the final state of the hadron vertex in the scattering reaction remains undetected a certain fraction of these DD reactions cannot be distinguished from the single-diffraction dissociation (SD) where the target proton stays intact.

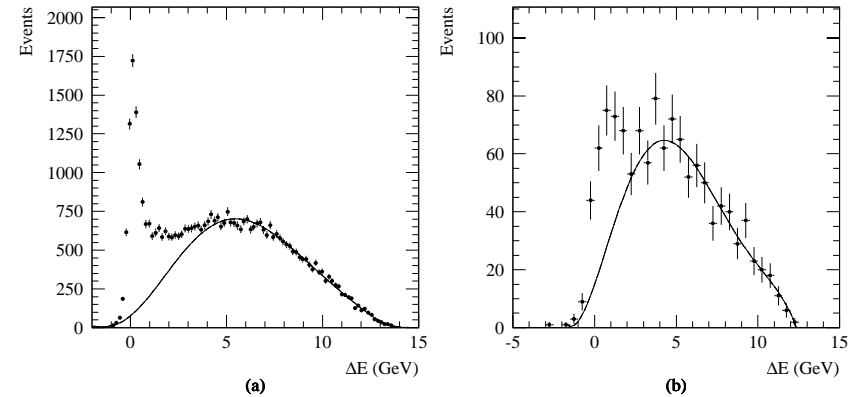


Figure 9.3: The DIS background Fit Method applied to the (a) ρ^0 and (b) ω sample. A polynomial function is fitted to the spectrum outside the exclusive region.

To estimate the DD contamination in our exclusive event samples, the measured baryonic spectrum was taken from $pp \rightarrow Xp$ scattering data [137], where the shape could be parametrized according to [99]

$$M_X^2 \frac{d\sigma}{dM_X^2} = \begin{cases} c \frac{M_X^2 - (M_p + M_\pi)^2}{1.8 [\text{GeV}^2] - (M_p + M_\pi)^2} & (M_X^2 < 1.8 \text{ GeV}^2) \\ c & (M_X^2 \geq 1.8 \text{ GeV}^2) \end{cases} \quad (9.15)$$

The $1/M_X^2$ behaviour at high M_X^2 in diffractive dissociation processes is actually predicted as being due to the dominance of triple pomeron exchange [9]. Using $d\sigma/d\Delta E = 2 M_p d\sigma/dM_X^2$ the DD background shape as depicted in figure 9.4 could be compared to a Monte Carlo ΔE distribution for exclusive vector meson production. To account for the experimental resolution in ΔE the shape given by equation 9.15 was convoluted with a Gaussian with a width of 0.25 GeV for the ρ^0 and 0.47 GeV for the ω as found in section 7.5.

The data are corrected for DD background by assuming the DD/SD ratio measured by H1 in [138] is valid for the HERMES kinematical region as well. They found $DD/SD = 0.65 \pm 0.17$ where the error contains both the statistical and systematic uncertainty, in the region $7 < Q^2 < 35 \text{ GeV}^2$ and $60 < W < 180 \text{ GeV}$. A similar value was found by ZEUS [129] reporting $DD/SD = 0.5 \pm 0.2$ for ρ^0 photoproduction in the region $50 < W < 100 \text{ GeV}$. These results suggest that at least for high energy the DD/SD ratio depends only weakly on the photon virtuality.

Using the H1 measurement to normalize the DD shape to the Monte Carlo ΔE distribution for exclusive events as shown in figure 9.5 yields, together with the applied ΔE cuts, estimations of DD/SD equal to $7.5 \pm 2.0 \%$ for the ρ^0 and $13.0 \pm 3.4 \%$ for the ω analysis, where the error reflects the uncertainty on the assumed normalization.

(Q^2, W) bin	s/b		
	MC Method	Zone Method	Fit Method
(1,1)	11.5 ± 3.0	9.4 ± 2.9	8.6 ± 0.9
(2,1)	12.3 ± 1.6	13.1 ± 2.5	6.2 ± 0.4
(3,1)	7.1 ± 0.9	16.2 ± 3.9	9.9 ± 1.1
(4,1)	5.2 ± 0.7	10.9 ± 3.1	4.9 ± 0.7
(1,2)	46.1 ± 18.0	10.6 ± 2.2	7.6 ± 0.7
(2,2)	23.4 ± 4.2	8.7 ± 1.3	14.4 ± 1.4
(3,2)	13.0 ± 2.1	13.5 ± 3.3	5.9 ± 0.6
(4,2)	7.7 ± 1.4	6.9 ± 2.1	9.1 ± 3.2
Total	11.5 ± 0.7	13.9 ± 1.1	9.7 ± 0.3

Table 9.2: The estimated s/b -ratios in the ρ^0 analysis for the different (Q^2, W) bins. The values denoted with ‘Total’ were obtained by applying the method over the entire kinematic range considered in the analysis.

bin		s/b		
		MC Method	Zone Method	Fit Method
Q^2	1	4.3 ± 2.3	12.4 ± 8.0	2.5 ± 0.5
	2	3.1 ± 1.1	4.1 ± 2.2	1.4 ± 0.4
W	1	3.5 ± 1.4	4.4 ± 2.5	4.9 ± 1.6
	2	3.6 ± 1.5	8.6 ± 5.7	3.2 ± 0.9
Total		3.5 ± 1.0	6.9 ± 2.7	2.0 ± 0.3

Table 9.3: The estimated s/b -ratios in the ω analysis for the different Q^2 and W bins. The values denoted with ‘Total’ were obtained by applying the method over the entire kinematic range considered in the analysis.

A systematic error to this correction of 4.4 % for the ρ^0 and 7.6 % for the ω is assigned to account for the predictions given in [139], where a DD/SD ratio of about 0.27 to 0.30 is expected.

The measured cross section σ^{SD+DD} can be corrected for the estimated DD contamination using

$$\sigma^{SD} = \frac{\sigma^{SD+DD}}{1 + DD/SD}. \quad (9.16)$$

9.6 Radiative Corrections

Radiative corrections relate the observed cross section to the Born cross section. Figure 9.6 shows the diagrams of the processes contributing to the Born (a) and next order cross section. Besides radiative diagrams (b) and (c), also contributions from vacuum polarization (e) and vertex corrections (d) play a role. Radiative corrections are partic-

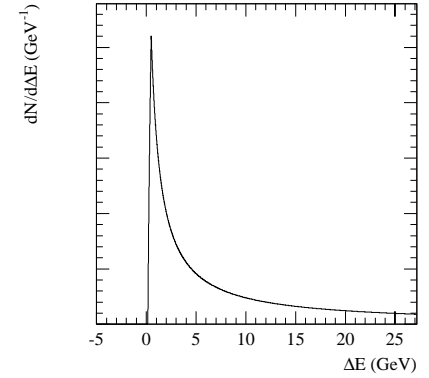


Figure 9.4: The assumed ΔE shape for double-diffraction dissociation data as derived from equation 9.15.

ularly important in electroproduction, due to the small electron mass. They are of less importance in muoproduction or (quasi) real photoproduction.

The radiative corrections (RC) were calculated with the DIFFRAD code [140] which computes the ratio of the measured to the Born cross section

$$\eta = \frac{\sigma_{obs}}{\sigma_{born}} = e^{\delta_{inf}}(1 + \delta_{VR} + \delta_{vac}) + \sigma_F, \quad (9.17)$$

where δ_{vac} corresponds to the contribution of vacuum polarization by leptons and hadrons, δ_{VR} and δ_{inf} come from contributions of vertex functions and soft photon emission (where the exponent is due to the multiple soft photon radiation), and σ_F denotes the hard photon emission contribution.

The DIFFRAD code actually comes in two different versions. The first one, IDIFFRAD, allows one to evaluate the RC using numerical integration methods and takes the mean kinematical value of Q^2 , W and $-t$ over the bins as input from the user. The second version, MDIFFRAD, uses Monte Carlo integration techniques and is able to integrate not only over the photon kinematic variables, but also over (bins in) the phase space of the final lepton. To calculate the RC and to perform the bin integrations in the case of MDIFFRAD, the code needs a model for the Born cross section. The DIFFRAD Born cross section is based on the same model as used in the DIPSI Monte Carlo generator discussed in section 7.2.

The Born cross section needed to compute the RC or to perform the integration over the kinematical bins in case of MDIFFRAD, is unknown. The model parameters cannot really be tuned to get the Born cross section to match the measured cross section as the radiative events are still included in the latter. Therefore a systematic uncertainty due

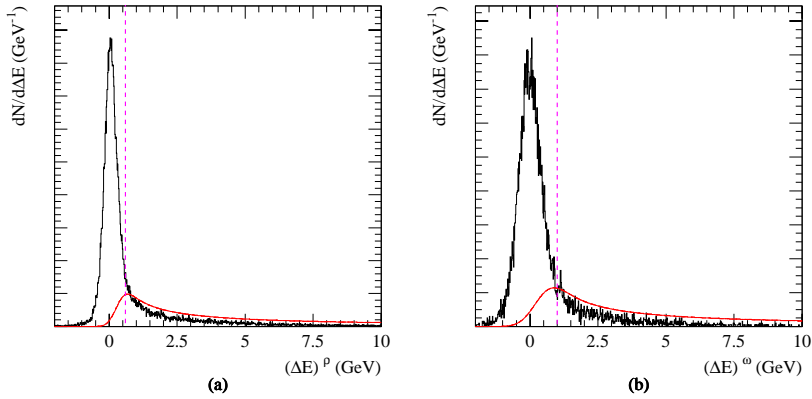


Figure 9.5: The estimation of the double-diffraction dissociation contamination for (a) the ρ^0 analysis and (b) the ω analysis. The histograms show the Monte Carlo ΔE distributions, while the curves are the DD shapes given by equation 9.15 convoluted with a Gaussian to account for the experimental resolution. The dashed lines indicate the ΔE cut applied to the exclusive samples.

to the model dependence of the RC has to be accounted for. The model dependence was estimated by varying the input gluon distribution in the Ryskin model, by varying the P_t slope and by changing the proton form factor from an exponential to dipole form.

Another systematic uncertainty arises when calculating the RC with either IDIFFRAD or MDIFFRAD. IDIFFRAD takes the mean kinematical values of the bins as input, while MDIFFRAD relies on the internal model for the Born cross section to compute the average RC for the considered bins. However, the average kinematics in the bins are actually affected by the RC itself as the uncorrected cross section can have a different behavior than the Born level cross section. Therefore, these mean values for the bins are in fact unknown. In our case the average bin kinematics are computed using our Monte Carlo models without radiative events, which is the best assumption for the true mean kinematical values. But as the Monte Carlo generator and DIFFRAD contain different models for the Born cross section the two versions of the latter code will come up with different results. This feature turns out to be especially important due to the large dependence of the RC on $-t$, and thus on the modelling of the t -dependence in the Born cross section. The Q^2 - and W -dependence seems less pronounced within our relatively small considered kinematical limits. As expected, the difference between the two versions of the code disappears when the size of the kinematical bins is decreased. Another small effect may come from the fact that the t -slope is known to be Q^2 - and W -dependent, while the code cannot handle this dependency.

The radiative corrections are also very sensitive to the exclusivity cut applied in the

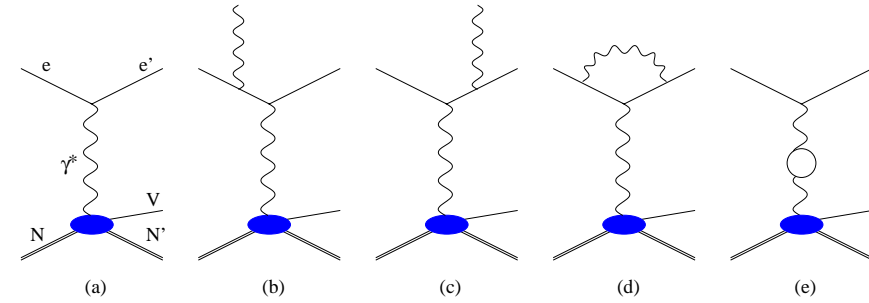


Figure 9.6: Diagram of the Born vector meson production cross section (a) and the diagrams contributing to the next order cross section (b,c,d,e) as included in the calculation of the radiative corrections.

analysis, which is natural as this cut determines how much of the hard radiative events, whose contribution to the correction is always positive, are included into the exclusive sample. It is therefore only to be expected that the radiative corrections in the ω analysis will be significantly smaller than for the ρ^0 , as in the former case a larger portion of the radiative tail of the ΔE peak is retained in the exclusive sample.

The uncertainty on the RC computed with MDIFFRAD due to the model dependence of the Born cross section varied over the bins between 1 and 2 %. The RC values calculated with IDIFFRAD were always systematically higher than the results from MDIFFRAD, with differences ranging from 3 to 5 % in the case of the ρ^0 analysis and 3.5 to 6.5 % in the ω analysis. In the end the RC factor in each bin was taken as the mean of the range of values seen in the systematic studies and an error covering the range was attributed to account for all systematic effects. For the ω analysis the final RC factors were typically around 8 % with a fractional error of about 2.5 %, while for the ρ^0 analysis the RC factors were around 12 % with a fractional uncertainty of about 2 %. All factors are listed in table 9.4 and 9.5.

(Q^2, W) bin	η
(1,1)	0.880 ± 0.014
(2,1)	0.880 ± 0.022
(3,1)	0.878 ± 0.027
(4,1)	0.859 ± 0.018
(1,2)	0.879 ± 0.011
(2,2)	0.879 ± 0.013
(3,2)	0.880 ± 0.019
(4,2)	0.881 ± 0.026

Table 9.4: Radiative correction factors obtained with DIFFRAD for exclusive ρ^0 production in the different (Q^2, W) -bins.

bin	1	2
Q^2	0.925 ± 0.029	0.902 ± 0.016
W	0.913 ± 0.022	0.921 ± 0.022

Table 9.5: Radiative correction factors obtained with DIFFRAD for exclusive ω production in the different bins in Q^2 and W .

9.7 The ρ^0 and ω Cross Section

The final results for the ρ^0 virtual photoproduction cross sections are displayed in figure 9.7 as function of W for different average values of Q^2 . The data are compared to results from other experimental groups. As these various data sets were all measured at different average values of Q^2 , the world data points were rescaled over a small Q^2 -interval to the same average Q^2 values of our measurement. For this scaling a VDM-like dependence of the cross section was assumed, where the difference in the various ϵ values belonging to the data sets was neglected. As one can see the HERMES points form the bridge between the previously measured data at low W where a strong decrease of the cross section with energy is found, and those at high W where the energy behavior is much flatter. Our results are compatible with the existing world data. The big discrepancy between the NMC and E665 data in the two highest Q^2 bins is probably due to a model-dependent subtraction of non-resonant background from the ρ^0 peak performed by NMC [100], which is not done here or by E665.

The result for the ω virtual photoproduction cross section is depicted in figure 9.8 as function of Q^2 . The figure also shows data points from previous measurements. The available world data on electroproduction of ω mesons is rather scarce, especially at higher W , making a more direct comparison with existing data as was done for the ρ^0 more difficult. The HERMES results exhibit a similar Q^2 -behavior as the other available measurements.

The final results for the ρ^0 and ω virtual photoproduction cross section are summarized in table B.3 and B.4 respectively. The systematic uncertainty contains the following items :

- The systematic error on the s/b ratio determination via the DIS Monte Carlo method was estimated by varying the lower ΔE limit for the normalization region (see paragraph 9.4.1). Note that the relative systematic error on the s/b ratio is propagated into the relative error on the cross section as

$$\delta_{s/b}^{rel}(\sigma^{\gamma^* p \rightarrow V p}) = \delta^{rel}(s/b) \frac{1}{1 + s/b}. \quad (9.18)$$

- The error on the acceptance correction was included. This contains both the uncertainty on the geometrical acceptance and the error due to the model dependence of the Monte Carlo generators (see paragraph 9.3).
- The uncertainty on the radiative corrections due to model dependence and method of calculation were taken into account (see paragraph 9.6).

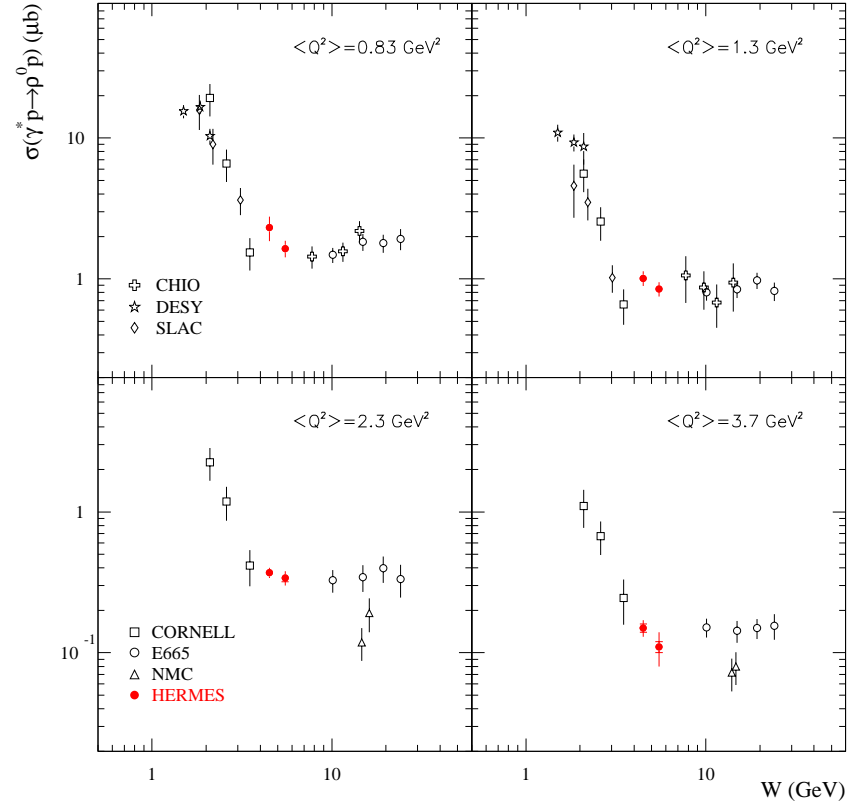


Figure 9.7: The exclusive virtual photoproduction cross section for ρ^0 mesons. The results are plotted as function of W for different average $\langle Q^2 \rangle$ values. The HERMES data points are compared to previous results obtained by CHIO [113], DESY [143], SLAC [27], CORNELL [105], E665 [99] and NMC [100]. The world data have been scaled to the HERMES $\langle Q^2 \rangle$ values assuming a VDM-like Q^2 -behavior of the cross section.

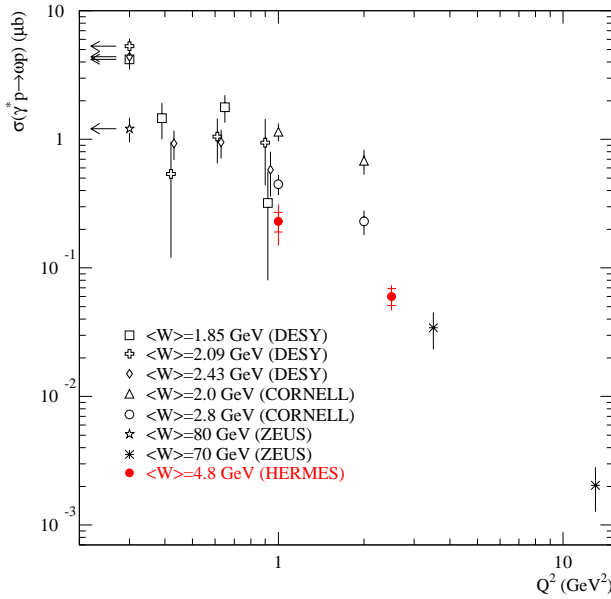


Figure 9.8: The exclusive virtual photoproduction cross section for ω mesons as function of Q^2 . The data are compared to results from previous measurements from DESY [144], CORNELL [105] and ZEUS [164, 165]. The data points marked with an arrow correspond to real photoproduction.

- The systematic error due to the variation of offline analysis cuts varied between roughly 2 and 14 % for both the ρ^0 and the ω analysis.
- The effect of changing the PID cut to separate leptons and hadrons yielded a systematic uncertainty of less than 1 %.
- A 6 % systematic uncertainty due to the luminosity normalization was included.
- The results were obtained by combining the HERMES 1996-97 data on ^1H , where both polarized and unpolarized data samples were added together. For the 1997 data part of the data was reconstructed with standard tracking, which may have a slightly lower tracking efficiency compared to the NOVC tracking method. The uncertainty due to the mixing of the different tracking methods in the event reconstruction was estimated by calculating the cross section using data with NOVC tracking only. This gave an uncertainty of 1 to 6 % for the ρ^0 and 3 to 16 % for the ω analysis.
- The systematic uncertainty on the determination of the fraction of double-dissociative

background in the event samples was included (see paragraph 9.5).

9.8 Q^2 -Dependence of the γ^*p Cross Sections

The Q^2 dependence of the virtual photoproduction cross sections can be parametrized with a VDM-like fit

$$\sigma(Q^2) = \sigma_0 \left(\frac{M_V^2}{Q^2 + M_V^2} \right)^n (1 + \epsilon R(Q^2)), \quad (9.19)$$

where σ_0 is the real photoproduction cross section.

In the VDM n is predicted to be equal to 2 and R is given by equation 2.71. Both the ρ^0 and ω cross section results were fitted using equation 9.19, taking σ_0 and ξ^2 as free parameters. The fitted parameters are listed in table 9.6 and the fits are displayed as ‘Fit 1’ in figure 9.9 and 9.10 for the ρ^0 and ω respectively. The extrapolated values of σ_0 for both the ρ^0 and the ω are in very good agreement with the world data on real photoproduction cross sections as can be seen from figure 9.16 and 9.17. In contrast to that the values of ξ^2 and thus of R are seen to be negative or compatible with zero, which points at a deficiency of this VDM description of the data. Similar values of ξ^2 close to or compatible with zero were also found in other high energy measurements [99, 113], while at lower energy larger values of ξ^2 were obtained [143, 27].

Parameters	$\sigma(\rho^0)$ fits		$\sigma(\omega)$ fits
	$\langle W \rangle = 4.5$ GeV	$\langle W \rangle = 5.5$ GeV	$\langle W \rangle = 4.8$ GeV
σ_0 (μb)	11.5 ± 1.6	10.4 ± 1.3	1.6 ± 0.9
ξ^2	-0.064 ± 0.030	-0.096 ± 0.042	-0.01 ± 0.19
σ_0 (μb)	15.6 ± 4.7	12.3 ± 3.2	1.5 ± 1.4
n	2.80 ± 0.20	2.66 ± 0.19	2.40 ± 0.61
σ_0 (μb)	11.5 (fixed)	10.4 (fixed)	1.6 (fixed)
n	2.60 ± 0.04	2.55 ± 0.05	2.43 ± 0.13

Table 9.6: Results of the fits of expression 9.19 to the Q^2 dependence of the ρ^0 and ω virtual photoproduction cross sections.

In a different approach we relied on the results of the ρ^0 decay angular distribution analysis, presented later on in chapter 11, where the R ratio was extracted from the data and parametrized using expression 11.27. Using this parametrization, the free parameters in the fits labeled as ‘Fit 2’, were now taken to be the exponent n of the VDM-propagator factor and σ_0 . In the case of the ω , we did not perform any extraction of R from the data. However, it was assumed that a similar parametrization as for the ρ^0 was also valid for the ω meson. The obtained values for σ_0 were again consistent with the existing world data, but the uncertainties on the values were larger as compared to the results from ‘Fit 1’. The obtained values for n were systematically higher than the VDM-value of 2. The increase of this exponent actually avoids the negative values of ξ^2 seen in ‘Fit 1’.

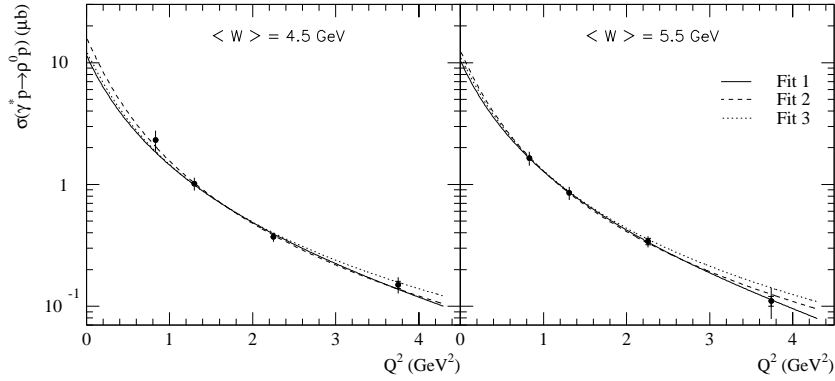


Figure 9.9: Fits of expression 9.19 to the Q^2 dependence of the ρ^0 virtual photoproduction cross section. The free parameters for the fit shown by the full line are σ_0 and ξ^2 , for the dashed line σ_0 and n , and for the dotted line n .

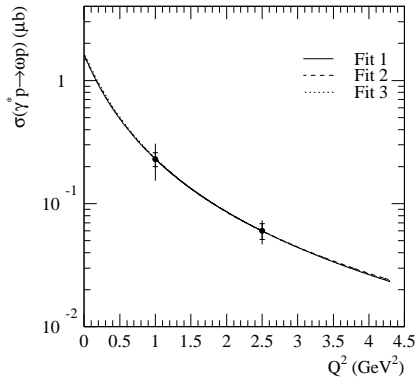


Figure 9.10: Fits of expression 9.19 to the Q^2 dependence of the ω virtual photoproduction cross section. The free parameters for the fit shown by the full line are σ_0 and ξ^2 , for the dashed line σ_0 and n , and for the dotted line n .

The error on n obtained with ‘Fit 2’ is rather large. A better measurement of this exponent can be made by fixing σ_0 in the latter fit at the value obtained with ‘Fit 1’ and performing a 1-parameter fit to the data. The results of these fits are displayed in figure 9.9 and 9.10 as ‘Fit 3’. The determined values for n were all close to around 2.5, which is in disagreement with the VDM prediction of $n = 2$. Similar values for the exponent in ρ^0 production were found earlier by E665 [99] ($n = 2.51 \pm 0.07$) and H1 [133] ($n = 2.5 \pm 0.5$).

The results obtained for the ω are in full agreement with the ρ^0 , which points towards the expected similar behavior of the production cross section of these two mesons.

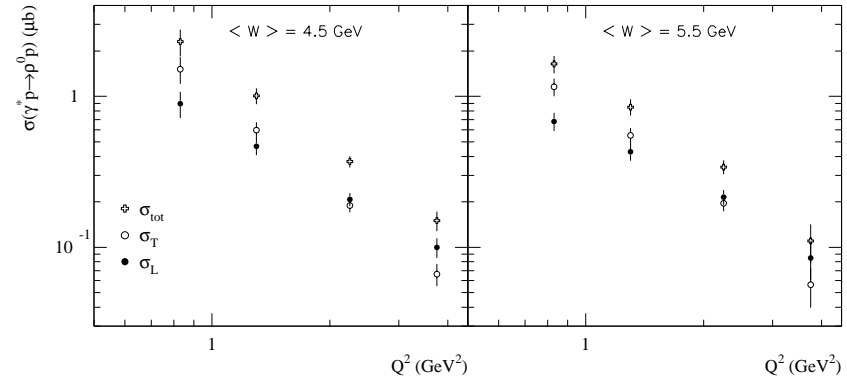


Figure 9.11: The measured σ_T and σ_L for ρ^0 production as function of Q^2 . The error bars correspond to the statistical and systematic uncertainty added in quadrature.

Using the R_{ρ^0} one can also separate the measured total cross section into a longitudinal and transverse part

$$\sigma_T = \frac{\sigma_{tot}}{1 + \epsilon R}, \quad \sigma_L = \frac{\sigma_{tot}}{\epsilon + 1/R}. \quad (9.20)$$

The ρ^0 transverse and longitudinal virtual photoproduction cross sections are depicted in figure 9.11 as function of Q^2 for the two bins in W . In the Q^2 region of our measurements σ_L exhibits a weaker Q^2 -dependence than σ_T . Towards low Q^2 the transverse component dominates the total cross section and σ_L should vanish asymptotically, as the cross section for real photons ($Q^2 = 0$) is purely transverse. σ_L and σ_T are seen to be equal for $Q^2 \approx 2 \text{ GeV}^2$, corresponding to $R \approx 1$. Towards higher Q^2 the longitudinal component becomes the dominant part of the total cross section.

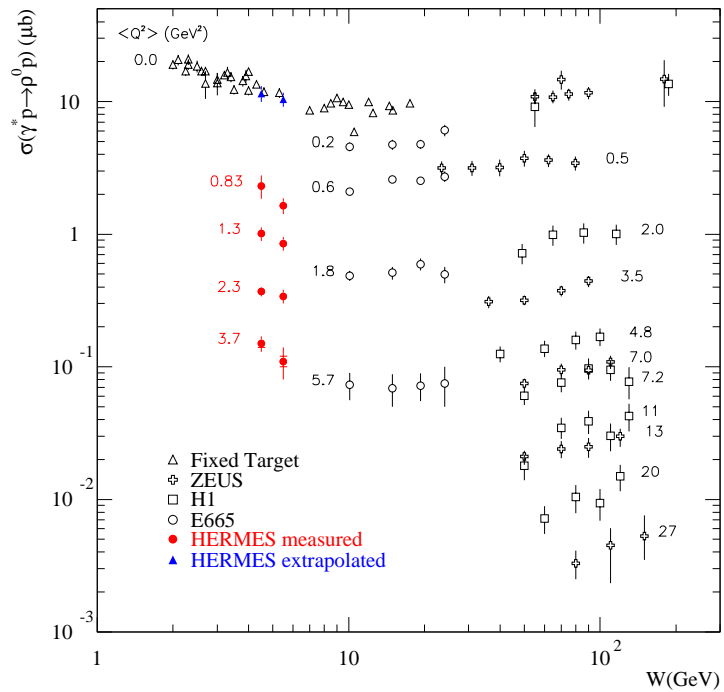


Figure 9.12: The final results for the ρ^0 production cross section measurements as function of W for different values of Q^2 . The data are compared to real photoproduction ($Q^2 = 0$) data points from fixed target experiments, H1 [132] and ZEUS [129, 115, 142] and to electroproduction data from E665 [99], H1 [130] and ZEUS [131].

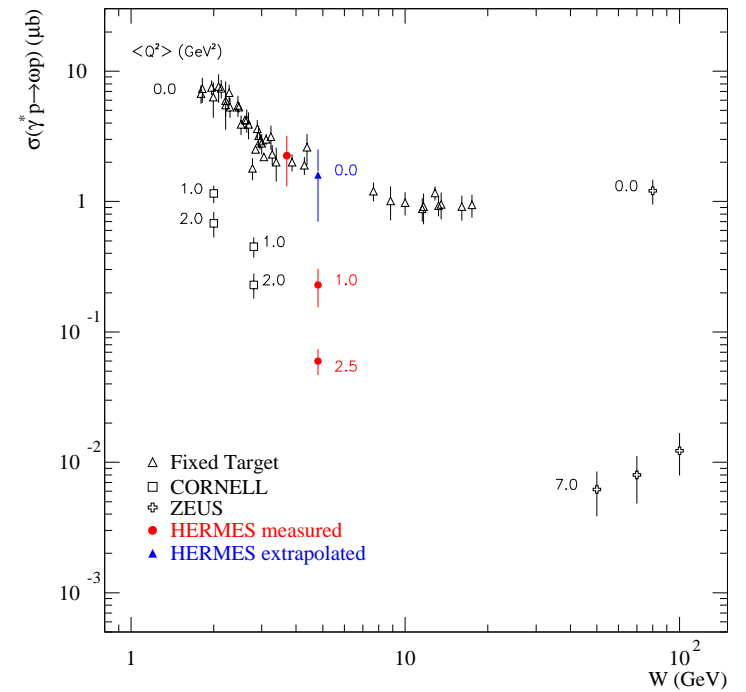


Figure 9.13: The final results for the ω production cross section measurements as function of W for different values of Q^2 . The data are compared to real photoproduction ($Q^2 = 0$) data points from fixed target experiments and ZEUS [164] and to electroproduction data from CORNELL [105] and ZEUS [165].

9.9 World Data on ρ^0 and ω Production

All results obtained in this work on the $\gamma^*p \rightarrow \rho^0p$ and $\gamma^*p \rightarrow \omega p$ cross section are summarized in figure 9.12 and 9.13 respectively, where the data are displayed as function of W for different values of Q^2 . The latter figure also includes the result for the ω real photoproduction cross section derived in chapter 10.

In the low energy region the production mechanism is dominated by Reggeon exchange and the cross sections exhibit a strong decrease with W . This W dependence flattens out in the intermediate energy region at HERMES kinematics, where one has a transition from Reggeon to Pomeron exchange. At high energy the cross sections are seen to rise with W due to the dominant contribution of Pomeron exchange to the production mechanism. At low Q^2 the interactions are governed by the soft Pomeron, which leads to the observed weak energy dependence of the cross sections. When going to higher Q^2 a hard scale is introduced in the reaction mechanism and pQCD models become applicable. In that region the cross sections exhibit a steeper rise with W due to contributions from hard Pomeron exchange.

9.10 Comparison to Model Calculations

The results for the ρ^0 and ω virtual photoproduction cross section as function of W are compared to the model calculations from Haakman *et al.* in figure 9.14 and 9.15 respectively. This model, which relates the vector meson cross sections to a Regge parametrization of the proton structure function $F_2(x, Q^2)$, predicts only the energy dependence of the cross sections. The absolute normalization of the curves has to be fitted to the data for each average value of Q^2 . In case of the ρ^0 , the curves were normalized to the HERMES results in combination with the E665 [99] measurements, where the latter data points were rescaled to the HERMES average Q^2 values, as explained in section 9.7. The model calculations are seen to describe the data very well down to W values of about 4.0 GeV.

In the case of the ω analysis, there was no higher energy data in the appropriate Q^2 region available, so that the theoretical curves were normalized to the present results only. Also here the calculations are seen to predict an energy behavior consistent with the measured cross section.

The observed agreement of the Haakman *et al.* calculations with the data supports the picture of the effective Pomeron trajectory approach to account for multiple Pomeron exchange in diffractive interactions. The model can be extended from the high energy region into the intermediate energy range of the HERMES data.

The real photoproduction cross sections for the ρ^0 and ω , obtained from the extrapolation of the virtual photoproduction cross sections as described in paragraph 9.8, are displayed in figure 9.16 and 9.17 respectively. The data are compared to the model calculations from Haakman *et al.* and to the improved Donnachie and Landshoff parametrizations given in [32]. The two Regge based predictions are seen to describe the ρ^0 data rather well. The ω cross section at low energy is underestimated by the models due to additional contributions to ω production from e.g. one-pion exchange diagrams [144], which are not included in the models.

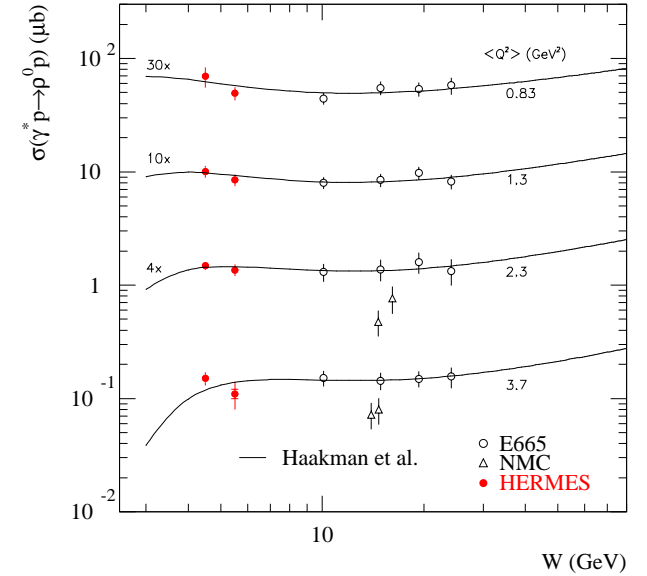


Figure 9.14: The measured ρ^0 virtual photoproduction cross section compared to the model calculations from Haakman *et al.* [33]. The normalization of the curves was based on the combined data points from HERMES and E665 [99].

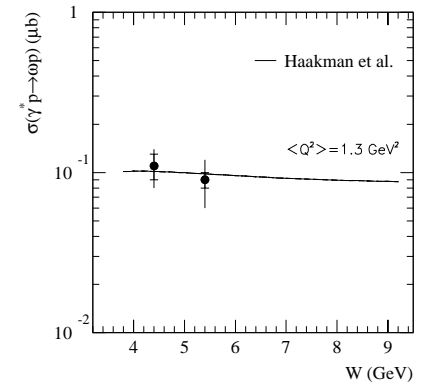


Figure 9.15: The measured ω virtual photoproduction cross section compared to the model calculations from Haakman *et al.* [33].

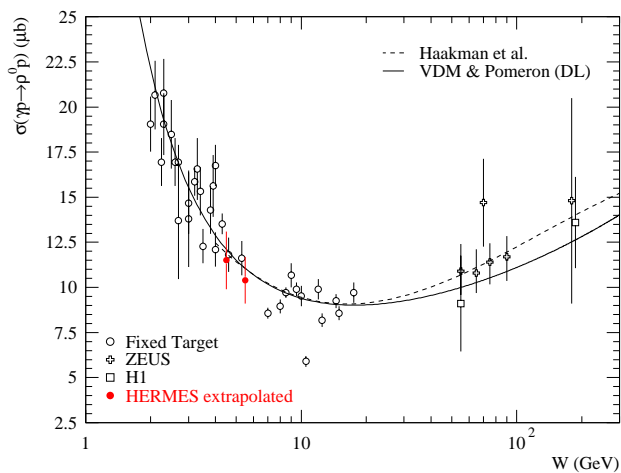


Figure 9.16: The real photoproduction cross section for ρ^0 mesons determined by extrapolation of the virtual photoproduction cross section. The curves are the model predictions from Haakman *et al.* [33] and the improved Donnachie and Landshoff parametrization given in [32].

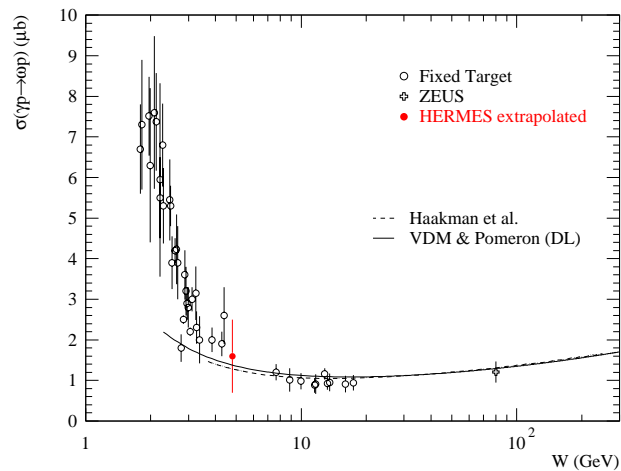


Figure 9.17: The real photoproduction cross section for ω mesons determined by extrapolation of the virtual photoproduction cross section. The curves are the model predictions from Haakman *et al.* [33] and the improved Donnachie and Landshoff parametrization given in [32].

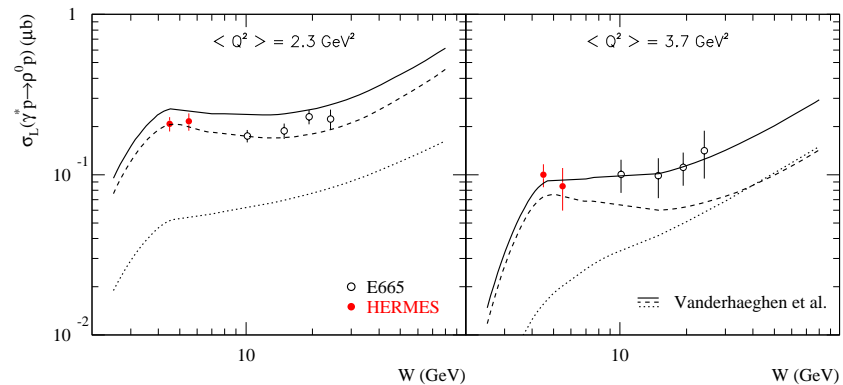


Figure 9.18: The measured longitudinal ρ^0 virtual photoproduction cross section as function of W for the two highest bins in Q^2 . The data points at higher energy are results from E665 [99] which have been rescaled to the HERMES average Q^2 values. The curves represent the model calculations from Vanderhaeghen *et al.* [46]. The dashed (dotted) line is the contribution due to quark (gluon) exchange, while the full line is the incoherent sum of the two.

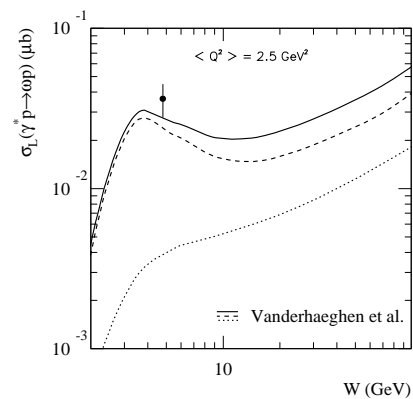


Figure 9.19: The measured longitudinal ω virtual photoproduction cross section as function of W for the two highest bin in Q^2 . The curves represent the model calculations from Vanderhaeghen *et al.* [46]. The dashed (dotted) line is the contribution due to quark (gluon) exchange, while the full line is the incoherent sum of the two.

The model of Vanderhaeghen *et al.* [46], which is based on the OFPD framework, predicts the behavior of the longitudinal component of the virtual photoproduction cross sections. The results of their calculations for the ρ^0 and ω are compared to our measured σ_L in figure 9.18 and 9.19 respectively. σ_L was derived from the total cross section according to equation 9.20 with the R parametrization given in equation 11.27. The comparison is only done for the bins with Q^2 above 2 GeV² to avoid the region at low Q^2 where the higher twist corrections become too large. The model can also not be extended much below $W \approx 4$ GeV as there the scattering mechanism becomes dominated by other reaction channels. The figures show the separate contributions due to quark and gluon exchange. The curves are seen to reproduce the correct order of magnitude of the cross sections and indicate that in the HERMES kinematical region the dominant contribution to diffractive scattering comes from quark exchange diagrams. The gluon exchange contribution alone is not able to explain the observed magnitude of our measurements. Note that the full curves in the figures denote the incoherent sum of the quark and gluon exchange contributions, which means that possible interference terms between the two are not included here.

Additional insight in the physics behind this model is gained when one considers the relation between Bjorken x and the energy, $W^2 = Q^2(1-x)/x + M^2$. At large values of Q^2 and small values of x the two variables x and W are inversely proportional. In the HERMES kinematical region x is roughly around 0.1, which means that scattering reactions are essentially probing the quark distributions in the proton. The small enhancement seen in the quark exchange curves at $W \approx 5$ GeV corresponds to the valence quark contribution in the exchange process. Going at constant Q^2 to higher energies or equivalently lower x means that scattering processes will now predominantly probe the nucleon sea quark degrees of freedom. Towards higher Q^2 at low Bjorken x , the proton gluon distribution rises rapidly and the scattering mechanism will be dominated by gluon exchange.

9.11 Cross Section Ratios

Another quantity of interest is the ratio between the production cross sections for light vector mesons. To compute the $\sigma^{\gamma^* p \rightarrow \omega p} / \sigma^{\gamma^* p \rightarrow \rho^0 p}$ ratio, the ρ^0 production cross section has to be known at the same kinematical points (i.e. same binning) where the ω cross section was evaluated. To avoid re-doing the entire ρ^0 cross section analysis, the Q^2 fits from paragraph 9.8 were used instead to extrapolate to the desired (Q^2, W) points. The fits in the two W bins were averaged to obtain the ρ^0 cross section at the mean value of W from the ω analysis, which is a good enough approximation given the small W range covered by the data. The final ρ^0 cross section value was calculated using ‘Fit 1’ and the errors on the fit parameters were propagated into the uncertainty on the extrapolated value. The difference between the extrapolated values obtained with ‘Fit 1’ and ‘Fit 2’ was accounted for by adding an additional systematic uncertainty to the final result for the ρ^0 cross section. The systematic uncertainty due to the absolute normalization was taken out of the error on the cross sections, as in the ratio this uncertainty drops out. The final systematic error is still somewhat overestimated. However, the uncertainties on both cross sections were dominated by contributions from e.g. the Monte Carlo model dependence,

so that the overestimation will be small. The ratio $\sigma^{\gamma^* p \rightarrow \omega p} / \sigma^{\gamma^* p \rightarrow \rho^0 p}$ evaluated as function of Q^2 is displayed in figure 9.20 and listed in table B.5.

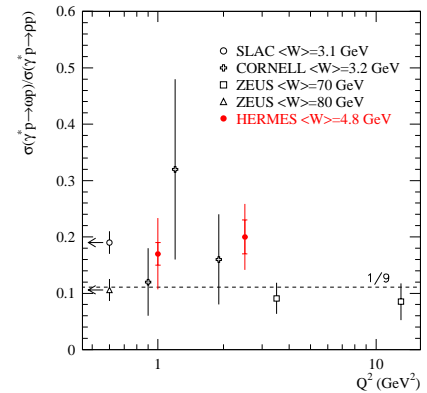


Figure 9.20: The measured ω/ρ^0 production ratio as function of Q^2 . The results are compared to previous measurements from SLAC [163], CORNELL [105] and ZEUS [164, 165].

The HERMES data do not exhibit any variation with Q^2 , consistent with previous measurements at lower and higher energy. At low energy the ω cross section obtains additional contributions compared to the ρ^0 due to e.g. one-pion exchange diagrams [144]. These contributions decrease with energy, leading to a decrease of the ω/ρ^0 production ratio. Asymptotically the ratio goes towards 1/9 which equals the prediction from the SU(4) quark model for the ratio of the photon-vector meson couplings. Based on photoproduction data one expects an ω/ρ^0 ratio in our W range of roughly 0.15, which is in relatively good agreement with our measurement.

9.12 Slope Parameters

Diffractive interactions are dominated by scattering at forward angles, i.e. at low $-t'$. In that region the cross section exhibits an exponential fall-off with $-t'$

$$\frac{d\sigma}{d|t'|} \propto e^{-b|t'|}, \quad (9.21)$$

where b is the characteristic slope parameter. This slope parameter can be related to the size of the interacting particles. Assuming vector meson dominance the electroproduction slope factor can be interpreted as belonging to a hadron-proton scattering process. In

that case the slope parameter b_{hp} can be related [136] through

$$b_{hp} = \frac{1}{3} (\langle r_h^2 \rangle + \langle r_p^2 \rangle) \quad (9.22)$$

to the mean square hadronic radii of the vector meson and proton. This hadronic radius seems to depend both on the number of valence quarks and on the flavor content : the more quarks the larger the system and the heavier the valence quarks the smaller the system becomes. As the ρ^0 and ω both have two valence quarks with similar flavor, similar slope parameters are expected.

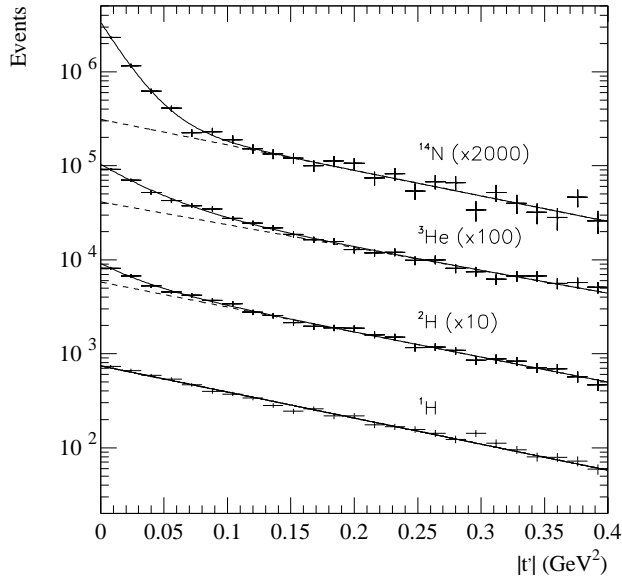


Figure 9.21: The raw $|t'|$ distributions for exclusive ρ^0 production on the different targets used during the 1995-97 running period. The data for ^1H can be described by a single exponential, while for the compound targets one needs a double exponential to fit both the coherent and incoherent contribution.

Our HERMES data clearly show the expected exponential behavior as can be seen from figure 9.21, where the measured $|t'|$ distributions for exclusive, diffractive ρ^0 production on the different targets considered in this work are shown. For a composite target, one has two contributions to the momentum transfer distribution : one coming from incoherent scattering where the nucleus goes into an excited state or breaks up and the scattering is seen to occur on an individual nucleon inside the target, and one corresponding to coherent scattering where the nucleus remains in its ground state and the scattering

is seen to occur on the entire nucleus. Due to the difference in electromagnetic radii between the compound target and a nucleon, the two contributions will show up in the t' -distribution with a different diffractive slope parameter and hence a double exponential is needed to describe the spectrum

$$\frac{d\sigma}{d|t'|} = \sigma_{coh} b_A e^{-b_A |t'|} + \sigma_{incoh} b_N e^{-b_N |t'|}, \quad (9.23)$$

where b_A and b_N are slope parameters corresponding to the coherent and incoherent part of the cross section. The fitted slope parameters for each of the targets are listed in table 9.7. For each of the composite targets, the incoherent slope parameter was compatible with the value for the proton.

Target	Slope Parameter (GeV^{-2})	
	Incoherent	Coherent
^1H	6.39 ± 0.13	
^2H	6.13 ± 0.36	31.7 ± 10.7
^3He	5.60 ± 0.75	26.2 ± 6.7
^{14}N	6.25 ± 0.46	52.2 ± 2.8

Table 9.7: The fitted ρ^0 production slope parameters for the different targets. No corrections were applied to the results listed here.

The obtained values for the coherent slope factors are fully compatible with the values predicted by the relation¹ $b_A \approx R_A^2/3$ with the measured electromagnetic radii $R_A = 2.1$ fm, $R_A = 1.9$ fm and $R_A = 2.5$ fm [145] for ^2H , ^3He and ^{14}N respectively.

To come to the final values of the diffractive slope parameters for vector meson production on ^1H , one has to correct the $|t'|$ distribution for DIS background, for acceptance and radiative effects. The amount of DIS events contamination in our exclusive samples varies with e.g. the kinematical variables $-t'$ and Q^2 . The background increases towards higher values of $-t'$ and Q^2 . This means that for each Q^2 -bin the slope parameter will be modified due the background and that this distortion becomes larger for higher Q^2 . To counteract this effect a tighter cut on ΔE can be applied, decreasing both the non-exclusive and double dissociative background contributions to the event sample. In case of the ρ^0 analysis a cut of $\Delta E < 0.4$ GeV^2 was used, which can be done without losing too much statistics. For the ω the ΔE cut was retained as before since there the statistical uncertainty is already quite large.

The $|t'|$ -distributions were corrected for DIS using the standard Monte Carlo method as outlined in section 7.6. The statistical error on the MC normalization factor was taken into account in the MC background $|t'|$ distributions, which were scaled according to the obtained signal-to-background ratios. The acceptance for the $|t'|$ spectra was determined using the VDM and DIPSI generator for the ρ^0 and ω analysis respectively and is shown in figures 9.22 (a) and (b).

The radiative corrections to exclusive vector meson production depend on $-t'$, especially at the low values where the slope parameter is measured [141]. This results in the

¹The contribution to the slope coming from the vector meson radius can be neglected here.

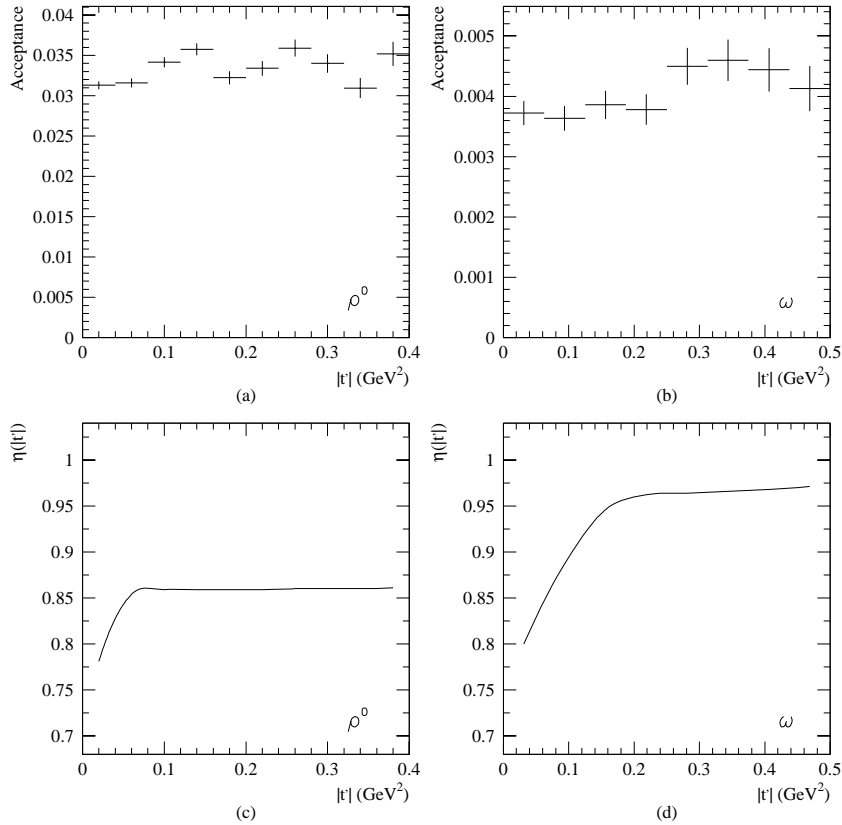


Figure 9.22: The acceptance (a) and (b) and radiative correction factors (c) and (d) for the $|t'|$ distribution of exclusive ρ^0 and ω production.

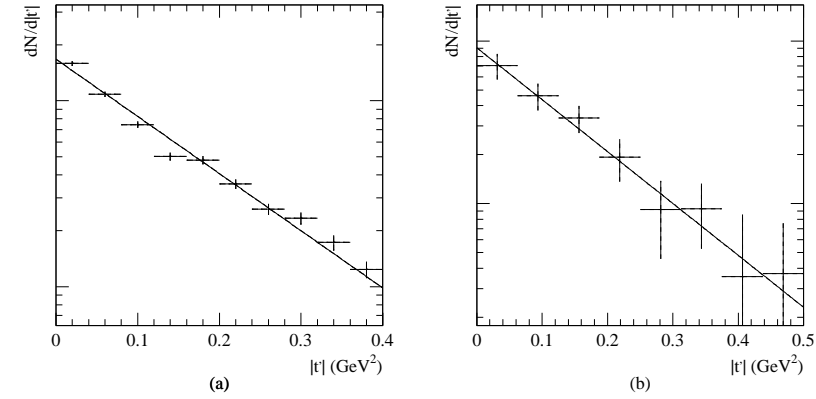


Figure 9.23: The $|t'|$ distribution for exclusive (a) ρ^0 and (b) ω production. The spectra were corrected for DIS background and acceptance and radiative effects.

fact that the slope of the Born cross section differs from the measured value, which leads to the necessity of including the RC. As the DIFFRAD code can only compute correction factors as function of t and not of t' , the average value $\langle t \rangle$ for each bin in $|t'|$ was computed using the Monte Carlo and given as input kinematics to the RC code. The resulting RC factors for the ρ^0 and ω are shown in figures 9.22 (c) and (d) respectively. The difference between the RC curve for the ω and ρ^0 stems mainly from the very different cuts in ΔE used.

The final values for the slope factors including all corrections obtained in the kinematic range $0.7 < Q^2 < 5.0 \text{ GeV}^2$ and $4.0 < W < 6.0 \text{ GeV}$ for production on ^1H were

$$b_{\rho^0} = 7.08 \pm 0.14 \text{ (stat.) } {}_{-0.08}^{+0.58} \text{ (syst.) GeV}^{-2}, \quad (9.24)$$

$$b_{\omega} = 7.34 \pm 0.67 \text{ (stat.) } {}_{-0.64}^{+1.59} \text{ (syst.) GeV}^{-2}. \quad (9.25)$$

As expected, the diffractive slope parameters for both mesons are compatible within their statistical uncertainty. The systematic errors include the following contributions :

- The effect due to the variation of the offline analysis cuts was taken into account.
- The upper limit of fitted region in $|t'|$ was varied.
- The dependence of the acceptance correction on the MC generator model was estimated by varying the diffractive slope parameter and the exponent of the VDM propagator factor describing the Q^2 dependence of the cross section in the generator.
- The uncertainty on the DIS background correction was estimated by varying the lower limit of the data-MC normalization region in ΔE .

- The uncertainty on the RC curve was determined by varying the model parameters of the DIFFRAD code.
- The double-dissociative background contained in the exclusive sample may distort the measured slope parameter. It was found by H1 [138] that the SD and DD diffractive slope typically differ by about 5 GeV^{-2} . Assuming this still holds for our kinematic region, the effect of the DD contamination on our measured SD slope parameter b_{SD} can be estimated by fitting the $|t'|$ spectrum with a double exponential

$$\frac{d\sigma}{d|t'|} = a \left(e^{-b_{SD}|t'|} + \left(\frac{DD}{SD} \right) e^{-(b_{SD}-5.0[\text{GeV}^{-2}])|t'|} \right), \quad (9.26)$$

where the DD/SD ratio was determined as described in paragraph 9.5. Note that with the lower ΔE cut used for the ρ^0 the DD/SD ratio was determined to be only $4.4 \pm 1.2 \%$ instead of the value quoted in that section.

In general it was observed that taking into account the RC increased the result of the diffractive slope parameter by about 4 to 10 %. The estimated increase of the result due to the presence of DD background in our exclusive samples amounts to about 0.5 GeV^{-2} for the ρ^0 and 1.3 GeV^{-2} for the ω .

The slope parameter of the ρ^0 was also studied as function of Q^2 , where the final $|t'|$ distributions are shown in figure 9.24. The obtained slope values are compared² to data from other experiments in figure 9.25. The data clearly indicate a common decrease of the slope parameter with Q^2 starting from the real photoproduction region.

The observed Q^2 -dependence of the diffractive slope parameter can be interpreted as an experimental indication of the decrease of the effective γ^*p interaction radius with Q^2 . When describing the vector meson production process as proceeding via an intermediate $q\bar{q}$ pair which is projected onto the vector meson state, then the transverse size r_Q of this quark configuration depends on the photon virtuality [146]

$$r_Q = \frac{2}{\sqrt{M_V^2 + Q^2}}, \quad (9.27)$$

which reflects itself qualitatively in the Q^2 dependence of the slope parameter. In the same way one could interpret this phenomenon in the VDM picture as being due to the changing with Q^2 of the transverse size of the vector meson in which the virtual photon fluctuates before the interaction with the target. Asymptotically the slope parameter is expected to be determined by the proton radius only, leading to a value of $b \approx R_p^2/3 \approx 5 \text{ GeV}^{-2}$, which agrees with the data as can be seen in figure 9.25. This value is also roughly

²When comparing this measured slope parameter to results from other experiments we should note that here we have measured the slope of the $|t'|$ distribution, while some high energy experimental groups reported on the $|t|$ slope parameter instead. Some collaborations even report on the p_T^2 slope, which is however, similar to the $|t'|$ slope. The definition of t' in equation 6.10 clearly indicates that the two slope parameters are related via t_0 . However, t_0 is not constant but depends on Q^2 , W and M_V^2 and results not only in a shift and distortion of the exponential function in the $|t|$ distribution, which can be seen in the data, but also in a slight modification of the Q^2 and W dependence of the slope parameter. However, at high energy $t \sim t' \sim p_T^2$ which justifies the comparison with the experimental high energy data shown here.

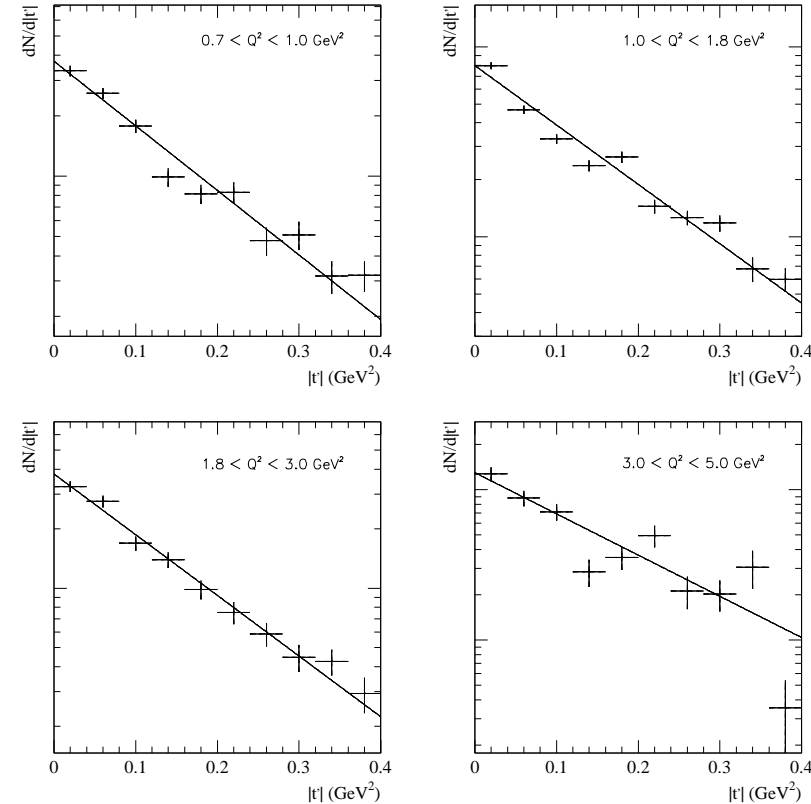


Figure 9.24: The measured $|t'|$ distribution for exclusive ρ^0 production as function of Q^2 . The spectra were corrected for DIS background and acceptance and radiative effects.

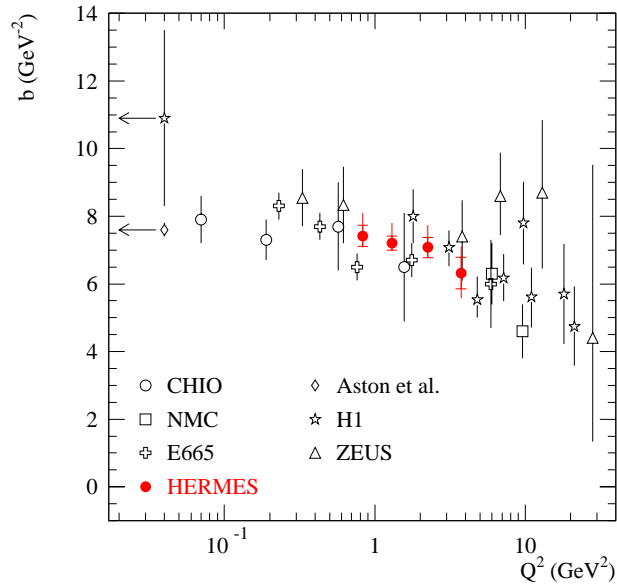


Figure 9.25: The measured Q^2 dependence of the diffractive slope parameter in exclusive ρ^0 production. The data are compared to electroproduction results from CHIO [113], E665 [99], NMC [100], H1 [130, 133], ZEUS [131] and to real photoproduction results from H1 [132] and Aston *et al.* [116], where the latter was measured in a similar energy region as our data.

compatible with the observed slope in pp interactions where $b \approx 2R_p^2/3$. The measured slope for ϕ mesons is systematically lower [55] than for the ρ^0 and ω indicating that the ϕ meson has a smaller radius than the ρ^0 . The decrease of the interaction radius with Q^2 points to the short distance scale of the high Q^2 interactions and proves the applicability of pQCD approaches to the description of vector meson production. In case of the heavy quark J/Ψ system, the slope is already in real ($Q^2 = 0$) photoproduction [55] close to the asymptotical value observed for the ρ^0 , meaning that here a perturbative approach is justified even for low Q^2 .

Apart from the Q^2 -dependence presented above, the diffractive slope parameter is also expected to exhibit a W -dependence, referred to as shrinkage, which was explained in section 2.6. Due to the limited W -region covered by the present experiment, this kind of effect was not investigated in the data.

9.13 Nuclear Transparency

The nuclear transparency for incoherent virtual photoproduction of vector mesons σ_A^{inc} on a nucleus containing A nucleons is defined as

$$T_A \equiv \frac{\sigma_A^{inc}}{A \sigma_H} = \frac{N_A}{A N_H} \frac{\mathcal{L}_H}{\mathcal{L}_A}, \quad (9.28)$$

where N_A and \mathcal{L}_A are the number of events and the total luminosity measured on the nuclear target. The calculations presented in [147] based on Glauber multiple scattering theory, indicate that this nuclear transparency may strongly depend on l_c/R_A , where R_A is the nuclear radius ($R_A \approx 1.2A^{1/3}$ fm) and l_c the coherence length as defined by

$$l_c = (q_L)^{-1} = (p^\gamma - p_L^V)^{-1} = \frac{2\nu}{Q^2 + M_V^2 + (p_T^V)^2}, \quad (9.29)$$

with q_L being the difference between the longitudinal momentum of the photon and that of the vector meson. The transverse momentum p_T^V of the vector meson is often neglected in the forward region. The incoherent cross section for virtual photoproduction is calculated and found to behave differently in the two limiting cases of $q_L \rightarrow 0$ and $q_L \rightarrow \infty$. In the low energy limit the attenuation of the outgoing vector meson is governed by the nuclear thickness it encounters from the point of its formation on, until it exits the nucleus. For high energy on the other hand, the attenuation of the meson is determined by the thickness of the target along the total path of the virtual photon and vector meson together and governed by the same inelastic meson-nucleon cross section, independently of whether it acts on the incoming photon or outgoing meson. This leads to the conclusion that in this case the photon has already fluctuated into a virtual vector meson long before the interaction with the target which puts the meson on-shell. This observation is actually similar to the VDM picture of vector meson production. The coherence length can in this respect be interpreted as a length or timescale during which a virtual state originating from a photon fluctuation can exist. If the coherence length is long with respect to the nuclear radius and mean free path of a vector meson in nuclear matter, then the probability is high that the photon already fluctuated into a virtual meson long before its interaction with the target. The authors of [147] predict the approximate relation

$$T_A(q_L \rightarrow 0) \approx [T_A(q_L \rightarrow \infty)]^2, \quad (9.30)$$

and find that the half value between the low and high energy limit is reached for $q_L R_A \approx 1.5$.

The nuclear transparency for exclusive ρ^0 production at HERMES was determined [148] for ^2H , ^3He and ^{14}N . Here we try to determine the same quantities for exclusive ω production. Based on the observations made in the analysis of the ρ^0 data both the correction for coherent events still present in the nuclear event sample and the nuclear dependent radiative effects on T_A are assumed to be small and are therefore not taken into account.

Due to the low statistics of especially the ^{14}N sample, the result for T_A turns out to be very unstable against offline cuts. The stability of the result was improved by applying the following procedure. As was shown in the previous paragraph, the slope for incoherent production does not depend on the nuclear target mass. Therefore the $-t'$ distribution

for the nucleon was fitted between $0.0 < -t' < 0.5 \text{ GeV}^2$ with an exponential to extract this slope parameter. Then for each of the nuclear targets a fit with an exponential was performed in the region $0.1 < -t' < 0.5 \text{ GeV}^2$, where only the normalization was left as a free parameter and the slope factor was fixed at the value determined for the nucleon. The nuclear transparency was then extracted via equation 9.28 where the ratio of the number of events was simply given by the ratio of the normalization factors of the exponentials.

The nuclear transparency as function of l_c for exclusive ω production is displayed in figure 9.26 together with the results of the previously performed ρ^0 analysis. The ω result is within its very large uncertainties compatible with the ρ^0 as expected. The results for the ω are summarized in table B.7. The quoted systematic uncertainties include the following contributions :

- The influence due to variation of the offline cuts was taken into account.
- The incoherent slope factor used in the fitting procedure was varied within its statistical uncertainty.
- The results were derived using only events with NOVC tracking.
- The change in the results was determined in the case where the number of events was corrected for DIS background by taking the s/b ratio into account in the standard way.
- The results obtained here are extracted from combinations of data sets taken during different running periods. To estimate the effect of any possible time dependence of the result (difference in normalization, yield fluctuations . . .), the nuclear transparency was determined using only data sets belonging to the same data taking year.

All items listed above resulted in rather similar contributions to the total systematic uncertainty. The curves in the figure represent the predictions from [147] and are seen to describe the ρ^0 data rather well. The dependence of the nuclear transparency on the coherence length is most pronounced for ^{14}N . For $l_c \ll R_A$ the transparency is only reduced by the vector meson final state interactions with the target. In that region we find for the ρ^0 meson $T_A \approx 0.7$. For $l_c \gg R_A$, the transparency is determined by both the initial state interactions (ISI) of the $q\bar{q}$ pair and the final state interactions (FSI) of the meson with the target. In that case the ρ^0 data give $T_A \approx 0.4$, which is in good agreement with expression 9.30. The results obtained here indicate that the $q\bar{q}$ pair and the meson have roughly equally strong interactions with the target.

The strong coherence length effect observed in the nuclear transparency for incoherent vector meson production is an important input for studies of so-called color transparency (CT). The color transparency phenomenon is the prediction that at high Q^2 and ν the $q\bar{q}$ pair and the vector meson are produced in a non-interacting configuration of reduced transverse size, which results in the nuclear transparency going to 1. Deviations from the predicted nuclear transparency behavior presented above may be indications of CT, although our energy range is rather low to expect large effects [147]. In [151] it is argued that coherent vector meson production would be more sensitive to signals of CT than incoherent production.

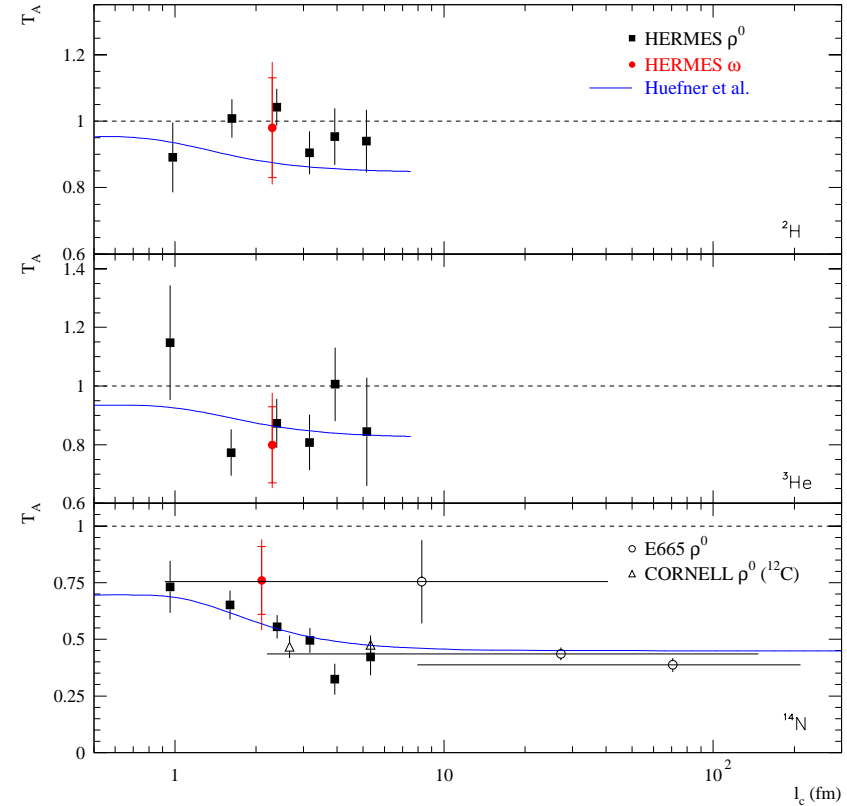


Figure 9.26: The measured nuclear transparency for ρ^0 and ω production as function of the coherence length l_c for ^2D , ^3He and ^{14}N . The HERMES ρ^0 data points are taken from [148] and are shown with the statistical and systematic uncertainties added together in quadrature. The results are compared to data from E665 [149] and CORNELL [150]. The curves correspond to the results of the model calculations from Hüfner *et al.* [147].

9.14 Coherent vs. Incoherent Cross Section

The fits of the $|t'|$ distribution performed in paragraph 9.12 allow a simple determination of the ratio of coherent to incoherent production cross section on composite targets. Rewriting of equation 9.23 as

$$\frac{d\sigma}{d|t'|} = c \left(\frac{\sigma_{coh}}{\sigma_{incoh}} b_A e^{-b_A |t'|} + b_N e^{-b_N |t'|} \right), \quad (9.31)$$

with c a normalization constant, gives immediate access to this ratio in a 4-parameter fit of this expression to the measured $|t'|$ distributions.

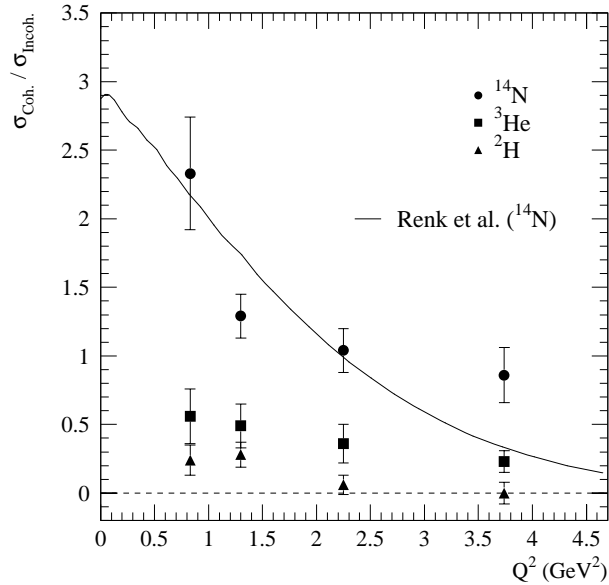


Figure 9.27: The ratio of the coherent to incoherent cross section for exclusive ρ^0 production on different targets. The values are extracted from a double exponential fit of the $-t'$ distribution for several Q^2 bins. Error bars are statistical only. The curve corresponds to the prediction from Renk *et al.* [151].

The results of a very preliminary analysis are listed in table 9.8 and presented in figure 9.27, where the coherent to incoherent ρ^0 production ratio for ²H, ³He and ¹⁴N is plotted as function of Q^2 . The error bars are statistical only. The results appear rather stable against systematic variations of the fitting procedure. However, no further studies

$\langle Q^2 \rangle$ (GeV ²)	$\sigma_{Coh.} / \sigma_{Incoh.}$		
	² H	³ He	¹⁴ N
0.83	0.24 ± 0.11	0.56 ± 0.20	2.33 ± 0.41
1.3	0.28 ± 0.09	0.49 ± 0.16	1.29 ± 0.16
2.3	0.06 ± 0.07	0.36 ± 0.14	1.04 ± 0.16
3.7	0.00 ± 0.08	0.23 ± 0.08	0.86 ± 0.20

Table 9.8: The measured ratio versus Q^2 of coherent to incoherent ρ^0 production for different targets. Error values are statistical only.

were performed as yet to investigate e.g. the effects of the detector acceptance or radiative corrections. The curve represents the predictions from a multiple scattering model of Renk *et al.* [151] for ¹⁴N in the HERMES kinematical region and is seen to describe the data rather well. Any effects of CT would show up as a deviation from this curve at large Q^2 .

Chapter 10

The ω Real Photoproduction Cross Section

The previous chapter dealt with the extraction of the virtual photoproduction cross section which could be derived from electroproduction data. In principle it is possible to estimate from these data the real photoproduction cross section by adding the VDM-like Q^2 -dependence to the virtual photon flux. An alternative way of accessing the real photoproduction cross section is provided by our quasi-real photoproduction trigger, which captures low Q^2 events containing at least two hadrons. In this chapter we describe the extraction of the $\gamma p \rightarrow \omega p$ cross section from the HERMES 1997 quasi-real photoproduction sample.

10.1 Reconstruction of Photoproduction Trigger Event Kinematics

The events collected using the HERMES photoproduction trigger contain no information on the scattered positron and hence the virtual photon kinematics cannot be directly calculated. Only the hadron kinematics with respect to the HERMES coordinate system can be fully reconstructed. However, as the average Q^2 of the event sample is close to zero, it is a fair assumption to set $Q^2 = 0$ and $q_T = 0$, where the latter is the transverse momentum of the photon with respect to the beam axis. It is then straightforward to derive from energy and momentum conservation in the γp system that the energy of the photon is given by

$$E_\gamma = \frac{E_v M - M_v^2/2}{M + v_z - E_v}, \quad (10.1)$$

where v_z is the momentum of the vector meson in the z -direction and E_v and M_v its energy and invariant mass. To prove the validity of this equation figure 10.1 shows the photon energy calculated using the above expression versus its actual value for Monte

Carlo events generated with the DIPSI generator with Q^2 values between $4 \cdot 10^{-10}$ and 2 GeV^2 . Knowing the photon's energy immediately gives us the γp center of mass energy $W = M^2 + 2ME_\gamma$, which is an important quantity for the cross section determination.

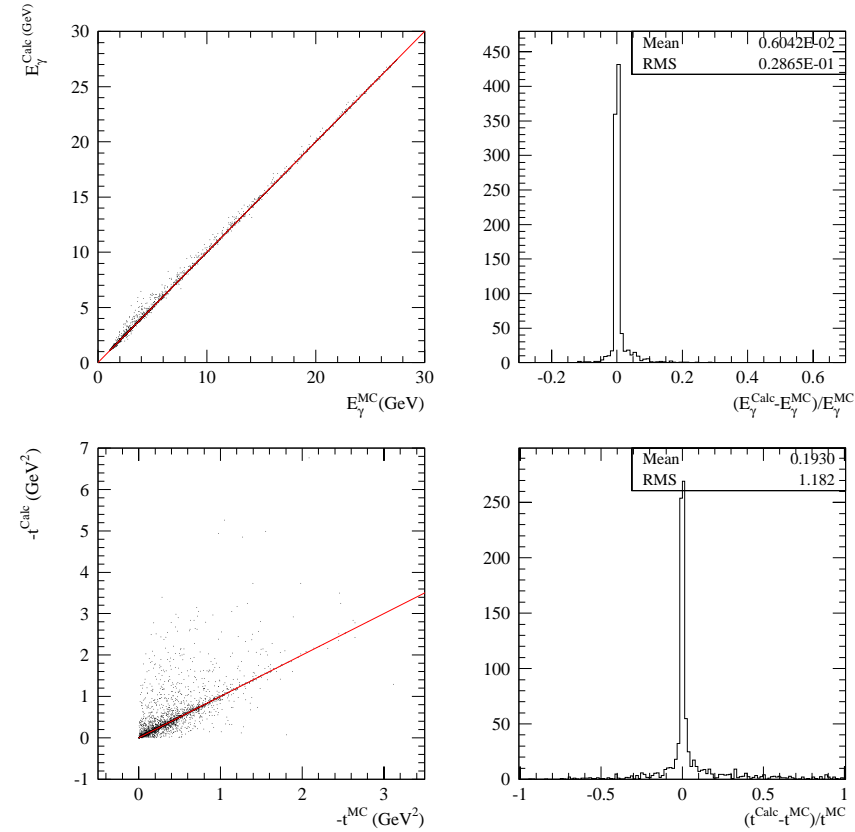


Figure 10.1: Correlation between the calculated and actual value and resolution of E_γ and $-t$ for quasi-real photoproduction ω events.

Using the same approximations as above one can easily come to the following expression for the momentum transfer

$$t = 2E_\gamma(v_z - E_v) + M_v^2. \quad (10.2)$$

However, as can be seen from figure 10.1, this turns out to be less accurate and not so useful in the analysis.

10.2 Photoproduction Trigger Efficiency

While the efficiency of the standard HERMES trigger is close to one above the calorimeter threshold [152], this is not true for the photoproduction trigger. When extracting absolute cross sections this trigger efficiency value needs to be folded into the normalization.

The efficiency of a trigger can be determined from the efficiency of its individual trigger components. The trigger logic of the photoproduction trigger together with some subtriggers is listed in table 3.3. The photoproduction trigger requires a coincidence between the top and bottom detector, with signals in the two hodoscopes H0 and H1, the preshower detector H2 and in the BC1. The efficiencies of the photoproduction trigger components are given by

$$\epsilon_{H0} = \frac{T18 \cdot T21}{T18}, \quad \epsilon_{H1} = \frac{T20 \cdot T21}{T20}, \quad \epsilon_{H2} = \frac{T19 \cdot T21}{T19}, \quad \epsilon_{BC \cdot H0_{cut}} = \frac{T21 \cdot T28}{T21}, \quad (10.3)$$

where the latter is the combined efficiency of the BC component, the H0 multiplicity cut and the top-bottom coincidence (2 tracks) requirement. As in this analysis the trigger is used to capture the two charged decay pions of the ω , these efficiencies have to be determined for the detection of charged hadrons. The hodoscope efficiencies were calculated using events containing one single hadron, while for the BC·H0_{cut} efficiency events were considered with at least one hadron in each detector half. Events containing leptons or positrons were discarded from the efficiency calculation. The efficiency of the photoproduction trigger itself is equal to

$$\epsilon_{tr28} = \epsilon_{H0}^2 \cdot \epsilon_{H1}^2 \cdot \epsilon_{H2}^2 \cdot \epsilon_{BC \cdot H0_{cut}}, \quad (10.4)$$

where the hodoscope efficiencies are to be squared since we detect two charged hadrons.

The trigger efficiency was calculated on a run-by-run basis. For the cross section calculation the average efficiency over the runs used in the analysis was taken. This gave for the 1997 data on ^1H an average efficiency of $67 \pm 4\%$.

The systematic error on this trigger efficiency is expected to be of minor importance and was neglected with respect to the other contributions to the total systematic uncertainty of the cross section result. More detailed information on the HERMES photoproduction trigger can be found in [152].

10.3 Determination of the Real Photon Flux

As for the photoproduction data we do not have any precise information on the scattered positron, one is not able to calculate the photon flux on an eventwise basis. Instead one has to integrate the flux over the kinematical range considered in the analysis. Since we want to extract a value for the real photoproduction ($Q^2 = 0$) cross section we should integrate the real photon flux factor. The correct expression for this flux can be obtained from the consideration that in the limit of Q^2 going to zero, one has that $\sigma_L^{\gamma^*p} \xrightarrow{Q^2 \rightarrow 0} 0$, while $\sigma_T^{\gamma^*p} \xrightarrow{Q^2 \rightarrow 0} \sigma^{\gamma p}$. Assuming a VDM like Q^2 dependence gives

$$\sigma_T^{\gamma^*p}(Q^2, W) = \left(1 + \frac{Q^2}{M_V^2}\right)^{-2} \sigma^{\gamma p}(W), \quad (10.5)$$

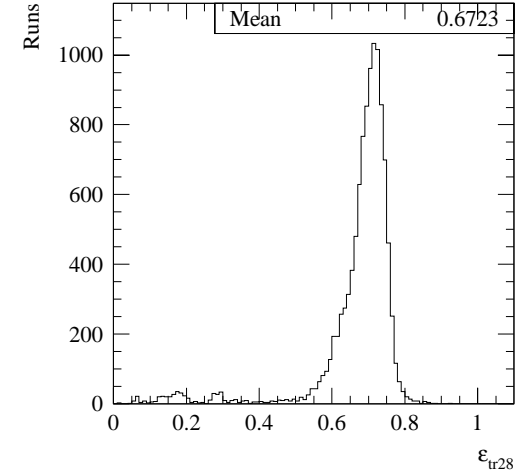


Figure 10.2: The HERMES photoproduction trigger efficiency computed for the 1997 runs on a H target.

$$\sigma_L^{\gamma^*p}(Q^2, W) = \left(1 + \frac{Q^2}{M_V^2}\right)^{-2} R_V \sigma^{\gamma p}(W), \quad (10.6)$$

where $R_V = \sigma_L^{\gamma^*p}/\sigma_T^{\gamma^*p} = \xi^2 Q^2/M_V^2$. Introducing the latter two expressions in equation 2.30 leads to the following relation between the electro- and real photoproduction cross section with the real photon flux factor $\Phi(Q^2, W)$

$$\frac{d^2\sigma_{ep \rightarrow ep\omega}}{dW dQ^2} = \Phi(Q^2, W) \cdot \sigma^{\gamma p \rightarrow \omega p}, \quad (10.7)$$

with

$$\Phi(Q^2, W) = \frac{\alpha W K}{2\pi Q^2 M_V^2} \left(1 + \frac{Q^2}{M_V^2}\right)^{-2} \cdot \left[y^2 + 2(1-y) \left[\frac{1}{1 + Q^2/\nu^2} \left(1 + \xi^2 \frac{Q^2}{M_V^2}\right) - \frac{Q_{min}^2}{Q^2} \right] \right], \quad (10.8)$$

where the term $Q^2/4E^2$ was neglected. $Q_{min}^2 = m_e^2 y^2 / (1-y)$ is the lowest physically possible value of Q^2 due to the finite electron mass and K is given by equation 2.29. The flux was integrated over the kinematical range $3.0 < W < 5.0$ GeV and $Q_{min}^2 < Q^2 < 1.0$ GeV² where Q_{min}^2 can be computed using $y_{min} = 0.040$ corresponding to the threshold for ω production. The integrated real photon flux was $\Phi = 0.03$ GeV⁻³. A systematic

uncertainty of 3.7 % was accorded due to the uncertainty in the value of ξ^2 which was varied between 0 and 1. Note that the upper limit in Q^2 is chosen arbitrarily at 1.0 GeV^2 as this is more or less corresponds to the limit of the acceptance for pure photoproduction trigger events. Due to the steep Q^2 -dependence of the flux, which decreases drastically with increasing Q^2 , a variation of this upper limit has only a negligible effect on Φ .

10.4 Non-exclusive Background Subtraction

Due to the lack of information on the scattered positron, we cannot compute any measure of exclusivity like ΔE for the standard trigger events. Hence, there is no direct way of suppressing non-exclusive background from the sample and the latter may actually comprise the dominant part of the events. The only way to correct for this background is to rely heavily on Monte Carlo simulation.

The background in our exclusive ω quasi-real photoproduction sample was simulated using the PYTHIA [89] generator. In the standard trigger data analysis the normalization of the background was based on the ΔE -spectrum in the vector meson invariant mass region. Here, we only have the invariant mass distribution to work with. The background generator is assumed to match the data outside the ω resonance, where only non-resonant 3-pion events contribute to the invariant mass distribution. The background 3-pion invariant mass distribution was scaled to the measured spectrum in the region $M_{3\pi} > 0.95 \text{ GeV}$. The resulting distributions are depicted in figure 10.3. A signal-to-background ratio for exclusive ω production was calculated according to equation 9.13 by taking the measured and simulated background events in the region $0.70 < M_{3\pi} < 0.88 \text{ GeV}$, giving a value of $s/b = 0.39 \pm 0.14$. This means that according to the Monte Carlo simulation roughly 70 % of the resonant ω events is due to non-exclusive processes.

The systematic error on the s/b -ratio was determined by checking the sensitivity of the result to the considered $M_{3\pi}$ interval and the lower $M_{3\pi}$ limit of the normalization region, which gave a fractional error of 13 %.

10.5 Acceptance Correction

Just like for the standard trigger data sample the acceptance for exclusive ω production was computed using the DIPSI generator. Events were generated in the Q^2 -region between $4 \cdot 10^{-10}$ and 2.0 GeV^2 , where the lower limit corresponds to Q_{min} as discussed above. As the sample of quasi-real photoproduction events is extremely dominated by low Q^2 events, the upper limit is of less importance. The input parameters like e.g. the gluon distribution were taken to be identical to the ones used in the optimal setting for the electroproduction data analysis. The mean value of Q^2 was around 10^{-4} GeV^2 .

The Monte Carlo generated data were reconstructed with HRC and fed through the entire analysis chain. Figure 10.4 shows the comparison between the measured photoproduction data and the generated Monte Carlo events. The data distributions were obtained by fitting the ω peak in the 3-pion invariant mass distribution for each kinematical bin with a Gaussian plus polynomial background curve. The agreement is not excellent but

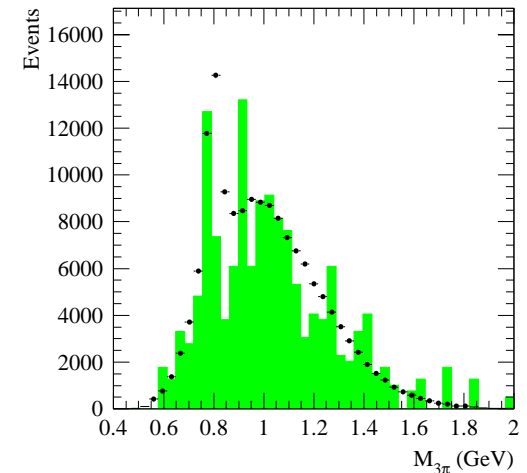


Figure 10.3: The measured 3-pion invariant mass distribution of the quasi-real photoproduction sample (dots) and the estimated non-exclusive background simulated with the PYTHIA generator (histogram).

yet satisfactory. One should recall that the measured data sample shown in the plot contains exclusive ω events plus, as shown in paragraph 10.4, a large fraction of non-exclusive ω events. To make a better, direct comparison one has to subtract these latter events, where in principle one could determine their kinematical distributions via Monte Carlo. The normalization to the measured data then can be done via the 3-pion invariant mass spectrum of the non-exclusive non-resonant 3-pion events, i.e. the events outside the ω invariant mass peak. In that case one has to trust the intrinsic ratio in the Monte Carlo generator of the non-exclusive resonant ω events to non-exclusive non-resonant 3-pion events. However, the statistics in our non-exclusive background event sample from the PYTHIA generator was not large enough to allow such a study.

The disagreement seen in figure 10.4 in the transverse vector meson momentum P_t relative to the beam axis, can be quantitatively understood as being indicative of this large fraction of non-exclusive ω events in the sample. Exclusive events are expected to occur predominantly at lower P_t as the recoil nucleon takes up very little momentum and the vector meson goes in the direction of the virtual photon. In non-exclusive ω events however, the vector meson can go up to higher P_t values due to the presence of other final state particles. Therefore, the non-exclusive ω events in the sample will push the average P_t distribution towards higher mean values as compared to a sample containing exclusive events only.

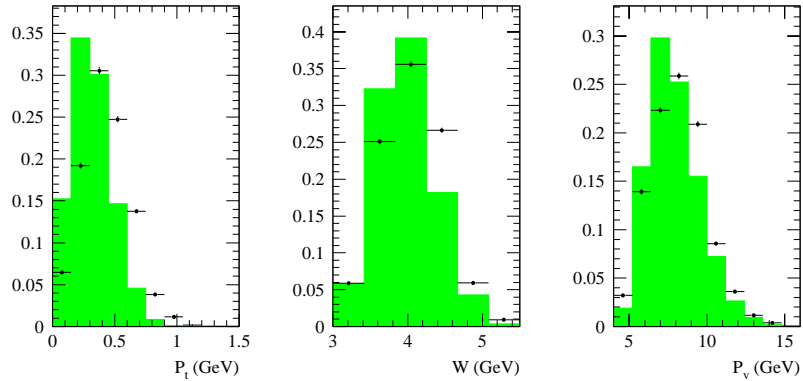


Figure 10.4: Comparison of the measured ω photoproduction data (dots) and the DIPSI Monte Carlo generator (histogram). The slightly higher mean values of the measured W and P_T distributions indicate the presence of a large fraction of non-exclusive ω events in the event sample.

The disagreement observed in the W -distribution is linked to the one in the P_T -spectrum due to the fact that the kinematics of the vector meson itself provide the virtual photon kinematics via equation 10.1. The disagreement can be largely tuned away by feeding different input gluon distribution to the DIPSI generator. The fact that this has little effect on the difference in the P_T -distribution between data and Monte Carlo supports the statements made in the previous paragraph. As we are not able with the present statistics in our PYTHIA background Monte Carlo sample to determine what the W -distribution computed with equation 10.1 for non-exclusive ω events looks like¹, we cannot really determine the optimal Monte Carlo parameters and hence this effect has to be included into the systematic error on the calculated acceptance.

The systematic error on the acceptance value due to the generator model dependence was estimated by using different input gluon distribution functions. The resulting W - and P_T -distributions were judged by eye to be relatively close to the measured data distributions. As this gluon distribution is one of the main input parameters of the DIPSI generator, no other input parameters were varied. The final acceptance was computed as the average of the values found in the systematic studies, where the standard deviation was taken as the systematic uncertainty. This gave a total acceptance of 0.152 % with a fractional error of 31 %. The statistical error on the acceptance was of order 10^{-3} % and could thus be neglected safely with respect to the systematic uncertainty. Based on the results for the virtual photoproduction cross section the systematic error due to the

¹Although we do not know what they look like, we do expect them to be rather similar distributions in the detector acceptance as the ones for the exclusive production events.

geometrical detector acceptance is expected to be much smaller than the error due to the model dependence and is therefore not considered here.

10.6 Extraction of the Absolute γp Cross Section

The exclusive $\gamma p \rightarrow \omega p$ cross section can be calculated according to

$$\sigma^{\gamma p \rightarrow \omega p} = \frac{N^{corr}}{\mathcal{L} \cdot \epsilon_{tr28} \cdot B \cdot \Phi \cdot Acc}, \quad (10.9)$$

where N^{corr} is given by equation 9.10.

The total number of ω events in the sample was determined via a fit to the 3-pion invariant mass distribution of a Gaussian function plus a 5th order polynomial curve for the background surrounding the ω resonance, as depicted in figure 10.5. This gave $N_\omega = 17210 \pm 250$, where the statistical uncertainty was derived from the errors on the parameters of the Gaussian curve.

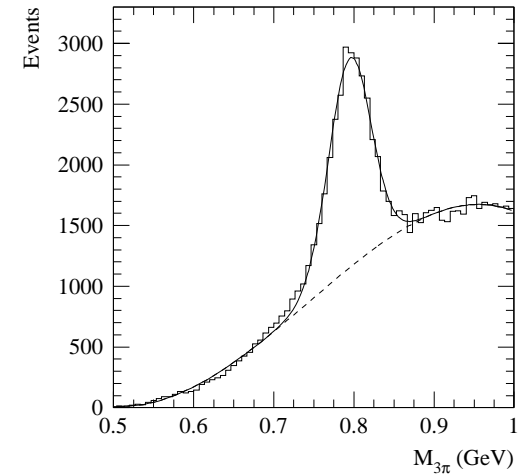


Figure 10.5: 3-pion invariant mass distribution for photoproduction trigger events with the Gaussian plus 5th order polynomial fit to the ω resonance and the surrounding background.

Given the poor statistical significance of the simulated background event sample (see paragraph 10.4) only one bin in W was considered in the cross section extraction. Moreover, as the statistical uncertainty on the s/b -ratio is clearly dominated by the Monte

Carlo sample, this error was propagated into the systematic error on the final result. The average $\gamma p \rightarrow \omega p$ cross section in the region $3.0 < W < 5.0$ GeV was

$$\sigma^{\gamma p \rightarrow \omega p} = 2.25 \pm 0.03 \text{ (stat.)} \pm 0.94 \text{ (syst.)} \mu\text{b.} \quad (10.10)$$

The average W -value in the considered interval was determined by Monte Carlo to be 3.7 GeV.

Radiative corrections to the cross section result are of less importance for quasi-real photoproduction and have been neglected here. The result presented here is also not corrected for the presence of double-diffractive dissociation background. Unlike for the electroproduction data analysis, where most of this type of background could be removed via the ΔE -cut, a similar procedure is not available here. Therefore, one can only rely on the DD/SD ratios which were already quoted in paragraph 9.5. Applying a DD/SD ratio ranging from 0.27 to 0.65 in the calculation of the DD background correction would result in a cross section value between 1.36 and 1.77 μb , which is still contained within the systematic error of the result given above. Therefore, given this compatibility and the very large uncertainty on what the correct DD/SD ratio for HERMES kinematics is, we prefer not to apply the DD background correction.

N_ω fitting procedure	3.8 %
Trigger efficiency	6.0 %
Luminosity	6.0 %
Acceptance correction	31 %
Background correction	27 %
Φ determination	3.7 %
Total	42 %

Table 10.1: Different contributions to the systematic uncertainty on the $\gamma p \rightarrow \omega p$ cross section.

The systematic uncertainty contains the items listed below added together in quadrature, where the different contributions are summarized in table 10.1.

- The function used in the fit to determine N_ω was varied by using different curves for the background surrounding the ω resonance peak in the 3-pion invariant mass distribution.
- The error on the average trigger efficiency value was included.
- A 6 % systematic error on the absolute luminosity normalization was taken into account.
- The model dependence of the acceptance correction was checked by using different input gluon distributions to the Monte Carlo generator (see paragraph 10.5).
- Due to the poor statistical accuracy of the background Monte Carlo sample the s/b -ratio had a large statistical uncertainty, which has to be propagated into the systematic error on the final result. Also the small systematic error on this ratio was taken into account (see paragraph 10.4).

- The real photon flux integration systematic uncertainty was taken into account (see paragraph 10.3).

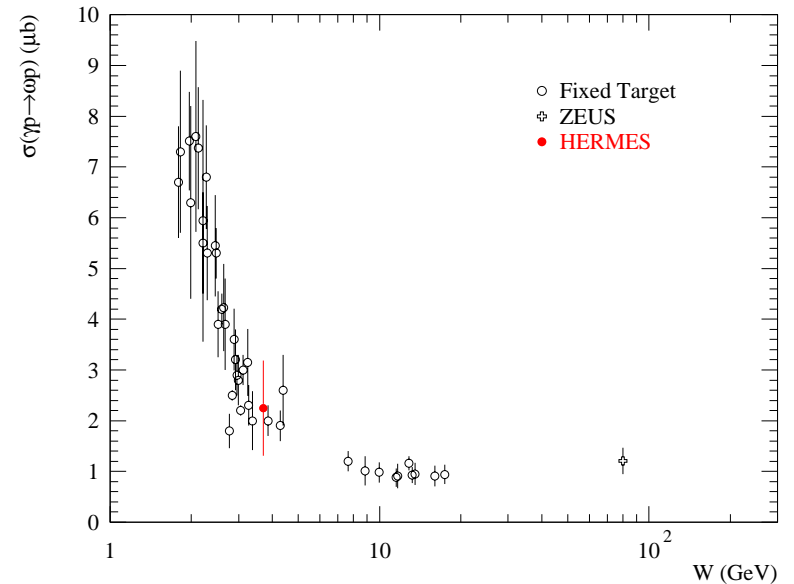


Figure 10.6: The HERMES measurement of the $\gamma p \rightarrow \omega p$ cross section compared to the previously measured world data. The data in the low W region are taken from fixed target experiments [116, 153, 154, 155, 156, 157, 158, 159, 160, 161, 162, 163], while the point at high W is taken from ZEUS [164]. The error bars represent the statistical and systematic uncertainties added in quadrature.

The HERMES result is compared to the ω real photoproduction world data in figure 10.6. A good agreement with the data from previous fixed target experiments in the low W region is found.

The fact that here, in contrast to the electroproduction data analysis, the amount of non-exclusive background present in the event sample turns out to be rather large and that there is no direct way to remove them with something like an exclusivity cut, has several consequences for the accuracy of the cross section determination. First, the large amount of DIS background can be removed only by Monte Carlo simulation and therefore calls for a much more extensive MC data sample than was used here. However, limitations in both computer CPU and disk space availability did not allow such an extended Monte Carlo study for the results presented here. Second, the presence of the background in

the sample may distort the kinematical distributions for our presumed exclusive event sample, hampering the comparison between the data and the exclusive MC generator. This enhances the uncertainty on the extracted acceptance correction. Third, the amount of double-diffractive dissociation background cannot be determined from our HERMES data and thus needs to be estimated based on theory or on other experimental results. The large uncertainties on these estimations directly transfer into the error on our cross section measurement. It is therefore only natural to see that the dominant contributions to the systematic uncertainty are due to the acceptance correction, the s/b -ratio and the DD background contribution.

Chapter 11

ρ^0 Decay Angle Distribution Analysis

In this chapter we study the helicity transfer in exclusive ρ^0 production on the proton. Different algorithms to extract the vector meson spin density matrix elements are presented. Results are obtained for the full set of 23 matrix elements at an average Q^2 value. The Q^2 dependence is studied for the 15 unpolarized matrix elements. The hypothesis of SCHC and NPE is tested against our measurements. The ratios of the helicity amplitudes are determined from the matrix elements and R_{ρ^0} is extracted. The results for the matrix elements and the helicity amplitude ratios are compared to predictions from theoretical models.

11.1 Spin Density Matrix Element Extraction Algorithms

To extract the SDME's from the data several different scenarios and algorithms can be constructed. Final results can thus be cross checked by applying different extraction methods on the same data sample. In this section we discuss all methods which were tried in the analysis. A comparison between all these methods is given and used in the discussion of the systematic uncertainties on the final SDME's.

11.1.1 The Method of Moments

In appendix C of reference [51] all 23 matrix elements are expressed as moments of 23 functions of the decay angles. As an example r_{1-1}^1 is given by

$$r_{1-1}^1 = \frac{1}{\epsilon} \frac{5}{2} \langle \sin^2 \theta \cos 2\phi \cos 2\Phi \rangle. \quad (11.1)$$

Before the moments can be calculated, the functions have to be corrected for detector acceptance effects. For each of the 23 functions an acceptance correction was computed

using the ρ^0 VDM Monte Carlo generator. After that the moments were calculated from the acceptance corrected histograms using

$$\langle f(\theta, \phi, \Phi) \rangle = \bar{f} = \frac{\sum_i n_{corr}^i f_i}{\sum_j n_{corr}^j}, \quad (11.2)$$

where the sum runs over the number of bins. In the i th bin of the histogram corresponding to the acceptance corrected decay angle function f the abscis is f_i , $n_{corr}^i = n^i / acc_i$ the content of the bin and acc_i the acceptance of f evaluated for the particular bin. The error on the moment was then given by

$$\sigma(\langle f(\theta, \phi, \Phi) \rangle) = \frac{1}{\sqrt{\tilde{n} - 1}} \left(\frac{\sum_i n_i / acc_i (f_i - \bar{f})^2}{\sum_i n_i / acc_i} \right)^{\frac{1}{2}}, \quad (11.3)$$

with \tilde{n} the equivalent number of events given by equation 7.10 with $w_i = 1 / acc_i$. From these computed moments the SDME's were easily derived using the expressions mentioned above.

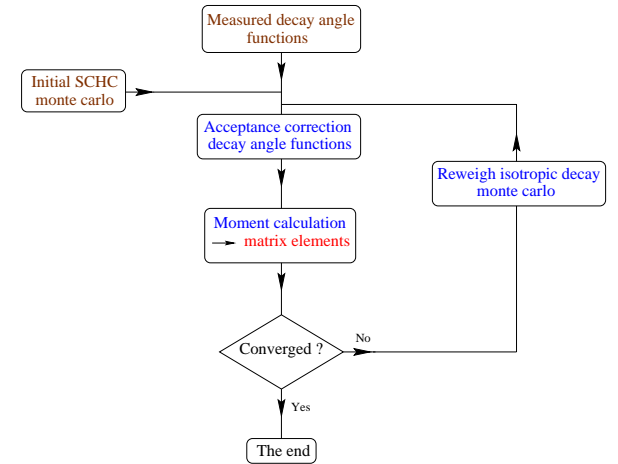


Figure 11.1: Diagram representing the iterative method of moments.

One problem here is that the acceptance corrections themselves depend on the SDME's. To deal with this issue, the extraction procedure was performed in an iterative way as depicted in figure 11.1. The initial acceptance correction used in the first step of the iteration was computed with the VDM generator under the assumption of the SCHC hypothesis. In the subsequent steps, an isotropically generated event sample was reweighted with equation 2.126 using the intermediate results for the 23 SDME. It was basically

judged by eye whether the procedure had converged after a certain amount of steps or not. In general about 5 to 10 steps were enough to produce a stable result for most of the SDME's. However, some SDME's were seen to continue fluctuating forever.

11.1.2 Modified Method of Moments

One drawback of the simple method of moments as described above, is that it does not contain a driving force ensuring that the iteration procedure ever converges for all SDME's. Also, even if the procedure does converge at some point, it is not clear whether the extracted SDME's really correspond to the optimal, real values. In other words, one needs some sort of minimization procedure in which the final SDME's correspond to a 'global minimum' and not to some 'local minimum'.

The method presented here is inspired by the method of moments, but instead of simply iterating the acceptance correction to the 23 decay angle functions, one uses a reconstructed Monte Carlo event sample to fit to the measured data. One starts off with an isotropic decay generated Monte Carlo event sample which is then fed through the reconstruction software chain and subjected to the offline analysis procedure and cuts. Afterwards the same 23 decay angle functions are computed as for the data and the comparison between the 23 Monte Carlo and measured data decay angle functions yields a χ^2 value. This χ^2 value can then be minimized by reweighting the Monte Carlo events according to equation 2.126 with the SDME's as free parameters in the minimization procedure. The minimization procedure itself is handled by the MINUIT package [167]. The final values of the SDME's correspond to the optimal values found by MINUIT. The χ^2 value can be computed by either evaluating the difference in moments of the data and Monte Carlo decay angle functions or by comparing (histograms of) the functions themselves.

11.1.3 The Maximum Likelihood Method

In a different approach the SDME's were essentially determined by minimizing the difference between the 3-dimensional $(\cos\theta, \phi, \Phi)$ decay angle matrix of the data and a sample of fully reconstructed Monte Carlo events. In this way the SDME's are computed directly from measured quantities, instead of (moments of) functions of the latter as in the method of moments.

The Monte Carlo events were generated with uniform angular distributions and were then iteratively reweighted with equation 2.126, with the matrix elements treated as free parameters. The best fit parameters were determined with a binned maximum log-likelihood method. The number of events d_i in each bin i was assumed to be Poisson distributed

$$P(d_i, c_N m'_i) = \frac{(c_N m'_i)^{d_i}}{d_i!} e^{-c_N m'_i} \quad (11.4)$$

with mean value $c_N m'_i$, where m'_i is the (re)weighted number of Monte Carlo events in bin i and $c_N = (\sum_j d_j) / (\sum_j m'_j)$ a normalization factor to account for the difference in the total number of events in the data and Monte Carlo sample. A likelihood function

was then defined as [166]

$$L(\lambda) = \prod_i^{bins} P(d_i, c_N(\lambda) m'_i(\lambda)), \quad (11.5)$$

where λ represents the 23 fit parameters being the 23 SMDE's. The best fit parameters were determined by maximizing the logarithm of the likelihood function

$$\ln L(\lambda) = \sum_i [d_i \ln(c_N(\lambda) m'_i(\lambda)) - c_N(\lambda) m'_i] + constant, \quad (11.6)$$

or equivalently by minimizing $-\ln L(\lambda)$. The minimization itself and the error calculation were performed using the MINUIT package [167].

11.1.4 1-dimensional Least Square Fitting Method

The method which was applied in the analysis of the 1995 ^3He data [168] was based on fitting the four 1-dimensional Monte Carlo distributions of $\cos\theta$, ϕ , Φ and Ψ to the corresponding measured data distributions. In the fitting procedure an isotropic decay Monte Carlo event sample was reweighted using equation 2.126, where the 23 SDME's were determined from 8 free parameters in the fit. The SDME's (or combinations of SDME's) r_{00}^{04} , r_{1-1}^{04} , r_{1-1}^{1-1} , r_{1-1}^{3-1} , $\text{Tr}(r^1) = 2r_{11}^1 + r_{00}^1$, $\text{Tr}(r^5) = 2r_{11}^5 + r_{00}^5$ and $\text{Tr}(r^8) = 2r_{11}^8 + r_{00}^8$, which determine the 1-dimensional decay angle distributions (see paragraph 11.7), were taken as free parameters. An additional free parameter was the phase difference δ between the longitudinal and transverse amplitude. The remaining SDME were then determined using the following relations

$$\text{Re } r_{10}^5 = -\text{Im } r_{10}^6 = \sqrt{\frac{R}{8}} \frac{\cos\delta}{1 + \epsilon R}, \quad (\text{SCHC}), \quad (11.7)$$

$$\text{Im } r_{10}^7 = \text{Re } r_{10}^8 = \sqrt{\frac{R}{8}} \frac{\sin\delta}{1 + \epsilon R}, \quad (\text{SCHC}), \quad (11.8)$$

$$r_{00}^{1,5,8} = \text{Tr}(r^{1,5,8}) r_{00}^{04}, \quad (11.9)$$

$$r_{11}^{1,5,8} = \text{Tr}(r^{1,5,8}) \frac{1}{2} (1 - r_{00}^{04}), \quad (11.10)$$

$$\text{Im } r_{1-1}^2 = -r_{1-1}^1 \quad (\text{SCHC}), \quad (11.11)$$

$$r_{1-1}^{5,6,7,8} = r_{10}^{1,2,3,04} = 0 \quad (\text{SCHC}), \quad (11.12)$$

with R given by equation 11.23.

11.1.5 Discussion of Different Extraction Methods

As indicated above the simple method of moments is not really suitable for a reliable extraction of the SDME's as it cannot be proven that the algorithm ever produces stable final values corresponding to the real SDME values. However, the method is very simple and fast and may serve as a rough indication of the final result. The output of this method

can therefore e.g. serve as initial values for the input parameters in the other more robust algorithms.

Both the modified method of moments and the maximum likelihood method turn out to be efficient methods. The results for the SDME's do not seem to be too much affected by the initial input values. However, the coding of the modified method of moments is a highly non-trivial task and is much more error-prone than the coding of the maximum likelihood algorithm. Also the uncertainties on the SDME's provided by the output of the modified method of moments seem rather sensitive to the settings of MINUIT and to the specific computation of the χ^2 function in the minimization procedure. Therefore the maximum likelihood method was the preferred algorithm for the extraction of the final results for the 23 SDME's.

The 1-dimensional least square fitting algorithm is not a favored method for several reasons. The main counterargument is the fact that the assumptions 11.7, 11.8, 11.11 and 11.12, made for some of the non-fitted SDME's, are based on the validity of s -channel helicity conservation, whereas verifying this assumption is actually one of the goals of this kind of decay distribution analysis. Second, the relations 11.9 and 11.10 are not dictated by any physical arguments and therefore need not necessarily be fulfilled by the data. Imposing all these assumptions can therefore introduce biases in the extracted SDME and may partially distort possible indications of SCHC violation. Another fact is that this method does not take into account any possible correlations between the decay angles as it is based on the 1-dimensional projections of the 3-dimensional decay angle matrix which is used in the maximum likelihood method. It is also true that given the accuracy and efficiency of the other methods discussed above, this algorithm provides much less information than can be extracted from the measured data.

11.1.6 Monte Carlo Tests

The ultimate test of the extraction methods consists of running the algorithms on a sample of Monte Carlo generated data with known input matrix elements. To this end several samples containing about 6k reconstructed ρ^0 events were generated where the events were weighted according to equation 2.126. The input matrix elements were chosen randomly, although care had to be taken that the event weight $W(\cos\theta, \phi, \Phi)$ did not reach negative values. This kind of testing was only performed for the maximum likelihood method as described in paragraph 11.1.3. The input matrix elements were chosen independent of Q^2 , which means that the extractions were only done for a single kinematical bin over the entire Q^2 range.

The results of the algorithm tests are shown in figure 11.2. In a first step a ρ^0 event sample was generated with the polarization of the beam set to zero. In this case only the 15 unpolarized SDME can be extracted from the data and as one can see from the figure the algorithm is able to reproduce the input values of the SDME within the statistical uncertainty. In the following step the beam polarization was taken to be 50% (which is close to the actual average values measured for each of the data samples in the experiment). In this case the algorithm extracted 23 SDME from the Monte Carlo sample, where the results in the figure indicate that the method was successful for most SDME's. However, one notices that the polarized SDME all have large uncertainties, due to the influence

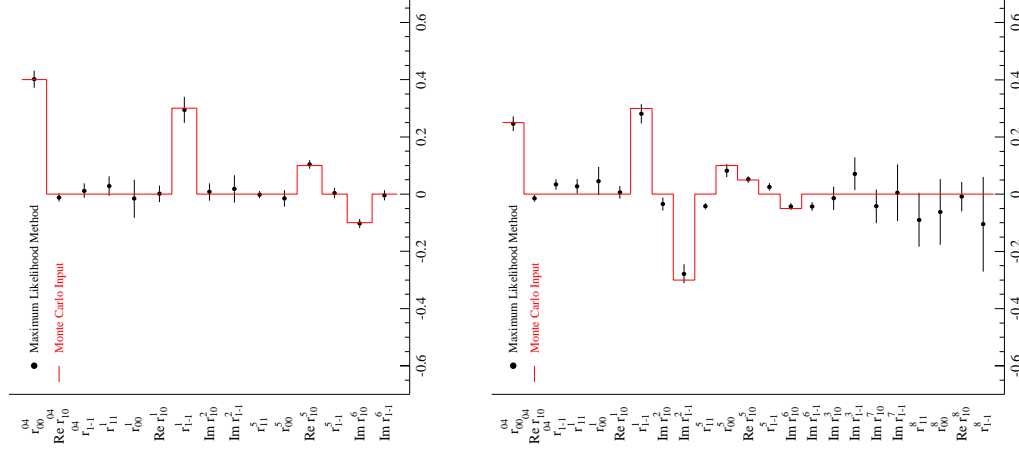


Figure 11.2: Tests of the maximum likelihood method using Monte Carlo data samples generated with known SDME as indicated by the lines. The figure on top shows results for a simulation with unpolarized beam, while the bottom part gives results for a sample generated with a 50% beam polarization.

of the beam polarization magnitude entering directly into their value. One can also see that some of the unpolarized SDME's are not reproduced by the algorithm within the statistical uncertainty. Systematic iterations of the test indicate that the final values and precision of the extracted SDME are influenced to a certain extent by the number of bins for the decay angles used internally in the algorithm, where too few or too many bins may lead to large uncertainties. One therefore has to find the optimum range of number of bins depending on the statistics of the event sample and one should include a systematic uncertainty due to the used binning in the final result. Doing so for this kind of Monte Carlo tests shows that the maximum likelihood method is indeed able to reproduce the input values for the SDME's within the total uncertainty.

11.2 Radiative Corrections

The radiative corrections for exclusive vector meson depend on the angle Φ between the lepton scattering and hadron production plane [169]. This angle is determined by the direction of the vector meson and of the virtual photon momentum, where the latter is determined experimentally from the difference between the incoming and scattered lepton momentum. The emission of a real photon will alter the virtual photon direction with respect to the non-radiative case and thus also the Φ angle. Therefore the hard photon radiation contribution to the RC can be a strong function of Φ . However, the effect becomes only significant for high $|t|$ where the hard photon radiation contribution to the total RC becomes relatively large. The remaining contributions to the RC depend only weakly on this angle. The total RC are also found not to influence the vector meson decay angles $\cos\theta$ and ϕ .

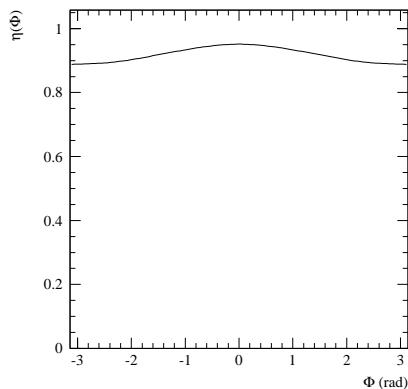


Figure 11.3: The computed radiative correction factor for exclusive ρ^0 production as function of the angle Φ .

The RC factor $\eta(\Phi)$ is computed using the DIFFRAD code and is displayed in figure 11.3 for our exclusive ρ^0 kinematics. As only the shape of the RC with respect to Φ is important and not the absolute magnitude, one can expect that in this case the RC will only have a minor effect on the data.

The implementation of the RC in the maximum likelihood procedure was done in two different ways. In the first method the measured data contained in the 3-dimensional angular matrix were corrected before the application of the likelihood algorithm by assigning a weight equal to $1/\eta(\Phi)$ to each event. This is made possible since also here only the shape of the 3-dimensional decay angle distribution is important and not the normalization. The change in the results for the SDME due to the RC implemented in this way was below 1%. The second method was based on the iterative numerical procedure proposed in [169], where one calculates the RC to the matrix elements directly. The QED correction, i.e. the difference between the measured and Born SDME ($\Delta r = r_{meas} - r_{Born}$), to be applied to every matrix element in each step of the iteration is a linear function of the magnitude of the SDME themselves with coefficients I_n defined by

$$I_n = \frac{\int_0^{2\pi} d\Phi \cos(n\Phi) \eta(\Phi)}{\int_0^{2\pi} d\Phi (1 + \eta(\Phi))}, \quad n = 1, 2 \dots 4, \quad (11.13)$$

containing the dependence on the $\eta(\Phi)$. As an example the correction to r_{00}^5 is calculated as

$$\Delta r_{00}^5 = \frac{1}{\sqrt{2\epsilon(1+\epsilon)}} \left[2 I_1 r_{00}^{04} + \sqrt{2\epsilon(1+\epsilon)} I_2 r_{00}^5 - \epsilon (I_1 + I_3) r_{00}^1 \right]. \quad (11.14)$$

Using the computed $\eta(\Phi)$ as displayed in figure 11.3 results in values below 1% for all coefficients $I_{1,2,3,4}$, so that the predicted change in the SDME results due to the RC with the iterative procedure is minimal.

As both methods agree on the fact that the RC in the SDME analysis for HERMES kinematics can be neglected, no RC were taken into account in the derivation of the final results.

11.3 The ρ^0 Spin Density Matrix Elements

For the derivation of the results presented here the maximum likelihood method was chosen as the main extraction tool. The internal number of bins for the 3-dimensional matrix in $(\cos\theta, \phi, \Phi)$ was taken to be $8 \times 8 \times 8$. The SDME's were extracted in the kinematical region $0.7 < Q^2 < 5.0 \text{ GeV}^2$ and $4.0 < W < 6.0 \text{ GeV}$ from the HERMES 1996-97 data taken on a ^1H target. The beam polarization value for the events in the sample is displayed in figure 11.4. During 1996 HERA ran the lepton beam with positive helicity. Before the 1997 running period, the beam helicity was reversed and two more helicity flips were performed during the 1997 data taking. The sign of the beam polarization enters directly into equation 2.126, which is used to reweigh the Monte Carlo events in the likelihood method. To deal with this different weighting, the extraction procedure was done separately for the samples with positive and negative beam helicity. Note that this is equivalent to running the procedure on the two helicity event samples together with one common set of SDME parameters. In that case the MC events are to be reweighted

twice, where a weight is computed for each beam helicity and the total likelihood is the sum of the likelihood functions of the two helicity states. The average beam polarization corresponding to the negative and positive beam helicity sample was -52.4% and $+50.0\%$ respectively.

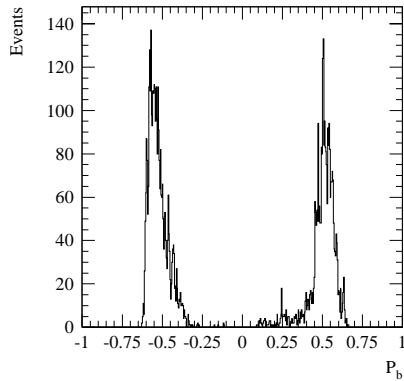


Figure 11.4: The beam polarization of the event sample. Positive (negative) values correspond to positive (negative) beam helicity.

As was shown in paragraph 11.2 the radiative corrections to the SDME's are negligible in our case and are thus not taken into account. The results are also not corrected for the presence of double-diffraction dissociation background in the sample. As the main physics addressed here is driven by the $\gamma^* \rightarrow V$ vertex in the scattering reaction, the effect from DD background is expected to be negligible. The decay angle distributions for the proton dissociative reaction were actually measured by ZEUS [170] and found to be consistent with those of exclusive events, which supports our assumption. The amount of DIS fragmentation background in the exclusive sample can be estimated with a DIS Monte Carlo as described in section 7.6. After the proper normalization of the Monte Carlo background events to the data, the 3-dimensional decay angle matrix of the background events can be subtracted from the corresponding matrix of the data sample before the likelihood procedure is started.

The results presented here are not corrected for the contribution from non-resonant $\pi^+\pi^-$ pair production and its interference with the resonant ρ^0 production amplitude (see section 8.1.5). In [170] a study was performed where the SDME's were extracted separately in the invariant mass regions $M_{2\pi} < M_{\rho^0}$ and $M_{2\pi} > M_{\rho^0}$, which receive different contributions from the non-resonant and interference terms. The observed variation of some SDME's suggested a possible influence of the non-resonant pion pair production on the extracted matrix elements. A similar study was not performed here.

Figure 11.5 displays the measured ρ^0 decay angle distributions for the two beam he-

licity samples. The plots also show the corresponding spectra for the uniform decay MC event sample, together with the distributions obtained after the maximum likelihood procedure. As one can see, the procedure is able to describe the data rather well.

The results for the 23 SDME's extracted from the two beam helicity samples are shown in figure 11.6. The error bars correspond to the statistical uncertainties as given by MINUIT. The 15 SDME's shown above the horizontal line are independent of the beam polarization, while the 8 SDME's on the bottom need a longitudinal beam polarization to be measured. The uncertainties on the latter ones are much larger than for the unpolarized SDME's, due to the fact that the lepton beam is not fully polarized, but only for about 50%. The two sets of SDME's extracted from the two helicity samples are fully compatible within the statistical uncertainties.

The final results for the 23 SDME's are obtained by taking the error weighted average of the values found for the two beam helicity samples. The results are listed in table B.8 and displayed in figure 11.7. The systematic error takes into account the following items :

- The internally used binning in the likelihood procedure was changed to $5 \times 5 \times 5$.
- The offline analysis cuts were varied.
- The sensitivity to the isotropic Monte Carlo model was estimated by changing the exponent n in the VDM propagator $1/(1 + Q^2/M_V^2)^n$ from 2.0 to 2.5.
- The effect on the SDME's due to the presence of DIS fragmentation background in the sample was accounted for by adding a systematic error equal to the difference in the results with and without background subtraction.
- The sensitivity of the results due to the extraction procedure was estimated by using the modified method of moments instead of the maximum likelihood procedure to determine the 23 SDME's for the two beam helicity samples.
- The effect due to the 3.4% systematic uncertainty of the beam polarization was estimated by shifting the average value of P_b up- and downwards by this amount.

No systematic uncertainty was assigned to either the RC or the possible effect of the DD background on the SDME's, as both were shown or assumed to be negligible. The dominant contributions in the systematic uncertainty came from the sensitivity to the extraction procedure and from the binning in the likelihood procedure. The uncertainty due to the beam polarization was negligible.

The results clearly show a non-zero result for the unpolarized matrix elements which are not restricted to zero in the case of SCHC, r_{00}^0 , r_{1-1}^1 , $\text{Im } r_{1-1}^2$, $\text{Re } r_{10}^5$ and $\text{Im } r_{10}^6$. The two polarized matrix elements which are allowed to be non-zero by SCHC, $\text{Im } r_{10}^7$ and $\text{Re } r_{10}^8$, are found to have a non-zero positive value, although with large uncertainties. The data also indicate values different from zero for some SCHC violating matrix elements, in particular $\text{Re } r_{10}^0$, $\text{Re } r_{10}^1$ and r_{00}^5 are seen to be significantly different from zero. These observations will be discussed in more detail in paragraph 11.6.

The Q^2 -dependence of the SDME's was studied by repeating the analysis in four bins in Q^2 ($0.7 < 1.0 < 1.4 < 2.5 < 5.0 \text{ GeV}^2$). As the available event statistics is a crucial

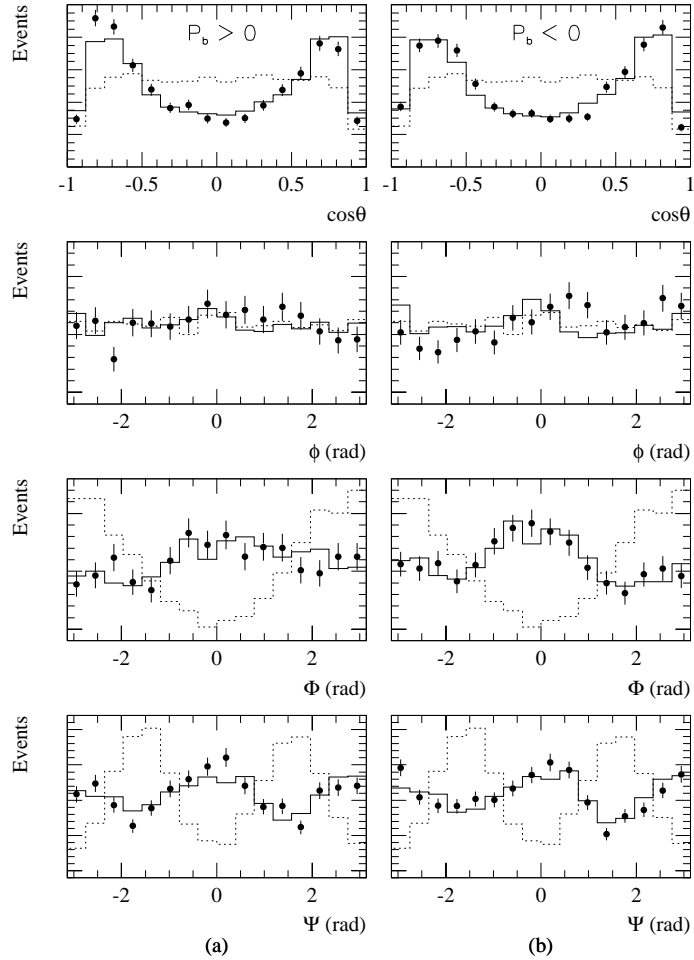


Figure 11.5: The observed distributions for $\cos\theta$, ϕ , Φ and Ψ for (a) positive beam helicity and (b) negative beam helicity. The dotted lines show the MC distributions obtained from a sample of isotropically generated ρ^0 events; the full line corresponds to the MC distributions fitted to the data with the maximum likelihood method.

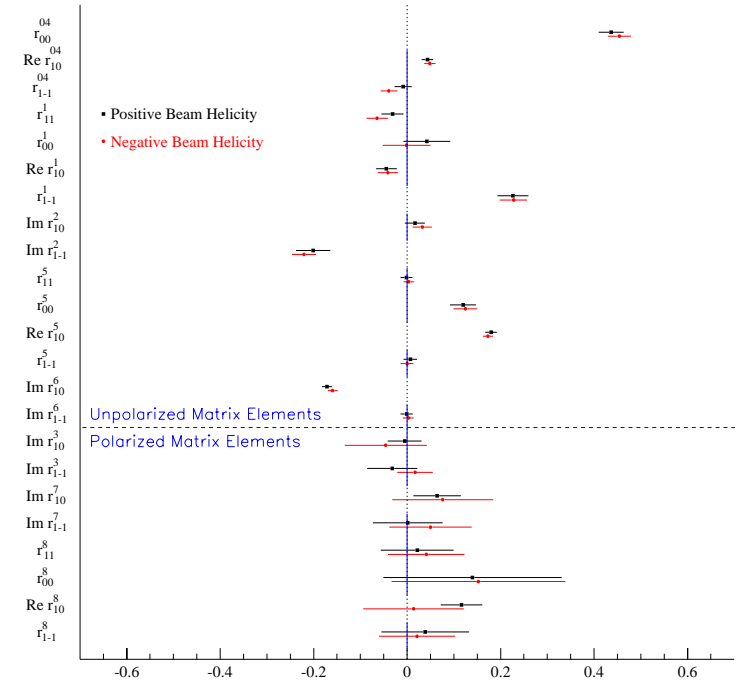


Figure 11.6: The results of the maximum likelihood method performed separately on the samples with positive and negative beam helicity. The indicated error bars are statistical uncertainties only. The vertical full lines indicate those SDME's which are expected to be zero based on the SCHC assumption.

point in this type of analysis, the binning was chosen somewhat different than before to obtain a more uniform distribution of the events among the different bins. The results presented above show that in the extraction of the SDME's from the full event sample at the average kinematical point in Q^2 the 8 polarized elements already suffer from large uncertainties. This makes it rather useless to try to extract the full set of SDME's as function of Q^2 . Therefore the two event samples belonging to the opposite beam helicities were added together, resulting in a sample with an average beam polarization of only a few percent. The correlation matrix calculated by MINUIT for the 23 SDME's indicates that the correlations between the unpolarized and polarized SDME's are of minor importance. Hence, it is a safe assumption to treat the combined event sample as belonging to an unpolarized beam and to extract only the 15 unpolarized SDME's in the four Q^2 bins. The results are summarized in table B.9 and displayed in figure 11.8 together with results

from theoretical model calculations, which will be discussed in the next paragraph.

The results of the Q^2 -dependent analysis show significant non-zero values for the SCHC violating matrix element r_{00}^5 .

11.4 Theory Predictions

The extracted 23 SDME's are compared to the model calculations from Ivanov *et al.* [54] in figure 11.7. The predictions, especially for the SCHC violating matrix elements, depend strongly on $|t|$. The calculations were performed at our average kinematics with $|t| = 0.14 \text{ GeV}^2$. Although the model is based on 2-gluon exchange, it is seen to be in good agreement with our data. However, the SCHC violating matrix elements r_{00}^5 and $\text{Re } r_{10}^{04}$ are underestimated. Note that the two polarized matrix elements $\text{Im } r_{10}^7$ and $\text{Re } r_{10}^8$, which can be different from zero according to SCHC, are well reproduced by the model.

The same figure also displays the predictions from the model of Royen *et al.* [53] for the 15 unpolarized SDME's. It should be noted that these calculations were actually performed for the H1 and ZEUS energy scale with $|t| = 0.14 \text{ GeV}^2$. However, the energy variation in the model is rather small. Here the magnitude of r_{00}^{04} is predicted too high, which is probably a consequence of the difference in center-of-mass energy between H1 and HERMES. This model is seen to reproduce the magnitudes of the SCHC violating matrix elements r_{00}^5 and $\text{Re } r_{10}^{04}$.

The two different models yield rather similar predictions for the Q^2 -dependence of most SDME's. Figure 11.8 shows the comparison of the measured Q^2 -dependence of the 15 unpolarized SDME's to the theoretical predictions. A good agreement between the data and the model calculations is found, in particular the behavior of the large matrix elements which are not restricted by SCHC, i.e. r_{00}^{04} , r_{1-1}^1 , $\text{Im } r_{1-1}^2$, $\text{Re } r_{10}^5$ and $\text{Im } r_{10}^6$, is well reproduced by both model calculations. The observed Q^2 -dependence of r_{00}^5 is in agreement with the model prediction from Royen *et al.*

11.5 Natural Parity Exchange

Without assuming SCHC, the hypothesis of natural parity exchange in t -channel alone leads to the following sum rule

$$1 - r_{00}^{04} + 2r_{1-1}^{04} - 2r_{11}^1 - 2r_{1-1}^1 = 0. \quad (11.15)$$

Using the results from table B.8, the left side of this equation equals $0.148 \pm 0.063 \text{ (stat.)} \pm 0.132 \text{ (syst.)}$, which is compatible with zero within large uncertainties. This observation supports the validity of the NPE assumption.

The Q^2 -dependence of the lefthand side of equation 11.15 is shown in figure 11.9. Also here, within large uncertainties, no clear indication is found for the non-validity of the NPE hypothesis.

The asymmetry parameter P_{σ_T} between natural (σ^N) and unnatural parity exchange

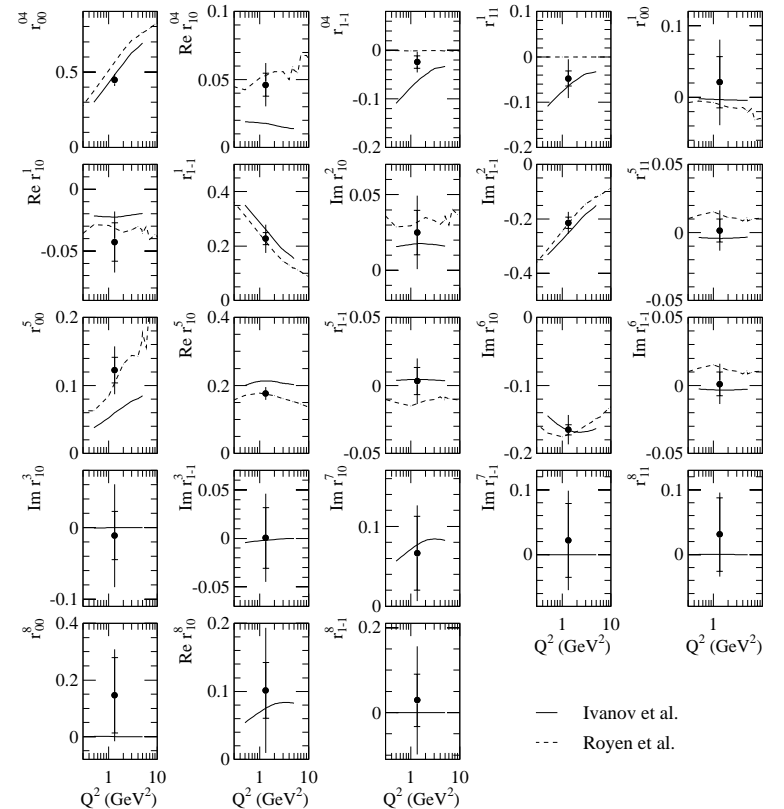


Figure 11.7: The 23 SDME's compared to theoretical model calculations from Ivanov *et al.* [54] and Royen *et al.* [53].

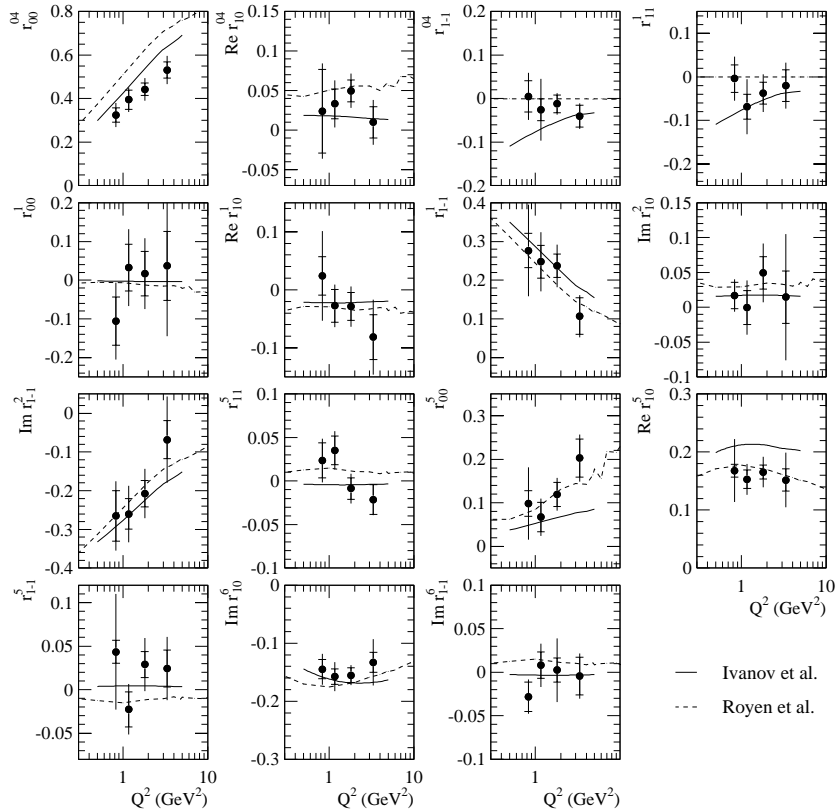


Figure 11.8: The 15 unpolarized SDME's as function of Q^2 compared to theoretical model calculations from Ivanov *et al.* [54] and Royen *et al.* [53].

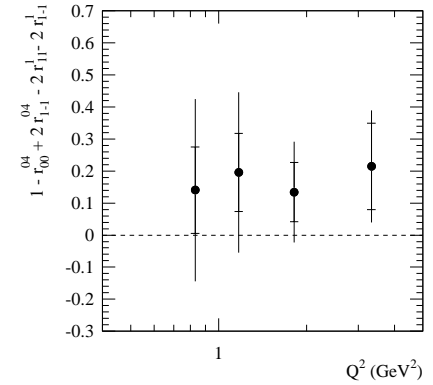


Figure 11.9: The verification of the natural exchange hypothesis by examining the validity of equation 11.15 as function of Q^2 .

(σ^U) is, for transverse photons, given by [51]

$$P_{\sigma_T} = \frac{\sigma^N - \sigma^U}{\sigma^N + \sigma^U} = (1 + \epsilon R_\rho) (2 r_{1-1}^1 - r_{00}^1). \quad (11.16)$$

Using the results given in table B.8 together with equation 11.23 for R_ρ (see paragraph 11.9) yields $P_{\sigma_T} = 0.782 \pm 0.014$ (stat.) ± 0.050 (syst.). This indicates that ρ^0 production by transverse photons in the HERMES kinematic region proceeds predominantly through natural parity exchange. A similar result was also found earlier in [113, 143].

11.6 s -Channel Helicity Conservation

The central vertical full (dotted) lines in figure 11.6 indicate the SDME's that are expected to be (non) zero based on the s -channel helicity conservation hypothesis. Basically all matrix elements except for r_{00}^{04} , r_{1-1}^1 , $\text{Im } r_{1-1}^2$, $\text{Re } r_{10}^5$, $\text{Im } r_{10}^6$, $\text{Im } r_{10}^7$ and $\text{Re } r_{10}^8$, are expected to vanish in case of SCHC. Moreover, the following relations between the non-vanishing SDME's are expected to hold

$$r_{1-1}^1 = -\text{Im } r_{1-1}^2, \quad \text{Re } r_{10}^5 = -\text{Im } r_{10}^6, \quad \text{Im } r_{10}^7 = \text{Re } r_{10}^8. \quad (11.17)$$

Under the combined assumption of SCHC and NPE one obtains another sum rule

$$1 - r_{00}^{04} - 2 r_{1-1}^1 = 0. \quad (11.18)$$

Using the results for the 23 SDME's listed in table B.8 one can easily verify that the data confirm the validity of the relations in equation 11.17. For the lefthand side

of equation 11.18 one obtains 0.100 ± 0.048 (stat.) ± 0.100 (syst.), which is compatible with zero within large uncertainties. Figure 11.10 shows the verification of these relations as function of Q^2 using the results for the 15 unpolarized SDME's given in table B.9. The data support the validity of the relations given in equation 11.17. The sum rule in equation 11.18 is satisfied within large uncertainties for most Q^2 bins.

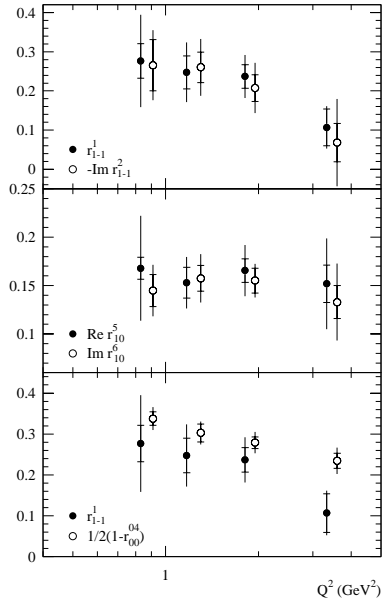


Figure 11.10: The verification of the s -channel helicity conservation hypothesis by examining the validity of the relations in equation 11.17 and the sum rule in equation 11.18 as function of Q^2 . Note that for the latter equation also NPE is assumed.

As already mentioned in paragraph 11.3 a significant deviation from zero was found for r_{00}^5 . This matrix element is proportional to the interference between the helicity conserving longitudinal amplitude T_{00} and the single-flip amplitude T_{01} . The latter amplitude corresponds to the production of longitudinally polarized ρ^0 mesons from transverse photons. In the theoretical models presented in paragraph 2.13.6 this was actually predicted to be the leading s -channel helicity violating effect. The fact that the relations given in equation 11.17 and 11.18 are seen to be satisfied by the data, indicates that the helicity violating effect cannot be large.

11.7 1-dimensional Decay Angle Distributions

Integrating the decay angle distribution $W(\cos\theta, \phi, \Phi)$ given by equation 2.126 over the angles ϕ and Φ yields the following angular distribution of $\cos\theta$

$$W(\cos\theta) = \frac{3}{4} [1 - r_{00}^{04} + (3r_{00}^{04} - 1) \cos^2\theta]. \quad (11.19)$$

This distribution depends only on r_{00}^{04} which represents the probability to produce a vector meson with longitudinal polarization. The $\cos\theta$ distribution is not restricted by SCHC.

Integrating equation 2.126 over $\cos\theta$ and Φ gives

$$W(\phi) = \frac{1}{2\pi} [1 - 2r_{1-1}^{04} \cos 2\phi + P_b \sqrt{1 - \epsilon^2} \text{Im } r_{1-1}^3 \sin 2\phi]. \quad (11.20)$$

This decay angle distribution depends on the two helicity violating matrix elements r_{1-1}^{04} and $\text{Im } r_{1-1}^3$. In the case of SCHC this distribution becomes $W(\phi) = 1/2\pi$.

Integrating equation 2.126 over $\cos\theta$ and ϕ gives

$$W(\Phi) = \frac{1}{2\pi} [1 - \epsilon \cos 2\Phi \text{Tr}(r^1) + \sqrt{2\epsilon(1+\epsilon)} \cos \Phi \text{Tr}(r^5) + P_b \sqrt{2\epsilon(1-\epsilon)} \sin \Phi \text{Tr}(r^8)], \quad (11.21)$$

with $\text{Tr}(r^\alpha) = 2r_{11}^\alpha + r_{00}^\alpha$. This distribution depends on the helicity non-conserving combinations of matrix elements $\text{Tr}(r^1)$, $\text{Tr}(r^5)$ and $\text{Tr}(r^8)$. In the case of SCHC, the distribution becomes $W(\Phi) = 1/2\pi$.

Assuming SCHC, the azimuthal dependence of the decay angle distribution is function of the polarization angle $\Psi = \phi - \Phi$ only. Integrating equation 2.126 over $\cos\theta$ yields

$$W(\Psi) = \frac{1}{2\pi} [1 + 2\epsilon r_{1-1}^1 \cos 2\Psi]. \quad (11.22)$$

This distribution depends only on r_{1-1}^1 . A positive value of r_{1-1}^1 indicates that the spin of the meson and the photon are aligned in such a way that the decay pions are predominantly emitted in the lepton scattering plane.

The measured four 1-dimensional decay angle distributions are displayed in figure 11.11 for both beam helicity samples. The distributions were corrected for acceptance using the ρ^0 VDM Monte Carlo generator. The acceptance correction was computed using an isotropic decay event sample reweighted with equation 2.126 where the results obtained in the full 23 SDME extraction (see table B.8) served as input. The acceptance corrected distributions were fitted using equation 11.19, 11.20, 11.21 and 11.22. The final results for the fitted matrix elements were computed by taking the error weighted average of the fit results obtained for the beam helicity samples. The results are listed in table 11.1 and are compared to the corresponding values obtained in the full 23 SDME extraction. The results are in very good agreement. In particular, the observed agreement for r_{1-1}^1 shows that SCHC is in fact a good approximation for the data presented here.

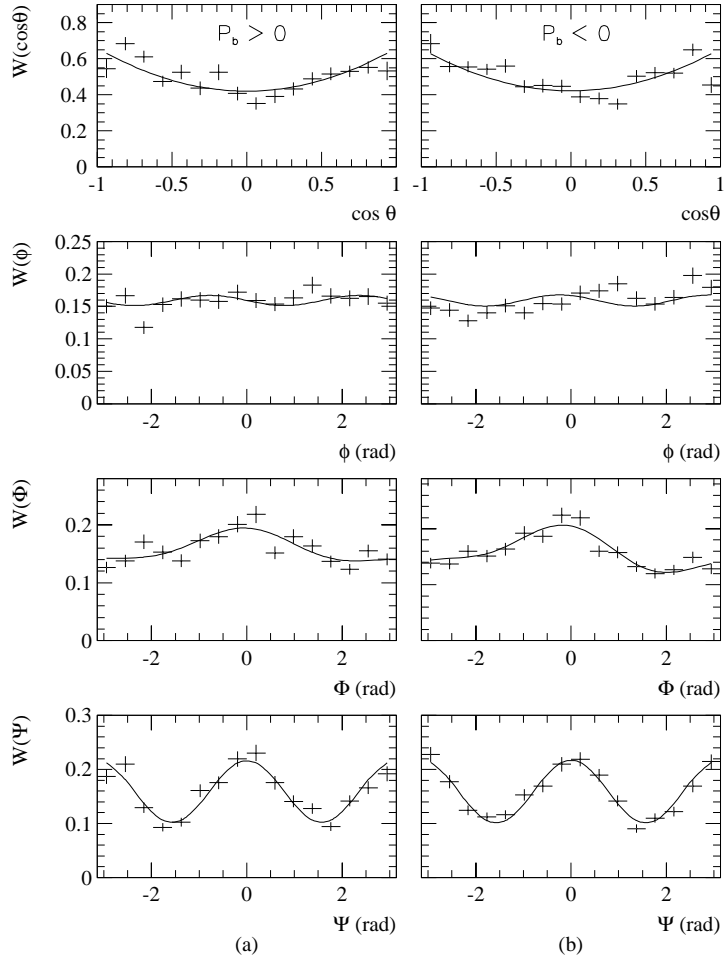


Figure 11.11: The acceptance corrected 1-dimensional decay angle distributions for (a) the positive beam helicity sample and (b) the negative beam helicity sample. The fits correspond (from top to bottom) to equation 11.19, 11.20, 11.21 and 11.22.

element	1-dim. fit	3-dim. method
r_{00}^0	0.439 ± 0.011	0.446 ± 0.018
r_{-1}^1	0.228 ± 0.010	0.227 ± 0.022
r_{-1}^0	-0.013 ± 0.009	-0.024 ± 0.013
$\text{Im } r_{-1}^3$	-0.036 ± 0.065	0.001 ± 0.031
$\text{Tr } (r^1)$	-0.092 ± 0.022	-0.075 ± 0.049
$\text{Tr } (r^3)$	0.109 ± 0.010	0.125 ± 0.025
$\text{Tr } (r^8)$	0.177 ± 0.066	0.208 ± 0.175

Table 11.1: The (combinations of) matrix elements obtained from the 1-dimensional decay angle distribution fits compared to the results from the full 23 SDME extraction. The errors are statistical only.

11.8 Extraction of Helicity Amplitudes

The 23 SDME extracted in the previous paragraphs provide a full description of the vector meson decay angle distribution. Each of these matrix elements is actually a sum of bilinear combinations of helicity amplitudes $T_{\lambda_V \lambda_\gamma}$. The expression of each matrix element as function of the helicity amplitudes is listed in Appendix D. These complex amplitudes are more fundamental quantities than the SDME and they allow a direct test of the s -channel helicity conversation hypothesis. The measured 23 SDME can in principle be used to determine these amplitudes.

With the virtual photon and vector meson being spin-1 objects, there are 9 independent complex amplitudes to be extracted from the data, which gives a total of 18 unknown parameters (each amplitude has a modulus and a phase factor, $T_{\lambda_V \lambda_\gamma} = |T_{\lambda_V \lambda_\gamma}| e^{i\phi_{\lambda_V \lambda_\gamma}}$). Determining 18 parameters from only 23 given quantities is possible, but would lead to very large uncertainties. However, as was shown in paragraph 11.5 the measured SDME satisfy the natural parity exchange hypothesis given by equation 2.132. This leads to $T_{-1-1} = T_{11}$, $T_{-10} = -T_{10}$, $T_{0-1} = -T_{01}$ and $T_{-11} = T_{1-1}$ and leaves us with only 5 independent amplitudes to be determined. The 10 unknown parameters can be determined via a minimum χ^2 -fit to the 23 measured SDME. In the extraction we applied the normalization $T_{00}=1$ and $\phi_{00} = 0$ deg. The parameters $|T_{1-1}|$, ϕ_{10} , ϕ_{01} and ϕ_{1-1} suffered from very large errors and were compatible with zero. For the computation of the final results these latter parameters were fixed at zero and only $|T_{11}|$, $|T_{01}|$, $|T_{10}|$ and ϕ_{11} were fitted. It was checked that setting the non-determined quantities to zero did not affect the results. The results are summarized in table B.10 and displayed in figure 11.12 together with results derived in [171] from ZEUS and H1 measurements.

The $|T_{11}|/|T_{00}|$ ratio exhibits a strong decrease with Q^2 , which reflects the dominance of the longitudinal over the transverse production amplitude at high Q^2 . The $|T_{01}|/|T_{00}|$ ratio is found to be $15.1 \pm 3.5\%$, which represents a 4σ difference from zero. This corresponds to a significant SCHC violation due the production of longitudinally polarized vector mesons by transverse photons. The obtained $|T_{10}|/|T_{00}|$ ratio is compatible with zero. The results are in good agreement with the data from ZEUS and H1, although a larger s -channel helicity violating effect due to T_{01} is found here. Similar helicity violating effects have

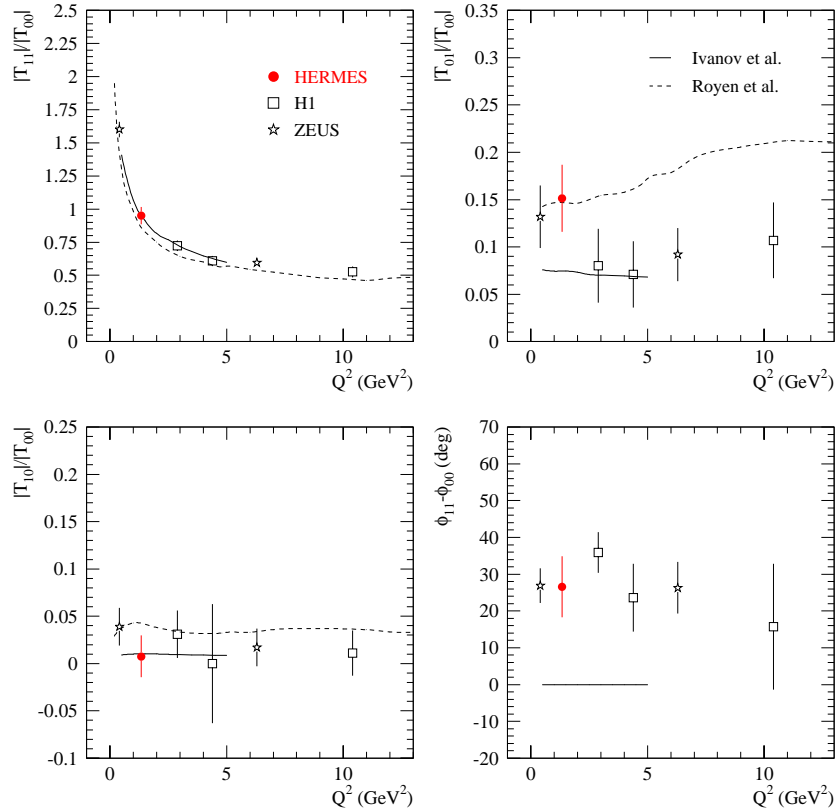


Figure 11.12: The extracted helicity amplitude ratios $|T_{11}|/|T_{00}|$, $|T_{01}|/|T_{00}|$ and $|T_{10}|/|T_{00}|$ and the phase difference $\phi_{11} - \phi_{00}$. The data are plotted as function of Q^2 and compared to the results derived in [171] from ZEUS and H1 measurements. The curves correspond to results from model calculations by Ivanov *et al.* [54] and Royen *et al.* [53].

been reported earlier in [113, 143].

Figure 11.12 also show the model calculations for the helicity amplitude ratios from Royen *et al.* [53] and Ivanov *et al.* [54]. The ratio of the transverse to the longitudinal helicity conserving amplitude is in very good agreement with the data. Both models predict that the dominant s -channel helicity violating amplitude is T_{01} , which is supported by the present result. The magnitude of T_{10} is predicted to be much smaller, which is also observed in the HERMES data.

11.9 Extraction of R_ρ

Under the assumption of SCHC the R_ρ ratio can be determined from

$$R_\rho = \frac{\sigma_L}{\sigma_T} = \frac{1}{\epsilon} \frac{r_{00}^{04}}{1 - r_{00}^{04}}, \quad (11.23)$$

which can be easily verified using the expressions listed in appendix D. When the SCHC requirement is relaxed, one obtains the following modification of equation 11.23

$$R_\rho = \frac{1}{\epsilon} \frac{r_{00}^{04} - \Delta^2}{1 - (r_{00}^{04} - \Delta^2)}, \quad (11.24)$$

with the correction Δ given by

$$\Delta^2 = \frac{|T_{01}|^2 - 2\epsilon|T_{10}|^2}{N_T + \epsilon N_L}. \quad (11.25)$$

The expressions of N_L and N_T in terms of the helicity amplitudes are given in equation D.25 and D.26 respectively. Taking into account the results presented in paragraph 11.8, one can safely neglect the terms containing $|T_{10}|$ with respect to $|T_{01}|^2$ in equation 11.25, leading to the following estimation of Δ

$$\Delta \approx \frac{|T_{01}|}{\sqrt{N_T + \epsilon N_L}} \approx r_{00}^5 \sqrt{\frac{\epsilon}{2r_{00}^{04}}}, \quad (11.26)$$

where it is assumed that T_{00} and T_{01} are in phase and where the term proportional to $|T_{01}|^2$ in r_{00}^{04} was neglected with respect to the term containing $|T_{00}|^2$. The obtained results for R_ρ as function of Q^2 are listed in table B.11. Taking the s -channel helicity non-conserving effects into account results in a decrease of R_ρ between 2.5 and 11 % depending on the bin in Q^2 . This change is still contained within the statistical uncertainty of the measurement and indicates that R_ρ is rather stable with respect to small violations of SCHC.

The results for R_ρ as function of Q^2 under the assumption of SCHC are compared to data from previous measurements in figure 11.13. A good agreement between the HERMES results and the existing high energy data is found. R_ρ exhibits a steep rise at low Q^2 , while at higher Q^2 the dependence of R_ρ on Q^2 becomes weaker. The longitudinal component of the cross section is seen to dominate the transverse part for $Q^2 \gtrsim 2 \text{ GeV}^2$. The observed agreement between the HERMES result at intermediate energy and the data from high energy measurements suggests that R_ρ is not a strong function of W .

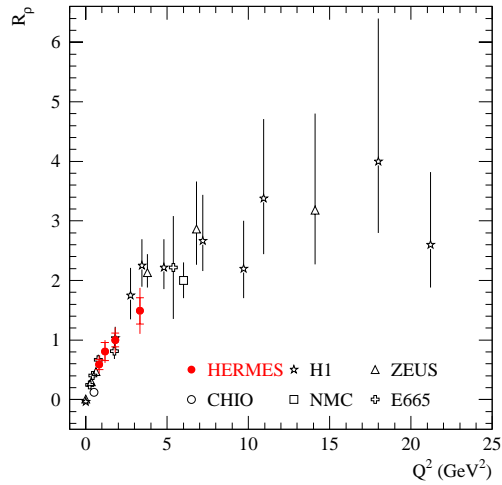


Figure 11.13: The R_ρ ratio as function of Q^2 , derived under the assumption of SCHC. The data are compared to previous measurements from CHIO [113], NMC [100], E665 [99], ZEUS [129, 131] and H1 [130, 132, 133].

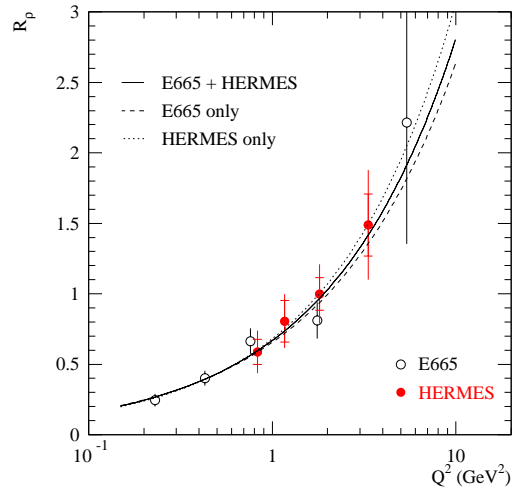


Figure 11.14: The measured R_ρ ratio fitted with expression 11.27. The full line shows the fit obtained with the combined data from E665 [99] and our result. For comparison, the dashed (dotted) line indicates the fit for the E665 (HERMES) data only.

The obtained Q^2 dependence of the R_ρ (assuming SCHC) was fitted using the form

$$R_\rho(Q^2) = c_0 \left(\frac{Q^2}{M_V^2} \right)^{c_1}, \quad (11.27)$$

with c_0 and c_1 as free parameters. This form is similar to the VDM-prediction given by equation 2.71, however the longitudinal and transverse cross section are allowed to differ by a certain power c_1 of Q^2 . As the available high Q^2 data indicate that the Q^2 -dependence of R_ρ flattens out above roughly 10 GeV^2 , this shape cannot be expected to describe all data lying much above the HERMES kinematical range. In a combined fit of the present result together with the data from E665 [99], the obtained values for the parameters were

$$c_0 = 0.48 \pm 0.03, \quad c_1 = 0.62 \pm 0.07. \quad (11.28)$$

The fitted curve is shown in figure 11.14. To verify that the inclusion of the E665 data in the fit does not bias the result, the fit was repeated for the HERMES and E665 data separately. The obtained values for c_0 and c_1 were all compatible within their uncertainty.

11.10 Extraction of δ

The phase difference δ between the transverse amplitude T_{11} and the longitudinal amplitude T_{00} can be derived from

$$\cos \delta = \frac{1 + \epsilon R_\rho}{\sqrt{R_\rho/2}} (\text{Re } r_{10}^5 - \text{Im } r_{10}^6), \quad (11.29)$$

$$\sin \delta = \frac{1 + \epsilon R_\rho}{\sqrt{R_\rho/2}} (\text{Im } r_{10}^7 + \text{Re } r_{10}^8). \quad (11.30)$$

Using the results listed in table B.8 one finds $\cos \delta = 0.872 \pm 0.028$ (stat.) ± 0.068 (syst.) and $\sin \delta = 0.43 \pm 0.16$ (stat.) ± 0.23 (syst.). These values are consistent with the result obtained in paragraph 11.8 for the phase difference $\phi_{11} - \phi_{00} = 26.5 \pm 8.3$ deg.

An alternative extraction of δ can be done using the 2-dimensional decay angle distribution given in equation 2.134, which assumes SCHC and NPE. This equation was used in a 2-dimensional maximum likelihood algorithm with only two parameters, R_ρ and δ . The procedure was performed separately for the negative and positive beam helicity sample as function of Q^2 in the same binning as for the full extraction. The final values were obtained as the error weighted average of the results belonging to the two different beam helicity samples.

Figure 11.15 displays the results for R_ρ and $\cos \delta$ as function of Q^2 extracted with the 2-parameter maximum likelihood method compared to the results obtained from the full 15 SDME extraction. The two sets of results are seen to be in very good agreement. The results for $\cos \delta$ obtained using equation 11.29 are listed in table B.11. The data indicate that the dominating transverse and longitudinal amplitudes are nearly in phase. The same observation was made in previous measurements [113, 143, 130].

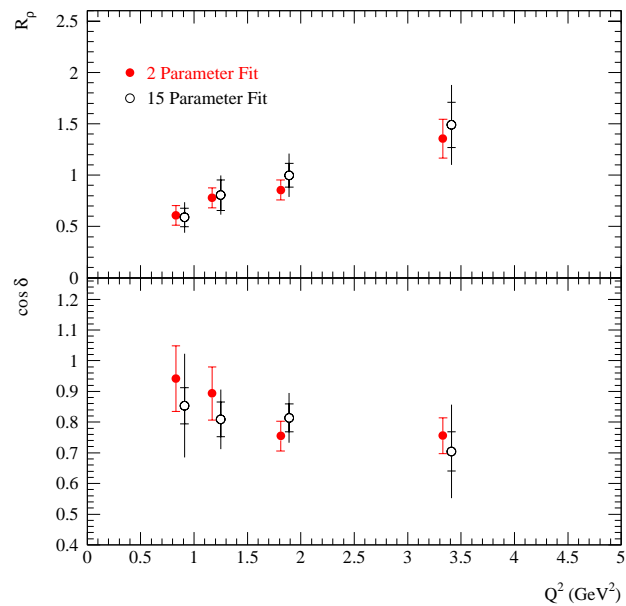


Figure 11.15: Results for R_ρ and $\cos \delta$ as function of Q^2 obtained from the full 15 SDME extraction and the simplified 2-parameter fit method. For the 2-parameter fit only statistical errors are shown. For the 15-parameter fit the inner error bars are statistical, the outer error bars have the systematic uncertainty added in quadrature.

resolution effects.

The ρ^0 and ω virtual photoproduction cross sections $\gamma^*p \rightarrow Vp$ were determined from the 1996-97 HERMES data taken on a proton target. The absolute luminosity normalization was derived from the number of DIS events in the data sample and the known value of the DIS cross section within the HERMES acceptance. Acceptance and reconstruction efficiency corrections were computed using a VDM-based generator for the ρ^0 and the DIPSI generator for the ω . The total acceptance varied between 1 % and 8 % for the ρ^0 and between 0.3 % and 0.8 % for the ω . The LEPTO generator was used to correct the data for background from deep-inelastic fragmentation processes. An average signal-to-background ratio of 11.5 for the ρ^0 and 3.5 for the ω was found. Radiative corrections were computed with the DIFFRAD code and amounted to about 12 to 15 % for the ρ^0 and about 8 to 10 % for the ω analysis. Based on the measured ratios of double to single-dissociative ρ^0 production by the ZEUS and H1 collaboration, the contribution to the ρ^0 and ω event sample due to double-dissociative diffraction was estimated to be about 7.5 % and 13 % respectively. The measured virtual photoproduction cross sections were found to be consistent with the existing world data. The HERMES data form the bridge between the strongly decreasing data at low W and the slowly rising data at high W .

Fits to the Q^2 -dependence of the cross sections yielded values for the real photoproduction cross sections compatible with world data collected at $Q^2 = 0$. A deviation from the predicted $1/(Q^2)^n$ behavior in the vector meson dominance model with $n = 2$ is observed. Both the ρ^0 and ω cross sections gave a value of $n \approx 2.5$, which is compatible with earlier measurements from E665 and H1. This indicated that the HERMES kinematic range is situated in the transition region between the VDM described non-perturbative region with $n = 2$ and the perturbative regime at high Q^2 where a behavior with $n = 3$ is predicted. A separation of the ρ^0 cross section into its transverse and longitudinal component indicated that the transverse contribution dominates the low Q^2 region, while from $Q^2 \approx 2 \text{ GeV}^2$ on the longitudinal part becomes the most important.

The cross sections could be described well by the model from Haakman *et al.*, which links vector meson production to a Regge based parametrization of the proton structure function F_2 . Model calculations from Vanderhaeghen *et al.* in the off-forward parton distribution formalism indicate that the dominant contribution to light vector meson production in the HERMES kinematic region comes from quark-exchange diagrams, while the 2-gluon exchange amplitude is too small to account for the observed magnitude of the cross section.

The measured ratio of exclusive ω to ρ^0 production was on average 0.19 ± 0.06 and showed no variation with Q^2 . This result comes close to the asymptotically expected additive quark model value of $1/9$.

The dependence on the momentum transfer t' of the cross section for ρ^0 and ω production could be well described by an exponential $e^{-b|t'|}$ characterized by a diffractive slope parameter b . The diffractive slope parameters for ρ^0 and ω production were found to be compatible and were around 7 GeV^{-2} . The ρ^0 slope parameter exhibited a decreasing behavior with Q^2 , which is interpreted as a shrinkage of the vector meson radius with Q^2 . This observation points towards the small distance scales of the interaction at high Q^2 , which justify the use of perturbative QCD models to describe vector meson production

Chapter 12

Conclusions

In this work the diffractive production of ρ^0 and ω vector mesons was studied experimentally at HERMES via positron scattering on the nucleon and on composite nuclear targets. The main results for the ρ^0 and ω were obtained in the kinematic region of the photon virtuality between $0.7 < Q^2 < 5.0 \text{ GeV}^2$ and the center-of-mass energy between $4.0 < W < 6.0 \text{ GeV}$. A separate analysis was performed for the ω meson in the quasi-real photoproduction region. The ρ^0 was identified in the 2-pion decay mode, while the dominant signal of ω production was found in the 3-pion channel. The results presented here were extracted from the HERMES data taken during the HERA 1995-97 running period.

The resonance corresponding to the ρ^0 meson in the 2-pion invariant mass distribution could not be described with a simple p -wave Breit-Wigner resonance shape. An excess of events towards the lower mass end and a lack of events at the high end of the resonance was observed in the data. This so-called skewing effect is assumed to be due to the interference of the ρ^0 production amplitude with the non-resonant pion pair production background process. The invariant mass distribution could be well described with the Ross and Stodolsky shape and the Söding parametrization, which take the observed skewing of the ρ^0 resonance with respect to a relativistic p -wave Breit-Wigner shape into account in a phenomenological way. The skewing was shown to be a strong function of Q^2 . Comparison with world data leads to the conclusion that the skewing is not very energy dependent, but decreases for increasing Q^2 to disappear completely at high Q^2 . The strong t dependence of the skewing seen by low Q^2 experiments was not observed here, indicating that this dependence seems to weaken towards higher Q^2 .

The data exhibited a clear signal of $\rho^0 - \omega$ interference. The magnitude and phase of the interference was determined and found to be compatible with previous measurements. The interference effect could be well described with a model from Niesler *et al.* based on the behavior of the pion form factor.

In the 3-pion invariant mass distribution the ω resonance was described well by a non-relativistic Breit-Wigner curve convoluted with a Gaussian shape to account for detector

in that region.

The effect of a nuclear medium on the production of ρ^0 and ω mesons was investigated by determining the nuclear transparency of ^2H , ^3He and ^{14}N for these reactions. The transparency expresses the ratio of the production cross section on a composite nuclear target to the cross section one would obtain in the absence of any initial or final state interactions between the scattering particles and the nucleus. Previous HERMES measurements of the nuclear transparency for ρ^0 production on ^{14}N allowed to separate the initial from the final state interactions and found that they were comparable in magnitude. Here the nuclear transparency determined for ω production was found compatible with the results obtained for the ρ^0 meson.

The $\gamma p \rightarrow \omega p$ cross section was determined from the 1997 HERMES data taken on a ^1H target with the quasi-real photoproduction trigger. This trigger is based on the detection of the produced hadrons only, since for low Q^2 events the incoming positron is scattered outside the detector acceptance. Due to the missing scattered positron information, the event kinematics can only be reconstructed partially and no measure of exclusivity of the reaction as in the case of the standard trigger events is available to suppress the non-exclusive background. Monte Carlo simulations based on the PYTHIA generator indicate that the background from fragmentation processes in the ω sample was about 70 %. This large amount of background in the sample hampered the comparison of the data with Monte Carlo simulations for exclusive ω production, which were needed to compute the acceptance correction for the absolute cross section. A single data point for the ω cross section was measured in the $3.0 < W < 5.0$ GeV region and was found to be compatible with the data from previous fixed target experiments. Although the statistical precision of the measurement was very high, the systematic uncertainty amounted to more than 40 %. The dominant contributions to the total error came from the uncertainty in the background subtraction and the acceptance correction.

The ρ^0 spin density matrix elements describing the helicity transfer were determined from the HERMES 1996-97 data on ^1H . Several extraction methods were discussed and the finally selected algorithm was a maximum likelihood procedure. With the longitudinal beam polarization HERMES is able to measure all 23 matrix elements. A small violation of the s -channel helicity conservation hypothesis was found via significantly non-zero values for r_{00}^s . The data indicated that ρ^0 production by transverse photons is dominated by natural parity exchange in the t -channel. The Q^2 -behavior of the 15 unpolarized SDME's was extracted from the data and indicated a rising behavior of the SCHC violating matrix element r_{00}^s . The magnitude of the different SDME's was well reproduced by the models based on 2-gluon exchange from Ivanov *et al.* and Royen *et al.*. From the 23 SDME's ratios of the helicity amplitudes and the phase difference between the transverse and longitudinal amplitudes were extracted. A ratio of the single-flip amplitude for the production of longitudinal mesons by transverse photons to the non-flip longitudinal amplitude was found of 15.1 ± 3.5 %. The single-flip amplitude for the production of transverse mesons by longitudinal photons was compatible with zero. The dominant helicity conserving transverse and longitudinal amplitudes were found to be nearly in phase. Finally, the SDME's allowed an extraction of F_p , which was consistent with previously measured world data.

Summarizing, in this work it was tried to provide a complete experimental picture of diffractive ρ^0 and ω production on the nucleon in the energy region $W \approx 5$ GeV at

moderate Q^2 below 5 GeV 2 . The results indicate that this kinematic domain forms the transition between the low energy region dominated by Reggeon exchange and the high energy domain where the production is governed by the Pomeron. In contrast to the high energy region, where the gluonic content of the Pomeron is probed, in this intermediate kinematic domain the quark contribution to the Pomeron becomes more important. The data point towards the need to include the effects of small helicity-flip amplitudes in the description of diffractive vector meson production.

Appendix A

Data Quality Summary Tables

The following tables summarize the results of the data quality burst selection criteria as explained and listed in section 6.1. Note that for the 1996-97 data the numbers given below correspond to the entire data taking year containing different polarized and unpolarized target gasses.

Quantity	# bursts passed (%)	# bursts remaining (incom., %)
Live time	93.01	93.01
Burst length	99.99	93.01
Beam current	99.47	92.57
Luminosity rate	98.50	91.51
First burst	97.69	89.55
Last burst	99.89	89.47
μ DST problems	86.72	78.93
Logbook DQ	81.02	65.13
GMS calorimeter	96.37	62.30
GMS H2 & Lumi. mon.	98.13	61.85
TRD DQ	95.50	60.88
HV trips	98.40	60.11
Čerenkov DQ	91.66	58.48
Total # bursts remaining		278556

Table A.2: The results of the 1996 data quality burst selection.

Quantity	# bursts passed (%)	# bursts remaining (incom., %)
First burst	94.76	94.76
Last burst	98.25	93.01
Live time	96.41	92.44
Burst length	99.50	92.43
Beam current	99.19	91.68
Target density	98.38	90.85
Luminosity rate	99.14	90.55
Lumi./curr./dens.	97.34	89.59
FC efficiency	80.41	72.84
BC efficiency	100.00	72.84
GMS calorimeter	97.88	71.15
GMS preshower	99.04	70.74
HI scaler	99.21	70.23
Preshower scaler	99.87	70.23
Čerenkov & TRD DQ	90.64	66.80
Logbook DQ	100.00	66.80
Previous / next burst	74.07	62.01
Total # bursts remaining		103506

Table A.1: The results of the 1995 data quality burst selection.

Quantity	# bursts passed (%)	# bursts remaining (incom., %)
Live time	94.51	94.51
Burst length	100.00	94.51
Beam current	99.94	94.47
Luminosity rate	99.37	94.04
First burst	98.07	92.21
Last burst	99.95	92.18
μ DST problems	98.60	91.01
Logbook DQ	97.78	89.24
GMS calorimeter	99.11	88.62
GMS H2 & Lumi. mon.	96.73	86.81
TRD DQ	98.67	86.36
HV trips	98.21	85.04
Čerenkov DQ	99.47	84.61
VC DQ	97.78	82.65
Total # bursts remaining		667924

Table A.3: The results of the 1997 data quality burst selection.

Appendix B

Tables

This appendix collects all tables containing the results obtained in this work.

$\langle Q^2 \rangle$ (GeV ²)	n_{skew}	A_I/A_{reso} (GeV)	$ A_{nr}/A_{reso} $ (GeV ^{-1/2})
0.83	$3.64 \pm 0.28^{+0.38}_{-0.18}$	$0.251 \pm 0.024^{+0.031}_{-0.024}$	$0.447 \pm 0.040^{+0.055}_{-0.034}$
1.3	$2.75 \pm 0.18^{+0.59}_{-0.06}$	$0.164 \pm 0.012^{+0.040}_{-0.006}$	$0.322 \pm 0.022^{+0.076}_{-0.005}$
2.3	$2.11 \pm 0.30^{+0.35}_{-0.44}$	$0.129 \pm 0.028^{+0.025}_{-0.035}$	$0.252 \pm 0.036^{+0.045}_{-0.055}$
3.7	$1.49 \pm 0.49^{+0.32}_{-0.39}$	$0.071 \pm 0.024^{+0.033}_{-0.005}$	$0.177 \pm 0.059^{+0.036}_{-0.041}$

Table B.1: The Q^2 dependence of the ρ^0 resonance skewing. The first errors are statistical, while the second errors are systematic uncertainties.

$\langle t \rangle$ (GeV ²)	n_{skew}	$ A_{nr}/A_{reso} $ (GeV ^{-1/2})
0.05	$2.79 \pm 0.18^{+0.27}_{-0.13}$	$0.333 \pm 0.023^{+0.027}_{-0.011}$
0.14	$2.72 \pm 0.23^{+0.56}_{-0.13}$	$0.320 \pm 0.028^{+0.058}_{-0.018}$
0.25	$2.10 \pm 0.33^{+0.39}_{-0.42}$	$0.244 \pm 0.039^{+0.048}_{-0.049}$
0.37	$1.63 \pm 0.52^{+0.96}_{-0.00}$	$0.206 \pm 0.066^{+0.120}_{-0.000}$

Table B.2: The $|t|$ dependence of the ρ^0 resonance skewing. The first errors are statistical, while the second errors are systematic.

$\langle Q^2 \rangle$ (GeV ²)	$\langle W \rangle$ (GeV)	$\langle \epsilon \rangle$	$\sigma(\gamma^*p \rightarrow \rho^0p)$ (μb)
0.83	4.5	0.89	$2.31 \pm 0.10 \pm 0.45$
1.3		0.88	$1.01 \pm 0.02 \pm 0.12$
2.3		0.87	$0.37 \pm 0.01 \pm 0.03$
3.7		0.84	$0.15 \pm 0.01 \pm 0.02$
0.83	5.5	0.71	$1.64 \pm 0.06 \pm 0.21$
1.3		0.70	$0.85 \pm 0.03 \pm 0.10$
2.3		0.67	$0.34 \pm 0.02 \pm 0.03$
3.7		0.63	$0.11 \pm 0.01 \pm 0.03$

Table B.3: The measured virtual photoproduction cross section for exclusive ρ^0 production. The first errors are statistical, the second are systematic.

$\langle Q^2 \rangle$ (GeV ²)	$\langle W \rangle$ (GeV)	$\langle \epsilon \rangle$	$\sigma(\gamma^*p \rightarrow \omega p)$ (μb)
1.3	4.4	0.88	$0.11 \pm 0.02 \pm 0.03$
	5.4	0.70	$0.09 \pm 0.01 \pm 0.03$
1.0	4.8	0.83	$0.23 \pm 0.03 \pm 0.07$
2.5		0.78	$0.060 \pm 0.009 \pm 0.010$

Table B.4: The measured virtual photoproduction cross section for exclusive ω production. The first errors are statistical, the second are systematic.

$\langle Q^2 \rangle$ (GeV ²)	$\sigma(\gamma^*p \rightarrow \rho^0p)$ (μb)	$\sigma(\gamma^*p \rightarrow \omega p)/\sigma(\gamma^*p \rightarrow \rho^0p)$
1.0	1.36 ± 0.20	$0.17 \pm 0.02 \pm 0.06$
2.5	0.30 ± 0.06	$0.20 \pm 0.03 \pm 0.05$

Table B.5: The ω/ρ^0 production ratio as function of Q^2 . The first error indicated is statistical, while the second is the systematic uncertainty. The 2nd column denotes the extrapolated ρ^0 cross section to the average kinematical values of the ω analysis.

$\langle Q^2 \rangle$ (GeV ²)	b (GeV ⁻²) (no RC)	b (GeV ⁻²)
0.83	$7.16 \pm 0.30^{+0.56}_{-0.04}$	$7.42 \pm 0.31^{+0.60}_{-0.15}$
1.3	$6.90 \pm 0.20^{+0.50}_{-0.00}$	$7.21 \pm 0.21^{+0.55}_{-0.05}$
2.3	$6.66 \pm 0.29^{+0.50}_{-0.02}$	$7.08 \pm 0.30^{+0.59}_{-0.08}$
3.7	$5.77 \pm 0.46^{+0.50}_{-0.66}$	$6.32 \pm 0.47^{+0.63}_{-0.58}$

Table B.6: The measured diffractive slope parameters for exclusive ρ^0 production. Results with and without radiative corrections are given. The first errors are statistical, the second are systematic.

Target	$\langle l_c \rangle$ (fm)	T_A
^2H	2.3	$0.98 \pm 0.15^{+0.13}_{-0.08}$
^3He	2.3	$0.80 \pm 0.13^{+0.12}_{-0.07}$
^{14}N	2.1	$0.76 \pm 0.15^{+0.10}_{-0.16}$

Table B.7: The obtained nuclear transparency for incoherent exclusive ω production on ^2H , ^3He and ^{14}N . The first errors are statistical, the second are systematic.

Element	$\langle Q^2 \rangle = 1.3 \text{ GeV}^2$
r_{00}^{04}	$0.446 \pm 0.018 \pm 0.035$
$\text{Re } r_{10}^{04}$	$0.046 \pm 0.008 \pm 0.013$
r_{11}^{04}	$-0.024 \pm 0.013 \pm 0.017$
r_{11}^1	$-0.048 \pm 0.017 \pm 0.039$
r_{00}^1	$0.021 \pm 0.036 \pm 0.048$
$\text{Re } r_{10}^1$	$-0.043 \pm 0.016 \pm 0.019$
r_{1-1}^1	$0.227 \pm 0.022 \pm 0.047$
$\text{Im } r_{10}^2$	$0.025 \pm 0.015 \pm 0.019$
$\text{Im } r_{2-1}^2$	$-0.214 \pm 0.021 \pm 0.035$
r_{11}^5	$0.001 \pm 0.008 \pm 0.012$
r_{00}^5	$0.122 \pm 0.019 \pm 0.030$
$\text{Re } r_{10}^5$	$0.176 \pm 0.008 \pm 0.017$
r_{1-1}^5	$0.003 \pm 0.010 \pm 0.014$
$\text{Im } r_{10}^6$	$-0.165 \pm 0.007 \pm 0.020$
$\text{Im } r_{1-1}^6$	$0.001 \pm 0.009 \pm 0.012$
$\text{Im } r_{3-1}^3$	$-0.011 \pm 0.337 \pm 0.064$
$\text{Im } r_{1-1}^7$	$0.001 \pm 0.031 \pm 0.033$
$\text{Im } r_{10}^7$	$0.066 \pm 0.046 \pm 0.038$
$\text{Im } r_{1-1}^7$	$0.021 \pm 0.057 \pm 0.051$
r_{11}^8	$0.031 \pm 0.057 \pm 0.032$
r_{00}^8	$0.146 \pm 0.133 \pm 0.092$
$\text{Re } r_{10}^8$	$0.101 \pm 0.041 \pm 0.082$
r_{1-1}^8	$0.029 \pm 0.061 \pm 0.112$

Table B.8: The 23 ρ^0 spin density matrix elements. The first errors are statistical, the second are systematic.

Table B.9: The 15 unpolarized SDME for different bins in Q^2 . The first errors are statistical, the second systematic.

Element	$\langle Q^2 \rangle = 0.83 \text{ GeV}^2$	$\langle Q^2 \rangle = 1.2 \text{ GeV}^2$	$\langle Q^2 \rangle = 1.8 \text{ GeV}^2$	$\langle Q^2 \rangle = 3.3 \text{ GeV}^2$
r_{00}^{04}	$0.325 \pm 0.033 \pm 0.045$	$0.395 \pm 0.044 \pm 0.035$	$0.443 \pm 0.029 \pm 0.044$	$0.531 \pm 0.037 \pm 0.053$
$\text{Re } r_{10}^{04}$	$0.024 \pm 0.053 \pm 0.029$	$0.033 \pm 0.019 \pm 0.023$	$0.050 \pm 0.014 \pm 0.016$	$0.010 \pm 0.020 \pm 0.015$
r_{11}^{04}	$-0.004 \pm 0.032 \pm 0.039$	$-0.068 \pm 0.029 \pm 0.056$	$-0.037 \pm 0.025 \pm 0.035$	$-0.020 \pm 0.025 \pm 0.037$
r_{1-1}^{04}	$-0.106 \pm 0.063 \pm 0.077$	$0.032 \pm 0.060 \pm 0.079$	$0.017 \pm 0.058 \pm 0.071$	$0.037 \pm 0.089 \pm 0.159$
r_{00}^{10}	$0.024 \pm 0.033 \pm 0.070$	$-0.028 \pm 0.028 \pm 0.023$	$-0.029 \pm 0.024 \pm 0.025$	$-0.082 \pm 0.039 \pm 0.052$
r_{1-1}^{10}	$0.277 \pm 0.109 \pm 0.247$	$0.247 \pm 0.042 \pm 0.064$	$0.237 \pm 0.030 \pm 0.049$	$0.107 \pm 0.047 \pm 0.027$
$\text{Im } r_{10}^{10}$	$0.017 \pm 0.019 \pm 0.014$	$0.000 \pm 0.025 \pm 0.030$	$0.049 \pm 0.023 \pm 0.035$	$0.015 \pm 0.038 \pm 0.082$
$\text{Im } r_{1-1}^{10}$	$-0.266 \pm 0.065 \pm 0.061$	$-0.260 \pm 0.039 \pm 0.061$	$-0.207 \pm 0.034 \pm 0.054$	$-0.068 \pm 0.049 \pm 0.100$
r_{00}^{11}	$0.024 \pm 0.020 \pm 0.015$	$0.035 \pm 0.016 \pm 0.015$	$-0.009 \pm 0.012 \pm 0.012$	$-0.021 \pm 0.017 \pm 0.004$
r_{00}^{15}	$0.098 \pm 0.029 \pm 0.078$	$0.067 \pm 0.034 \pm 0.026$	$0.120 \pm 0.028 \pm 0.025$	$0.203 \pm 0.044 \pm 0.032$
$\text{Re } r_{10}^{15}$	$0.168 \pm 0.011 \pm 0.053$	$0.163 \pm 0.016 \pm 0.021$	$0.165 \pm 0.012 \pm 0.023$	$0.152 \pm 0.019 \pm 0.043$
r_{1-1}^{15}	$-0.145 \pm 0.017 \pm 0.021$	$-0.157 \pm 0.013 \pm 0.021$	$-0.155 \pm 0.013 \pm 0.021$	$-0.133 \pm 0.017 \pm 0.036$
$\text{Im } r_{10}^{15}$	$-0.028 \pm 0.017 \pm 0.010$	$0.008 \pm 0.015 \pm 0.020$	$0.002 \pm 0.014 \pm 0.034$	$0.004 \pm 0.022 \pm 0.014$

	$\langle Q^2 \rangle = 1.3 \text{ GeV}^2$
$ T_{11} / T_{00} $	0.952 ± 0.065
$ T_{01} / T_{00} $	0.151 ± 0.035
$ T_{10} / T_{00} $	0.008 ± 0.022
$\phi_{11} - \phi_{00}$ (deg)	26.5 ± 8.3

Table B.10: The results for the ρ^0 helicity amplitude ratios $|T_{11}|/|T_{00}|$, $|T_{01}|/|T_{00}|$ and $|T_{10}|/|T_{00}|$ and the phase difference $\phi_{11} - \phi_{00}$, extracted from the 23 SDME's.

$\langle Q^2 \rangle > (\text{GeV}^2)$	R_{ρ^0} (SCHC)	R_{ρ^0} (SCHNC)	$\cos \delta$
0.83	$0.59 \pm 0.09 \pm 0.12$	$0.56 \pm 0.09 \pm 0.13$	$0.854 \pm 0.059 \pm 0.159$
1.2	$0.81 \pm 0.15 \pm 0.12$	$0.79 \pm 0.15 \pm 0.12$	$0.809 \pm 0.056 \pm 0.079$
1.8	$1.00 \pm 0.12 \pm 0.18$	$0.95 \pm 0.11 \pm 0.17$	$0.814 \pm 0.045 \pm 0.067$
3.3	$1.49 \pm 0.22 \pm 0.32$	$1.32 \pm 0.21 \pm 0.29$	$0.704 \pm 0.064 \pm 0.138$

Table B.11: The results for R_{ρ^0} and $\cos \delta$ for different bins in Q^2 . The 2nd column gives the values for R_{ρ^0} under the assumption of SCHC. The 3rd column lists the results for R_{ρ^0} when the small SCHC non-conserving (SCHNC) effects are included. The first errors are statistical, the second are systematic.

Appendix C

Additional Figures

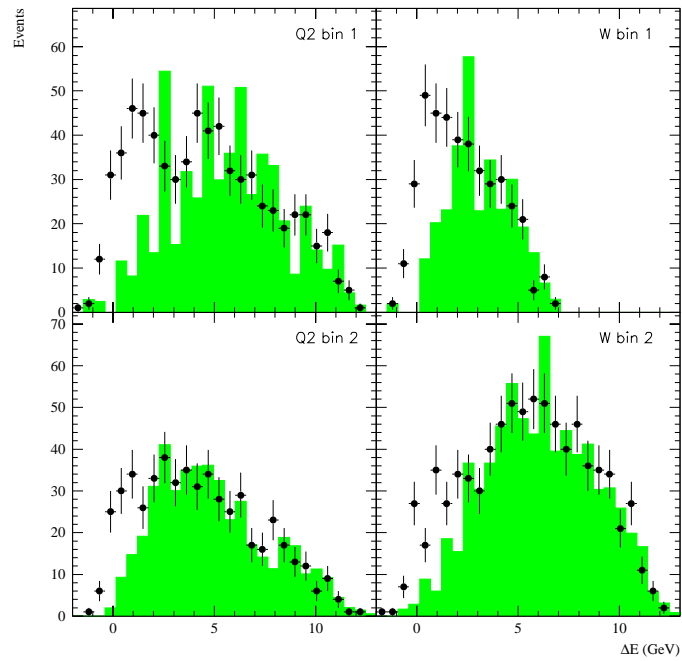


Figure C.1: The ω DIS background Monte Carlo Method applied to the different Q^2 and W bins. The dots represent the data, while the histograms are the DIS background Monte Carlo distributions normalized to the data in the region $\Delta E > 3.0$ GeV.

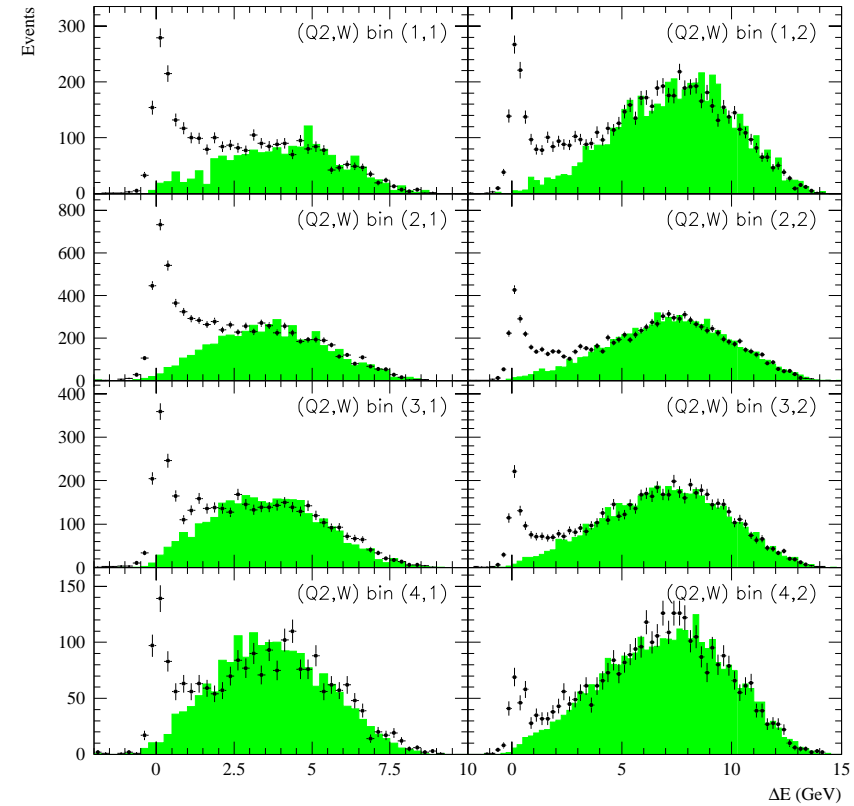


Figure C.2: The ρ^0 DIS background Monte Carlo Method applied to the different (Q^2, W) bins. The dots represent the data, while the histograms are the DIS background Monte Carlo distributions normalized to the data in the region $\Delta E > 3.0$ GeV.

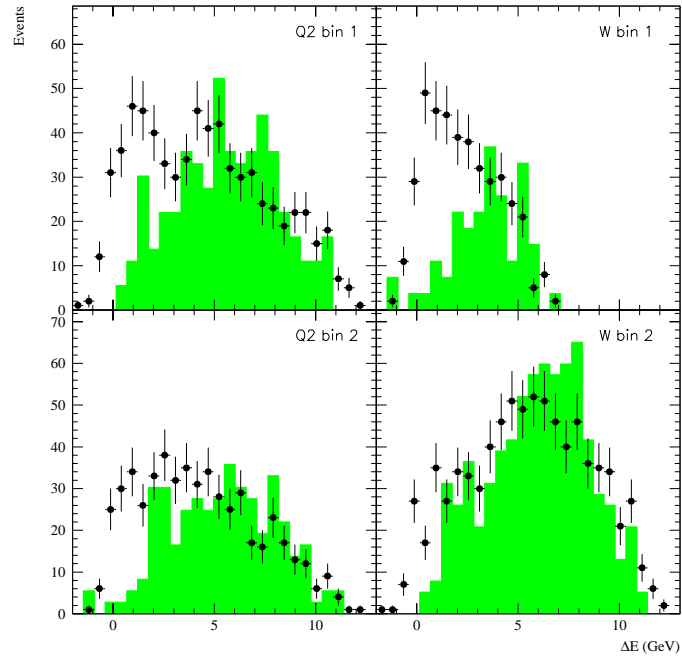


Figure C.3: The ω DIS background Zone Method applied to the different Q^2 and W bins. The dots represent the data, while the histograms are the DIS background distributions measured at $-t' > 0.8 \text{ GeV}^2$ and normalized to the data in the region $\Delta E > 3.0 \text{ GeV}$.

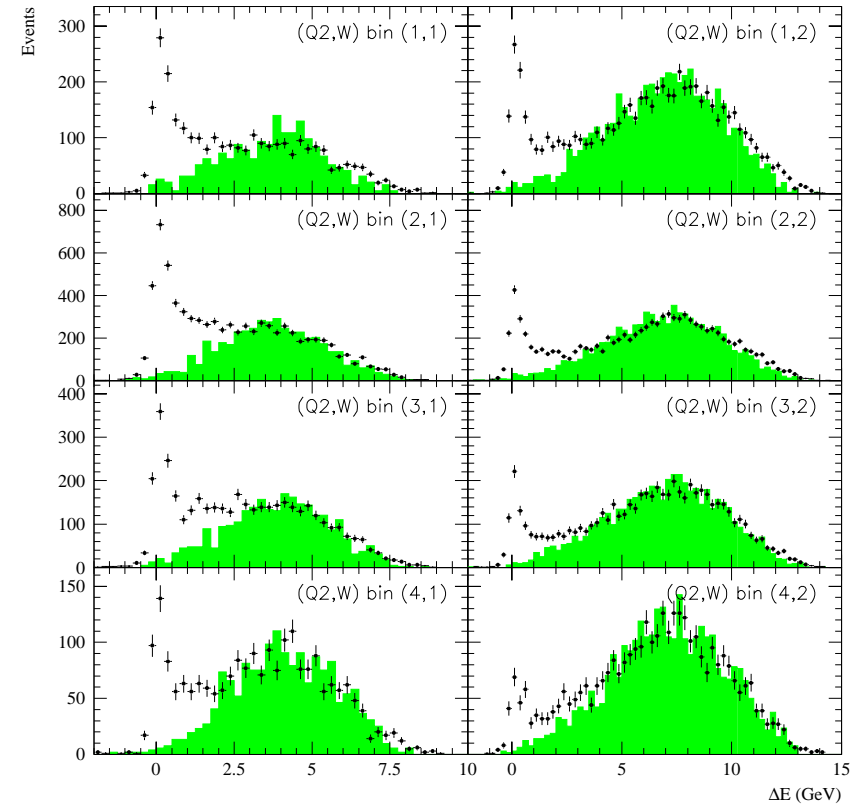


Figure C.4: The ρ^0 DIS background Zone Method applied to the different (Q^2, W) bins. The dots represent the data, while the histograms are the DIS background distributions measured at $-t' > 0.8 \text{ GeV}^2$ and normalized to the data in the region $\Delta E > 3.0 \text{ GeV}$.

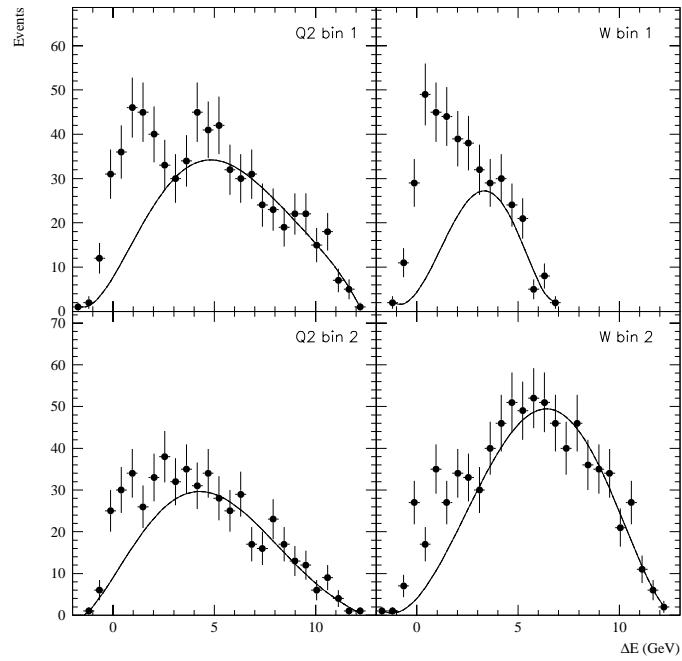


Figure C.5: The ω DIS background Fit Method applied to the different Q^2 and W bins. A 5th order polynomial function is fitted to the spectrum outside the region $[-0.75, 3.0]$, where the extrapolation of the function inside the exclusive region provides the amount of background contamination.

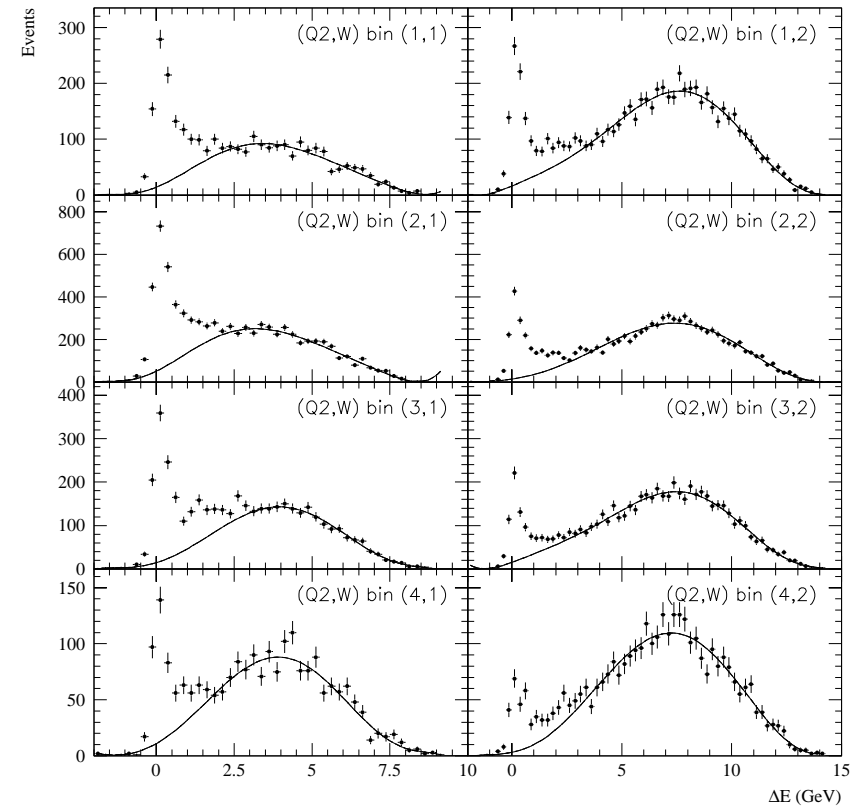


Figure C.6: The ρ^0 DIS background Fit Method applied to the different (Q^2, W) bins. A 7th order polynomial function is fitted to the spectrum outside the region $[-0.6, 3.0]$, where the extrapolation of the function inside the exclusive region provides the amount of background contamination.

Appendix D

Vector Meson Spin Density Matrix Elements

Here the 23 vector meson spin density matrix elements are given in terms of the helicity amplitudes $T_{\lambda_V \lambda_\Lambda}$. The expressions are derived from the equations listed in appendix A in reference [51]. The nucleon helicities are omitted and we assume an implicit summation over them.

$$r_{00}^{04} = \frac{1}{1 + \epsilon R} \left[\frac{1}{2N_T} (|T_{01}|^2 + |T_{0-1}|^2) + \frac{\epsilon R}{N_L} |T_{00}|^2 \right] \quad (\text{D.1})$$

$$\text{Re } r_{10}^{04} = \frac{1}{1 + \epsilon R} \text{Re} \left[\frac{1}{2N_T} (T_{11}T_{01}^* + T_{1-1}T_{0-1}^*) + \frac{\epsilon R}{N_L} T_{10}T_{00}^* \right] \quad (\text{D.2})$$

$$r_{1-1}^{04} = \frac{1}{1 + \epsilon R} \text{Re} \left[\frac{1}{2N_T} (T_{11}T_{-11}^* + T_{1-1}T_{-1-1}^*) + \frac{\epsilon R}{N_L} T_{10}T_{-10}^* \right] \quad (\text{D.3})$$

$$r_{00}^{11} = \frac{1}{1 + \epsilon R} \frac{1}{2N_T} (T_{0-1}T_{01}^* + T_{01}T_{0-1}^*) \quad (\text{D.4})$$

$$r_{11}^{11} = \frac{1}{1 + \epsilon R} \frac{1}{2N_T} (T_{1-1}T_{11}^* + T_{11}T_{1-1}^*) \quad (\text{D.5})$$

$$\text{Re } r_{10}^{11} = \frac{1}{1 + \epsilon R} \frac{1}{2N_T} \text{Re} (T_{1-1}T_{01}^* + T_{11}T_{0-1}^*) \quad (\text{D.6})$$

$$r_{1-1}^{11} = \frac{1}{1 + \epsilon R} \frac{1}{2N_T} (T_{1-1}T_{-11}^* + T_{11}T_{-1-1}^*) \quad (\text{D.7})$$

$$\text{Im } r_{10}^{20} = \frac{1}{1 + \epsilon R} \frac{1}{2N_T} \text{Re} (T_{1-1}T_{01}^* - T_{11}T_{0-1}^*) \quad (\text{D.8})$$

$$\text{Im } r_{1-1}^{20} = \frac{1}{1 + \epsilon R} \frac{1}{2N_T} \text{Re} (T_{1-1}T_{-11}^* - T_{11}T_{-1-1}^*) \quad (\text{D.9})$$

$$\text{Im } r_{10}^{33} = \frac{1}{1 + \epsilon R} \frac{1}{2N_T} \text{Im} (T_{11}T_{01}^* - T_{1-1}T_{0-1}^*) \quad (\text{D.10})$$

$$\text{Im } r_{1-1}^{33} = \frac{1}{1 + \epsilon R} \frac{1}{2N_T} \text{Im} (T_{11}T_{-11}^* - T_{1-1}T_{-1-1}^*) \quad (\text{D.11})$$

$$r_{00}^{55} = \frac{\sqrt{R}}{1 + \epsilon R} \frac{1}{\sqrt{2N_T N_L} 2} (T_{00}T_{01}^* + T_{01}T_{00}^* - T_{00}T_{0-1}^* - T_{0-1}T_{00}^*) \quad (\text{D.12})$$

$$r_{11}^{55} = \frac{\sqrt{R}}{1 + \epsilon R} \frac{1}{\sqrt{2N_T N_L} 2} (T_{10}T_{11}^* + T_{11}T_{10}^* - T_{10}T_{1-1}^* - T_{1-1}T_{10}^*) \quad (\text{D.13})$$

$$\text{Re } r_{10}^{55} = \frac{\sqrt{R}}{1 + \epsilon R} \frac{1}{\sqrt{2N_T N_L} 2} \text{Re} (T_{10}T_{01}^* + T_{11}T_{00}^* - T_{10}T_{0-1}^* - T_{1-1}T_{00}^*) \quad (\text{D.14})$$

$$r_{1-1}^{55} = \frac{\sqrt{R}}{1 + \epsilon R} \frac{1}{\sqrt{2N_T N_L} 2} (T_{10}T_{-11}^* + T_{11}T_{-10}^* - T_{10}T_{-1-1}^* - T_{1-1}T_{-10}^*) \quad (\text{D.15})$$

$$\text{Im } r_{10}^{66} = \frac{\sqrt{R}}{1 + \epsilon R} \frac{1}{\sqrt{2N_T N_L} 2} \text{Re} (T_{10}T_{01}^* - T_{11}T_{00}^* + T_{10}T_{0-1}^* - T_{1-1}T_{00}^*) \quad (\text{D.16})$$

$$\text{Im } r_{1-1}^{66} = \frac{\sqrt{R}}{1 + \epsilon R} \frac{1}{\sqrt{2N_T N_L} 2} \text{Re} (T_{10}T_{-11}^* - T_{11}T_{-10}^* + T_{10}T_{-1-1}^* - T_{1-1}T_{-10}^*) \quad (\text{D.17})$$

$$\text{Im } r_{10}^{70} = \frac{\sqrt{R}}{1 + \epsilon R} \frac{1}{\sqrt{2N_T N_L} 2} \text{Im} (T_{10}T_{01}^* + T_{11}T_{00}^* + T_{10}T_{0-1}^* + T_{1-1}T_{00}^*) \quad (\text{D.18})$$

$$\text{Im } r_{1-1}^{70} = \frac{\sqrt{R}}{1 + \epsilon R} \frac{1}{\sqrt{2N_T N_L} 2} \text{Im} (T_{10}T_{-11}^* + T_{11}T_{-10}^* + T_{10}T_{-1-1}^* + T_{1-1}T_{-10}^*) \quad (\text{D.19})$$

$$r_{00}^{80} = \frac{\sqrt{R}}{1 + \epsilon R} \frac{i}{\sqrt{2N_T N_L} 2} (T_{00}T_{01}^* - T_{01}T_{00}^* - T_{00}T_{0-1}^* + T_{0-1}T_{00}^*) \quad (\text{D.20})$$

$$r_{11}^{80} = \frac{\sqrt{R}}{1 + \epsilon R} \frac{i}{\sqrt{2N_T N_L} 2} (T_{10}T_{11}^* - T_{11}T_{10}^* - T_{10}T_{1-1}^* + T_{1-1}T_{10}^*) \quad (\text{D.21})$$

$$\text{Re } r_{10}^{80} = -\frac{\sqrt{R}}{1 + \epsilon R} \frac{1}{\sqrt{2N_T N_L} 2} \text{Im} (T_{10}T_{01}^* - T_{11}T_{00}^* - T_{10}T_{0-1}^* + T_{1-1}T_{00}^*) \quad (\text{D.22})$$

$$r_{1-1}^{80} = \frac{\sqrt{R}}{1 + \epsilon R} \frac{i}{\sqrt{2N_T N_L} 2} (T_{10}T_{-11}^* - T_{11}T_{-10}^* - T_{10}T_{-1-1}^* + T_{1-1}T_{-10}^*) \quad (\text{D.23})$$

The ratio R of the longitudinal to transverse $\gamma^* p$ cross section and the two normalization factors N_L and N_T are given by

$$R = \frac{N_L}{N_T}, \quad (\text{D.24})$$

$$N_L = |T_{00}|^2 + |T_{10}|^2 + |T_{-10}|^2, \quad (\text{D.25})$$

$$N_T = \frac{1}{2} (|T_{11}|^2 + |T_{-1-1}|^2 + |T_{01}|^2 + |T_{0-1}|^2 + |T_{1-1}|^2 + |T_{-11}|^2). \quad (\text{D.26})$$

Bibliography

- [1] K. Akerstaff *et al.*, Phys. Lett. **B404** (1997) 383;
A. Airapetian *et al.*, Phys. Lett. **B442** (1998) 484
- [2] K. Akerstaff *et al.*, Phys. Lett. **B464** (1999) 123
- [3] A. Airapetian *et al.*, Phys. Rev. Lett. **84** (2000) 2584
- [4] F.E. Close, *An Introduction to Quarks and Partons*, Academic Press (1979)
- [5] G. Altarelli and G. Parisi, Nucl. Phys. **B126** (1977) 298;
V.N. Gribov and L.N. Lipatov, Sov. J. Nucl. Phys. **15** (1972) 438,675
- [6] Y.Y. Balitsky and L.N. Lipatov, Sov. J. Nucl. Phys. **28** (1978) 822;
E.A. Kuraev, L.N. Lipatov and V.S. Fadin, Sov. Phys. JETP **45** (1977) 199;
L.N. Lipatov, Sov. J. Nucl. Phys. **23** (1976) 338
- [7] F.J. Gilman, Phys. Rev. **167** (1967) 1365
- [8] L.N. Hand, Phys. Rev. **129** (1963) 1834
- [9] E. Predazzi, *Diffraction: Past, Present and Future*, Proceedings of the International Workshop on Hadron Physics 98, Florianopolis, Ilha de Santa Catarina, Brazil, 1998, World Scientific Publishing (1999)
- [10] F.L. Pedrotti and L.S. Pedrotti, *Introduction to Optics*, Prentice-Hall International (1993)
- [11] G. Alberi and G. Goggi, Phys. Rep. **74** (1981) 1
- [12] A.B. Kaidalov, Phys. Rep. **50** (1979) 157
- [13] D.H. Perkins, *Introduction to High Energy Physics*, Addison-Wesley Publishing Company (1987)
- [14] K. Goulianos, Phys. Rep. **101** (1983) 169
- [15] P.D.B. Collins, *An Introduction to Regge Theory and High Energy Physics*, Cambridge University Press (1977)
- [16] V.N. Bolotov *et al.*, Nucl. Phys. **B73** (1974) 365
- [17] A. Donnachie and P.V. Landshoff, Nucl. Phys. **B311** (1989) 509
- [18] A. Donnachie and P.V. Landshoff, Phys. Lett. **B296** (1992) 227
- [19] J.R. Cudell, K. Kang and S.K. Kim, Phys. Lett. **B395** (1997) 311
- [20] A. Donnachie and P.V. Landshoff, Phys. Lett. **123B** (1983) 345; Nucl. Phys. **B231** (1984) 189
- [21] A. Brandt *et al.*, Phys. Lett. **B297** (1992) 417
- [22] G. Ingelman and P.E. Schlein, Phys. Lett. **B152** (1985) 256
- [23] C. Adloff *et al.*, Z. Phys. **C76** (1997) 613;
H1 Collab., *Measurement and Interpretation of the Diffractive Structure Function $F_2^{D(3)}$ at HERA*, Conf. Paper 571, 29th Intern. Conf. on High-Energy Physics, Vancouver, Canada, July 1998
- [24] M. Derrick *et al.*, Phys. Lett. **B356** (1995) 129
- [25] D.R. Yennie, Rev. Mod. Phys. **47** (1975) 311
- [26] J.J. Sakurai, Phys. Rev. Lett. **22** (1969) 981
- [27] C. del Papa *et al.*, Phys. Rev. **D19** (1979) 1303
- [28] J.J. Sakurai and D. Schildknecht, Phys. Lett. **40B** (1972) 121
- [29] D. Schildknecht, G.A. Schuler and B. Surrow, Phys. Lett. **B449** (1999) 328
- [30] H. Fraas, B.J. Read and D. Schildknecht, Nucl. Phys. **B86** (1975) 346
- [31] A. Donnachie and P.V. Landshoff, Phys. Lett. **B348** (1995) 213
- [32] J. Grosse-Knetter, *Measurement of Elastic ω Photoproduction at HERA*, PhD thesis, University of Hamburg (1997)
- [33] L.P.A. Haakman, A. Kaidalov and J.H. Koch, Phys. Lett. **B365** (1996) 411
- [34] A. Capella *et al.*, Phys. Lett. **B337** (1994) 358
- [35] X. Ji, Phys. Rev. Lett. **78** (1997) 610; Phys. Rev. **D55** (1997) 7114
- [36] M. Diehl, T. Gousset and B. Pire, *Exclusive Electroproduction and Off-diagonal Parton Distributions*, DESY-98-168, hep-ph/9811220
- [37] J.C. Collins, L. Frankfurt and M. Strikman, Phys. Rev. **D56** (1997) 2982
- [38] M.G. Ryskin, Z. Phys. **C57** (1993) 89
- [39] M.G. Ryskin, R.G. Roberts, A.D. Martin and E.M. Levin, Z. Phys. **C76** (1997) 231
- [40] C. Adloff *et al.*, Phys. Lett. **B483** (2000) 23
- [41] S.J. Brodsky, L. Frankfurt, J.F. Gunion, A.H. Mueller and M. Strikman, Phys. Rev. **D50** (1994) 3134

- [42] L. Frankfurt, W. Koepf and M. Strikman, Phys. Rev. **D54** (1996) 3194
- [43] V.L. Chernyak and A.R. Zhitnitski, Phys. Rep. **112** (1984) 173
- [44] A.D. Martin, M.G. Ryskin and T. Teubner, Phys. Rev. **D55** (1997) 4329
- [45] M. Vanderhaeghen, P.A.M. Guichon and M. Guidal, Phys. Rev. Lett. **80** (1998) 5064
- [46] M. Vanderhaeghen, P.A.M. Guichon and M. Guidal, Phys. Rev. **D60** (1999) 094017
- [47] A.D. Martin, R.G. Roberts, W.-J. Stirling and R.S. Thorne, Eur. Phys. J. **C4** (1998) 463
- [48] I. Royen and J.R. Cudell, Nucl. Phys. **B545** (1999) 505
- [49] J.R. Cudell and I. Royen, Phys. Lett. **B397** (1997) 317
- [50] K. Schilling, P. Seyboth and G. Wolf, Nucl. Phys. **B15** (1970) 397
- [51] K. Schilling and G. Wolf, Nucl. Phys. **B61** (1973) 381
- [52] H. Fraas, Ann. Phys. **87** (1974) 417
- [53] I. Royen, *Helicity in Diffractive Vector-meson Production*, submitted to Phys. Lett. B, hep-ph/0006044
- [54] I.P. Ivanov and N.N. Nikolaev, JETP Lett. **69** (1999) 294; E.V. Kuraev, N.N. Nikolaev and B.G. Zakharov, JETP Lett. **68** (1998) 696; I.P. Ivanov, private communication
- [55] J.A. Crittenden, *Exclusive Production of Neutral Vector Mesons at the Electron-Proton Collider HERA*, Springer Tracts in Modern Physics Volume 140, Springer-Verlag Berlin Heidelberg 1997
- [56] H. Newman *et al.*, *The First Year of MARK-J at PETRA*; Ch. Berger, *Results from the PLUTO Experiment on e^+e^- Reactions at High Energies*; TASSO Collaboration, G. Wolf, *TASSO Results on e^+e^- Annihilation Between 13 and 31.6 GeV and Evidence for Three Jet Events*; JADE Collaboration, S. Orito, *First Results from JADE*, Proc. of the 1979 International Symposium on Lepton and Photon Interactions at High Energies, Batavia, Illinois, USA, August 23-29, 1979, pp. 3, 19, 34, 52
- [57] I.M. Ternov, Yu. M. Loskutov and L.I. Korovina, Sov. Phys. JETP **14** (1962) 921
- [58] A.A. Sokolov and I.M. Ternov, Sov. Phys. Dokladi **8** (1964) 1203
- [59] L. Thomas, Philos. Mag. **3** (1927) 1; V. Bargmann, L. Michel and V.L. Telegdi, Phys. Rev. Lett. **2** (1959) 435
- [60] D.P. Barber *et al.*, Phys. Lett. **B343** (1995) 436
- [61] D.P. Barber *et al.*, Nucl. Instr. and Meth. **A338** (1994) 166

- [62] The HERMES Collaboration, *Technical Design Report*, DESY-PRC 93/06 (1993)
- [63] J. Buon, K. Steffen, Nucl. Instr. and Meth. **A245** (1986) 248
- [64] K. Steffen, "Siberian Snake" with Small Orbit Displacement for the Inversion of Transverse Spin Components in Ring Accelerators, DESY PET-78/11 (1978)
- [65] U. Fano, J. Op. Soc. Am. **39** (1949) 859
- [66] D. De Schepper *et al.*, Nucl. Instr. and Meth. **A419** (1998) 16
- [67] J.L. Friar *et al.*, Phys. Rev. **C42** (1990) 2310
- [68] F.D. Colegrove, L.D. Schearer and G.K. Walters, Phys. Rev. **132** (1963) 2561
- [69] M. Pinard and J. Van Der Linde, Can. J. Phys. **52** (1974) 1615
- [70] H. Kolster, *The HERMES Gaseous Internal Polarized Proton Target and its use in the HERA Positron Storage Ring*, PhD thesis, Ludwig-Maximilians-Universität München (1998)
- [71] J. Stewart, *The HERMES Polarized Hydrogen Internal Gas Target*, Proc. of the 7th International Workshop on Polarized Gas Targets and Polarized Beams, Urbana-Champaign, USA, Aug. 18-22, 1997, p. 69
- [72] B. Braun, *Spin Relaxation of Hydrogen and Deuterium in Storage Cells*, PhD thesis, Ludwig-Maximilians-Universität München (1995)
- [73] T. Benish, *Polarisierte Bhabha-Streuung und Lumineszenzmessung im HERMES-Experiment*, PhD thesis, Friedrich-Alexander-Universität Erlangen-Nürnberg (1998)
- [74] K. Ackerstaff *et al.*, Nucl. Instr. and Meth. **A417** (1998) 230
- [75] CERN-CN Division, *EPIO-Experimental Physics Input Output Package*, CERN Program Library Long Writeup H01, CERN (1993)
- [76] CERN-ECP Division, CERN PTG, Programming Techniques Group, *ADAMO-Entity-Relationship Programming System, Version 3.3*, CERN (1993), <http://www1.cern.ch/Adamo/>
- [77] W. Wander *et al.*, *DAD-Distributed Adamo Database System at HERMES*, Proc. of the International Conference on Computing in High Energy Physics, CHEP 95, Rio de Janeiro, Sep. 18-22, 1995
- [78] K. Ackerstaff *et al.*, *PINK: A Tcl/Tk-based Database Interface to ADAMO and DAD*, Proc. of the International Conference on Computing in High Energy Physics, CHEP 95, Rio de Janeiro, Sep. 18-22, 1995
- [79] M. Amarian *et al.*, , HERMES Internal Note 97-004, 1997
- [80] T. Ypsilantis and J. Seguinot, Nucl. Instr. and Meth. **A343** (1994) 30

- [81] E. Cisbani *et al.*, *The HERMES Implementation of the PCOS₄ System*, Proc. of the 1997 International Conference on Electronics for Particle Physics, LeCroy Corporation, Chestnut Ridge, New York, May 1997
- [82] R. De Leo *et al.*, Nucl. Instr. and Meth. **A401** (1997) 187
- [83] R. Forty, *RICH Detectors for LHC-B*, CERN LHC-B/96-5, 1996
- [84] R. De Leo *et al.*, *Chromatic Aberration and Forward Scattering of Light in Silica Aerogel*, Nucl. Instr. and Meth., in press
- [85] W. Wander, *Rekonstruktion hochenergetischer Streueignisse im HERMES Experiment*, PhD thesis, University Erlangen-Nürnberg (1996)
- [86] R. Kaiser, *Measurement of the Spin Structure of the Neutron using Polarised Deep Inelastic Scattering*, PhD thesis, Simon Fraser University (1997)
- [87] M. Dueren, P. Geiger, N. Makins, E. Volk *et al.*, *The HERMES Monte Carlo program*, <http://hermes.desy.de/hmc/>
- [88] G. Ingelman, A. Edin and J. Rathsmann, Comp. Phys. Comm. **101** (1997) 108
- [89] T. Sjöstrand, Comp. Phys. Comm. **82** (1994) 74
- [90] B. Andersson, G. Gustafson, G. Ingelman and T. Sjöstrand, Phys. Rep. **97** (1983) 31
- [91] M. Maul, *The PEPSI Page - Polarized Electron-Proton Scattering Interactions*, <http://www.th.physik.uni-frankfurt.de/~maul/pepsi.html>
- [92] G. Ingelman, J. Rathsmann, G.A. Schuler, Comp. Phys. Comm. **101** (1997) 135
- [93] CERN-CN Division, *GEANT - Detector Description and Simulation Tool*, CERN Program Library Long Writup W5013, CERN (1993)
- [94] Particle Data Group, C. Caso *et al.*, Eur. Phys. J. **C3** (1998) 1
- [95] HERMES g_n^1 group, N. Akopov *et al.*, *Determination of the 1995 Data Quality and the Extraction of the Spin Structure Function of the Neutron*, HERMES Internal Note 97-007
- [96] M. Kolstein, *ACE Manual, Efficiencies*, <http://www-hermes.desy.de/~machiel/ACEmanu/ACEmanu.html>
- [97] M. Amarian *et al.*, *Proposal for the Development of Recoil Detection at HERMES*, HERMES Internal Note 97-002
- [98] T.G. O'Neill, Private Communications
- [99] M.R. Adams *et al.*, Z. Phys. **C74** (1997) 237
- [100] M. Arneodo *et al.*, Nucl. Phys. **B429** (1994) 503; P. Amaudruz *et al.*, Z. Phys. **C54** (1992) 239

- [101] V.V. Anisovich and V.M. Shekhter, Nucl. Phys. **B55** (1973) 455
- [102] L. Cerrito, *Elettroproduzione di mesoni pseudoscalari con l'esperimento HERMES*, Diploma thesis, University of Rome 'La Sapienza' (1998)
- [103] T.G. O'Neill, no documentation available
- [104] L. Lyons, *Statistics for Nuclear and Particle Physicists*, Cambridge University Press (1986)
- [105] D.G. Cassel *et al.*, Phys. Rev. **D24** (1981) 2787
- [106] M.H. Schmitt, PhD thesis, Harvard University (1991)
- [107] M. Kolstein, *Exclusive ρ^0 Meson Electroproduction at HERMES*, PhD thesis, Vrije Universiteit Amsterdam (1998)
- [108] M. Arneodo, L. Lamberti and M. Ryskin, *DIPSI : a Monte Carlo Generator for Elastic Vector Meson Production in Charged Lepton-Proton Scattering*, Phys. Comp. Comm. **100** 195
- [109] H. Plotnow-Besch, Comp. Phys. Comm. **75** (1993) 396
- [110] J.E. Belz, *Rho Polarization in Exclusive $A(e, e'\rho^0)$* , HERMES Internal Note 96-052
- [111] L. Lamberti and A. Solano, *How to Use MC Weights for Physics Analysis*, ZEUS Internal Note 94-091
- [112] J.D. Jackson, Nuovo Cimento **34** (1964) 1644
- [113] W.D. Shambroom *et al.*, Phys. Rev. **D26** (1982) 1
- [114] F. Selleri, *Off-shell Pion-pion Scattering in the $T = J = 1$ State*, Phys. Lett. **3** (1962) 76
- [115] M. Derrick *et al.*, Z. Phys. **C69** (1995) 39
- [116] D. Aston *et al.*, Nucl. Phys. **B209** (1982) 56
- [117] M. Ross and L. Stodolsky, Phys. Rev. **149** (1966) 1172
- [118] P. Söding, Phys. Lett. **19** (1966) 702
- [119] S.D. Drell, Phys. Rev. Lett. **5** (1960) 278; Rev. Mod. Phys. **33** (1961) 458
- [120] M.G. Ryskin and Yu.M. Shabelski, Phys. Atom. Nucl. **61** (1998) 81
- [121] J. Park *et al.*, Nucl. Phys. **B36** (1972) 404
- [122] F. Bulos *et al.*, Phys. Rev. Lett. **22** (1969) 490
- [123] H.B. O'Connell, *Recent Developments in rho-omega mixing*, Proc. of the Joint Japan-Australia Workshop, Quarks, Hadrons and Nuclei, Institute for Theoretical Physics, Adelaide, Nov. 15-24, 1995, Austral. J. Phys. **50** (1997) 255

- [124] H.J. Behrend *et al.*, Phys. Rev. Lett. **27** (1971) 61
- [125] P.J. Biggs *et al.*, Phys. Rev. Lett. **24** (1970) 1201
- [126] G. Niesler, G. Piller and W. Weise, Phys. Lett. **B389** (1996) 157
- [127] L.M. Barkov *et al.*, Nucl. Phys. **B256** (1985) 365
- [128] T.H. Bauer, R.D. Spital, D.R. Yennie and F.M. Pipkin, Rev. Mod. Phys. **50** (1978) 261
- [129] J. Breitweg *et al.*, Eur. Phys. J. **C2** (1998) 247
- [130] C. Adloff *et al.*, Eur. Phys. J. **C13** (2000) 371
- [131] J. Breitweg *et al.*, Eur. Phys. J. **C6** (1999) 603
- [132] S. Aid *et al.*, Nucl. Phys. **B463** (1996) 3
- [133] S. Aid *et al.*, Nucl. Phys. **B468** (1996) 3
- [134] S. Brons, Private Communications
- [135] A. Bruell, Private Communications
- [136] B. Povh and J. Hüfner, Phys. Rev. Lett. **58** (1987) 1612
- [137] Y. Akimov *et al.*, Phys. Rev. **D14** (1976) 3148
- [138] C. Adloff *et al.*, Z. Phys. **C75** (1997) 607
- [139] H. Holtmann *et al.*, Z. Phys. **C69** (1996) 297
- [140] I. Akushevich, Eur. Phys. J. **C8** (1999) 457
- [141] I. Akushevich, *QED Radiative Effects in Diffractive Vector Meson Electro- and Photoproduction at HERA Energies*, hep-ph/9906410
- [142] M. Derrick *et al.*, Z. Phys. **C63** (1994) 391
- [143] P. Joos *et al.*, Nucl. Phys. **B113** (1976) 53
- [144] P. Joos *et al.*, Nucl. Phys. **B122** (1977) 365
- [145] H. de Vries *et al.*, At. Data Nucl. Data Tables **36** (1987) 495
- [146] B.Z. Kopeliovich, J. Nemchik, N.N. Nikolaev and B.G. Zakharov, Phys. Lett. **B309** (1993) 179
- [147] J. Hüfner, B. Kopeliovich and J. Nemchik, Phys. Lett. **B383** (1996) 362
- [148] K. Ackerstaff *et al.*, Phys. Rev. Lett. **82** (1999) 3025
- [149] M.R. Adams *et al.*, Phys. Rev. Lett. **74** (1995) 1525

- [150] G.N. McClellan *et al.*, Phys. Rev. Lett. **23** (1969) 554
- [151] T. Renk, G. Piller and W. Weise, *Coherence Effects in Diffractive Electroproduction of ρ Mesons from Nuclei*, hep-ph/0008109
- [152] F. Meißner, *Measurement of the J/P si -Cross Section and Double-Spin Asymmetries in Vector Meson Production in Polarised Lepton-Nucleon Scattering at HERMES*, PhD thesis, Humboldt-Universität Berlin (2000)
- [153] R.M. Eglhoff *et al.*, Phys. Rev. **43** (1979) 1545; Phys. Rev. **44** (1980) 690
- [154] A.M. Breakstone *et al.*, Phys. Rev. Lett. **47** (1981) 1782
- [155] M. Atkinson *et al.*, Nucl. Phys. **B231** (1984) 15
- [156] J. Busewitz *et al.*, Phys. Rev. **D40** (1989) 1
- [157] H.R. Crouch *et al.*, Phys. Rev. **155** (1967) 1468
- [158] R. Erbe *et al.*, Phys. Rev. **175** (1968) 1669
- [159] M. Davier *et al.*, Phys. Rev. **D1** (1970) 790
- [160] Y. Eisenberg *et al.*, Phys. Rev. **D5** (1972) 15
- [161] W. Struczinski *et al.*, Nucl. Phys. **B108** (1976) 45
- [162] D.P. Barber *et al.*, Z. Phys. **C26** (1984) 343
- [163] J. Ballam *et al.*, Phys. Rev. **D7** (1973) 3150
- [164] M. Derrick *et al.*, Z. Phys. **C73** (1996) 73
- [165] J. Breitweg *et al.*, Phys. Lett. **B487** (2000) 273
- [166] G. Zech, *Comparing Statistical Data to Monte Carlo Simulation - Parameter Fitting and Unfolding*, DESY-Report 95-115
- [167] CERN-CN Division, *MINUIT - Function Minimization and Error Analysis*, CERN Program Library Long Writeup **D506**, CERN (1992)
- [168] K. Ackerstaff *et al.*, Eur. Phys. J. **C18** (2000) 303
- [169] I. Akushevich and P. Kuzhir, Phys. Lett. **B474** (2000) 411
- [170] J. Breitweg *et al.*, Eur. Phys. J. **C12** (2000) 393
- [171] B. Clerbaux, *Elastic Production of Vector Mesons at HERA: Study of the Scale of the Interaction and Measurement of the Helicity Amplitudes*, hep-ph/9908519

Samenvatting

Het begrijpen en beschrijven van de fundamentele structuur van de materie vormt sinds het begin van vorige eeuw een belangrijke uitdaging voor zowel de experimentele als de theoretische natuurkunde. Volgens het standaardmodel van de deeltjesfysica vormen zes quarks en zes leptonen de basisbouwstenen van de materie. De gluonen, de ijkbosonen van de sterke wisselwerking, zijn verantwoordelijk voor de interacties tussen de quarks en binden deze samen in hadronen (opgebouwd uit drie quarks) en mesonen (bestaande uit één quark en één anti-quark).

Verstrooiingsexperimenten hebben steeds een cruciale en doorslaggevende rol gespeeld in de vooruitgang van de kennis over de substructuur van de materie. Een allereerste aanduiding voor de aanwezigheid van puntdeeltjes binnenin nucleonen werd gegeven door metingen van diep-inelastische verstrooiing. Hoewel heden ten dage de substructuur van nucleonen in termen van quarks en gluonen relatief goed begrepen wordt, was de ver-rassing groot toen met behulp van gepolarizeerde diep-inelastische verstrooiingsperi-menten aangetoond werd dat de spin van een nucleon voor minder dan de helft gedragen wordt door de spin van de quarks. Het ontbrekende gedeelte van de nucleonspin dient gezocht te worden bij de spin van de gluonen en bij het orbitaal impulsmoment van de quarks en gluonen in het nucleon. De nood aan een beter inzicht in deze complexe nucleonspinstructuur vormde de aanleiding voor een reeks nieuwe metingen, waarbij in 1995 aan het HERA (Hadron-Electron Ring Accelerator) complex te DESY (Deutsches Elektronen Synchrotron) het HERMES (HERA Measurement of Spin) experiment van start ging. HERMES was ontworpen als een precisie-experiment met als doel een zo com-pleet mogelijk beeld te geven van de spinstructuur van nucleonen. Dit werd bewerkstelligd via de verstrooiing van de gepolarizeerde elektron/positron bundel van HERA aan een (on)gepolarizeerde gasvormige target. Metingen van gepolarizeerde inclusieve verstrooiing $e\vec{p} \rightarrow e'X$ levert de inclusieve nucleonstructuurfunctie g_1 op, waaruit de totale bijdrage van de quarkspin tot de spin van het nucleon kan afgeleid worden. De bijdragen van de individuele quarks tot de spin kunnen bepaald worden via gepolarizeerde semi-inclusieve metingen $e\vec{p} \rightarrow e'hX$ van hadron productie.

De deeltjesidentificatiecapaciteiten van de HERMES detector laten naast een uitgebreid spinfysicaprogramma eveneens ruimte voor de studie van een brede waaier aan meson productieprocessen. Daarbij wordt een belangrijke klasse van mesonen gevormd door de zogenaamde vector mesonen, waar de spin-1/2 van de quark en anti-quark gekop-

peld zijn tot een spin-1 toestand. Dit werk behandelt de experimentele studie van diffrac-tieve ρ^0 en ω vector meson productie door middel van elektronverstrooiing in het kinema-tisch gebied van het HERMES experiment. De benaming 'diffractief' wordt in deze con-text gebruikt naar analogie met het in de optica reeds lang gekende fenomeen van diffractie van licht. Diffractieve interacties in hadron-hadron en foton-hadron verstrooiing vertonen een aantal typische kenmerken : de werkzame doorsnede heeft een sterk variërende ver-strooiingshoekdistributie met in de voorwaartse richting een maximum dat via een steile helling naar grotere hoeken toe afloopt, net zoals in de optica wordt waargenomen; bij hogere energie is de totale werkzame doorsnede vrijwel constant ofwel heel traag stij-gend; de helling van de aflopende flank van het centraal maximum in de hoekdistributie wordt groter naarmate de energie toeneemt. In deeltjesfysica omschrijft men diffractieve processen als zijnde reacties waarbij geen kwantumgetallen uitgewisseld worden tussen de verstrooiende deeltjes. Diffractieve interacties worden in de 's-kanaal' benadering beschreven met behulp van geometrische modellen. In deze modellen wordt de helling van de flank van het centraal maximum in de hoekdistributies gerelateerd aan de inter-actiestraal van de deeltjes in het verstrooiingsproces. De verstrooiing wordt gezien als een differentieële absorptie van de inkomende deeltjesgolven door het trefdeeltje, waarbij de golven elk met een verschillende werkzame doorsnede verstrooid worden en zo aanleiding geven tot de vorming van nieuwe deeltjes in de finale toestand. In de t-kanaal benade-ring worden diffractieve interacties goed beschreven door de zogenaamde Regge theorie, waarbij het gedrag van hadron-hadron interacties bepaald wordt door het optreden van singulariteiten of polen in de amplitude in het complexe angulaire momentenvlak. Het voorkomen van een zogenaamde Regge-pool in de verstrooiingsamplitude correspondeert met de uitwisseling van een deeltjesresonantie in het t-kanaal van de reactie, waarbij alle mogelijke uitwisselbare resonanties op een rechte lijn, een Regge-traject of Reggeon, liggen in een zogenaamd Chew-Frautschi diagram. Het energiegedrag van diffractieve in-teracties wordt dan volledig bepaald door dergelijke Regge-trajecten. Het geobserveerde licht stijgend gedrag van de werkzame doorsnede voor diffractieve interacties bij hoge energie leidde tot de postulering van het bestaan van een nieuw traject, het Pomeron. Het Pomeron draagt de kwantumgetallen van het vacuüm en is verantwoordelijk voor diffractieve productie bij hoge energie.

Diffractieve productie van vector mesonen wordt door een grote verscheidenheid aan theoretische modellen behandeld. In het vector meson dominantiemodel fluctueert het foton in een vector meson vóór de interactie met de trefkern, waarna het vector meson na een elastische verstrooiing in de finale toestand verschijnt. Op deze manier wordt fotoprotuctie van vector mesonen gelinkt aan elastische hadron-hadron interacties, die goed beschreven worden in termen van Regge- en Pomeronuitwisseling. Dit beeld van vector meson productie faalt echter zodra een 'harde' schaal in de reactie aanwezig is, i.e. reacties met hoge fotovirtualliteit, productie van zware quarks of processen met hoge impulsoverdracht. In dat geval baseert men zich op een beschrijving in perturbatieve kwantum chromodynamica. Men kan aantonen dat het reactieproces in het perturbatief gebied factoriseert in drie afzonderlijke delen : de fluctuatie van het foton in een quark-anti-quarkpaar, de harde interactie van het quark-anti-quark paar met het trefdeeltje en de vorming van het vector meson in de finale toestand. De harde interactie wordt meestal geparametriseerd als de uitwisseling van een kleurloos gluonpaar of een gluonladder.

Het HERMES experiment gebruikt de longitudinaal gepolarizeerde HERA leptonbun-

del om te verstrooien aan een gasvormige target bestaande uit al dan niet longitudinaal gepolariseerde nucleonen of lichte kernen. De HERMES spectrometer bestaat uit twee identieke helften gesitueerd boven en onder de HERA bundellijn. Geladen deeltjes worden onder invloed van een verticaal dipoolmagneetveld afgebogen in het horizontaal vlak, waarbij de impuls en het teken van de lading van de deeltjes kan bepaald worden uit de afbuigingshoek. Met behulp van vertexdetectoren en dradenkamers vóór en na de dipoolmagneet worden de trajecten en dus de verstrooiingshoeken van de geproduceerde deeltjes en het verstrooide lepton gereconstrueerd. Deeltjesidentificatie wordt verkregen via een elektromagnetische calorimeter, een shower-hodoscoop, een transitiestralingsdetector en een drempel-Cerenkovdetector. In de periode van 1995-97 liet dit systeem een zeer goede separatie van leptonen en hadronen toe. Vanaf 1998 werd de drempel-Cerenkovdetector vervangen door een ring-imaging Cerenkov detector (RICH) die toelaat een hadronidentificatie door te voeren over het volledige kinematische gebied bestreken door het HERMES experiment. In het experiment wordt de uitlezing van de detectoren gestuurd door verschillende soorten triggers. De standaard trigger registreert alle evenementen waarbij een verstrooid lepton gezien wordt door de detector. Processen bij lage Q^2 waarbij het lepton verdwijnt tussen de twee helften van de detector in, maar waarbij wel hadronen gezien worden in beide detectorhelften, worden geregistreerd door de zogenaamde fotoproductie trigger.

De identificatie van het ρ^0 en ω meson gebeurde aan de hand van detectie van hun vervaldeeltjes. Het ρ^0 vervalvrijwel uitsluitend in een $\pi^+\pi^-$ paar, terwijl de belangrijkste vervalmoden voor het ω meson het $\pi^+\pi^-\pi^0$ kanaal is, waarbij het π^0 op zijn beurt in 2 fotonen vervalv. Kandidaat evenementen voor de ρ^0 analyse bevatten 1 deeltjesspoor overeenkomend met het verstrooide lepton en 2 sporen corresponderend met hadronen met tegengestelde lading. Voor de ω analyse werden evenementen geselecteerd die 1 verstrooid positron bevatten, 2 tegengesteld geladen hadronen en 2 fotonen die gereconstrueerd konden worden tot een π^0 . Bijkomende voorwaarden op de reactiekinematieken werden opgelegd om exclusieve en diffractieve productie in de voorwaartse richting te selecteren. In het geval van de fotoproductie trigger wordt het verstrooid lepton niet geregistreerd en kan enkel met informatie van de vervalproducten van de mesonen gewerkt worden. De finale identificatie van de mesonen gebeurde aan de hand van het reconstrueren van invariante massaspectra, waarbij de resonanties behorende bij de mesonen als pieken tevoorschijn komen.

De verkregen massa en breedte van de ρ^0 en ω resonantie blijken in overeenstemming te zijn met de gegevens gepubliceerd door de 'particle data group'. De geobserveerde vorm van de ρ^0 meson resonantie in het 2-pion invariante massaspectrum vertoont afwijkingen t.o.v. de gebruikelijke p -golf Breit-Wigner resonantie vorm. Men observeert een onderschatting van de resonantie bij lage invariante massa, terwijl het hoge massa gedeelte overschat wordt. Dit zogenaamde 'skewing' effect kan verklaard worden als zijnde veroorzaakt door een interferentie van de amplitude voor resonante ρ^0 meson productie en een bijdrage van niet-resonante pionpaarproductie dat in feite als achtergrondproces optreedt. De ρ^0 meson resonantie in de invariante massa distributie kan goed beschreven worden met behulp van de Ross en Stodolsky vorm en de Söding parameterizatie, die de geobserveerde afwijking t.o.v. van de p -golf Breit-Wigner functie op fenomenologische wijze in acht nemen. De sterkte van de 'skewing' van de resonantie blijkt een sterke afhankelijkheid van de fotonvirtualiteit Q^2 te vertonen, waarbij het effect asymptotisch schijnt te verdwijnen.

De gemeten afhankelijkheid is in overeenstemming met gegevens van hoge energie experimenten, hetgeen doet vermoeden dat de sterkte van de 'skewing' weinig varieert met energie. In tegenstelling tot reële photoproductie metingen werd hier geen sterke variatie van de 'skewing' gevonden als functie van de impulsverdracht t' , hetgeen opnieuw in overeenstemming is met hoge energie gegevens. Het 2-pion invariante massa spectrum vertoont eveneens een duidelijk signaal van $\rho^0 - \omega$ interferentie. De gemeten amplitude en fase van de interferentie zijn consistent met bestaande gegevens. De interferentie wordt goed gereproduceerd in een model voor ρ^0 productie gebaseerd op het verloop van de pionvormfactor. De vorm van de ω resonantie in het 3-pion invariante massaspectrum wordt goed beschreven met behulp van een niet-relativistische p -golf Breit-Wigner resonantie vorm, geconvolueerd met een Gauss-curve die de detectorresolutie in acht neemt.

De totale werkzame doorsnede voor virtuele fotoproductie van ρ^0 en ω mesonen op het proton, $\gamma^*p \rightarrow Vp$, werd afgeleid uit de HERMES 1996-97 gegevens gemeten op een ^1H kern. De absolute normering van de gegevens was gebaseerd op een methode waarbij de totale geïntegreerde luminositeit bepaald werd uit de kennis van de werkzame doorsnede voor diep-inelastische verstrooiing en het gemeten aantal diep-inelastische verstrooiings-evenementen in het sample. De electroproductie werkzame doorsnede werd omgezet in een fotoproductie werkzame doorsnede door middel van een wegingsprocedure van de evenementen met een virtuele fotonfluxfactor. De metingen werden gecorrigeerd voor de detectorgeometrie-effecten en voor de detectie-efficiëntie met behulp van Monte Carlo simulaties gebaseerd op een vector meson dominantiemodelgenerator voor het ρ^0 en de DIPS1 generator voor het ω meson. De totale detectie-efficiëntie voor exclusieve productie van ρ^0 en ω mesonen was respectievelijk ongeveer 5% en 0.5%. Correcties voor achtergrond komende van fragmentatieprocessen werden bepaald via een Monte Carlo simulatie gebaseerd op de LEPTO generator voor diep-inelastische verstrooiing. Stralingscorrecties werden berekend met de DIFFRAD code en waren typisch van de orde van 10 tot 15%. Tenslotte werd een afschatting gemaakt van de dubbel-dissociatie diffractieve achtergrond, waarbij we beroep deden op de door ZEUS en H1 gemeten verhouding van dubbel- tot enkel-dissociatieve processen in ρ^0 productie. De finaal bekomen werkzame doorsneden zijn consistent met vorige metingen. Ze vormen de overgang van de gegevens bij lage energie, waar een sterk dalende werkzame doorsnede met energie wordt gevonden, en de gegevens bij hogere energie, waar het verloop van de werkzame doorsnede licht stijgend is. Modellen gebaseerd op meervoudige Pomeronuitwisseling geven een goede beschrijving van de energie-afhankelijkheid van de metingen. Uit een model dat gebruikt maakt van het zogenaamde 'off-forward' parton distributie formalisme, kunnen we afleiden dat in het HERMES kinematisch gebied de reactie-amplitude voor exclusieve ρ^0 en ω vector meson productie gedomineerd wordt door uitwisseling van quark-anti-quark paren, terwijl de bijdrage door 2-gluon uitwisseling te klein is om de grootte-orde van de gemeten werkzame doorsnede te verklaren. Vervolgens werd de Q^2 -afhankelijkheid van de werkzame doorsnede geparametriseerd met behulp van een door het vector meson dominantiemodel geïnspireerde vorm. Deze parameterizaties leveren de waarde voor de reële fotoproductie werkzame doorsnede op, die voor zowel het ρ^0 als het ω meson in overeenstemming is met bestaande gegevens. Diezelfde parameterizaties tonen ook aan dat de Q^2 -afhankelijkheid van de gemeten werkzame doorsnede afwijkt van het door het vector meson dominantiemodel voorspelde $1/(Q^2)^n$ gedrag met $n = 2$. Zowel de ρ^0 als de ω gegevens leveren een waarde voor $n \approx 2.5$ op. Dit gedrag wijst erop dat het HER-

MES kinematisch gebied zich in een overgangsfase bevindt tussen het niet-perturbatieve en perturbatieve QCD regime, waarbij voor het laatste een Q^2 verloop met $n = 3$ van de werkzame doorsnede verwacht wordt. Tenslotte werd de verhouding van de productieve werkzame doorsneden voor ω en ρ^0 mesonen bepaald. Deze verhouding vertoont geen Q^2 -afhankelijkheid en bedraagt ongeveer 0.19, hetgeen dicht bij de door het additief quarkmodel asymptotisch verwachte waarde 1/9 is.

Kenmerkend voor diffractieve interacties bij lage impulsoverdracht t is het exponentieel verloop $\propto e^{-|t|}$ van de werkzame doorsnede. De diffractieve hellingsparameter b kan gerelateerd worden aan de grootte of de interactiestraal van de botsende deeltjes. De gemeten hellingsparameters voor ρ^0 en ω productie blijken gelijk te zijn, hetgeen verwacht wordt uit de gelijksoortige quarkinhoud van beide mesonen. De hellingsparameter voor ρ^0 productie vertoont een dalend verloop met Q^2 , wat erop wijst dat de interactieschaal in ρ^0 (en ω) productie afneemt met Q^2 . Asymptotisch wordt de hellingsparameter alleen nog bepaald door de grootte van het proton.

Het effect van een nucleair medium op de productie van vector mesonen werd bestudeerd door de nucleaire transparantie te bepalen voor ${}^2\text{H}$, ${}^3\text{He}$ en ${}^{14}\text{N}$ kernen. Deze transparantie drukt de verhouding uit van de effectieve productie werkzame doorsnede op een kern tot de fictieve werkzame doorsnede zonder interactie van de reactie-deeltjes met het omgevende kernmateriaal. Metingen van deze transparantie laten toe een afzonderlijke maat af te schatten voor de initiële en finale toestandsinteracties van het foton en het vector meson met het kernmateriaal. De gemeten transparantie voor ω productie blijkt consistent te zijn met de resultaten voor het ρ^0 meson.

De gegevens behorende bij de fotoprotuctie trigger bieden een alternatieve manier om de werkzame doorsnede voor ω productie bij $Q^2 = 0$ te bepalen. Voor deze gegevens beschikt men niet over de kinematische informatie van het verstrooide positron, zodat geen rechtstreekse onderdrukking van achtergrond d.m.v. kinematische restricties kan doorgevoerd worden. Simulaties gebaseerd op de PYTHIA generator tonen aan de bijdrage van fragmentatieprocessen tot ω productie in het fotoprotuctie sample loopt op tot ongeveer 70 %, hetgeen aanleiding geeft tot zeer grote systematische fouten op het eindresultaat. De totale efficiëntie voor reconstructie van exclusieve ω productie met de fotoprotuctie trigger werd berekend via de DIPSI generator en bedroeg ongeveer 0.2 %. De efficiëntie van de fotoprotuctie trigger werd geschat op ongeveer 67 % voor de HERMES 1997 gegevens. De electroprotuctie werkzame doorsnede werd getransformeerd naar een reële fotoprotuctie werkzame doorsnede via een geïntegreerde flux factor voor reële fotonen. De finaal bekomen werkzame doorsnede was in goede overeenstemming met de resultaten van vorige experimenten, hoewel dit onderdeel van de analyse gekenmerkt wordt door zeer grote systematische onzekerheden.

De helicititeit van het spin-1 ρ^0 (ω) meson komt tot uiting in het angulair moment van de twee (drie) spin-0 pionen waarin het meson vervalt. Uit een studie van de hoekdistributies van deze vervaltproducten kan men informatie halen over de helicititeitsoverdracht in exclusieve vector meson productie. Een algemeen gangbare hypothese in vele theoretische berekeningen en in het vector meson dominante model is die van behoud van helicititeit in het s -kanaal, i.e. de helicititeit van het virtueel foton wordt onveranderd doorgegeven aan het vector meson en de protonspintoestand blijft behouden. De spintoestand van het vector meson wordt algemeen beschreven a.d.h.v. zijn spindichtheidsmatrix, waar-

van de matrixelementen verband houden met de helicititeitsamplitudes $T_{\lambda_V \lambda_\gamma}$ die de overgang van een foton met helicititeit λ_γ naar een vector meson met helicititeit λ_V weergeven. Na toepassing van symmetrie-eigenschappen, bekomt men 23 onafhankelijke matrixelementen. Met behulp van een niet-gepolarizeerde leptonbundel kan men er 15 van bepalen; de overblijvende 8 matrixelementen kunnen verkregen worden met een longitudinale bundel polarizatie. Verschillende algoritmes voor de extractie van deze matrixelementen uit de meetgegevens werden voorgesteld. Uiteindelijk werd gekozen voor een maximale waarschijnlijkheidsmethode, waarmee de 23 matrix elementen voor het ρ^0 meson bepaald werden. De resultaten tonen een kleine schending van de hypothese van behoud van helicititeit in het s -kanaal aan. Theoretische modellen gebaseerd op 2-gluon uitwisseling geven een goede beschrijving van de matrixelementen, hoewel de betrouwbaarheid van deze modellen in het HERMES kinematisch gebied in vraag kan gesteld worden. De extractie van de 15 niet-gepolarizeerde matrixelementen als functie van Q^2 werd eveneens uitgevoerd. De theoretische modellen geven ook hier een goede beschrijving van het verloop van de matrixelementen in Q^2 . Uit de matrixelementen werd uiteindelijk ook de verhouding van de helicititeitsamplitudes bepaald, hetgeen een verhouding van de spinflip tot de niet-flip amplitude van ongeveer 15 % opleverde. De Q^2 -afhankelijkheid van de amplitudeverhoudingen wordt correct beschreven door de modelberekeningen. Tenslotte werd uit de resultaten voor de matrixelementen de R -verhouding voor ρ^0 productie bepaald, die consistent blijkt te zijn met eerdere metingen bij hogere energie.

I owe a word of thanks to Justus Koch, Michel Guidal, Marc Vanderhaeghen, Igor Ivanov, Isabelle Royen and Thorsten Renk for providing me with the results of their theoretical model calculations. I also would like to mention Barbara Clerbaux who was so kind to send me several 'world data' kumacs making my life a bit easier during the writing phase.

Finally, I want to express my deepest gratitude towards my parents and my little partner in life, Ann, for their everlasting love and support and for wanting me to come home whenever I was on the move for the sake of science.

January 2001,

Michael

Acknowledgements

Although writing this thesis lying in front of you turned out to be a rather lonely activity, the long road of work preceding this final phase was definitely crowded with many people. Obtaining a PhD degree really seems to be a common group effort and it is therefore only natural to thank the large number of people for their direct or indirect contribution to this work.

In the first place I believe I should give credit to the HERMES Collaboration as a whole, as this was the apparatus generating the possibility to make this PhD. I enjoyed working together with the HERMES vector meson crew, being Sasha Borissov, Greg Rakness, Eric Belz, Machiel Kolstein, Falk Meissner, Tom O'Neill and Stephan Brons. Although it's always been a small group, it was nevertheless successful in producing a lot of interesting and beautiful HERMES results. Gratitude also goes to Elke Aschenauer for spending an at the time seemingly never ending amount of weeks, days, evenings and nights working together with me in the East Hall and Hall 2 during the assembling phase of the RICH. We've seen many good times and some bad times, but after all, it was a great experience. Finally I would like to thank all the people of the collaboration who were also there with me in Hamburg at moments when we had (no) time to have fun after (during) work and who made it worthwhile to be part of HERMES. They were the eating, drinking and party buddies, the Bistro pool players, the American football team and most certainly the hacky sack gang, being apart from those already mentioned, Balijeet Bains, Jeff Martin, Paul Carter, Hideyuki Kobayashi, Brendan Fox, Bryan Tipton, Antje Bruell, Johan Blouw, Evaristo Cisbani, Ralf Kaiser, James Ely, Taeksu Shin, Peter Jung, Naomi Makins, Kevin McIlhany, Andreas Most, Hugh Tallini, Mannuella Vinciter, Jan Visser, Erik Volk and probably many more whose name I forgot to mention here.

Back home in the institute in Gent I am indebted to my advisor Dirk Ryckbosch for keeping me in the experimental intermediate energy physics group after my diploma thesis and for letting me find my own way in the vast and still not entirely understood field of HERMES physics. I also want to thank our group leader Robert Van de Vyver together with the other colleagues Heidi Holvoet, Natalie Degrande, Luc Van Hoonbeke, Brecht Hommez and former group members Bob Lannoy, Gert de Meyer, Katty Van de Kerckhove, John MacKenzie and Dominique Marchand for creating a fun and most enjoyable daily working atmosphere, which always provided a welcome relief whenever our physics brains got overheated.